Quantum Transport in Encapsulated Graphene P-N junctions

Inauguraldissertation

zur
Erlangung der Würde eines Doktors der Philosophie
vorgelegt der
Philosophisch-Naturwissenschaftlichen Fakultät
der Universität Basel

von

Clevin Jürg Handschin
aus Rickenbach, Schweiz

Basel, 2017

Genehmigt von der Philosophisch-Naturwissenschaftlichen Fakultät
auf Antrag von
Prof. Dr. C. Schönenberger
Prof. Dr. P. Kim
Dr. J. Eroms

Basel, 19.09.17

Prof. Dr. Martin Spiess
Dekan

Contents

1 Introduction

Quantum transport

Two dimensional electron gases (2DEGs) have been an exceptional platform and a constant source of new discoveries in quantum physics [2] during the last decades. While for a long time 2DEGs fabricated by molecular beam epitaxy have been the working-horse of quantum transport measurements, with the discovery of graphene in 2004 [3] a new, truly two-dimensional material entered the field. Graphene is the name of a monolayer of sp^2 hybridized carbon atoms being packed into a two-dimensional (2D) honeycomb lattice. It is the basic building block for many other materials, such as 0D Buckminster fullerenes [4], 1D nanotubes [5] or 3D graphite. In theory graphene was studied already in the 1940s [6]. However, strictly 2D crystals such as graphene were presumed to be thermodynamically unstable [7, 8]. Experimental "indication" was given by the rapidly decreasing melting temperatures of thin films with decreasing thickness, where they become unstable at a thickness of typically a few tens of atomic layers. Therefore, until 2004 atomic monolayers where only known to exist as an integral part of 3D structure [9–11]. Soon after the discovery of graphene in 2004, in 2005 the two groups of A. Geim [12] and P. Kim [13] published just a few days apart from each other the observation of massless Dirac fermions in graphene. Within the few years since the experimental discovery of graphene it has risen from relative obscurity to the status of an exciting and promising model for 2D solids. The great interest in graphene can be attributed to its exceptional band structure which is described at low energies by the massless Dirac Hamiltonian, where the valence- and conduction-band touch each other at a single point (Dirac point). Being a zero-gap semi-conductor separates graphene from conventional metals and semi-conductors, making it unique of its kind.

Probably the most well known consequence of the Dirac spectrum is the observation of the half-integer quantum Hall effect [12, 13]. However, besides this there is a full list of features characteristic to graphene, ranging from Klein-tunneling through the gapless p-n junctions [14, 15], weak anti-localization in disordered graphene [16–18] to the additional valley degree of freedom which is a consequence of the two-atomic unit-cell [19, 20]. In fact, the latter is true for many layered 2D materials whose properties span a large spectrum including

insulators [21], semi-conductors [22], superconductors [23, 24] and even ferromagnets [25] which were recently discovered. The ability to combine graphene with various 2D materials in so called Van der Waals heterostructures [19] allows to taylor its properties almost at will.
The nearly defect-free grapene lattice holds the potential for ballistic transport over long distances. Futhermore, the refraction index across an *n-n'* (unipolar) junction or *p-n* (bipolar) junction can be tuned seamlessly from positive to negative which is unique for graphene. Combining the ballistic transport with the tunability of the refraction index across an interface makes clean graphene an excellent platform for the investigation of various electron optical experiments. Prominent examples of the latter, which have an optical counterpart, are electron guiding [26, 27] or lensing [28]. In contrast to photons, a magnetic field can be used additonaly to tune the motion of the charge carriers. Therefore, examples of ballistic transport effects without an optical counterpart are for example bend-resistances [29, 30], magnetic focusing [31–34] or snake states [35–38].
While the classical billiard model is sufficient for the explanation of the previously listed electron optical effects, there is as well a long list of effects for which quantum mechanical concepts have to be taken into account. Examples are Fabry-Pérot interferences [39–44] where the phase-relation between interfering waves is essential, or valley-valves [45] which depend on the valley-index of the wave-function.

Outline of this Thesis

This Thesis focuses on quantum transport phenomena in two-terminal graphene *p-n* junction, as this combines two bench-mark signatures in graphene, namely the observation of massless Dirac-fermions and the ability to establish gapless *p-n* junction. The Thesis starts with **chapter 2** where important concepts related to the unique electronic band structure of graphene are introduced. This includes the ability to establish gapless *p-n* junctions, approaches how to characterize clean graphene, including a definition and examples of ballistic and phase-coherent transport phenomena, the possibility to form superlattices with other layered materials such as hexagonal boron-nitride (hBN) or the possibility to address additional degrees of freedom such as the valley-isospin. In **chapter 3** a short comparison between suspension and encapsulation (in hBN) of graphene is given, since these two techniques are the most common ones to fabricate ultra-clean graphene. However, the fabricational details in **chapter 4** are restricted to the encapsulation technique since the most experiments presented in this Thesis are based on the latter. Furthermore, details on how to fabricate local top- and bottom-gates, which are needed to establish *p-n* junctions, are given. The currently most common method to establish electrical contact with hBN/graphene/hBN heterostructures is via so called "side-contacts" [1]. In **chapter 5** an alternative approach is introduced to establish inner point contacts, being compatible with the encapsulation-technique. The latter might be of special interest if an isolated electrical contact has to be established in the middle of a hBN/graphene/hBN heterostructure. With **chapter 6** the experimental part of the Thesis involving quantum transport in *p*-*n* junctions starts. In this chapter Fabry-Pérot resonances in a *p*-*n*-*p* device in the absence and presence of a Moiré superlattice are discussed. Fabry-Pérot resonances can be used to gain information about the exact position of the *p*-*n* junction as a function of charge carrier doping and on the yet not fully known band-reconstruction due to the Moiré superlattice. In **chapter 7** we report on three types of magnetoconductance oscillations which can occur along a graphene *p*-*n* junction. While several previous studies have tried to explain the observation of individual magnetoconductance oscillations [37, 38, 46, 47], none of them describes all at the same time. On the contrary, we present experimental results where three different kinds of oscillations are observed within the same device/measurement. The latter allows for a more direct comparison between the different types of mangetoconductance oscillations and we can rule out differences in various device architectures. Finally, we can describe the underlying physics of the different types of magnetoconductance oscillations with a consistent model. Upon further increasing the magnetic field to very high values, the transport is governed by the lowest Landau level. In combination with a *p*-*n* junction, which is located perpendicular to the transport direction, conductance oscillations resulting from valley-isospin physics are expected [45]. In **chapter 8** experimental results are presented which show signatures of this effect for the first time. By tuning the position of the *p*-*n* junction this allows to locally probe the relative edge configuration, giving rise to conductance oscillations in the order of e^2/h. In the last chapter, **chapter 9**, preliminary experimental results and theoretical calculations on the electrical counterpart of the Michelson Morley interferometer are presented.

2 Theoretical background

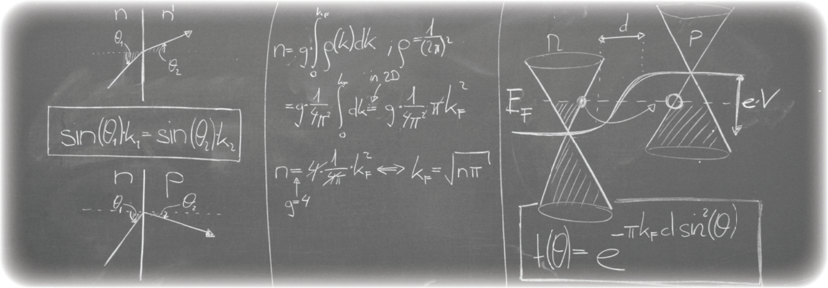

In this chapter the most important theoretical concepts of graphene, with regards to the experiments presented late on, are provided. First, the crystal-lattice of graphene and the resulting band structure are discussed, followed by some implications of this very unique band structure. This includes the pseudospin, the valley degree of freedom, the half-integer quantum Hall effect or the (gap-less) *p*-*n* junctions in graphene which allow negative refraction. Furthermore several methods to characterize the graphene quality are introduced, including a short introduction into ballistic and phase coherent transport. An additional section is dedicated to the formation of a Moiré superlattice and its implication for the graphene band structure. The first part of this chapter follows partially the References [48–50] where extensive details can be found.

2.1. Pristine Graphene

2.1.1. Band structure

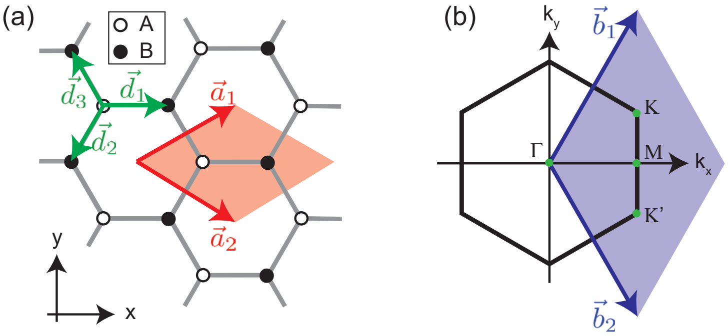

Figure 2.1. Graphene lattice in real and reciprocal space. a, The unit-cell (shaded in red) is spanned by the two unit vectors $\vec{a}_1$ and $\vec{a}_2$ including one atom of the A and B sublattice each. **b,** First Brillouin zone in reciprocal space with the reciprocal lattice vectors ($\vec{b}_1$ and $\vec{b}_2$). The 6 corners of the Brillouin zone are assigned to two inequivalent valleys K and K'.

Graphene consists of sp^2-hybridized carbon-atoms which are arranged in a honeycomb lattice as shown in Fig. 2.1a. While for each carbon-atom three of the four sp^2-hybridized electrons are used to form a covalent σ-bond to its neighbours, the last electron is placed in the π-orbital. The overlap between neighbouring π-bonds ensure that the electrons placed in this orbital are no longer localized, but form a de-localized π-electron system. The primitive unit-cell of the honeycomb lattice, which is spanned by the two lattice vectors

$$\vec{a}_1 = \frac{a_0}{2}\begin{pmatrix} 3 \\ \sqrt{3} \end{pmatrix} \qquad \text{and} \qquad \vec{a}_2 = \frac{a_0}{2}\begin{pmatrix} 3 \\ -\sqrt{3} \end{pmatrix}, \tag{2.1}$$

includes two atoms, which are commonly labelled as the A and B sublattice. The lattice vectors are given in units of a_0, which is the inter-carbon distance of $\sim 1.42\,\text{Å}$ [6]. Furthermore, the Bravais lattice of graphene is C_6 rotation symmetric. The first Brillouin zone of the honeycomb lattice is shown in Fig. 2.1b, where the reciprocal lattice vectors are given by

$$\vec{b}_1 = \frac{2\pi}{3a_0}\begin{pmatrix} 1 \\ \sqrt{3} \end{pmatrix} \qquad \text{and} \qquad \vec{b}_2 = \frac{2\pi}{3a_0}\begin{pmatrix} 1 \\ -\sqrt{3} \end{pmatrix}. \tag{2.2}$$

Of special interest are the the so called Dirac-points (DPs) which are situated at the K and K' points of the Brillouin zone. The latter are located at the positions

$$\vec{K} = \frac{2\pi}{3a_0}\begin{pmatrix}1\\ \sqrt{3}\end{pmatrix} \qquad \text{and} \qquad \vec{K}' = \frac{2\pi}{3a_0}\begin{pmatrix}1\\ -\sqrt{3}\end{pmatrix}, \tag{2.3}$$

respectively. The band structure of graphene can be derived with a tight-binding model, assuming that the charge carriers can hop to nearest neighbours. The nearest-neighbour vectors in real space are given by

$$\vec{d}_1 = a_0\begin{pmatrix}1\\ 0\end{pmatrix} \qquad \text{and} \qquad \vec{d}_2 = \frac{a_0}{2}\begin{pmatrix}-1\\ -\sqrt{3}\end{pmatrix} \qquad \text{and} \qquad \vec{d}_3 = \frac{a_0}{2}\begin{pmatrix}-1\\ \sqrt{3}\end{pmatrix}. \tag{2.4}$$

Since the unit-cell of graphene consists of two atoms, we start with the following Ansatz for the wave-functions:

$$\psi_{\mathrm{j}}(\vec{r}) = \frac{1}{\sqrt{N}}\sum_{\vec{R}_{\mathrm{j}}} e^{i\vec{q}\vec{R}_{\mathrm{j}}}\phi_{\mathrm{j}}(\vec{r}-\vec{R}_{\mathrm{j}}), \tag{2.5}$$

where N is the number of lattice points, $\vec{q}$ is the wave vector, $\phi(\vec{r})$ is the π-orbital wave-function of an isolated atom, j is the sublattice index (A and B atoms) and $\vec{R}_{\mathrm{j}}$ is the location of the j-th atom. Due to the two sublattices, the Hamiltonian takes the form of a 2×2 matrix with the elements:

$$H = \begin{pmatrix}H_{AA} & H_{AB}\\ H_{BA} & H_{BB}\end{pmatrix}. \tag{2.6}$$

The diagonal terms of the Hamiltonian can be calculated according to:

$$H_{\mathrm{AA}} = \langle\psi_{\mathrm{A}}(\vec{r})|\, H\, |\psi_{\mathrm{A}}(\vec{r})\rangle\,. \tag{2.7}$$

By explicitly writing down equation 2.7 using equation 2.5, one finds a term given by $\langle\phi_{\mathrm{A}}(\vec{r})|\, H\, |\phi_{\mathrm{A}}(\vec{r})\rangle$, which defines the on-site energy term (ϵ). The latter is commonly set to zero for undoped graphene. Furthermore $H_{\mathrm{AA}} = H_{\mathrm{BB}}$, since the A and B sublattice are the same. The off-diagonal terms can be calculated according to:

$$H_{\mathrm{AB}} = \langle\psi_{\mathrm{A}}(\vec{r})|\, H\, |\psi_{\mathrm{B}}(\vec{r})\rangle \tag{2.8}$$

with $H_{\mathrm{AB}} = H^*_{\mathrm{BA}}$. Upon considering only nearest-neighbour hopping ($\vec{d}_{\mathrm{i}} = \vec{r} - \vec{R}$ with $i = 1, 2, 3$) and defining the nearest-neighbour hopping energy as $t = \langle\phi_{\mathrm{A}}(\vec{r})|\, H\, |\phi_{\mathrm{B}}(\vec{r})\rangle$ which is roughly $-2.7\,\mathrm{eV}$ [50], equation 2.8 reads as

$$H_{\mathrm{AB}} = t\cdot\left(e^{i\vec{q}\vec{d}_1} + e^{i\vec{q}\vec{d}_2} + e^{i\vec{q}\vec{d}_3}\right) = t\cdot f(\vec{q}) \tag{2.9}$$

and the full Hamiltonian is then given by:

$$H = t \cdot \begin{pmatrix} 0 & f(\vec{q}) \\ f(\vec{q})^* & 0 \end{pmatrix}. \tag{2.10}$$

Solving the eigenvalue problem one ends up with $E_\pm = \pm t\sqrt{|f(\vec{q})|^2}$ where the plus sign accounts for the conduction band, and the negative sign for the valence band. By plugging in the nearest-neighbour coordinates $\vec{d}_1, \vec{d}_2, \vec{d}_3$ one obtains:

$$E_\pm(\vec{q}) = \pm t\sqrt{1 + 4\cos\left(\frac{3}{2}q_\mathrm{y}a_0\right)\cos\left(\frac{\sqrt{3}}{2}q_\mathrm{x}a_0\right) + 4\cos\left(\frac{\sqrt{3}}{2}q_\mathrm{y}a_0\right)^2} \tag{2.11}$$

which is plotted in Fig. 2.2a for the first Brillouin zone[1]. At zero energy, the valence- and conduction band touch at the 6 DPs, which can be separated into K and K' valley as it is already shown in Fig. 2.1b. The energy dispersion reveals that graphene is a zero-gap semiconductor, which distinguishes it from conventional metals and semiconductors. In the former the valence- and conduction band are overlapping while in the latter they are separated by a finite energy-gap. In pristine graphene the Fermi energy is located at $E = 0$ and it can be tuned into the valence or conduction band (p- and n-doped respectively) upon introducing a finite on-site energy. In experiments this can be realized via electrostatic gating as done in this Thesis.

In most transport experiments it is only the low-energy spectrum which can be accessed. The full Hamiltonian can be expanded around the $\vec{K}$ ($\vec{K}'$) vector by introducing $\vec{q} = \vec{K} + \vec{k}$, where $|\vec{K}| \gg |\vec{k}|$ and $\vec{k}$ is the vector measured relative to the corresponding DP. The linearised Hamiltonian around the K and K' points reduces then to [6, 50–52]:

$$H = \pm\hbar v_\mathrm{F}\vec{k}\vec{\sigma} = \hbar v_\mathrm{F}\begin{pmatrix} 0 & \pm k_\mathrm{x} - ik_\mathrm{y} \\ \pm k_\mathrm{x} + ik_\mathrm{y} & 0 \end{pmatrix} \quad \text{with} \quad \vec{\sigma} = \begin{pmatrix} \pm\sigma_\mathrm{x} \\ \sigma_\mathrm{y} \end{pmatrix}, \tag{2.12}$$

where the plus and minus sign account for the K and K' valley, $v_\mathrm{F} = 3ta_0/(2\hbar)$ $\sim 10^6$ m/s is the Fermi velocity [53] and $\vec{\sigma}$ is given by the Pauli-matrices σ_x and σ_y. The resulting low-energy spectrum, plotted in Fig. 2.2b, is then given by

$$E_\pm(\vec{k}) = \pm\hbar v_\mathrm{F}|\vec{k}| \tag{2.13}$$

where the plus and minus sign account for the conduction and valence band. Notice that equation 2.13 is independent of the valley and one thus obtains a two-fold valley degeneracy (discussed in section 2.5) which adds to the two-fold

---

[1] In Fig. 2.2a next-nearest neighbour hopping was included which accounts for the asymmetric valence- and conduction band.

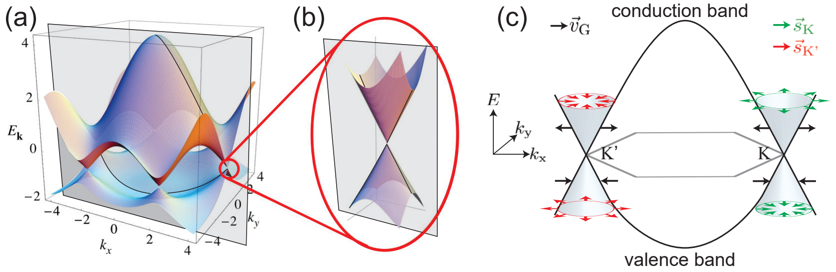

Figure 2.2. Band structure of graphene. a, Energy spectrum (in units of t) for t =2.7 eV and t' =−0.2 t. Figure adapted from Ref. [50]. **b,** Low-energy spectrum near the Dirac-point. **c,** Cut for $k_{\mathrm{y}} = 0$ as indicated in (a,b) with the black, semi-transparent plane. The orientation of the pseudospin ($\vec{s}_{\mathrm{K,K'}}$) is parallel (anti-parallel) to the the group-velocity ($\vec{v}_{\mathrm{G}}$) in K and K' cone. Furthermore $\vec{v}_{\mathrm{G}}$ is parallel (anti-parallel) to $\vec{k}$ in the conduction (valence band).

spin degeneracy.
In Fig. 2.2c an illustration of a cut though the first Brillouin-zone at $k_{\mathrm{y}} = 0$ is shown. The group-velocity ($\vec{v}_{\mathrm{G}}$), indicated in Fig. 2.2c with the black arrows, is given by:

$$\vec{v}_{\mathrm{G}} = \frac{1}{\hbar}\frac{\partial E}{\partial \vec{k}}, \tag{2.14}$$

where $\vec{v}_{\mathrm{G}}$ is parallel to $\vec{k}$ for electrons in the conduction band, while $\vec{v}_{\mathrm{G}}$ is anti-parallel to $\vec{k}$ for holes in the valence band. The charge carriers in graphene are called "massless" in analogy to photons obeying a similar Dirac equation.

The density of states (DOS) in graphene can be calculated according to $\rho(E) = \partial N(E)/\partial E$, where $N(E)$ is the number of states at energy E. Since $N(E)$ is not known, one can start with:

$$N(|\vec{k}|) = g \int dV \int_0^k \rho(\vec{k})d\vec{k} \tag{2.15}$$

where g is the degeneracy of the k-states in graphene, and $\rho(|\vec{k}|)$ is given by $(2\pi)^{-d}$ ($d = 2$ is the dimensionality of the system). In graphene the Fermi surface in a given valley describes a circle with radius k, therefore the integration over $d\vec{k}$ simply yields $\pi|\vec{k}|^2$, thus equation 2.15 turns into

$$N(|\vec{k}|) = g\frac{V}{4\pi}|\vec{k}|^2. \tag{2.16}$$

By replacing $\vec{k}$ with the low-energy dispersion relation given in equation 2.13, and taking the derivative with respect to the energy, the DOS is given by

$$\rho(E) = g\frac{V}{2\pi}\frac{E}{(v_\mathrm{F}\hbar)^2}. \tag{2.17}$$

From the above given equation it can be seen, that $\rho(E)$ scales linear with the energy E. From equation 2.16 one can furthermore derive the relation between charge carrier density n and the wave vector. Using $n = N(|\vec{k}|)/V$ and $g = 4$, one ends up with:

$$|\vec{k}| = k_\mathrm{F} = \sqrt{\pi n}. \tag{2.18}$$

2.1.2. Pseudospin

A consequence of the two-atomic unit-cell in graphene is that the charge carriers have an additional degree of freedom, commonly called the pseudospin. Starting with the Hamiltonian given in equation 2.12 it can be rewritten using $\vec{k} = k_\mathrm{F}e^{i\theta_{\vec{k}}}$:

$$H = \pm\hbar v_\mathrm{F} k_\mathrm{F}\begin{pmatrix} 0 & \pm e^{\mp i\theta_{\vec{k}}} \\ \pm e^{\pm i\theta_{\vec{k}}} & 0 \end{pmatrix} \tag{2.19}$$

where $\theta_{\vec{k}} = \arctan(k_\mathrm{y}/k_\mathrm{x})$ and the plus and minus sign account for the K and K' valleys. Solving the eigenvalue and eigenvector problem for equation 2.19, a possible solution of the normalized eigenvectors in the conduction $|EV_\mathrm{C}\rangle$ and valence band $|EV_\mathrm{V}\rangle$ is given by:

$$|EV_\mathrm{C}\rangle = \frac{1}{\sqrt{2}}\begin{pmatrix} e^{\mp i\theta_{\vec{k}}/2} \\ e^{\pm i\theta_{\vec{k}}/2} \end{pmatrix} \quad \text{and} \quad |EV_\mathrm{V}\rangle = \frac{1}{\sqrt{2}}\begin{pmatrix} e^{\mp i\theta_{\vec{k}}/2} \\ -e^{\pm i\theta_{\vec{k}}/2} \end{pmatrix} \tag{2.20}$$

where the plus and minus sign account again for the K and K' valleys. Equation 2.20 can be generalized by introducing the parameter s which accounts for the valence band (holes, $s = -1$) and conduction band (electrons, $s = 1$) respectively, which then yields

$$|s\rangle = \frac{1}{\sqrt{2}}\begin{pmatrix} e^{\mp i\theta_{\vec{k}}/2} \\ s e^{\pm i\theta_{\vec{k}}/2} \end{pmatrix}. \tag{2.21}$$

It is equation 2.21 which defines the amplitude of the electronic wave-function on the A and B sublattice respectively. In fact, the vector can be viewed as the result of a spinor-rotation of $\theta_{\vec{k}}$ around the z-axis ($R(\theta_{\vec{k}})$) which reads as

$$R(\theta_{\vec{k}}) = e^{-i\theta_{\vec{k}}/2\sigma_\mathrm{z}} = \begin{pmatrix} e^{-i\theta_{\vec{k}}/2} & 0 \\ 0 & e^{i\theta_{\vec{k}}/2} \end{pmatrix}, \tag{2.22}$$

where σ_z is a Pauli-matrix. By performing a rotation around 2π of equation 2.22, which is equivalent to a charge carrier encircling the origin in k-space, a phase of π is picked-up. This phase is the so-called the Berry-phase.

Assuming an initial state $|s_0\rangle$ pointing in the $\pm x$-direction, an arbitrary state (equation 2.21) can be written as:

$$|s\rangle = R(\theta_{\vec{k}})\,|s_0\rangle = \begin{pmatrix} e^{-i\theta_{\vec{k}}/2} & 0 \\ 0 & e^{i\theta_{\vec{k}}/2} \end{pmatrix} \frac{1}{\sqrt{2}} \begin{pmatrix} 1 \\ s \end{pmatrix} \tag{2.23}$$

where $|s\rangle_0$ is defined for $\theta_{\vec{k}} = 0$. From equation 2.21 it can be seen that the pseudospin is tied to the $\vec{k}$-vector, which results in the following two relations: i) In the K-cone the pseudospin is parallel to the $\vec{k}$-vector in the conduction band (right-handed Dirac fermions) while it is anti-parallel in the valence band (left-handed Dirac anti-fermions). In the K'-cone these relations are reversed. ii) The pseudospin is parallel (anti-parallel) to $\vec{v}_\mathrm{G}$ in the $K-$ ($K'-$) cone. This is summarized in Fig. 2.2c. The observation of the Berry's phase of π was first given by McEuen et *al.* [54] with the observation of a higher conductance of metallic over semi-conducting carbon nanotubes[2] based on the theory of Ando et *al* [55]. The first experimental proof of a Berry's phase of π in graphene was given by the observation of the anomalous half-integer quantum Hall effect [12, 13] as a consequence of the exceptional topology of the graphene band structure [55–57]. Later on the Berry's phase of π was additionally observed as a sudden phase-shift at finite magnetic field in the transmission resonance in a ballistic, phase coherent graphene *p-n-p* device [58] based on the theory of Shytov et *al.* [59].

2.1.3. Quantum Hall effect in graphene

One of the benchmarks of single-layer graphene is the half-integer Hall-effect, which shall be discussed in the following. Let us start with a macroscopic conductor of width W, along which a current flows in the x-direction (I_x). If a magnetic field is applied perpendicular to the current flow (B_z), then the charge carriers with charge q exhibit a combination between electrostatic- ($\vec{F}_\mathrm{E}$) and Lorenz-force ($\vec{F}_\mathrm{L}$), which is given by $\vec{F} = q \cdot (\vec{E} + \vec{v} \times \vec{B})$. The Lorenz-force causes the charge carriers to perform a circular motion, which are called cyclotron orbits, if the device is clean such that the charge carriers are not scattered. Furthermore, the cyclotron orbits have a radius R_C, called the cyclotron radius, which is given by:

$$R_\mathrm{C} = \frac{\hbar\sqrt{n\pi}}{eB}. \tag{2.24}$$

charge carriers which are located in the very vicinity of a physical edge of the sample cannot perform a full cyclotron orbit because they hit the sample

---

[2] Metalic carbon nanotubes have a linear dispersion relation comparable to graphene, while semi-conducting carbon nanotubes have a parabolic one where Klein tunneling is absent.

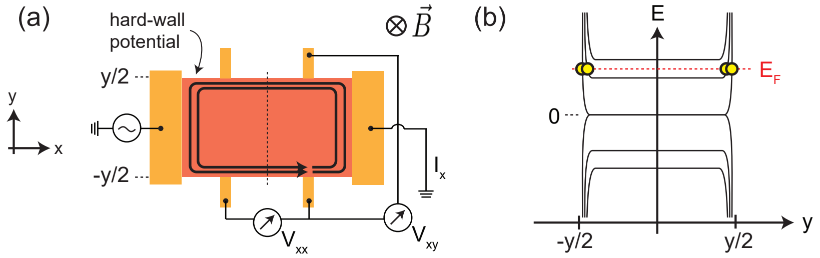

Figure 2.3. Edge states in the QHE regime. a, Illustration of two populated edge states in a four-terminal junction where the graphene is n-doped (red). Contacts are shown in orange. **b,** Energy dispersion along a linecut as indicated in (a) with the black, dashed line. The yellow dots indicate the location of the edge states along the y-axis.

edge instead. This results in so called skipping orbits moving along the edges. Furthermore, the equilibrium between $\vec{F}_\mathrm{E}$ and $\vec{F}_\mathrm{L}$ result in an accumulation of charge carriers along the y-direction, which can be measured as the so called Hall-resistance ($R_\mathrm{H} = R_\mathrm{xy}$, where $R_\mathrm{H} = V_\mathrm{xy}/I_\mathrm{x}$, see Fig. 2.3a) [60]. The quantum Hall effect is the quantum mechanical version of the Hall effect which is observed by reducing the dimensionality of the system to a two-dimensional electron gas (2DEG) which is of high mobility and typically being measured at low temperatures where scattering events due to e.g. phonons are strongly suppressed. At low magnetic field R_H scales linearly with the magnetic field comparable to the conventional Hall effect. For high enough magnetic fields ($B_\mathrm{z} > B_\mathrm{C}$) the Hall-resistance starts to be quantized [61]. Above $B_\mathrm{z} > B_\mathrm{C}$ the charge carriers can perform a full cyclotron orbit without being scattered [62], which corresponds to $2\pi R_\mathrm{C} \geq l_\mathrm{mfp}$, where l_mfp is the mean free path (section 2.3). In conventional 2DEG's with a parabolic band dispersion the quantization conditions at a finite magnetic field leads to discrete energy levels, so called Landau levels. Note that in real samples the energy-levels are not discrete, but broadened (δE) mostly due to impurities and a finite temperature. Their energy is equidistant depending on the Landau level index j (integer) and the perpendicular magnetic field B_z according to

$$E_\mathrm{j}(\mathrm{2DEG}) = \frac{\hbar e B_\mathrm{z}}{m_\mathrm{eff}}(j + \frac{1}{2}). \tag{2.25}$$

Furthermore, for the observation of the QHE the ratio between level-broadening and level-spacing ($\delta E/(E_\mathrm{j+1} - E_\mathrm{j})$) must be small enough such that the DOS between two neighbouring Landau levels can vanish. Compared to equation 2.25, in single layer graphene (SLG) with its linear energy dispersion the Landau levels are given by [57, 63]:

$$E_\mathrm{j}(\mathrm{SLG}) = \mathrm{sign}(j)\sqrt{2e\hbar v_\mathrm{F}^2|j|B_\mathrm{z}}. \tag{2.26}$$

Comparing equation 2.25 and equation 2.26, two differences are evident: i) The lowest Landau level (LLL) in SLG is at zero energy, being half filled with electrons and half filled with holes. ii) The energy-spacing between the different Landau levels is not equidistant, but has a square-root dependence on the Landau-level index j and the perpendicular magnetic field. In fact, the energy-splitting between the $j = 0$ and $j = 1$ Landau levels is large enough to observe the quantum Hall effect even at room-temperature [64].
The bulk of the 2DEG is only fully insulating if the Fermi energy is located in between two Landau levels as sketched in Fig. 2.3b. In that case the current flows exclusively along the edges in so called chiral edge states and back-scattering along a channel is suppressed ($R_\mathrm{xx} = 0$). The real-space position of the edge states is given by the intersection between the Fermi energy and the energy levels which bend up or down at the graphene edges ($\lim\limits_{y\to\pm y/2} E(y) = \pm\infty$) due to the confinement originating from the edges, as sketched in Fig. 2.3b. The propagation along these edge states in x-direction is dissipation-less ($R_\mathrm{xx} = 0$) because the strong magnetic field ($R_\mathrm{C} \ll W$) prevents back-scattering. The latter would correspond to scattering events between edge states propagating in opposite directions which are separated by roughly W as they lie on opposite sides of the sample. A plane wave, representing an edge state of the j-th Landau level running along the edges in x-direction can be written as:

$$S_\mathrm{j}(x, y) = a_\mathrm{j} e^{i|\vec{k}_\mathrm{j}|x} \chi_\mathrm{j}(y) \tag{2.27}$$

where a_j, $\vec{k}_\mathrm{j}$ and $\chi_\mathrm{j}(y)$ are the amplitude, the wave vector in the x-direction and the corresponding transverse mode of the j-th Fermi level wave-function. The width of such an edge state is roughly given by the magnetic length [65–67], given by:

$$l_\mathrm{B} = \sqrt{\frac{\hbar}{eB}}. \tag{2.28}$$

Since in graphene the charge carriers are four-fold degenerate (spin and valley), every completely filled Landau level occupies 4 edge states with exception of the LLL, which occupies only two edge states. Each edge state contributes one conductance unit (e^2/h) because back-scattering is suppressed, therefore the plateaus in SLG are characterized by the sequence

$$G_\mathrm{H} = \frac{4e^2}{h}(j + \frac{1}{2}). \tag{2.29}$$

More often the above given equation is written as a function of the filling factor

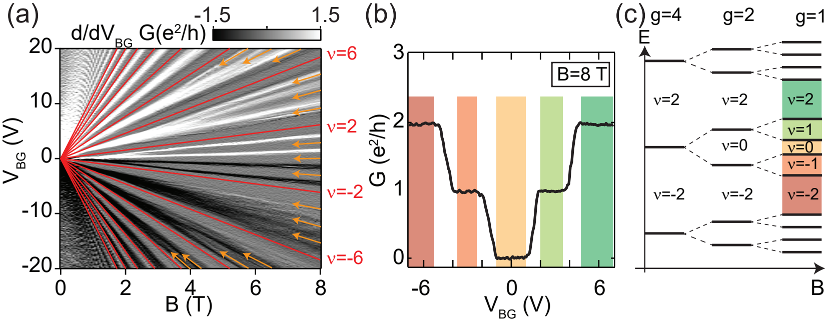

Figure 2.4. Quantum Hall effect on a single layer graphene in a two-terminal device. a, Numerical derivative of the conductance as a function of V_{BG} (back-gate voltage) and B of a two-terminal junction. The evolution of the filling factors according to equation 2.30 (with $g = 4$) is indicated with the red lines. The Orange arrows indicate a degeneracy lifting due to spin and/or valley. **b,** At the LLL the degeneracy is fully lifted. A constant resistance was subtracted to match the expected plateau-values.**c,** Illustration of no ($g = 4$), partial ($g = 2$) of full ($g = 1$) degeneracy lifting with increasing magnetic field.

ν which represents the charge carrier density (n) per flux quantum given as:

$$\nu = \frac{nh}{eB}. \tag{2.30}$$

In the absence of any degeneracy splitting this leads to equation 2.29 with the famous sequence of $\nu = \pm 2, \pm 6, \ldots$ at fully filled Landau levels. At these filling factors the Fermi energy is located between two neighbouring Landau levels, which is equivalent to a plateau of G_{H}. In Fig. 2.4a the evolution of the filling factors are indicated with the red lines as a function of gate voltage ($n \propto V_{\mathrm{BG}}$ assuming a plate capacitor model) and magnetic field, tracking the Hall-plateaus (G_{H} =const.). More general, in a four-terminal measurement the Hall conductance is given by:

$$G_{\mathrm{H}} = \frac{\nu e^2}{h} \tag{2.31}$$

where in clean samples the fourfold spin-valley-degeneracy can be partially or fully lifted[3]. Full degeneracy lifting of the LLL is shown in Fig. 2.4b and illustrated in Fig. 2.4c. From symmetry arguments alone it is not possible to discriminate whether the spin or the valley degeneracy is preferentially lifted.

---

[3] The splitting of the degeneracy is typically first seen for the lowest Landau levels, since there the energy-spacing is largest.

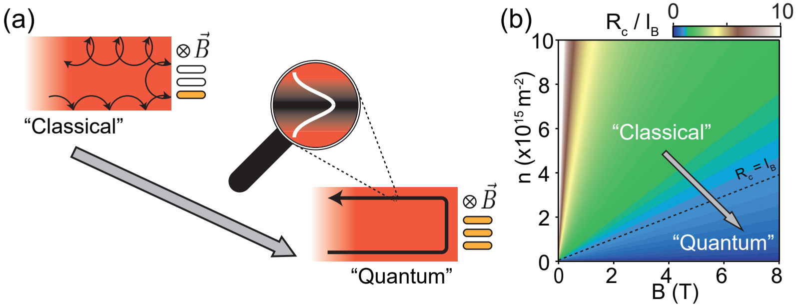

Figure 2.5. Classical versus quantum description. a, Illustration of charge carrier trajectories evolving from skipping orbits at low magnetic field towards edge states at high-magnetic field. **b,** Ratio between the cyclotron radius and magnetic length as a function of density and magnetic field.

It turns out that the order of degeneracy lifting depends on external symmetry-breaking fields [68]. To gain knowledge whether a given degeneracy-splitting is due to the spin or valley degree of freedom one might consider measurements in tilted magnetic fields. While spin-splitting (defined by the Zeeman-energy) depends on the total magnitude of the magnetic field, the in-plane motion relevant to electron-orbital interactions (e.g. valley-splitting) depend only on the magnetic field perpendicular to the graphene plane [69, 70]. The hierarchy of the energy-scales for spin- and valley-splitting furthermore determines if at zero energy an edge state is present or not (insulator scenario) [68, 69, 71, 72]. The quantum Hall effect is ideally measured in a Hall-bar as sketched in Fig. 2.3a, where σ_{xx} and σ_{xy} can be measured separately. Note that here σ_{xy} and G_{xy} are equivalent, since the Hall resistance is independent on the sample width. However, most of the measurements done in this Thesis involve only two-terminal devices where a mix between σ_{xx} and σ_{xy} is measured. The mixing manifests itself in a over-shooting (under-shooting) of the conductance at the beginning (end) of the plateau depending on the aspect-ration (L/W, where L is the length and W is the width of the graphene) of the device [73, 74]. Over-shooting is the case for $L/W < 1$ while under-shooting is the case for $L/W > 1$, and perfect plateaus are expected for $L/W = 1$. In Fig. 2.4 a constant resistance-value was subtracted which accounts for the contact resistance and the resistance of the cryostat-lines. More details on this can be found in section 4.2.1.

While at low magnetic field the charge carriers move in cyclotron orbits (classical regime), at high magnetic fields they form edge states (quantum regime) as shown in Fig. 2.5a. In many cases it is the ratio between the cyclotron radius

(R_C, equation 2.24) and the the magnetic-length (l_B, equation 2.28) which defines the crossover from classical to quantum regime around $l_\mathrm{B}/R_\mathrm{C} \sim 1$. Therefore, for $l_\mathrm{B}/R_\mathrm{C} \ll 1$ the cyclotron motions dominate over the width of the wave-function while in the opposite case, $l_\mathrm{B}/R_\mathrm{C} \gg 1$, the skipping trajectories do not influence the path of the wave-function much, thus resulting in edge states. Furthermore, using $k_\mathrm{F} = \sqrt{n\pi}$ and the the definition of the filling factor (equation 2.30), one finds that the condition of $R_\mathrm{C} = l_\mathrm{B}$ is given for $\nu = 2$. The criterion of $R_\mathrm{C} \ll l_\mathrm{B}$ ($R_\mathrm{C} \gg l_\mathrm{B}$) defining the classical-regime (quantum-regime) is consequently equivalent to $\nu \gg 2$ ($\nu \ll 2$), which is sketched in Fig. 2.5b.

2.2. *P-n* junctions

For the realization of many experiments in graphene regions of different charge carrier densities are required, which can be achieved by applying an external potential (e.g. via electrostatic gating) [50]. At the interface between two region of different charge carrier density, so called *p-n* and *n-n'* junctions are formed. They can be operated in the unipolar regime where both regions have the same polarity but different doping-levels (*n-n'* or *p-p'*) or they can be operated in the bipolar regime where the regions have opposite polarity (*p-n* or *n-p*). In the following section the most important aspects of these *p-n* junctions, with regards to the experiments performed in this Thesis, shall be discussed. This includes Klein tunneling, the ability of positive and negative refraction and the angle dependent transmission probability for sharp and smooth *p-n* junctions.

2.2.1. Klein tunneling

A direct implication of the pseudospin which is tied to the $\vec{k}$-vector (section 2.1.2) is that the transmission probability of charge carriers incident perpendicular to a graphene *p-n* junction is equal to one (back-reflection $\vec{k} \rightarrow -\vec{k}$ is forbidden), independent on the height of the potential step [15]. Let us consider an electron in the K cone and with $\vec{k} = |\vec{k}|\vec{e}_\mathrm{x}$ which is approaching a *p-n* junction located along the y-axis. Reflection of the electron at the *p-n* junction from k_x to $-k_\mathrm{x}$ within the same valley would require a pseudospin flip event (Fig. 2.6a), which is forbidden at low energies. Alternatively one might consider a scattering process to $-k_\mathrm{x}$ in the K' cone which does not require a pseudospin flip (Fig. 2.6b). However, the latter requires intervalley scattering i.e. scattering over large $\vec{k}$-vectors. This is equivalent to short-range scatterers in real space such as e.g. defects or edges, which are absent in clean graphene. Consequently the only option left is intra-valley scattering into the valence band, where a hole with $-k_\mathrm{x}$ and identical pseudospin is present (Fig. 2.6c).

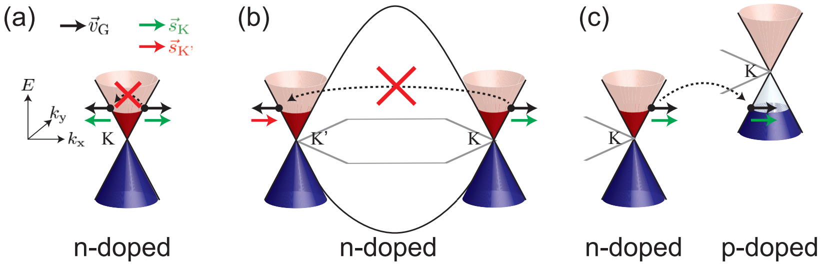

Figure 2.6. Klein tunnelling at graphene *p-n* junctions. a,b Reflection processes (here sketched for the n-doped side) are absent because pseudospin flip and intervalley scattering are suppressed in clean graphene. **c,** The intervalley scattering which leads to transmission from the n-doped to the p-doped side.

This event corresponds to a transmission of a charge carrier across the *p-n* junction. Because this effect was postulated by O. Klein for Dirac-fermions [14] in 1929, one speaks of Klein-tunnelling.

2.2.2. Snell's law in graphene

In the previous section we looked at charge carriers with trajectories perpendicular to the *p-n* junction. Now we concentrate on the situation where they have a finite incident angle ($\theta \neq 0$) with respect to the *p-n* junction normal. If a wave with momentum $\vec{p}$ and $\theta \neq 0$ hits the interface (the refractive indices on both sides are different), then the momentum-component parallel to the interface ($p_{||}$) is conserved while the momentum-component perpendicular to the interface ($p_{\perp}$) is not. Let us consider a *n-n'* junction which is located parallel to the y-axis as sketched in Fig. 2.7. Using the relations $\vec{p} = \hbar\vec{k}$, thus $k_\mathrm{y,L} = k_\mathrm{y,R}$ and $\sin(\theta) = k_y/|\vec{k}|$, one ends up with Snell's law which is given by:

$$|\vec{k}_\mathrm{L}| \cdot \sin(\theta_\mathrm{L}) = |\vec{k}_\mathrm{R}| \cdot \sin(\theta_\mathrm{R}) \tag{2.32}$$

where $\theta_\mathrm{L,R}$ are the angles with respect to the interface-normal on the left (incident) and right (emerging) side of the *n-n'* junction. In Fig. 2.7a the density in the left cavity (n_L) is larger than in the right cavity (n_R), leading to a reduced $k_\mathrm{x,R}$ compared to $k_\mathrm{x,L}$ since $k_\mathrm{x}^2 + k_\mathrm{y}^2 = n\pi$ and k_y is conserved. According to equation 2.32 the angle of the emerging wave (θ_R) is therefore larger compared to the angle of the incident wave (θ_L). In analogy to optics the critical angle (θ_C) upon which total-reflection is expected is defined as $\theta_\mathrm{C} = \arcsin(|\vec{k}_\mathrm{R}|/|\vec{k}_\mathrm{L}|)$ if $|n_\mathrm{L}| > |n_\mathrm{R}|$ is fulfilled.

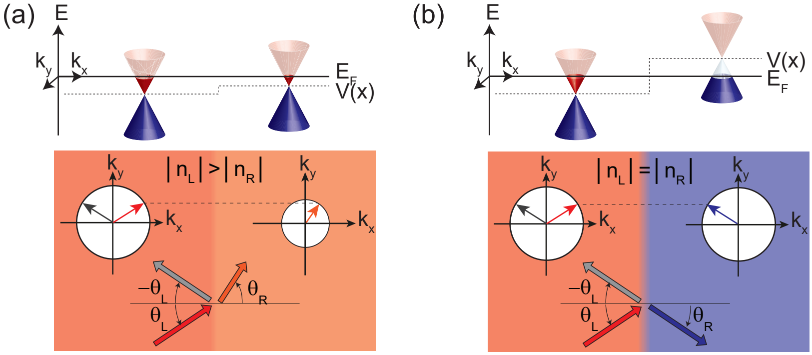

Figure 2.7. Illustration of Snell's law in unipolar *n-n'* and bipolar *p-n* junctions. a, Positive refraction across the junction is observed in the unipolar regime. The bold arrows indicate the group-velocity of the electrons. **b,** If operated in the bipolar regime, the charge carriers undergo negative refraction. Figure adapted from Ref. [75]

So far the situation is still comparable to optics with positive refraction. However, if we tune the interface from the unipolar to the bipolar regime, one ends up with negative refraction. We recapitulate that the group-velocity ($\vec{v}_{\mathrm{G}}$) in the conduction band is parallel to its wave vector $\vec{k}$, while is anti-parallel in the valence band. Because on both sides of the *p-n* junction the electrons propagate into the same x-direction ($\mathrm{sign}(v_{\mathrm{G,x,l}}) = \mathrm{sign}(v_{\mathrm{G,x,r}})$, since on the right side the wave propagate away from the interface), one ends up with:

$$\mathrm{sign}(k_{\mathrm{x,R}}) = -\mathrm{sign}(k_{\mathrm{x,L}}) \qquad \text{and consequently} \qquad \mathrm{sign}(\theta_{\mathrm{R}}) = -\mathrm{sign}(\theta_{\mathrm{L}}), \tag{2.33}$$

which means that the refraction angle, on the contrary to optical experiments, is negative as sketched in Fig. 2.7b. Besides refraction, reflection can occur, which is always specular.

In summary, the index of refraction, which is defined as $\sin(\theta_{\mathrm{R}})/\sin(\theta_{\mathrm{L}})$, is positive in the unipolar regime and negative in the bipolar regime. Snell's law was experimentally verified using transverse magnetic focusing (see section 2.3.2) across a *p-n* and *p-p'* junction [34].

2.2.3. Sharp and smooth *p-n* junctions

In the previous section Snell's law was introduced for charge carriers passing though a *n-n'* and *p-n* junction. Now we concentrate on the transmission probability of charge carriers as a function of incident angle θ, the Fermi

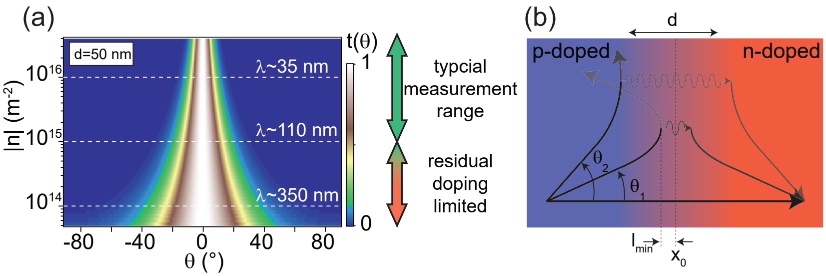

Figure 2.8. Angle dependent transmission probability trough a smooth *p-n* junction. a, Calculated transmission probability as a function of charge carrier density and incident angle for a symmetric *p-n* junction with a smoothness of d =50 nm according to equation 2.35. Corresponding wavelengths are given for selected densities. On the right hand side: typical density ranges reached in encapsulated graphene. **b,** Illustration of charge carrier trajectories with different incident angles (θ). Tunnelling is indicated with oscillating lines. The intensities of the lines are proportional to occupation-probability before and after reflection/transmission. Figure adapted from Ref. [76].

wavelength λ_F and the electrostatic profile of the *p-n* junction itself. In experiments, the charge carrier density does not change abruptly but rather varies gradually within a distance d, which depends on the relative distances between the gates, and the spacing between the gate and the graphene. One can distinguish between “sharp” and “smooth” *p-n* junctions depending on the ratio between the Fermi wavelength λ_F and d. A *p-n* junction is considered as sharp, if $\lambda_\mathrm{F} \gg d$, and as smooth, if $\lambda_\mathrm{F} \ll d$. In the following we only consider symmetric *p-n* junctions, which means that the doping on both sides of the cavity is equivalent, but opposite in sign.

In the case of a sharp *p-n* junctions, it is valid to substitute the gradual density-profile with a step-potential ($V(x) = -V/2$ for $x < 0$ and $V(x) = V/2$ for $x > 0$). The angle dependent transmission probability can consequently be calculated by matching the wave-functions on both sides of the *p-n* junction, leading to [15]:

$$t(\theta) = \cos(\theta)^2. \tag{2.34}$$

However, in most experimental measurements the ratio of λ_F/d is typically in the range of ~0.5 to 5 for encapsulated devices and even larger for suspended devices, which implies that the *p-n* junction can be considered to be rather smooth. In this case the problem becomes more complex as the density-gradient varies within a length-scale not being negligible. It turns out that for a smooth p-n junctions the angle dependent transmission probability is given by [15]:

$$t(\theta) = \exp(-\pi k_{\mathrm{F}} d \sin(\theta)^2) \tag{2.35}$$

in good agreement with experimental findings [34]. In Fig. 2.8a the transmission-probability is plotted as a function of the charge carrier density in the bulk and the incident angle for a p-n junction with a smoothness of 50 nm. This value is realistic for encapsulated devices (see section 3), where d is roughly given by the thickness of the hBN separating the gates from the graphene.
An qualitative understanding of equation 2.35 is given in the following. At zero incident angle the charge carriers have a transmission-probability of one due to Klein-tunnelling [14, 77] (section 2.1.2). However, at finite incident angle, the charge carriers are gradually deflected away from the p-n junction as indicated in 2.8a. The deflection can be seen as a sequence of positive refractions at regions with different charge carrier densities (n varies upon approaching the center of the p-n junction). Once the charge carrier trajectory is parallel to the p-n interface, is has reached its minimal distance from the center of the p-n junction (x_0) which is denoted as $l_{\min}$. This distance can be calculated according to $l_{\min} = v_{\mathrm{F}} p_{\mathrm{y}} / |\vec{E}|$, where $\vec{E}$ is the electric field present in the p-n junction due to the potential-gradient [76]. At the turning-point, the charge carriers have the choice, to i) either stay at the same side of the p-n junction, which results in reflection or ii) to tunnel to the other side of the p-n junction, which results in transmission. With increasing incident angle of the charge carriers (corresponding to an increasing p_{y} component) $l_{\min}$ increases, which consequently reduces the tunnelling-probability across the p-n junction (tunnelling processes are known to depend exponentially on the tunnelling-distance).

2.3. Characterization of the device quality

In order to characterize the device quality, several different values and signatures can be investigated. In the following section some of these relevant values/signatures shall be discussed, even though it is not a complete list.

2.3.1. Conductivity, mobility and residual doping

In contrast to four-terminal measurements which probe only the graphene resistance, a two-terminal measurement probes the sum of the graphene resistance and the contact resistance (R_{CT}, neglecting the line-resistance of the cryostat). In Fig. 2.9a the conductance as a function of back-gate voltage of a typical two-terminal device is shown. Starting from classical transport theory (Drude), the relation between current and electric field is given by $\vec{E} = \vec{j} \cdot \rho$, with $\rho = m/(ne^2\tau)$ and τ being the average scattering time of the charge carriers. By replacing the charge carrier mass in graphene with $m = |\vec{p}|/v_\mathrm{F}$, the conductivity ($\sigma = 1/\rho$) in the diffusive regime can be written as:

$$\sigma = \frac{2e^2 \tau v_\mathrm{F} \sqrt{\pi n}}{h}, \tag{2.36}$$

where τ is the average time between two momentum scattering events. The behaviour of τ on $|\vec{k}_\mathrm{F}|$ can depend on many factors such as the influence of the substrate, surface contaminations, static distortions (e.g. ripples) and phonons. Usually, the two main scattering mechanisms are [78] the charge impurity scattering with $\tau \propto |\vec{k}_\mathrm{F}|$ [79] and the local impurity scattering with $\tau \propto |\vec{k}_\mathrm{F}|^{-1}$ [80], even though many more mechanisms exist [81–85]. It turns out that for graphene encapsulated in hBN the conductivity is described quite well with a linear dependence according to:

$$\sigma \sim ne\mu \tag{2.37}$$

where μ is the charge carrier mobility [21]. The fact that equation 2.37 holds well with a density independent mobility suggests that charge impurities are likely to dominate over local impurities. The relation between the measured conductance G and the conductivity is defined via the aspect-ratio (W/L) as $G = \sigma W/L$. Upon increasing the charge carrier density in a two-terminal device the conductance becomes non-linear as shown in Fig. 2.9a because the contact resistance start to dominate over the graphene resistance. Taking the contact resistance of a two-terminal device into account, the conductivity as a function of charge carrier density is given by:

$$\sigma = \left[\frac{1}{ne\mu + \sigma_0} + R_\mathrm{CT} \right]^{-1} \tag{2.38}$$

where σ_0 is the minimal conductivity which originates from the residual doping (charge puddles). In a quantum Hall configuration the quantized plateaus of the conductance is exclusively defined via the charge carrier doping and the magnetic field. Thus, by combining equation 2.30 and equation 2.31 the charge carrier doping can be extracted according to:

$$n = \frac{G_\mathrm{H} B}{e}. \tag{2.39}$$

However, in a two-terminal devices G_H is not directly accessible. We therefore used a plate capacitor model with $C = \epsilon_0 \epsilon_\mathrm{r} A/d$ to approximate the gate capacitance. For the global back-gate the capacitance per unit-area is given by

$$C^{-1} = \frac{1}{\epsilon_0} \left(\frac{d_{\mathrm{SiO}_2}}{\epsilon_{\mathrm{SiO}_2}} + \frac{d_\mathrm{hBN}}{\epsilon_\mathrm{hBN}} \right), \tag{2.40}$$

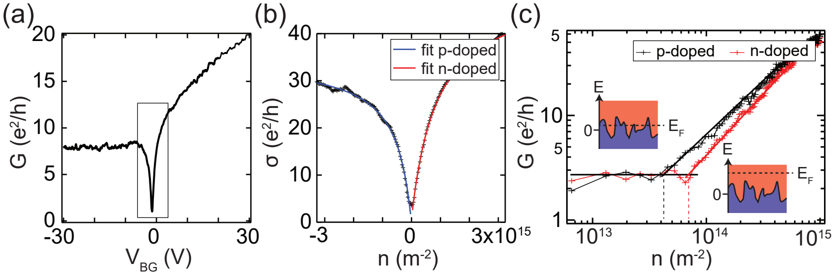

Figure 2.9. Field-effect measurements. a, Conductance of a two-terminal device as a function of global back-gate. **b,** Conductivity fitted with equation 2.38 within a restricted range as indicated in (a) yielding μ_e =150 000 cm^{-2}/(Vs). **c,** Residual doping (n_0 ~3×10^{13} m^{-2} to 6×10^{13} m^{-2}) extracted from the saturation in conductance (four-terminal measurement) in the double-logarithmic representation. Inset: Illustration of the puddle-landscape with respect to the Fermi energy.

with dielectric constants of $\epsilon_{\mathrm{SiO_2}} \sim \epsilon_{\mathrm{hBN}} \sim 4$, $d_{\mathrm{SiO_2}}$ ~300 nm and d_{hBN} ~20 nm to 60 nm.

An alternative way to extract the mobility compared considers the onset of the quantum Hall plateaus [86]. The onset of the observation of a quantized conductance indicates that the charge carriers can perform a full cyclotron-orbit without being scattered [62] as described in section 2.1.3. This is equivalent with $\tau > 1/\omega_C$, where ω_C is the cyclotron frequency given as $\omega_C = eB/m$. With the conductivity given as $\sigma = 1/\rho = ne\mu$, where $\rho = m/(ne^2\tau)$ (Drude-model), one ends up with $\mu = 1/B$. This definition of the mobility will be of special interest in chapter 5 as no knowledge on the aspect-ratio of the device is required in contrast to equation 2.38.

The strong asymmetry between n- (electron) and p- (hole) doping originates from the formation of a *p-n* junction near the Cr/Au side-contacts which strongly dopes the graphene with electrons in its proximity. In Fig. 2.9b the conductivity is fit with equation 2.38 in order to extract the mobility. The mobility values extracted from the hole-side are often significantly smaller than the ones from the electron-side due to the formation of this additional *p-n* junction near the contacts (if the graphene is hole-doped). This effect is not taken into account in equation 2.38. The mean free path (l_{mfp}) of the charge carriers is given by $l_{\mathrm{mfp}} = v_F\tau$, where τ can be deduced from equation 2.36. Furthermore, by using equation 2.37 l_{mfp} can be written as:

$$l_{\mathrm{mfp}} = \frac{\hbar}{e}\mu\sqrt{n\pi}. \tag{2.41}$$

Note that in very short graphene junctions the mobility is limited by the device size since scattering events at the contacts start to dominate over those within the graphene. Consequently equation 2.38 and equation 2.41 under-estimate the real values of μ and l_{mfp} within the bulk of graphene.
Upon reaching ballistic transport equation 2.38 and equation 2.41 start to fail since in this regime scattering only happens at the edges and the contacts, hence μ and l_{mfp} will be limited by the device size. Consequently the values of μ and l_{mfp} should be used with care as they can give only a rough estimate upon approaching the ballistic regime. On the other hand, by following a purely ballistic approach the conductance depends only on the width of the graphene junction which defines the number of modes fitting trhough the device. The conductance can then be given by [87]

$$G = \frac{4e^2}{h}\frac{W}{\lambda/2}. \tag{2.42}$$

where each modes carries a conduction-quantum of $4\,\mathrm{e}^2/\mathrm{h}$ due to the spin- and valley-degeneracy of the charge carriers in graphene. With $\lambda = 2\pi/|\vec{k}|$ and $|\vec{k}| = \sqrt{\pi n}$ the conductance can be rewritten as:

$$G = \frac{4e^2}{h}W\sqrt{\frac{n}{\pi}}. \tag{2.43}$$

In section 4.4 it is shown that equation 2.43 fits quite well for narrow constrictions (W ~100 nm) in agreement with the results found in Ref. [87]. According to equation 2.37 (diffusive) and equation 2.43 (ballistic) the conductivity is supposed to vanish in the limit of $n \to 0$. However, according to various theoretical studies [82, 88–90] the conductivity does not go below a minimal value (σ_{D}) even at $n = 0$. Even though this is well established, the value of σ_{D} varies with possible results of [89]:

$$\sigma_{\mathrm{D}} = \frac{4e^2}{\pi h}, \qquad \frac{\pi e^2}{2h}, \qquad \frac{e^2}{\pi h}, \qquad \text{etc.} \tag{2.44}$$

The large number of σ_{D} depends on the exact order how the function dependent parameters of σ, namely the temperature, frequency, Fermi energy, impurity scattering strength and the system size are tuned to zero (CNP). These values are just slightly below the minimal conductivity extracted from measurements as shown in Fig. 2.9c where σ_0 ~$3\,\mathrm{e}^2/\mathrm{h}$.

Besides the mobility, the residual doping is another important value in order to characterize the graphene. In the double-logarithmic plot shown in Fig. 2.9c the residual doping is given as the value below which the conductance saturates ($\sigma \neq ne\mu$). Below this doping level electrostatic-gating is inefficient since the doping in graphene is dominated by the puddle-landscape (potential fluctuations which cannot be screened due to the low density of charge carriers) as

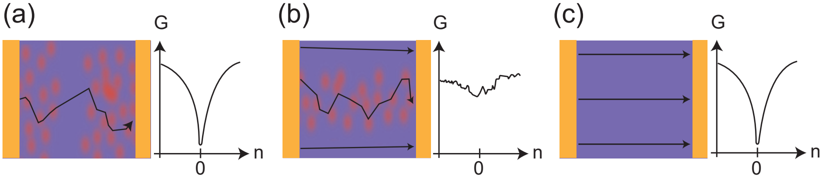

Figure 2.10. Different scenarios of partially or fully clean graphene with the corresponding field-effect measurements. **a,** Central region of graphene is clean while close to the contacts the graphene is diffusive. **b,** Graphene is e.g. clean near the edges, but diffusive in the middle part. **c,** Graphene is clean everywhere.

illustrated in the insets of Fig. 2.9c. Extracting the mobility, mean free path and residual doping from field-effect measurements as shown previously gives a first hint on the device quality, but it does not allow to draw any conclusion on the spatial distribution of possible contaminations. In Fig. 2.10 three different scenarios with their corresponding conductance as a function of charge carrier density are illustrated. In Fig. 2.10a the graphene is diffusive except of one region spanning the whole width of the device, which is ballistic. Even though the sample is mostly diffusive, charge carrier have to pass this clean region which is tuned very effectively by the gate, thus revealing a sharp dip in the conductance at the CNP. On the other hand, if the graphene is clean only on the sides but continuously diffusive in the inner part of the device (or vice versa) as shown in Fig. 2.10b, then the device will not show a Dirac-peak behaviour. If the device is completely clean as shown in Fig. 2.10c, the conductance as a function of the charge carrier density shows again the typical Dirac-peak behaviour. This example illustrates that in order to distinguish between the situation sketched in Fig. 2.10a and Fig. 2.10c more measurements are required. Effects such as e.g. snake states, transverse magnetic focusing, bend-resistences or Fabry-Pérot resonances are useful to do so.

2.3.2. Ballistic transport

Charge carriers are considered to be ballistic, if scattering events, and thus a change of the $\vec{k}$-vector, is negligible within the bulk of the sample ($L \ll l_{\mathrm{mfp}}$). Prominent examples of ballistic transport in graphene are transverse magnetic focusing (TMF) [31, 33], snake states [37, 38] or bend-resistance measurements [29, 30]. In Fig. 2.11a a classical illustration of TMF is shown, where a magnetic field perpendicular to the graphene plane is applied. The charge carriers which are injected at the bottom-left contact undergo a cyclotron motion with a radius of R_{C} (equation 2.24). With the sketched measurement configuration

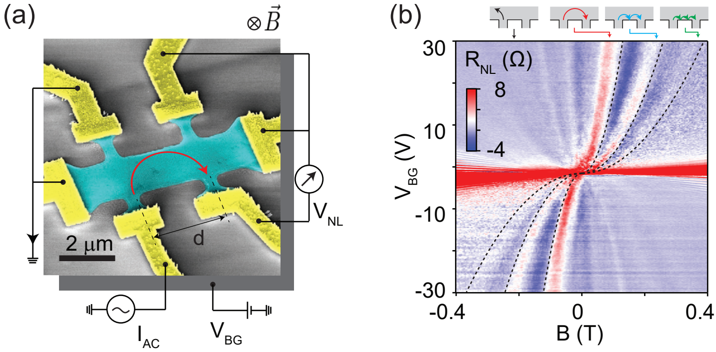

Figure 2.11. Transverse magnetic focusing. a, False-color SEM-image where the leads are indicated with yellow, and the hBN/graphene/hBN stack is indicated in cyan. With a magnetic-field applied perpendicular to the graphene plane charge carriers perform a cyclotron motion as indicated with red arrow. **b,** Non-local resistance as a function of charge carrier density ($n \propto V_{\mathrm{BG}}$) and magnetic field. Black-dashed lines indicate expected peak-maximum.

a non-local resistance $R_{\mathrm{NL}} = V_{\mathrm{NL}}/I_{\mathrm{AC}}$ is observed whenever the condition $d = i \cdot 2R_{\mathrm{C}}$ is fulfilled, where d is the distance between injector- and collector-lead and i is an integer. The dashed lines in Fig. 2.11b correspond to the expected peak-maximum with no fitting-parameters included. Observing one or several peaks directly implies ballistic transport over a distance of at least πd. Furthermore, TMF is an excellent tool to characterize the edge quality [91] since for the observation of higher-order peaks ($i = 2, 3, 4...$) specular reflection at the graphene edges is required [33]. The latter occurs if the graphene edge is smooth on the order of the wavelength which implies λ_{F} being much larger than the edge roughness. Effects which only depend on ballistic transport, such as TMF or snake states, are quite robust with temperature (they survive up to ~100 K [31, 33, 38]), since phonon-scattering and electron-electron scattering [33], which suppress ballistic transport, are strongly reduced below these temperatures.

2.3.3. Phase coherent transport

Besides the discrimination in ballistic ($L \ll l_{\mathrm{mfp}}$) and diffusive ($L \gg l_{\mathrm{mfp}}$) transport, one can additonally distinguish between phase coherent and non phase coherent transport (applies to ballistic and diffusive samples). One speaks of phase coherent transport over length L if the phase of charge carriers is preserved over a distance L, namely $l_\Phi > L$ where l_Φ is the phase

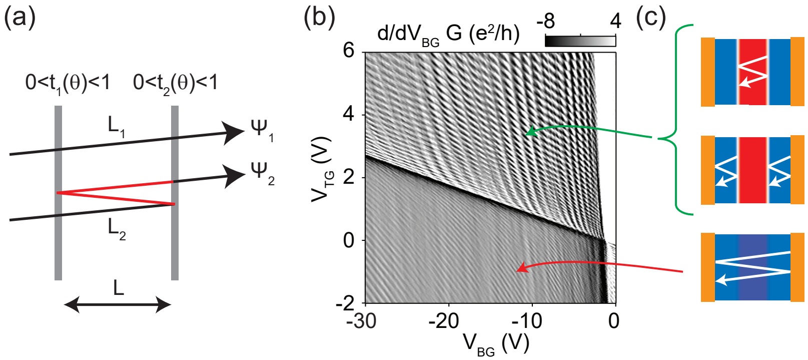

Figure 2.12. Fabry-Pérot resonances in a *p-n-p* junction. a, Schematic sketch of Fabry-Pérot resonances between two semi-transparent interfaces. **b,** Numerical derivative of the conductance as a function of local top-gate and global bottom-gate in a two-terminal *p-n-p* junction with a total length of ∼1 µm between the contacts. **c,** Illustration of the different resonances present in the system.

coherence length. Example of coherent transport in diffusive samples are universal conductance fluctuations (UCF) and weak localization effects, while in ballistic samples Fabry-Pérot resonances is a prominent example.

In the following, the details of phase coherent transport shall be discussed with the example of Fabry-Pérot resonances. In Fig. 2.12a a cavity with two semi-transparent interfaces ($0 < t_{1,2}(\theta) < 1$ where $t_{1,2}(\theta)$ are the angle dependent transmission coefficient) and a length L is sketched. Constructive interference is observed, if the path-difference between the waves Ψ_1 and Ψ_2 (indicated as the red section for the most simple case) satisfies the relation $2L = i\lambda$ where i is an integer. In graphene, the semi-transparent interfaces are established via *p-n* junctions and the wavelength is tuned according to $\lambda = 2\sqrt{\pi/n}$ [40, 41, 92]. If Fabry-Pérot resonances are observed, it is a clear signature of phase coherent transport within a distance of at least $2L$. In Fig. 2.12b multiple types of Fabry-Pérot resonances can be seen, as sketched in Fig. 2.12c. Since we see Fabry-Pérot resonances in the unipolar regime, it indicates that at least a certain part of the charge carriers trajectories are phase coherent (and in this case as well ballistic) over a distance of at least 2 µm down to a very low doping-range. The oscillation amplitude (ΔG_{osc}) of the Fabry-Pérot resonances is proportional to [58]:

$$\Delta G_{\mathrm{osc}} \propto \sum_{\theta} e^{-2L/l_{\Phi}} \cdot \Big(|t_1(\theta)|^2 |t_2(\theta)|^2 |r_1(\theta)||r_2(\theta)| \Big). \tag{2.45}$$

Equation 2.45 describes the sum over all trajectories (varying incident angle θ) where $\exp(-2L/l_\Phi)$ is proportional to the vanishing fraction of phase coherent (and ballistic) trajectories and the expression within the bracket (where $r(\theta) = 1 - t(\theta)$) depends on the p-n junction smoothness. More details of ΔG_{osc} on the p-n junction smoothness will be given in chapter 6.
The vanishing of phase coherent transport originating from temperature smearing can be estimated by comparing the thermal fluctuations with the phase difference between the interfering paths. In the single-particle interference model [93] the interference-signal decays due to the temperature-smearing of the charge carrier source, which is given by $\Delta E \sim k_{\mathrm{B}}T$ (k_{B} being the Boltzmann constant). The phase coherence is completely lost if charge carriers along two paths of different length (e.g. L_1 and L_2 in Fig. 2.12a), and emitted at different energies, acquire a phase-difference around $\Delta\Phi \sim 2\pi$. Furthermore, $\Delta\Phi = |\Delta\vec{k}_{\mathrm{F}}| \cdot \Delta L$, where $\Delta L = L_2 - L_1$ is the path difference between the interfering paths [94]. If the path-length of the two interfering trajectories is equivalent ($\Delta L = 0$), all charge carriers will interfere constructively within the cavity, independent on their $\vec{k}$-vectors. This consequently does not lead to a smearing effect within the cavity due to energy-broadening. However, for $\Delta L \neq 0$, different $\vec{k}$-vectors will experience different resonance conditions (varying from constructive to destructive interference), leading to a smearing of the signal within the cavity due to the energy-broadening. With $\Delta E = \hbar v_{\mathrm{F}}|\Delta\vec{k}_{\mathrm{F}}|$ coherent transport in graphene is expected to survive up to temperatures on the order of [58, 95]:

$$T = \frac{h v_{\mathrm{F}}}{k_{\mathrm{B}}\Delta L}. \tag{2.46}$$

Alternative mechanisms accounting for a loss of the phase coherence might be an enhanced coupling between graphene and its environment or a change of the scattering rates (e.g. via enchanced electron-electron interactions at elevated temperature[33, 96]). However, in order to make quantitative predictions one needs a detailed knowledge of the scattering mechanisms.

2.4. Moiré superlattice on hBN substrate

Graphene and hBN are isomorph materials which means that they both have a hexagonal unit-cell. However, hBN has a two-atomic unit-cell with two different atoms, namely boron and nitrogen, which alternate as illustrated in Fig. 2.13a. The lattice constant of hBN is 1.8 % larger than the one of graphene and instead of a zero-gap semiconductor hBN is an insulator with a large bandgap of 5.97 eV. In the case of graphene encapsulated in hBN (chapter 3 and chapter 4), a Moiré superlattice can be formed between hBN and graphene due to the small lattice mismatch between hBN and graphene. A superlattice is

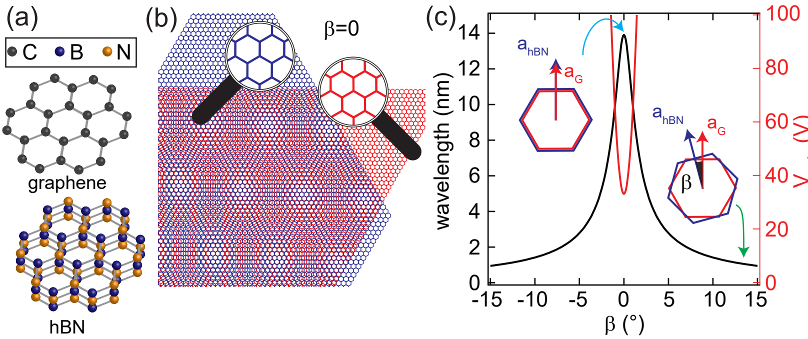

Figure 2.13. Superlattice wavelength as a function of relative angle mismatch between hBN and graphene. a, Graphene and hBN are isomorph crystals, but graphene consists of only carbon atoms, while hBN consists of two different atoms, namely boron and nitrogen. **b,** Illustration of the Moiré superlattice between two lattices with a different lattice constant and $\beta = 0°$. **c,** Superlattice wavelength according to equation 2.47 (black curve). The red curve indicates the gate voltage ($d_{\mathrm{SiO_2}} = 300\,\mathrm{nm}$, $d_{\mathrm{hBN}} = 30\,\mathrm{nm}$) where the satellite Dirac-peaks are expected according to equation 2.48.

a superior lattice structure which forms if two or more materials, each having their own periodic lattice structure, are superimposed as shown in Fig. 2.13b. This was first observed by Johansson and Linde in 1925 by studying the X-ray diffraction on gold-copper and palladium-copper systems [97]. In the following section, the implication of such a Moiré superlattice on the electronic band structure of graphene are discussed. From simple trigonometric considerations, the superlattice wavelength (λ) which forms between hBN and graphene can be calculated according to [98]:

$$\lambda = \frac{(1+\beta)a}{\sqrt{2(1+\delta)(1-\cos\beta)+\delta^2}}, \tag{2.47}$$

where $\delta = 0.018$ is the difference of the lattice constants between hBN and graphene, $a = 2.46\,\text{Å}$ ($a = \sqrt{3}a_0$) is the graphene lattice constant and β is the relative rotation angle between graphene and hBN. For $\beta = 0°$ the superlattice wavelength reaches its maximum with $\lambda \sim 15\,\mathrm{nm}$, while it decreases rapidly with increasing rotation-angle as shown in Fig. 2.13c. The presence of the Moiré superlattice causes a band reconstruction in graphene, which includes the emergence of so called satellite Dirac peaks (satellite DPs). At these satellite DPs the band structure of graphene is strongly modified as shall be discussed in the next section in more detail. It is worth mentioning, that even though on hBN there is always a Moiré superlattice present, the effects of the band reconstruction are experimentally only observable for small misalignment angles (β) between hBN and graphene [98, 99]. This is due to the fact that for small lattice periods the band reconstruction appears at high energy, which is not accessible by conventional gating. This is shown in Fig. 2.13c where the gate voltage required to observe the satellite DPs is calculated for typical experimental device parameters using equation 2.47 and equation 2.48. The formation of a Moiré superlattice has been demonstrated in various spectroscopy [98, 100, 101] and transport [33, 102–109] experiments. Besides experiments, considerable effort has been invested to calculate the band structure of graphene under the influence of such a Moiré superlattice [110–112], which is in the focus of the following section.

2.4.1. Band reconstruction

The band reconstruction in graphene manifests itself in transport measurements as an increased resistance at high doping at the position of the satellite DPs, comparable to the main DP at the CNP. Since the wavevector of the superlattice Brillouin zone is given by $G = 4\pi/(\sqrt{3}\lambda)$ [103], and the energy is given by $E_\mathrm{S} = \hbar v_\mathrm{F} G/2$, the relative rotation-angle between hBN and graphene can be extracted from experiments as shown in Fig. 2.14a, using:

$$\lambda = \sqrt{\frac{4\pi e}{3(V_{\mathrm{g},\pm} - V_0)C}} \tag{2.48}$$

where $V_{\mathrm{g},\pm}$ (V_0) is the gate voltage at which the satellite (main) DP is observed, and assuming a parallel plate capacitor model (equation 2.40) to calculate the charge carrier density. A representative field-effect measurement at zero magnetic field and a quantum Hall measurement of a two-terminal device is shown in Fig. 2.14a,b. In Fig. 2.14b the evolution of the filling factors follow equation 2.30 with a degeneracy of $g = 4$ for main and satellite DPs. Even though the filling factors emerging from the satellite DPs follow equation 2.30, the absolute density is replaced by the density relative to the satellite DP according to $n' = n - (n_{\mathrm{g},\pm} - n_0)$. While the origin of the satellite DPs is well understood, the exact shape of the band reconstruction is still not fully known yet. In the following a family of possible Moiré band reconstructions for graphene on hBN substrate are discussed which were calculated by J. Wallbank *et al.* [110] using a general symmetry-based approach. Because the relatively large number of model-dependent parameters of the symmetry breaking potential can strongly influence the obtained Moiré perturbation, the focus was on the generic features for different sets of parameters used. In Fig. 2.15, the density of states (DOS) for three different sets of parameters is plotted. Details on the parameters can be found in Ref. [110]. Independent of the model-parameters

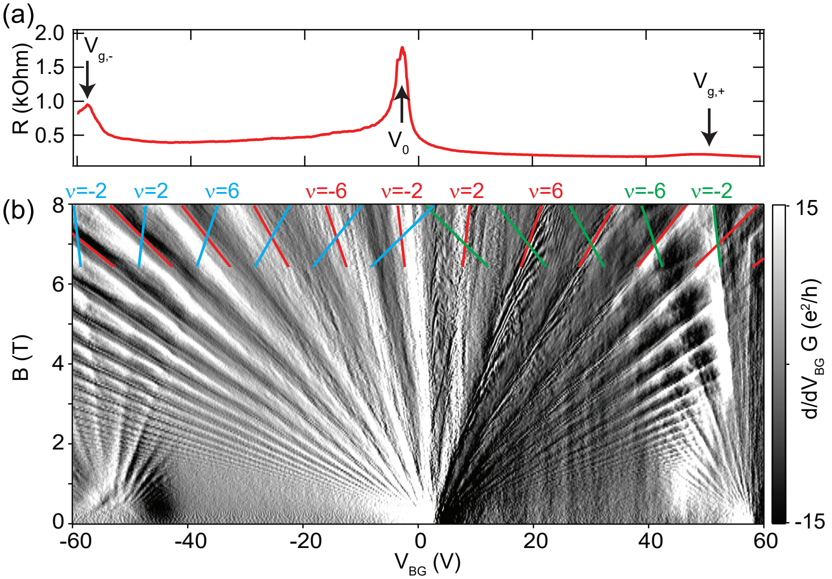

Figure 2.14. Transport measurements. a, Field effect measurement at B =0 T. **b,** Quantum Hall measurement where the numerical derivative of the conductance is plotted. The evolution of the filling factors of the main and satellite DPs are shown in red, blue ($E_\mathrm{F} < 0$) and green ($E_\mathrm{F} > 0$).

the DOS drops to zero at a single point only for the satellite DP on the hole side ($E_\mathrm{F} < 0$) while on the electron side ($E_\mathrm{F} > 0$) only a modulation of the DOS can be observed. Since a vanishing DOS at a single point is one of the benchmarks of a Dirac cone, only the satellite DP at the hole side actually qualifies as a “real” DP. Energy-spacings between various points can be extracted from Fig. 2.15, using $b = \frac{4\pi}{3a_0}\sqrt{\delta^2 + \beta^2}$. Comparable to the main DP, in the vicinity of the satellite DPs ($E_\mathrm{F} < 0$), where the band structure is roughly linear, the doping can be converted into an energy according to:

$$E = \hbar v_{\mathrm{F,sat.DP}} \sqrt{\frac{\pi \Delta n}{g_{\mathrm{SDP}}}} \tag{2.49}$$

where $v_{\mathrm{sat.DP}}$ =0.45 × 10^6 m/s is the rescaled Fermi velocity extracted from capacitance measurements at the satellite DP [100], Δn is the density measured from the satellite DP and g_{SDP} is the additional degeneracy of the satellite DP with respect to the main DP. The number of satellite DPs generated in the mini-Brillouin zone for each main DP can be extracted from quantum

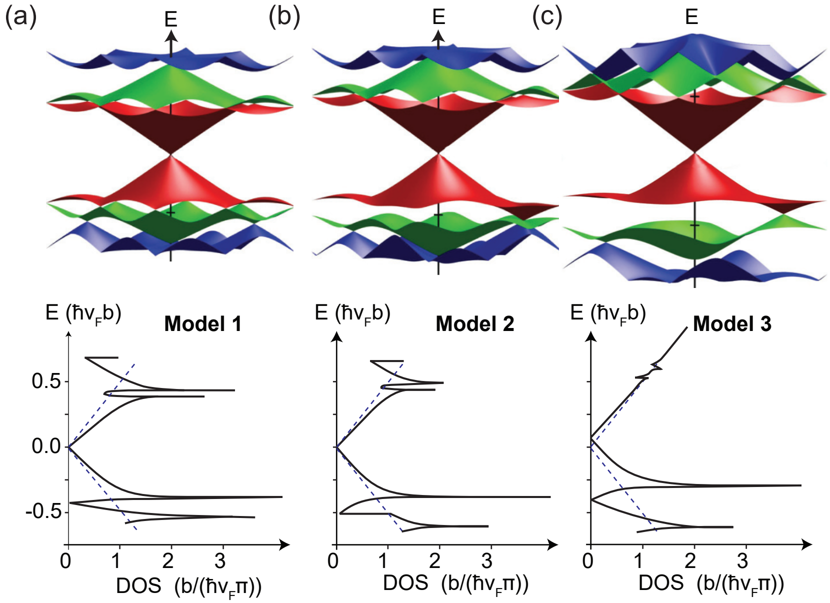

Figure 2.15. Band-reconstruction including Moiré mini-bands. a-c, Calculations of three different families of band reconstructions using different model-parameters. Top: Energy as a function of the $\vec{k}$-vectors. Bottom: DOS as a function of the energy. The blue, dashed line indicates the DOS of graphene in the absence of a Moiré superlattice. Figure adapted from Ref. [110].

Hall measurements [103, 104, 113] by fitting the evolution of the filling factors (ν) at fully filled Landau levels according to equation 2.30. For the main DP $g = 4$, reflecting the spin- and valley-degeneracy. For the satellite DPs a degeneracy of $g = 4$ is found which implies that there is only one satellite DP in the mini-Brillouin zone for each main DP. This 1:1 correspondence is somewhat surprising, since following a simple band-folding picture one would expect two satellite DPs per main DP [98, 103]. However, it is in agreement with the two models shown in Fig. 2.15b,c [110], capacitance measurements [100], angel-resolved photoemission spectroscopy (ARPES) [114] and more recent band structure calculations [115].

The comparison between experiments and simulation of transverse magnetic focusing (TMF) on graphene with a Moiré superlattice [33] suggest that model 3 (Fig. 2.15c) is the most likely band reconstruction.

2.5. Valley Isospin

Charge carriers in graphene are 4-fold degenerate, due to the spin- (up- or down) and valley- (K or K') degree of freedom (chapter 2.1.1). Within the recent years valleytronics became a rapidly growing field since it was realized that not only the charge or spin-degree of freedom, but as well the valley degree of freedom can be used for encoding or processing informations. Comparable to the spin degree of freedom, the valley degree of freedom can be described with a two-component spinor wave-function with quantization axis $\vec{\nu}$, which can be represented on the Bloch sphere according to:

$$|\vec{\nu}\rangle = \begin{pmatrix} \cos\frac{\beta}{2} \\ e^{i\alpha}\sin\frac{\beta}{2} \end{pmatrix} \tag{2.50}$$

where $\alpha = [0; 2\pi]$ is the angle within the equatorial-plane and $\beta = [0; \pi]$ is the angle with respect to north-pole of the sphere which represents the K' (or K) valley. An ideal material system to observe valley-physics has a band structure consisting of two (or more) degenerate, but inequivalent valleys (local energy extrema). The latter can be manipulated in order to encode, process and store information. However, the valley degree of freedom is only a good quantum number, and thus useful for valleytronics, if unwanted valley-scattering due to defects (leading to large k-scattering) is sufficiently suppressed. In systems that lack inversion symmetry, such as for example monolayers transition metal dichalcogenides (TMDC's), charge carriers in different valleys are subject to different Berry curvatures, which act like an effective magnetic fields in the presence of an in-plane electric field. These materials may therefore exhibit Hall-like currents, which are opposite for K and K' valley, flowing transversely to the applied electric field even in the absence of an external magnetic field. In optics right and left circular polarized light can be used to selectively address the two valleys due to different selection rules [116, 117]. As graphene lacks a broken inversion symmetry it does not seem to be an ideal candidate for valleytronics. However, the inversion-symmetry of single layer graphene can be artificially broken using a graphene/hBN Moiré superlattice [105]. Alternatively one might consider bilayer graphene where the inversion symmetry can be broken upon applying an electric field perpendicular to the graphene plane [118, 119].

Besides the above mentioned results there exist several theoretical proposals on how to address the valley degree of freedom in single-layer graphene, including strained graphene [120, 121] or p-n junctions in graphene nanoribbons (GNRs) at high magnetic fields [45]. Before discussing the basics of the latter proposal, a short introduction in GNRs is given.

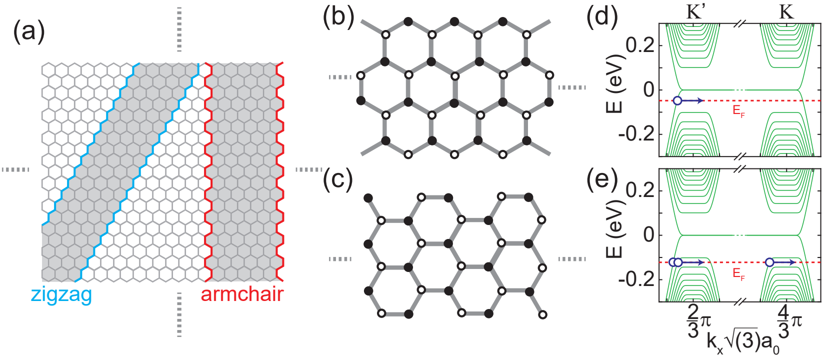

Figure 2.16. Graphene nanoribbons with different chiralities a, Graphene sheet where zigzag and armchair GNR are indicated. **b,** For a zigzag GNR, the top- and bottom-edge consists of A- and B-atoms (indicated with the black and white dots respectively) exclusively. **c,** For armchair GNR, both edges consist of A- and B-atoms. **d,e,** Band structure of a zigzag GNR in magnetic field. Only if the lowest Landau level is occupied the charge carriers moving along the edges are valley-polarized (K or K') as shown in (d) for holes with a positive group-velocity. Band structure courtesy of M.-H. Liu.

2.5.1. Graphene nanoribbons

While in theory graphene is always considered as an infinite sheet, in real devices the graphene has a finite size. Nevertheless, edge effects are in most cases negligible as the most structures are rather large, where the transport is dominated by the bulk. However, by reducing the confinement in one or even two dimensions down to a few tens of nanometers, edge effects start to dominate. Examples of narrow confinements are quantum dots with an energy-spacing and possibly the observation of localized edge states [122], but probably the best studied systems revealing a confinement are the GNRs. They consist of graphene which is translation invariant in one direction (transport direction), while they are confined in the direction perpendicular to it. GNRs can have any arbitrary chirality, but the two most studied GNRs are zigzag or armchair GNRs as shown in Fig. 2.16a. GNRs are of special interest, as their properties can be tuned by carefully choosing their width and chirality. In perfect zigzag GNRs, as shown in Fig. 2.16b, spin-polarized transport [123, 124] and valley helical edge modes [125] are predicted. Armchair GNRs, as shown in Fig. 2.16c, exhibit a width dependent energy-gap near the charge neutrality point (CNP) [123, 126] which might be of interest for graphene based field-effect transistors with a high on-off ratio [127].

At finite magnetic field it turns out that the A and B sublattice are directly linked to the valley degree of freedom (K and K') if only the LLL is occupied [57]. Since in the quantum Hall regime edge states carry the current, the termination of the edges in GNRs will be linked to the valley-polarization of the edge states. In Fig. 2.16d this can be clearly seen as illustrated for a zigzag GNR where the charge carriers moving along the edge, which is defined by either A or B atoms, is fully polarized in either the K or K'-valley respectively. As soon as higher Landau levels are occupied charge carriers moving along the edges can have contributions from both valleys, as it is shown in Fig. 2.16e.
While GNRs are an ideal playground for various theoretical studies, the fabrication of clean GNR with a well defined chirality and width is still challenging. Defining the GNRs via reactive ion etching (RIE) [126, 128] can have limitations such as i) the creation of localized states due to dangling bonds and chemical edge modifications, and ii) the edge roughness which is in the order of a few nanometers, since this is the resolution-limit of standard e-beam lithography required to define the etching mask. A more suitable top-down approach is the definition of GNRs via hydrogen-plasma etching [129–131] where the chirality of the GNR is well defined. However, the exact width is still difficult to control. Bottom-up approaches, such as the surface assisted self-assembly [132], allows an exact control of the chirality and width, but they are yet limited to very small GNRs [127].

2.5.2. Valley-valve effect

Based on the finding of direct coupling between sublattice and valley in the LLL, Tworzydło et *al.* predicted a valley-isospin dependence of the conductance in GNRs with a smooth *p*-*n* junction located perpendicular to the transport direction [45]. The device is based on a two-terminal GNR with perfect edges (armchair or zigzag) where a *p*-*n* junction is located perpendicular to the transport direction is sketched in Fig. 2.17a. In magnetic fields the charge carriers injected at the bottom right contact travel in skipping orbits along the edge [12, 13, 133] while the bulk is insulating. In the presence of a *p*-*n* junction the charge carriers additionally flow along the *p*-*n* junctions within the bulk, connecting the bottom- and top-edge [134, 135]. These edge states are furthermore valley-degenerate if the *p*-*n* junction is smooth on the scale of the lattice constant [136, 137]. Surprisingly, in high magnetic fields where only the LLL is occupied the conductance is solely determined by the chirality and width (number of unit-cells (N) between bottom- and top-edge) of the GNR, assuming a perfect bulk where no scattering events are present. The suggested device operates in close analogy to a spin-valve [138], where the bottom- and top-edges are the polarizer and analyzer units, while the *p*-*n* junction is the channel. Even more, in a perfect armchair GNR the conductance is given by

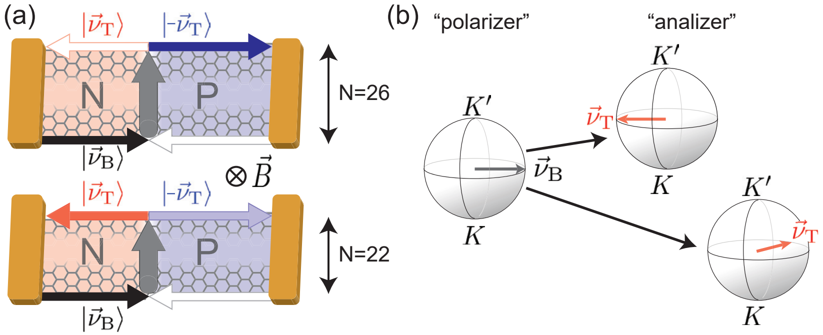

Figure 2.17. Illustration of a the valley-valve effect on an armchair GNR. a, Two armchair GNRs with the same chirality, but different widths, where the charge carriers are injected at the bottom-edge and guided along the *p*-*n* junction to the top-edge. If the relative angle (Φ) between the valley-isospins at the two edges (same polarity) is equal to π (e.g. for N=26), back-reflection is forbidden. **b,** Illustration of the valley-isospin configuration for bottom- (black, $\vec{\nu}_{\mathrm{B}}$) and top-edge (red, $\vec{\nu}_{\mathrm{T}}$) where Φ is π (N=26) and $\pi/3$ (N=22) respectively.

the simple relation [45]:

$$G = \frac{e^2}{h}\left(1 - \cos\Phi\right), \tag{2.51}$$

where Φ denotes the relative angle between the two valley-isospin configurations at the bottom- ($\vec{\nu}_{\mathrm{B}}$) and top-edge ($\vec{\nu}_{\mathrm{T}}$) for the same polarity. Equation 2.51 can be easily derived if we remember that in the LLL the valley-isospin is directly coupled to the sublattice [57]. Since the edges of a armchair GNR consist equally of A- and B-atoms as shown in Fig. 2.16c, the valley-isospin has to be located in the equatorial plane on the Bloch sphere. The valley-isospin is consequently a coherent superposition of the K- and K'-valley [139], which can be written as:

$$|\vec{\nu}_{\mathrm{B}}\rangle = \frac{1}{\sqrt{2}}\begin{pmatrix} 1 \\ e^{i\alpha_{\mathrm{B}}} \end{pmatrix} \qquad \text{and} \qquad |\vec{\nu}_{\mathrm{T}}\rangle = \frac{1}{\sqrt{2}}\begin{pmatrix} 1 \\ e^{i\alpha_{\mathrm{T}}} \end{pmatrix}. \tag{2.52}$$

The expectation value for charge carrier to be transmitted across the *p*-*n* junction is then given by:

$$T = 1 - |\langle \vec{\nu}_{\mathrm{T}} | \vec{\nu}_{\mathrm{B}} \rangle|^2. \tag{2.53}$$

By introducing a relative angle between the bottom- and top-edge isospin configuration given as $\Phi = \alpha_{\mathrm{T}} - \alpha_{\mathrm{B}}$, and assuming that in the LLL the transmission corresponds to $T = 2\,\mathrm{e}^2/\mathrm{h}$ since two edge states are populated (section 2.1.3), one ends up with equation 2.51. For the case of an armchair GNR, the measured conductance across the *p*-*n* junction is given by

$$G = \begin{cases} 2\ e^2/h & N \bmod 3 = 2 \quad (\Phi = \pi) \\ 0.5\ e^2/h & \mathrm{N\ otherwise} \quad (\Phi = \pm\pi/3) \end{cases} \tag{2.54}$$

where Φ is the relative angle between "analyzer" and "polarizer" edge as sketched in Fig. 2.17b. Furthermore, the condition $N \bmod 3 = 2$ is equivalent for obtaining a metallic GNR. Similar results can be obtained for zigzag GNRs, leading to conductance values given by:

$$G = \begin{cases} 2\ e^2/h & \mathrm{N\ odd} \\ 0\ e^2/h & \mathrm{N\ even.} \end{cases} \tag{2.55}$$

It is worth noting that the results of equation 2.55 do not originate from equation 2.51, which is only valid for armchair GNRs. The rigorous derivation of equation 2.55 is more complicated and goes beyond the scope of this Thesis, therefore it shall not be discussed in more detail.

Diffusive devices

So far many studies concentrated on the equilibration of edge states in diffusive *p*-*n* or *p*-*n*-*p* junctions which does not allow the observation of valley-isospin oscillations, since scattering events do not preserve the valley-isospin degree of freedom. Edge state equilibration means that the Landau-levels are not decoupled from each other and that charge carriers can scatter from one edge state into another, mediated by scattering events. For the most simple device, namely a two-terminal *p*-*n* junction, and assuming that all Landau levels mix equivalently (full equilibration), the conductance in the bipolar regime is given by [134]:

$$G = \frac{e^2}{h}\frac{|\nu_\mathrm{l} \cdot \nu_\mathrm{r}|}{|\nu_\mathrm{l}| + |\nu_\mathrm{r}|}, \tag{2.56}$$

where ν_l and ν_r are the filling factors (equation 2.30) within the left and right cavities. In the unipolar regime the conductance is simply given by (no equilibration):

$$G = \frac{e^2}{h}\min\left[|\nu_\mathrm{l}|, |\nu_\mathrm{r}|\right]. \tag{2.57}$$

The concept of edge state equilibration can be easily extended to a *p*-*n*-*p* junction, which yields in the bipolar regime [140]:

$$G = \frac{e^2}{h}\frac{|\nu_\mathrm{in}||\nu_\mathrm{out}|}{2|\nu_\mathrm{in}| + |\nu_\mathrm{out}|} \tag{2.58}$$

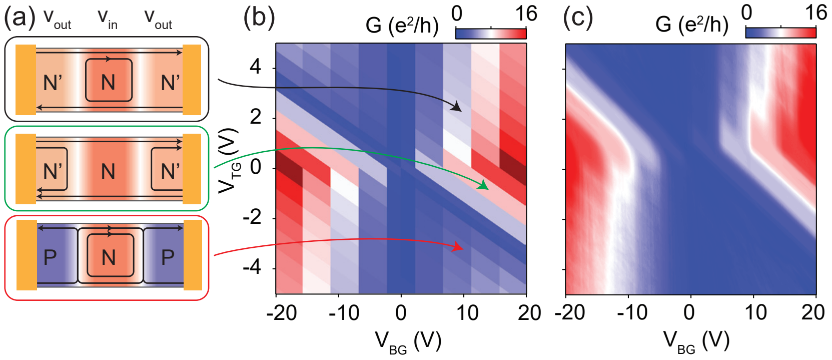

Figure 2.18. Equilibration of edge states in a *p*-*n*-*p* junction at B = 3 T. a, In the unipolar regime (top and middle row) the edge states equilibrate along the graphene edges while in the bipolar regime (bottom row) the equilibration takes place along the *p*-*n* junctions. **b,** Simulation assuming full equilibration of all edge states [140] in comparison with **c,** the experimental data.

where ν_{in} (ν_{out}) are the filling factors in the inner (outer) region as sketched in Fig. 2.18a. In the unipolar regime the conductance is given by:

$$G = \frac{e^2}{h}\frac{|\nu_{\text{in}}||\nu_{\text{out}}|}{2|\nu_{\text{in}}| + |\nu_{\text{out}}|} \qquad \text{if} \qquad |\nu_{\text{out}}| \leq |\nu_{\text{in}}| \tag{2.59}$$

or

$$G = \frac{e^2}{h}|\nu_{\text{in}}| \qquad \text{if} \qquad |\nu_{\text{out}}| > |\nu_{\text{in}}|. \tag{2.60}$$

Analysing the experiments, it turns out that the equilibration along the graphene edges (unipolar regime) is much more efficient compared to equilibration along the electrostatically defined *p*-*n* junction (bipolar regime) as shown in Fig. 2.18b,c. In fact, equilibration along the *p*-*n* junction is almost negligible as shown in Ref. [47]. There are mostly two effects accounting for this observation: i) At the graphene edges (hard-wall potential) the potential-profile is much steeper compared to the *p*-*n* junction, which causes a stronger overlap, between the wave-functions of the different Landau levels. ii) The roughness of the graphene edge, often defined via reactive ion etching, is in most cases significantly higher compared to the electrostatically defined *p*-*n* junction, which can mediate the mixing between different edge states.

This kind of measurement can therefore reveal valuable informations about the graphene edge and *p*-*n* interface roughness since little edge state equilibration is an indication for a good quality of the graphene edges/*p*-*n* junction [141]. More recent studies on edge state equilibration along the *p*-*n* junction include only mixing between the lowest Landau level, while higher Landau levels remain unaffected [133]. This model is more suitable for samples with better graphene edge quality.

3 Suspension and Encapsulation

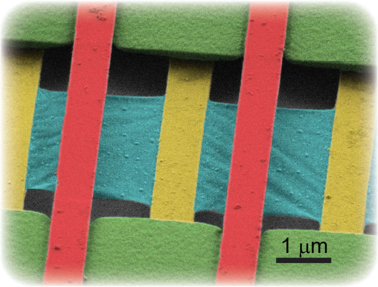

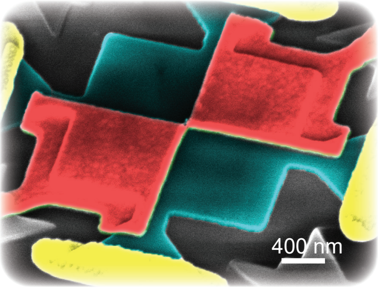

The very first experiments on graphene were performed on a SiO_2 substrate [3, 12, 13]. However, quite soon after these first measurements, the limitations of SiO_2 as a substrate became evident. The most limiting factors are: i) The relatively rough surface [21, 142, 143] of the SiO_2 dielectric, which is most commonly grown either thermally or using a chemical process, giving rise to strain in graphene [144, 145]. ii) During the growth process of SiO_2 charged species can be trapped, giving rise to a non-homogeneous potential landscape [142, 143, 146], which leads to impurity scattering in graphene [147]. These effects significantly limit the residual doping and mobility (table 3.1), making the interesting Dirac-physics close to the charge neutrality point inaccessible. In order to overcome these limitations, new techniques to decouple the graphene from its environment were explored. Nowadays the two most prominent ones are suspension and encapsulation which shall be discussed in the following chapter.

	mobility [$cm^2V^{-1}s^{-1}$]	residual doping [m^{-2}]
SiO_2	1×10^3 to 1×10^4 [50, 148]	$>5 \times 10^{14}$ [149]
hBN	1×10^5 to 1×10^6 [29, 30, 148]	$>5 \times 10^{13}\,m^{-2}$ (Fig. 2.9)
suspended	5×10^5 to 3×10^6 [150]	$>5 \times 10^{12}\,m^{-2}$ [86]

Table 3.1. Typical values in graphene on different substrates.

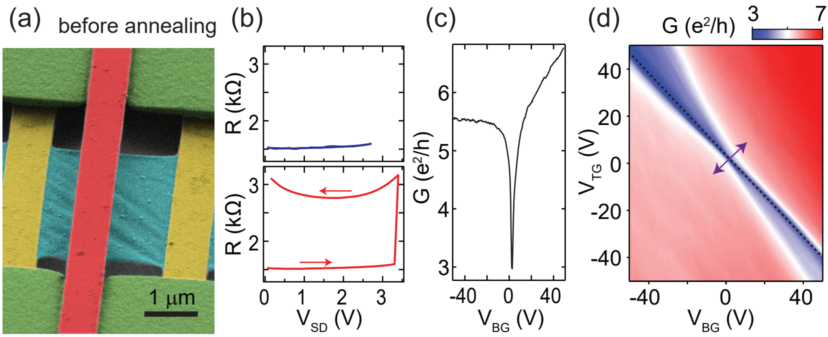

Figure 3.1. Current-annealing of suspended graphene devices. a, False-color SEM image of a suspended graphene (cyan) on LOR (green), with contacts (yellow) and top-gates (red) before annealing. **b,** Representative traces (resistance-voltage curve) for the first (top) and last (bottom) steps during the current-annealing process. **c,** Conductance as a function of the global back-gate after current-annealing ($V_{\mathrm{TG}}=0\,\mathrm{V}$). **d,** Conductance as a function of global bottom-gate and local top-gate ($T=230\,\mathrm{mK}$).

3.1. Suspension

Probably the most straight-forward approach to increase the graphene quality is to suspend it. This can be achieved by etching the SiO_2 below the contacts away using Hydrofluoric acid (HF) [151, 152]. The drawback of this technique is that only a very limited amount of materials survive the aggressive HF etching step. An alternative approach suspending devices without the need of HF etching was given by Tombros et *al* [153] using a polymer-support (LOR: lift-off-resist) onto which the graphene is exfoliated or transferred. This process is compatible with most standard e-beam lithography and evaporation processes using PMMA. Suspension of the grahene is done in the last step by exposing the LOR-resist with a very high e-beam dose (significantly higher than that required for the PMMA) and subsequent developing in Ethyl-lactate. The suspension-process based on this technique has several advantages: i) No dangerous chemicals are required. ii) It is compatible with a wide range of materials. iii) The leads can be fully suspended in comparison with HF etching where the leads remain partially supported by the SiO_2. This can be an advantage as will be explained later on. Independent on the specific type of suspension, directly after fabrication the graphene is strongly contaminated with various polymer and solvent residues as shown in Fig. 3.1a. Before measurement the graphene has therefore to be current-annealed: a process where a high current is applied, heating up the device to several hundreds of degrees [154]. For the current-annealing a voltage biased configuration is chosen which is favoured over the current biased one. This is because upon approaching clean graphene, the resistance at the Dirac-peak ($V_{\mathrm{gate}} = 0\,\mathrm{V}$) increases, thus lowering the dissipated power (current) across the device (the opposite is the case in the current biased configuration). During the annealing procedure, the voltage is ramped up and down, with a continuously increasing amplitude. In the last annealing-step, the resistance usually increases step-like as shown in Fig. 3.1b, since nearly all contaminations are evaporated while the clean graphene remains (Fig. 3.1c,d). The current-annealing step is not only the last step before measurement, it is very often as well the most delicate one during the whole fabrication. The probability with which it is possible to get rid of all the contaminations without destroying the graphene is very small. During the annealing-procedure the contaminations tend to aggregate at the coldest spot of the sample. Therefore, having fully suspended leads (suspension via LOR) which are significantly less substrate-cooled [75] compared to partially supported leads (HF etching), allows the fabrication of graphene which is not only clean in the center of the device, but as well in the very proximity of the leads.

3.1.1. Top-gated devices on LOR

To tune the charge carrier density in graphene one might consider using a global back-gate or local bottom-gates. However, this is not sufficient for several experiments including electric fields [118, 119, 155, 156], which can be achieved by combining bottom- and top-gates. In suspended devices using HF-etching this is typically done via so called “air-bridges“ [157], where prior to the suspension with HF amorphous SiO_2 is evaporated between graphene and the top-gate, defining the spacing between the graphene and the metal-gate. On the other hand, the fabrication of top-gates in suspended devices on LOR is far from being straight forward [158]. The first attempts to establish top-gates in suspended graphene on LOR involved a dielectric between the top-gate and the graphene, namely: i) The evaporation of a thin MgO layer between the graphene and top-gate prior to suspension. ii) The transfer of a hBN flake on top of the already suspended device and the subsequent fabrication of the top-gates in a separate step. However, both techniques result in significantly lower current-annealing yields because the top-gates which are separated by the MgO and hBN respectively can act as heat sinks. In the latter case the hBN might furthermore prevent the evaporation of contaminations as it is likely to fully cover the suspension-mask. Here we present a new method based on fully suspended top-gates and present measurements in a dual-gated bilayer graphene as a proof of principle [158].

The fabrication procedure of the fully suspended top-gates is sketched in

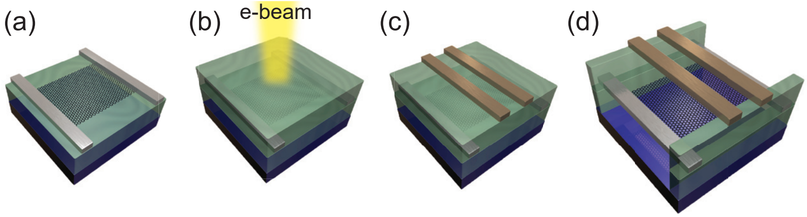

Figure 3.2. Fabrication of local top-gates. a, Fabrication of contacts (grey) to graphene on LOR (green) [153]. **b,** Spin-coating of the spacing layer (PMMA + LOR) between graphene and top-gate and exposing the suspension mask. **c,** Evaporation of top-gates and **d,** subsequent suspension of the device. Figure adapted from Ref. [158].

Fig. 3.2. Similar to Ref. [153] it starts by etching the graphene in its desired shape (if needed) and evaporation of the metal-contacts as shown in Fig. 3.2a. This is followed by spin-coating a second layer of LOR (~500 nm thick) which defines the spacing between the graphene and top-gate. In between the two layers of LOR a thin (80 nm) layer of PMMA is added, since without this protection layer the contacts can be deformed during the spin-coating of the second layer of LOR, and no electrical contact between the contacts and graphene can be created. Prior to the evaporation of the top-gates the suspension mask is exposed using a high e-beam dose (1100 µC/cm^2) as shown in Fig. 3.2b,c. However, the suspension using Ethyl-lactate is done in the very last-step (Fig. 3.2d).

A field-effect measurement of a bilayer graphene after current-annealing is shown in Fig. 3.1c. In Fig. 3.1d a conduction-map as a function of global back-gate and local top-gate is shown. In bilayer-graphene an energy-gap can be opened upon applying a displacement-field ($\vec{D}$) [156] which is defined by:

$$\vec{D} = (\alpha V_{\mathrm{TG}} - \beta V_{\mathrm{BG}})/2e\epsilon_0 \tag{3.1}$$

where the parameters α and β describe the gate coupling parameters for V_{TG} and V_{BG} respectively. Moving along the black, dashed line in Fig. 3.1d tunes the magnitude of the energy-gap in the dual-gated region of graphene while keeping the Fermi-energy simultaneously at zero (zero charge carrier doping). This results in a suppression of the conductance across the device with increasing displacement field. The effect of the gap-opening is very moderate in comparison with the results presented in Ref. [156]. Possible reasons for this might be the limited device quality (μ ~25 000 cm^{2}V^{-1}s^{-1}) and/or the use of a local top-gate instead of a global top-gate. By moving along the direction indicated with the purple arrow, the energy-gap remains zero while the doping can be tuned.

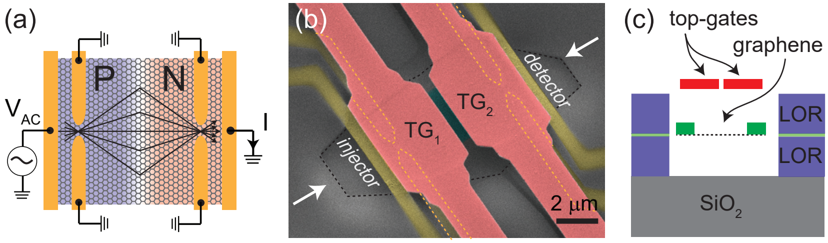

Figure 3.3. Top-gated multi-terminal device. a, Illustration of a suspended, multi-terminal device intended to measure Veselago-lensing using pinhole collimators. **b,** False-color SEM image of a device as shown in (a) with top-gates (red). **c,** Cross-sectional view as indicated in (b) with the white arrows.

Suspension of graphene turned out to be very successful for two-terminal devices with a rectangular graphene flake in order to investigating e.g. ballistic transport [159], the disorder limit [86], quantum Hall effects [160], broken-symmetry and spontaneously gapped states in bilayer graphene [156, 161], Fabry-Pérot resonances [40, 41, 162] and snake states [37]. However, there are major limitations to this techniques, such as the length over which the contacts/top-gates can be suspended (typically a few microns), the current-annealing which becomes much more challenging for multi-terminal devices or devices with a more complex graphene shape as described in the following section.

3.1.2. Complex device designs

In two-terminal devices with a rectangular graphene flake the current-annealing is straight-forward since the current-density throughout the whole device is roughly homogeneous. While for multi-terminal devices with a rectangular graphene shape current-annealing is still doable [37, 135, 151, 152, 160, 163], the suspension-technique certainly reaches its limitation for more complex device designs as e.g. sketched in Fig. 3.3. This device, intended to measure Veselago-lensing [33, 164] as sketched in Fig. 3.3a, includes 6 contacts, a narrow graphene constriction, and two local top-gates. However, from a total of more than 40 devices, not a single one could successfully be current-annealed. This is because any contacts which are not actively involved in the current-annealing process act as heat-sinks and the current distribution in graphene can be strongly non-uniform. Both effects leads to locally varying temperatures of the graphene which makes it very challenging to get rid of all contaminations in the device. We implemented top-gates instead of prepatterned bottom-gates [27, 37, 41] as they were thought to complement the local bottom-gates in further projects [158].

3.2. Encapsulation

While suspension allowed already quite early the fabrication of high-quality graphene, no real alternative to SiO_2 as a support was available until hexagonal boron-nitride (hBN) was introduced as a gate dielectric in 2010 by Dean et *al.* [21]. The crystal-growth of hBN allows to reduce the density of charge impurities to a much lower level and since it is a layered material it holds the potential to be atomically flat [21, 142, 143, 148]. Similar to the exfoliation of graphene, the exfoliation of hBN follows the scotch-tape technique (section 4.1) which yields hBN flakes of all kind of sizes, thickness and shapes. Since the size of the hBN flakes is typically in the order of a few tens of micrometers in each direction, it is typically used in combination with a SiO_2 gate dielectric. The latter separates the leads from the global back-gate, while the hBN is primarily used to decouple the graphene from the SiO_2.

3.2.1. Hexagonal boron-nitride

In the early days of hBN supported graphene, the graphene was transferred on top of the hBN using a wet-transfer method including a polymer [21]. While this method yielded the highest graphene quality on substrate at that time, it comes with the disadvantage that after the transfer-process the graphene is still strongly contaminated with polymer-residues. Even though various processes such as thermal annealing or “AFM ironing” [165] remove most of these residues, a residual contamination will always remain. This shortage was overcome by introducing an all-dry stacking-process [1], where the graphene never comes directly into contact with any polymer or solvent, and therefore should yield an increased quality. While several variations of this dry-stacking process exist (using slightly different transfer-polymers for the hBN), the assembly of the heterostructure (described in more detail in section 4.1) used in this Thesis follow the original approach by Wang et *al* [1]. In contrast to suspension, encapsulation using the dry-stacking does not require any annealing step after fabrication. Furthermore, encapsulation allows much more complicated device structures because almost no limitations on the number of leads, top- and/or bottom-gates (chapter 4) and the shape of the graphene are given. Furthermore, encapsulation of graphene in hBN does not only allow quasi-ballistic and phase coherent transport, but is as well suitable to obtain a Moiré superlattice in graphene due to the small lattice mismatch between graphene and hBN (1.8 %) as described in section 2.4.

3.2.2. Other substrates

Soon after it was realized that hBN, a crystal-grown and layered material, has such a dramatic impact on the whole graphene community, other layered substrates moved into the spotlight [19, 166]. They are of particular interest since they can be used for the assembly of complex Van der Waals heterostructure including semi-conducting [22], superconducting [23, 24] or even ferromagnetic [25, 167] layered materials [168]. However, not all of them are stable in air, such as e.g. black phosphorous [169], which requires encapsulation in e.g. hBN or storage in vacuum to protect it from degradation [170] in ambient conditions. Using the wide range of layered materials, effects normally absent in graphene, such as strong spin-orbit interaction [171–173] or superconductivity [24] can be introduced by simply establishing a Van der Waals heterostructure choosing the appropriate materials.

3.3. Conclusion

Suspension and encapsulation have both their advantages and disadvantages. Therefore, depending on the project the more suitable method has to be chosen. The quality of suspended graphene is still difficult to reach with encapsulated devices as shown in table 3.1, even though considerable improvements have been made within the last years. Suspension is furthermore very suitable to establish relatively soft p-n junctions. In contrast, encapsulated devices hold the potential to establish very sharp p-n junctions because its smoothness is basically limited by the thickness of the insulator (e.g. hBN) which defines the spacing between the electrostatic gate and the graphene. Furthermore the encapsulation poses fewer limitations on the device fabrication as compared to suspension. However, the great success of the encapsulation technique can be mostly attributed in its huge versatility which allows to combine the whole class of Van der Waals crystals into complex heterostructures. This paved the road to taylor the property and shape of the final device nearly at will and with very few restrictions.

4 Fabrication and basic characterization

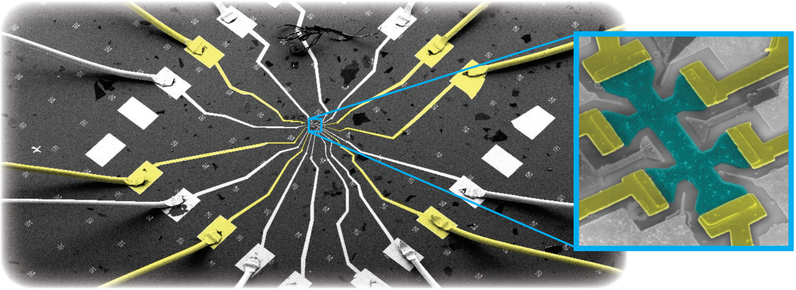

This chapter describes the fabrication of the hBN/graphene/hBN heterostructures via Van der Waals assembly and the implementation of contacts and local gates in detail. It is organized chronologically, starting with the assembly of the hBN/graphene/hBN heterostructure [1] as introduced in section 3.2. This is followed by the detailed description of how to establish self-aligned side-contacts, local top-gates and local bottom-gates. The exact parameters for both, the hBN/graphene/hBN assembly and the fabrication of the contacts and local gates are given in Appendix A. The chapter is closed with a rough statistics on the contact resistance and the mobility of the fabricated devices, some remarks on thermal annealing and a brief description of the measurement set-up.

4.1. Assembly of the hBN/graphene/hBN heterostructures

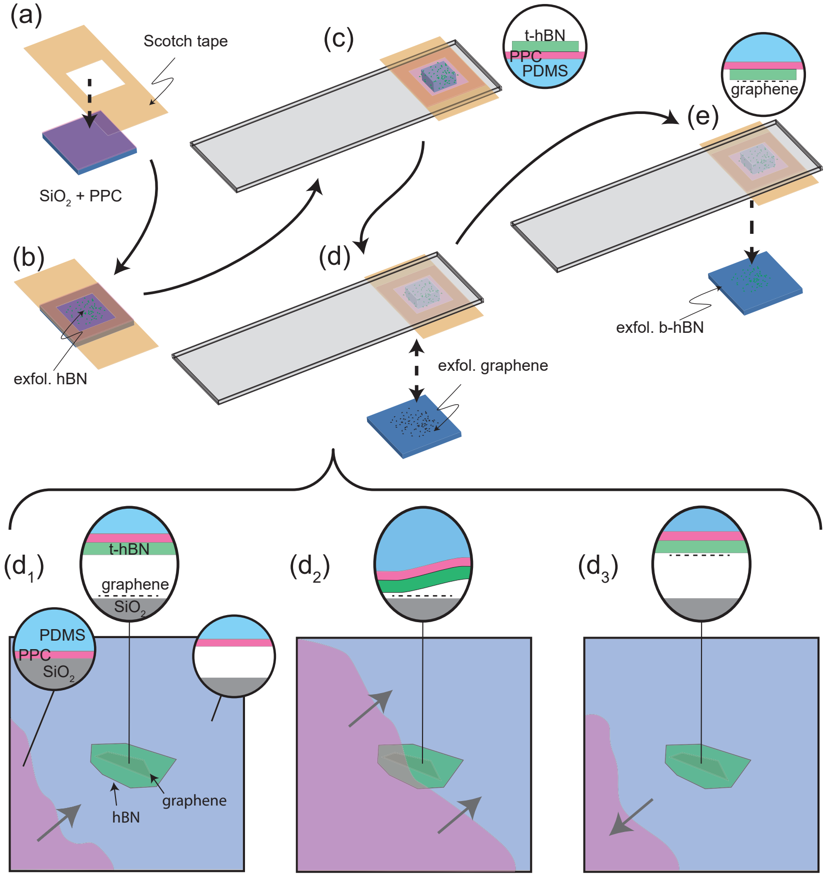

Figure 4.1. Fabrication of encapsulated graphene following the method introduced by Wang et *al.* [1]. a,b, Exfoliation of the top-hBN on PPC. **c,** The polymer is then peeled-off and transferred on a PDMS stamp placed on a glass-slide. **d,e,** Pick-up of graphene from SiO_2 and subsequent release on the bottom-hBN.

A flow-chart illustrating the assembly of a hBN/graphene/hBN heterostructure is shown in Fig. 4.1. It starts with spin-coating a ∼1 µm thick poly-propylene-carbonate (PPC) film on a Si^{++}/SiO_2 chip. A scotch-tape with a frame removed in the center is then fixed on top of the PPC film as shown in Fig. 4.1a, followed by the exfoliation of the top-hBN shown in Fig. 4.1b. All components of the stack, namely bottom-hBN, top-hBN and graphene (from natural graphite) were obtained by exfoliation of their corresponding bulk-crystals using Nitto tape[1]. The high-quality hBN used in all devices was obtained from T. Taniguchi and K. Watanabe [174]. Using an optical microscope with bright- and dark-field, we scanned the chip for hBN flakes, being ideally 10 nm to 30 nm thick and atomically flat. Having found a suitable hBN flake the PPC layer is peeled of from the Si^{++}/SiO_2 support and transferred on top of a ~0.5 mm thick, home-made Polydimethylsiloxane (PDMS) pad, which was previously placed on a glass-slide as shown in Fig. 4.1c. The PDMS pad is used as a soft spacer between the thin PPC and hard glass-slide. The latter is then fixed up-side down in a transfer stage which allows manipulation with roughly µm-precision using micro-screws. In parallel, graphene was exfoliated on a Si^{++}/SiO_2 chip, which was previously cleaned with a Piranha solution (H_2O_2:H_2SO_4 mixture removing organic residues on the chip, Appendix A.1.1). The thickness of graphene (single-, bi- or multi-layer) was optically identified using a microscope-camera with contrast enhancement. In over 95 % of all fabricated devices (> 80) the targeted number of graphene layers was obtained without using Raman-microscopy for verification of the graphene thickness. Using a long-distance microscope mounted on top of the transfer-stage, the top-hBN and graphene can be aligned respectively to each other as shown in Fig. 4.1d. By lowering the glass-slide with the top-hBN, the PPC/PDMS stamp is brought into contact with the Si^{++}/SiO_2 chip and eventually the hBN touches the graphene as shown in Fig. 4.1d_1 and 4.1d_2. By gently retracting the glass-slide, the PPC detaches again from the Si^{++}/SiO_2 chip as shown in Fig. 4.1d_3. The pick-up of graphene by the hBN relies on the strong Van der Waals interactions forces between graphene and hBN (atomically flat crystal) which are larger than the forces between graphene and SiO_2 (amorphous, rough substrate). When bringing the hBN and the graphene (or any other layered materials) into contact with each other, this should be done as slow as possible since this allows the Van der Waals forces, which are very strong between layered materials, to push remaining contaminations/adsorbate being trapped between the layers into pockets (so called “bubbles“) [166, 175, 176]. Generally the larger flake picks up the smaller flake with few exceptions. The top-hBN is chosen to be significantly larger than any other layered material to be picked-up since it is the starting layer for the whole assembly-process. The pick-up process is done at room-temperature and can in principle be repeated multiple times using various materials to obtain complicated multi-layer devices [22]. Finally the hBN/graphene is brought into

---

[1] SPV 224P, Nitto Europe NV

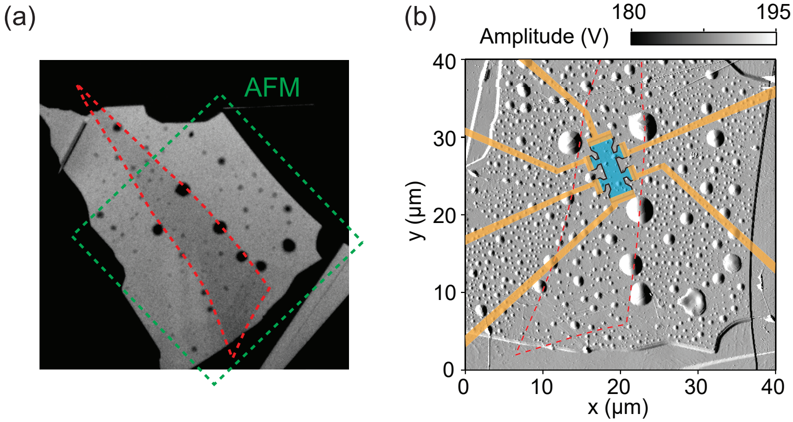

Figure 4.2. Identification of clean areas. a, Contrast enhanced optical image where the location of the graphene is indicated with the red, dashed line. **b,** AFM image as indicated in (a) with the green, dashed square. The location of the device (Hall-bar in this case) was chosen where the least bubbles were observed. The contacts and the etching mask as designed are indicated in orange and cyan.

contact with a bottom-hBN which was exfoliated on a Si^{++}/SiO_2 substrate, as shown in Fig. 4.1e. The heterostructure is released on the Si^{++}/SiO_2 substrate by raising the temperature up to 80 °C which causes the PPC to detach from the PDMS stamp. The PPC is dissolved in Chloroform followed by an annealing step in a $Ar:H_2$ atmosphere. Even though contaminations cannot be removed by annealing because they are trapped between the two layers, it can cause an aggregation of several smaller bubbles into a larger one, leaving extended areas free of contaminations. After the complete assembly of the hBN/graphene/hBN heterostructure it is inspected using an optical microscope with contrast enhancement (Fig. 4.2a) and an atomic force microscope (AFM, Fig. 4.2b) in order to identify the cleanest areas.

4.1.1. Alignment for a Moiré superlattice

In graphene superlattices can be formed using narrow spaced electrostatic gates [177, 178] or taking advantage of the formation of a Moiré superlattice upon precisely aligning the graphene with respect to either the top- or bottom-hBN layer, as discussed in section 2.4. The rotation-angle is measured between the main crystallographic axis being either armchair or zig-zag. Since we used exfoliated graphene and hBN, the flakes tend to tear along their

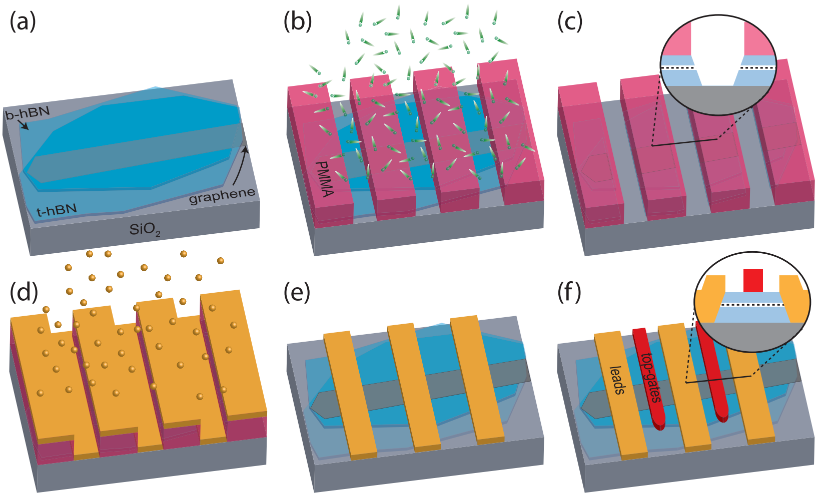

Figure 4.3. Fabrication of side-contacts. a, Full hBN/graphene/hBN heterostructure on substrate. **b-e,** Exposing the graphene edges using a CHF_3:O_2 plasma and subsequent metalization to establish the side-contacts. **e,** Additional option to implement local top-gates as described in section 4.3.1.

main-crystallographic axis, which manifests itself in straight edges and angles between the edges which are a multiple of 30° [179]. In our devices we manually aligned a straight edge of the top-hBN with a straight edge of the graphene with a precision of a few degrees. The aligned half-stack was then placed with a significant rotation angle on the bottom-hBN to ensure that only one type of Moiré superlattice is formed.
An alternative approach to obtain a small rotation angle between two hexagonal, layered materials is based on thermal self-alignment [180, 181]. In that case much less care has to be taken for the alignment between graphene and hBN, since upon thermal annealing the two lattices tend to align with respect to their main-crystallographic axis due to energetically favourable reasons.

4.2. One-dimensional side-contacts

Before the dry-stacking technique was introduced the graphene being placed on top of e.g. SiO_2, hBN or LOR was electrically contacted using so called top-contacts, where metals such as e.g. Ti/Au or Pd were directly evaporated on top of the exposed graphene. However, in a hBN/graphene/hBN heterostructure where the graphene is sandwiched between two layers of hBN as illustrated in Fig. 4.3a, the former is no longer directly accessible. In this case the graphene can be contacted by etching though the hBN/graphene/hBN heterostructure and subsequently evaporating Cr/Au contacts on the exposed graphene edge, forming so called one-dimensional side-contacts [1]. In this Thesis a slightly modified version on how to establish these side-contacts with respect to Ref. [1] was used. The major difference lies in the fabrication of self-aligned side-contacts as shown in Fig. 4.3b,c. Self-aligned means that the same PMMA mask is used for etching the hBN/graphene/hBN heterostructure (Fig. 4.3b,c, Appendix A.3.1) and subsequent evaporation of the Cr/Au contacts (10 nm/50 nm, Appendix A.4) as shown in Fig. 4.3d. This leads to very transparent contacts (50 Ωµm to 100 Ωµm) (see section 4.2.1) since the exposed graphene edge never comes into contact with any solvent or polymer in contrast to the fabrication of side-contacts as introduced by Wang et *al* [1]. For all e-beam lithographic processes involved in the fabrication, we used 100 nm to 300 nm thick PMMA 950K as a resist, exposed with a dose of 450 µC/cm^2 to 500 µC/cm^2 and developed with chilled (∼5 °C) IPA:H_2O (7:3). This low-stress development significantly improved the yield of non-cracked PMMA on hBN since it reduces swelling of PMMA during development [33, 182]. The cracking occurs on the first-hand due to the lower adhesion of PMMA to hBN compared to SiO_2.

4.2.1. Contact resistances

In a two-terminal measurement as illustrated in Fig. 4.4a, the overall resistance is the sum of several contributions such as the line-resistance of the cryostat (R_{lines}, which is a priori known), the contact resistance between leads and graphene (R_{CT}) and the graphene resistance (R_{G}). All together it can be written as:

$$R = 2R_{\text{lines}} + 2R_{\text{CT}} + R_{\text{G}}. \tag{4.1}$$

Since normally R_{G} is not know, it is impossible to extract R_{CT} from equation (4.1). However, in the quantum Hall regime R_{G} is well known, namely $R_{\text{G}} = G_{\text{H}}^{-1}$ where G_{H} is given by equation 2.29. In this case, R_{CT} can be extracted from equation (4.1) the following way (Fig. 4.4b): by subtracting a fixed resistance value (which corresponds to $2R_{\text{CT}}$) from the raw measurement values (dashed lines) all the quantum Hall plateaus can be shifted to their expected values (dashed, horizontal lines). The contact resistance per unit-length is then given as $R_{\text{CT}} \cdot W$. While the best self-aligned contacts were as low as ∼50 Ωµm (Fig. 4.5a), the average is in the order of 100 Ωµm to 200 Ωµm. For many devices the fixed resistance value which has to be subtracted from the raw-data is higher for the hole-side compared to the electron-side. This is because an additional *p*-*n* junction, giving rise to a *p*-*n* junction resistence

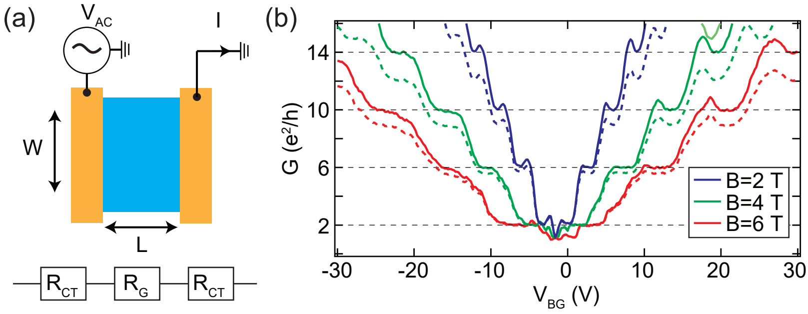

Figure 4.4. Contact resistance extracted from quantum Hall measurements. a, Two-terminal measurement configuration (R_{lines} not included in the sketch) where the leads are given in orange, and the graphene in cyan. **b,** Original conductance (dashed lines) and conductance where contact and line resistance were subtracted.

R_{pn}, is established in the proximity of the contacts (which are n-doped) only if the graphene is p-doped (see section 2.3.1). On the hole-side the subtracted resistance value therefore accounts in fact for $2R_{\text{CT}} + 2R_{\text{pn}}$. Since R_{pn} is unknown, we concentrate on the values extracted on the electron-side where R_{pn} is absent. In Fig. 4.5a a summary of R_{CT} (using equation 2.38 in the n-doped

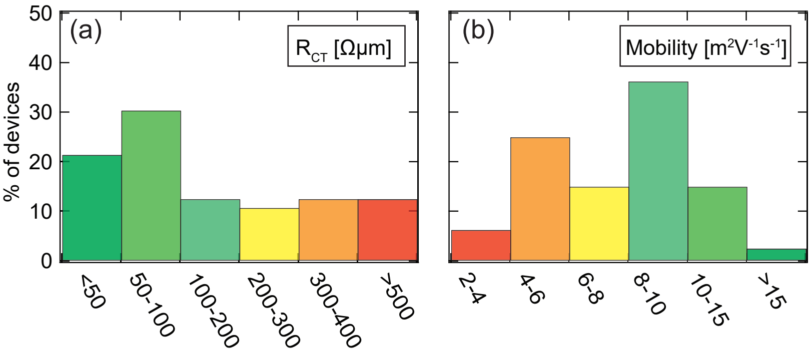

Figure 4.5. Device statistics. a, Contact resistance extracted from quantum Hall measurements as shown in Fig. 4.4b. Total number of measurements: 56. **b,** Field-effect mobility extracted from two-terminal measurements using equation 2.38. Total number of measurements: 80.

regime) is given for over 50 measured junctions. The contact resistance were extracted only for a fraction of all measured junctions, and contacts which are not-working at all are extremely rare (below the percent range). An alternative approach to investigate the contact resistance at zero magnetic field even as a function of charge carrier density is the transfer-length-method described e.g. in Ref. [1]. However, since the dependence of the contact resistance on charge carrier density was not the main focus of this Thesis, we did not investigate it in more detail. A statistics for the charge carrier mobility extracted from field-effect measurements using equation 2.38 is shown in Fig. 4.5b.

4.3. Local gates

In this Thesis several physical transport effects relying on *p*-*n* junctions were investigated. A prerequisite to form such *p*-*n* junctions is the ability to tune multiple graphene regions independently (section 2.2). This can be realized via the implementation of local electrostatic gates in combination with a global back-gate. Here the fabrication details of two device types are given, which consist either of a single *p*-*n* junction or two *p*-*n* junctions in series. While the former was achieved via local bottom-gates, the latter was done via local top-gates.

4.3.1. Local top-gates

The assembly of hBN/graphene/hBN heterostructures used for two-terminal *p*-*n*-*p* junctions is summarized in section 4.2, with the additional modification that in most cases narrow graphene flakes (<2 µm) are used. This is illustrated in Fig. 4.3a. Narrow flakes are beneficial when fabricating *p*-*n*-*p* junctions using local top-gates (in Fig. 4.3f) for two reasons: i) The spacing between the top-gate and graphene is only defined by the thickness of the top-hBN layer which can be chosen very thin. Therefore we can achieve high carrier concentrations and we are able to establish relativly sharp *p*-*n* junctions. ii) No additional etching step is needed to shape the graphene. Using the global back-gate and a local top-gate the charge carrier density in the inner (n_{in}) and outer (n_{out}) regions can be controlled separately. In order to reduce the cross-talk between the gates we used a thin (10 nm to 30 nm) hBN layer. The charge carrier density in the outer (n_{out}) and inner (n_{in}) cavity can be calculated according to:

$$n_{\text{out}} = (V_{\text{BG}} - V_{\text{BG}}^0) \cdot \left(\frac{1}{C_{\text{SiO}_2}} + \frac{1}{C_{\text{hBN,b}}} \right)^{-1} \tag{4.2}$$

and

$$n_{\text{in}} = (V_{\text{BG}} - V_{\text{BG}}^0) \cdot \left(\frac{1}{C_{\text{SiO}_2}} + \frac{1}{C_{\text{hBN,b}}} \right)^{-1} + (V_{\text{TG}} - V_{\text{TG}}^0) \cdot C_{\text{hBN,t}} \tag{4.3}$$

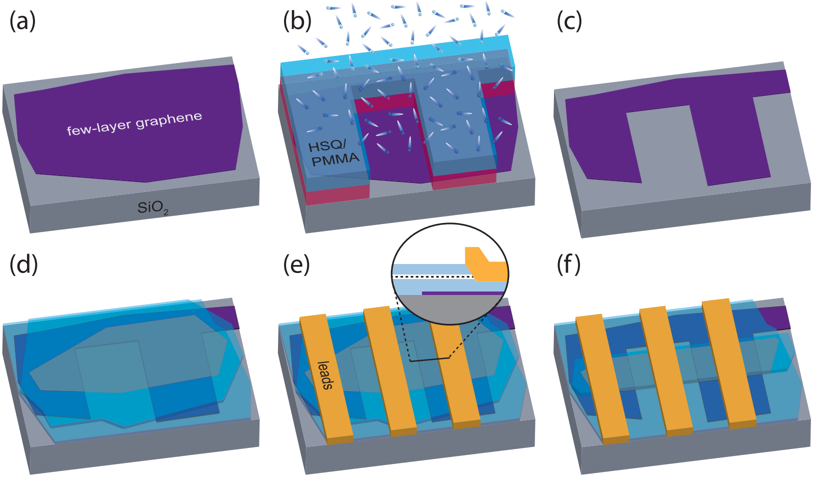

Figure 4.6. Fabrication of two-terminal *p*-*n* devices with local bottom-gates based on few-layer graphene. a, Few-layer graphene used for bottom-gates on substrate. **b,c,** Shaping the bottom-gates with a PMMA:HSQ negative mask and subsequent O_2 plasma etching. **d,** Transferring the pre-assembled hBN/graphene/hBN heterostructure on top. **e,** Exposing the graphene edges using a CHF_3:O_2 plasma and subsequent metalization to establish the side-contacts. It is important that the bottom-hBN is not completely etched through. **f,** Shaping the graphene using again a CHF_3:O_2 plasma.

where $C_{\mathrm{SiO_2}}$,$C_{\mathrm{hBN,b}}$,$C_{\mathrm{hBN,t}}$ are the geometrical capacitances per unit area (equation 2.40) of the SiO_2, bottom and top hBN, V_{BG},V_{TG} are the applied back- and top-gate voltages and V^0_{BG},V^0_{TG} are the offset voltages of the Dirac-peak. The Cr/Au contacts dope the graphene in its proximity *n*-type, independent of V_{BG}.

For more complex device structures (e.g. Hall-bar) an additional etching-step to shape the device prior to the fabrication of the top-gates might be necessary. In this case the evaporation of a thin insulating layer (e.g. MgO) just before evaporation of the top-contacts (using the same PMMA mask) has to be added in order to passivate the exposed graphene edges. The latter prevents shortening between top-gates and graphene.

4.3.2. Local bottom-gates

The formation of p-n junctions using local top-gates is not very well suited, as a very thick insulating layer would be required to separate the top-gate from the leads[2]. Therefore we used local bottom-gates based on few-layer graphene to locally tune the graphene in combination with the global back-gate [178]. The fabrication of the local bottom-gates starts by etching the few-layer graphene using a PMMA:HSQ hard-mask and a O_2-plasma as shown in Fig. 4.6a,b. The PMMA below the HSQ is used as a sacrificial layer which makes the lift-off very simple using acetone. Afterwards a pre-assembled hBN/graphene/hBN heterostructure is transfered on top of the local bottom-gates, shown in Fig. 4.6c, followed by the etching and evaporaton of the side-contacts shown in Fig. 4.6d. Here an accurate control of the etching-rates is crucial since the bottom-hBN must not be fully etched through to prevent shortening between the leads and the local bottom-gates. This is illustrated in the inset of Fig. 4.6d. In the last step the device is shaped into 1.5 µm wide graphene channels shown in Fig. 4.6e,f. Again, the bottom hBN must not be fully etched through as with this one might disconnect the various bottom-gate fingers which are connected by one common contact. The charge carrier density in the two cavities tuned by the global back-gate (n_{BG}) and a local bottom-gate (n_{lbg}) can be calculated according to $n_{\mathrm{BG}} = V_{\mathrm{BG}} \cdot (1/C_{\mathrm{SiO_2}} + 1/C_{\mathrm{hBN,b}})^{-1}$ and $n_{\mathrm{lbg}} = V_{\mathrm{lbg}} \cdot C_{\mathrm{hBN,b}}$. Again, the Cr/Au contacts dope the graphene in its proximity n-type.

4.4. Etching of constrictions

In the previous sections the graphene heterostructures were etched into rectangular devices. However, etching processes can as well be used to create nanoribbons as introduced in section 2.5.1 [126, 183–185], anti-dot arrays [186, 187], narrow constrictions comparable to quantum point contacts [87] or even quantum dots [188, 189]. In Fig. 4.7 transport through a narrow constriction of W =110 nm (150 nm by design) is shown at zero and finite magnetic field. The constriction was established by reactive ion etching the hBN/graphene/hBN heterostructure using a PMMA mask and a SF_6 plasma (see Appendix A.3.2). The conductance as a function of gate voltage is shown in Fig. 4.7a in direct comparison with the fully ballistic model given in equation 2.43 (including a shift n_0), which is in agreement with the measurement on the n-doped side. A constant resistance accounting for the contact and line resistance was subtracted by matching the quantum Hall plateaus (plateaus were adjusted on

---

[2] An alternative approach is to transfer an additional thin layer of hBN on top of the device with the contacts established. However, in this case the capacitive coupling of the top-gate to graphene varies within the first few hundred nanometers apart from the contacts, since this is the distance it takes the hBN to fully relax for contacts being ~70 nm thick.

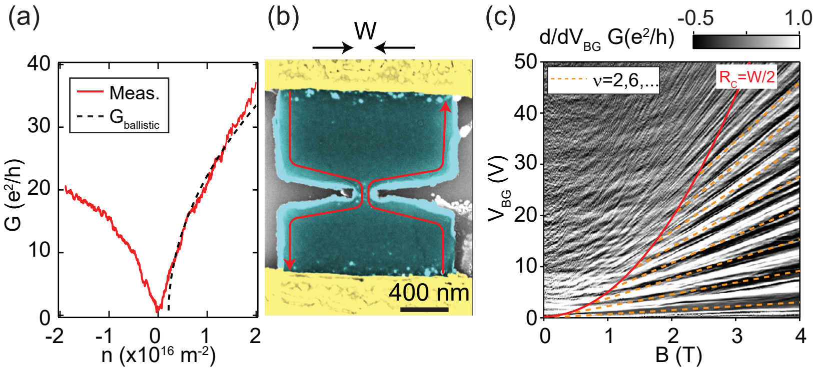

Figure 4.7. Constrictions in a two-terminal hBN/graphene/hBN heterostructure. a, Conductance (contact resistance subtracted) as a function of gate voltage through a constriction as shown in (b). The black,dashed line is the fit (equation 2.43) yielding $W = 111\,\mathrm{nm}$. **b,** Illustration of transport at finite magnetic field, where edge states can be transmitted or reflected at the constriction. **c,** Numerical derivative of the conductance with increasing magnetic field. The conditions of $R_\mathrm{C} = W/2$ is indicated with the red line, and the filling-factors are indicated with the orange, dashed lines.

the n-doped side, section 4.2.1). By applying a perpendicular magnetic field the charge carriers are moving in skipping orbits/edge states (section 2.1.3) along the perimeter of the device as sketched in Fig. 4.7b. If the charge carriers perform very small cyclotron orbits such that $R_\mathrm{C} \ll W$ (for R_C the charge carrier density within the bulk was assumed, equation 2.24), then they can pass the constriction and the usual fan-plot is seen as shown in Fig. 4.7c with the orange, dashed lines. However, by reducing the magnetic field and/or doping, R_C increases and around $R_\mathrm{C} = W/2$ the charge carriers start to be reflected at the constriction [87].

4.5. Thermal annealing of hBN/graphene/hBN heterostructures

Thermal annealing is supposed to aggregate contaminations in pockets resulting in larger areas of clean graphene [166, 175, 176] as mentioned in section 4.1. The positive effect of thermal annealing was not only realized during fabrication, but as well in between measurements. Upon applying high gate voltages to our heterostructures, the device quality sometimes degraded over a longer

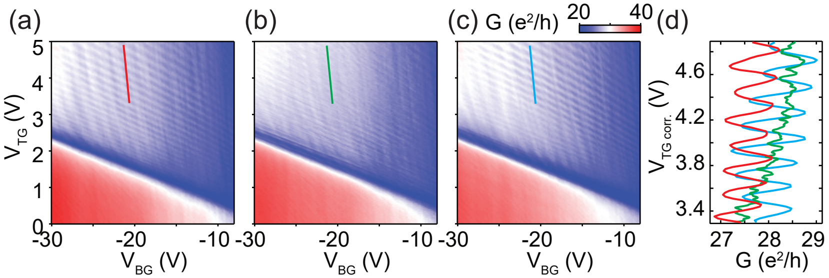

Figure 4.8. Self-cleaning properties of hBN/graphene/hBN heterostructures upon thermal annealing. a, Conduction map with FP resonances clearly visible in the bipolar region. **b,** Same map after degradation of the sample where the FP resonances are nearly absent. **c,** Most of the FP resonances are restored after thermal annealing at 200 °C for 20 min (outside the cryostat). **d,** Linecuts as indicated in (a)-(c) in comparison.

time period (2 weeks). The degradation over time and the subsequent improvement upon thermal annealing was observed in several samples independently. In between the maps shown in Fig. 4.8a and 4.8b, the global and local gates were swept over a wide range (e.g. ±60 V for the global back-gate) for an extended time period (2 days). An example before and after thermal annealing[3] is shown in Fig. 4.8a-c. In Fig. 4.8d an identical linecut of the original (red), degraded (green) and annealed (blue) sample are shown in comparison. We speculate that the decrease of the device quality might come a charge transfer into trapped-impurities in the SiO_2 or hBN which cannot be de-charged at low temperatures. An alternative explanation might be the migration of contaminations when continuously sweeping the gates to high voltages. By applying a thermal annealing step, these trapped charges (contaminations) might be removed (aggregate again in pockets), leading to the recovery of the high sample quality.

4.6. Cryogenic measurement setup

Measurements of all samples were performed in a cryogenic set-up with a variable temperature insert (VTI) having a base-temperature of 1.5 K as sketched in Fig. 4.9. Unless stated otherwise, measurement were performed at the base-temperature. The system is equipped with a vector-magnet with maxi-

---

[3] No significant difference between annealing on a hotplate in air at 200 °C to 250 °C or in a rapid thermal annealer under forming-gas atmosphere (Ar/H_2) at 300 °C could be found.

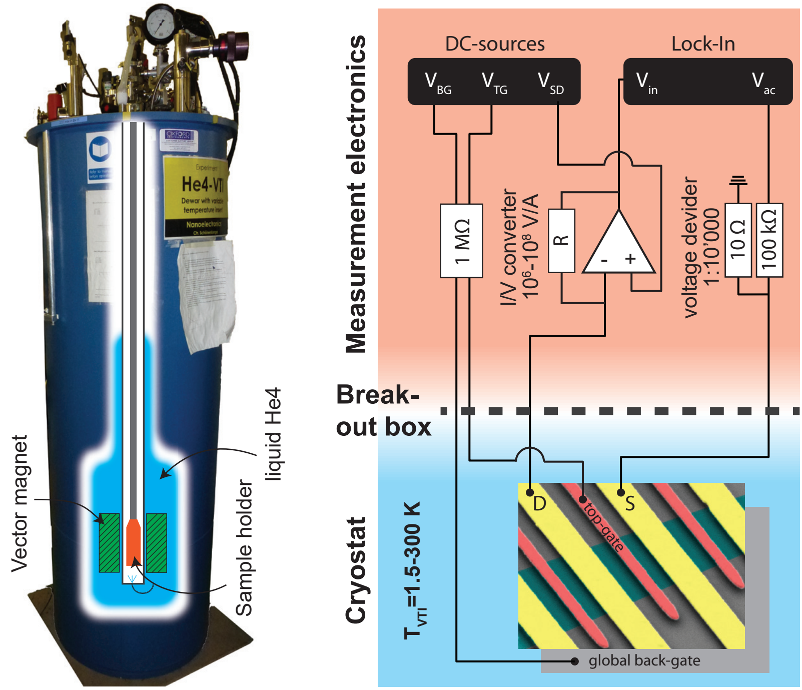

Figure 4.9. Cryogenic measurement setup. Schematic of a set-up for a typical voltage-biased measurement of the differential conductance at low temperatures using standard low-frequency lock-in techniques. Adapted from Ref. [190].

mum fields of $B_Z = 9\,\mathrm{T}$ and $B_X = 3\,\mathrm{T}$. For the measurements, standard low-frequency lock-in technique (Stanford SR830, frequencies were set in the range of $f = 77.77\,\mathrm{Hz}$ to $277.77\,\mathrm{Hz}$) was used to measure the differential conductance. Unless stated otherwise, the excitation voltage was $V_{AC} = 10\,\mu\mathrm{V}$ such that the electronic excitation is below the bath-temperature ($V_{AC} < k_B T/e$ where k_B is the Boltzmann constant). As DC-sources (for the gates or bias spectroscopy) we used Yokogawa YK7651 with a maximum output voltage of 32 V. If needed, home-made voltage-amplifiers were attached in order to reach ±60 V or more as required for the measurements described in chapter 6. Furthermore home-built low-noise I/V-converters were used. All measurement programs are based on Labview.

5 Point contacts in encapsulated graphene

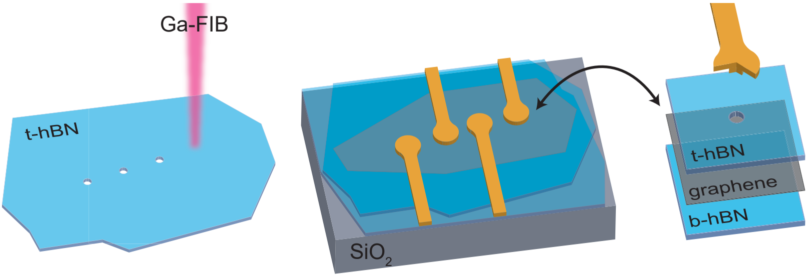

In previous chapters we have shown that high mobility graphene can be achieved via encapsulation. However, in the fabrication shown before only the edge of the graphene can be accessed via side-contacts [1]. A different type of contacts, namely inner point contacts (PCs), are desirable to realize several theoretical proposals on graphene such as e.g. the Veselago lensing [164] in single [28, 95, 191] layer graphene, valley [192, 193] or spin focussing [194] in graphene or for the investigation of skipping and snake orbits of charge carriers at a p-n junction at high magnetic fields [195, 196]. In order to make PCs in the middle of the graphene sheet evaporated, sputtered or atomic layer deposited dielectrics (e.g. MgO, SiO_2 or Al_2O_3) have been used so far [163]. However, these materials are inferior to hBN when it comes to the preservation of the graphene quality [21]. Even though it is possible to establish PCs on graphene using a STM tip, this is extremely challenging at low temperatures, especially upon involving several PCs at the same time. While recently PCs were realized to suspended graphene using the air-bridge technique [197, 198], their contact-diameter remains quite large ($\sim$1 µm). The results presented in this chapter are describing a method to establish PCs in encapsulated graphene by pre-patterning the hBN flake prior to the dry-stacking process. This allows to contact the graphene at arbitrary position with contacts smaller than 100 nm in diameter. The graphene quality is extracted from two- and four-terminal resistance measurements which are compared with a simple electrostatic model. Furthermore localization of the edge states around the PCs in a magnetic field is shown, as expected for a proper inner contact in the quantum Hall regime.

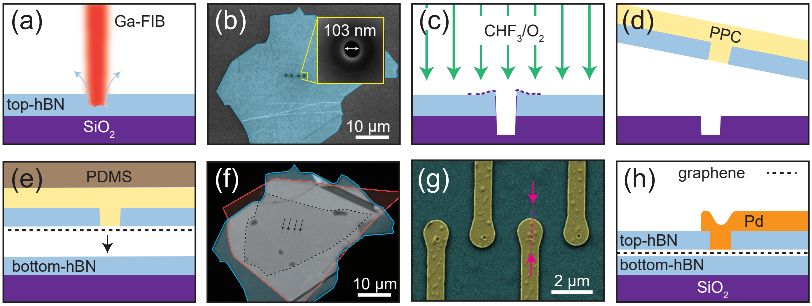

Figure 5.1. Fabrication of PCs on a hBN/graphene/hBN heterostructure (not to scale). a, Drilling the holes into the top-hBN using a Ga-FIB. **b,** False color SEM image of the top-hBN on SiO$_2$ substrate after drilling the holes with the Ga-FIB. Inset: Close-up of a single hole. **c,** Exposing the top-hBN flake to a CHF$_3$/O$_2$ plasma to avoid pinning of flake to the SiO$_2$ substrate. **d,** Removing the top-hBN flake with the holes from the SiO$_2$ support by spin-coating PPC on top of the wafer and then peeling it gently of. **e,** The remaining assembly of the hBN/graphene/hBN stack follows Ref. [1]. **f,** Optical image of a final stack where the different layers are indicated in red (bottom hBN), black (graphene) and blue (top hBN). The holes are indicated with arrows. **g,** False color SEM image of the final stack (cyan) with Pd contacts (yellow) overlapping the drilled holes. **h,** Schematic of the cross-section as indicated in (g) with pink arrows and the dashed line.

5.1. Fabrication

The herein presented method to establish PCs is based on pre-patterning the top-hBN with a gallium based focused ion beam (Ga-FIB) prior to the dry-stack assembly in contrast to establishing the holes with conventional e-beam lithography and subsequent etching. The former method has the advantage that the drilled holes are better defined in shape and the diameter can be adjusted more reliably. For the Ga-FIB an acceleration voltage of 30 keV and the smallest possible current (1.1 pA) was used in order to obtain highest resolution.

The hBN to be patterned was exofliated on a Si^{++}/SiO$_2$ substrate with a 315 nm thick oxide, using the scotch-tape technique. The chips were previously carefully cleaned using Piranha solution (Appendix A.1.1) since it is the bottom face of the hBN which will later on contact the graphene. Once an ideal hBN flake (10 nm to 30 nm) was identified by optical microscopy, the Ga-FIB was used to drill several holes into the flake (with diameter d ~100 nm and a equidistant spacing of 1 µm to 2.2 µm) as sketched in Fig. 5.1a,b. Before picking-up the hBN from the SiO_2 wafer, it was briefly exposed to a CHF_3/O_2 plasma (Appendix A.3.1, but etching for only 15 s) as shown in Fig. 5.1c. It turned out that without exposing the hBN flakes to the plasma, the hBN flakes could not be picked-up from the SiO_2 substrate. A possible explanation might be that during the drilling of the holes with the Ga-FIB, SiO_2 from the wafer is sputtered on the side of the holes which pins the flake to the wafer. The CHF_3/O_2 plasma removes this layer and allows therefore a successful pick-up of the flake from the SiO_2 chip. To pick-up the top-hBN, the SiO_2 chip was spin-coated with ∼1 µm of poly-propylene-carbonate (PPC) and backed at 80 °C for 5 minutes. By peeling-off the PPC gently from the substrate, as shown in Fig. 5.1d, all hBN flakes are transferred from the SiO_2 onto the PPC polymer. Peeling-off the PPC without breaking the hBN flakes works best when slowly releasing the PPC at a low angle from the SiO_2 chip (drilled flakes are more likely to break). Since only the top side of hBN comes in contact with the polymer, the method preserves the clean fabrication of dry-stacking graphene. The PPC with the hBN flake was then placed on a home-made PDMS stamp (∼0.5 mm thick). The remaining assembly procedure of the hBN/graphene/hBN heterostructure follows the dry-stacking approach as described in chapter 4 and shown in Fig. 5.1e. [1]. A contrast adjusted optical image of the finished stack is shown in Fig. 5.1f. In the last step the 100 nm thick palladium (Pd) contacts were established using standard e-beam lithography and e-gun evaporation. A false color SEM image of the contact area is shown in Fig. 5.1g with a cross-sectional schematic of the final device shown in Fig. 5.1h as indicated with the purple arrows/dashed line in Fig. 5.1g. In total 4 different samples were produced all showing a similar behaviour.

For the characterization we fabricated devices having 4 PCs (having an equidistant spacing of 1 µm to 2.2 µm) as described above. In the following, first the contact resistance and the field-effect measurements at zero magnetic field are discussed. In the second part, the behaviour of the devices at high magnetic field perpendicular to the graphene plane is presented.

5.2. Zero magentic field measurements

For the calculation of the charge carrier mobility, a model fitting the device geometry is introduced. The nomenclature of the various differential resistances is given as $R_{\mathrm{ij,nm}} = dV_{\mathrm{nm}}/dI_{\mathrm{ij}}$, with I_{ij} flows from PC $i \rightarrow j$ and the voltage V_{nm} measured as the difference between PC n and m, with $i, j, n, m \in 1-4$.

5.2.1. Four-terminal measurements

Figure 5.2a shows $R_{\mathrm{ij,nm}}$ for all possible four-terminal configurations. Out of the six possible configurations, only three are independent: measurements

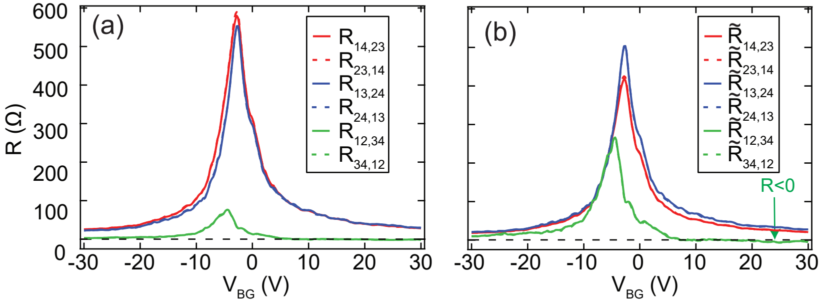

Figure 5.2. Four-terminal measurement of the graphene resistance between different combinations of PCs. a, The original four-terminal resistance $R_{\mathrm{ij,nm}}$ measured between the six different lead combinations. Measurements with inverse voltage and current probes are identical. **b,** Resistance of the same data presented in (a) multiplied by a factor depending on the measurement geometry as given by equation 5.2. In the non-local measurement $R_{12,34}$, the voltage $V = V_{\mathrm{n}} - V_{\mathrm{m}}$ was negative in the n-doped region.

with inverted current and voltage probes are identical as expected from the Onsager relations [199]. The resistance traces show a sharp maximum around zero doping, corresponding to the charge neutrality point (CNP) of graphene. For rectangular graphene devices, where the current density within the graphene sheet is constant, the mobility μ can be deduced by measuring the field-effect of the longitudinal resistance R_{xx}, taking the length and width of the Hall bar into account (equation 2.37). For PCs, which are situated in the middle of the graphene sheet, a different formula has to be used since the current density within the graphene sheet varies. Here a model to extract the sheet conductivity (σ) from the four-terminal measurement of the resistance is introduced, assuming an infinite graphene sheet with a constant σ. The four contacts are at positions $\vec{r}_{\mathrm{x}}$ with $x = i, j, n, m$ and assuming diffusive transport. Starting from a single PC at position $\vec{r}_{\mathrm{i}}$, the current spreads isotropically into the graphene. This leads to a current density of $\vec{j}(\vec{r}) = I/(2\pi|\vec{r}-\vec{r}_{\mathrm{i}}|)$ at distance $|\vec{r}-\vec{r}_{\mathrm{i}}|$ away from the PC, where I is the current. According to $\vec{j}(\vec{r}) = \vec{E}(\vec{r})\sigma$, the electric field $\vec{E}(\vec{r}) \sim 1/|\vec{r}-\vec{r}_{\mathrm{i}}|$ leads to an electrostatic potential $V(\vec{r}) \sim \ln(|\vec{r}-\vec{r}_{\mathrm{i}}|)$. Assuming a current flow between two PCs from $i \to j$, the potential at position $\vec{r}$ is obtained by the superposition principle:

$$V(\vec{r}) = -\frac{I_{\mathrm{ij}}}{2\pi\sigma}\ln(|\vec{r}-\vec{r}_{\mathrm{i}}|) + \frac{I_{\mathrm{ij}}}{2\pi\sigma}\ln(|\vec{r}-\vec{r}_{\mathrm{j}}|) + C, \tag{5.1}$$

where C is an integration constant. In the four-terminal measurement only the voltage difference between the two leads at position n and m ($V_{\mathrm{nm}} =$

$V(\vec{r}_\mathrm{n}) - V(\vec{r}_\mathrm{m}))$ is measured. For simplicity it is assumed that the voltage probes do not influence the electric field pattern in graphene as shown in Fig. 5.3a and b. This leads to

$$V_\mathrm{nm} = \frac{I_\mathrm{ij}}{2\pi\sigma} \ln\left(\frac{|\vec{r}_\mathrm{n} - \vec{r}_\mathrm{j}|}{|\vec{r}_\mathrm{n} - \vec{r}_\mathrm{i}|}\frac{|\vec{r}_\mathrm{m} - \vec{r}_\mathrm{i}|}{|\vec{r}_\mathrm{m} - \vec{r}_\mathrm{j}|}\right), \tag{5.2}$$

from which the conductivity σ can be extracted from the measurement. Note that equation 5.2 is mathematically equivalent to the van der Pauw method [200, 201]. Using the linear relation between the conductivity and the charge carrier density (equation 2.37) it is possible to deduce the mobility from equation 5.2. The hole and electron doped region revealed mobilities of μ_h $\sim$35 000 $\mathrm{cm^2V^{-1}s^{-1}}$ and $\mu_e$$\sim$25 000 $\mathrm{cm^2V^{-1}s^{-1}}$ respectively. Similar mobilities have been obtained using the onset of the Shubnikov de Haas oscillations (section 2.1.3 and section 5.3). Confirmation that a single layer graphene is encapsulated in hBN was given by the observed sequence of filling factors in magnetic field and by Raman spectroscopy (not shown). From equation 5.2 it follows that in case of a homogeneous σ, all four-terminal resistance measurements can be renormalized according to

$$\widetilde{R}_\mathrm{ij,nm} = R_\mathrm{ij,nm} \ln\left(\frac{|\vec{r}_\mathrm{n} - \vec{r}_\mathrm{j}|}{|\vec{r}_\mathrm{n} - \vec{r}_\mathrm{i}|}\frac{|\vec{r}_\mathrm{m} - \vec{r}_\mathrm{i}|}{|\vec{r}_\mathrm{m} - \vec{r}_\mathrm{j}|}\right)^{-1}. \tag{5.3}$$

With all four contacts at equidistant spacing the logarithm in equation 5.3 simplifies to ln(4), ln(3) or ln(3/4) depending on the measurement configuration. If the model with all the assumptions is valid, all $\widetilde{R}_\mathrm{ij,nm}$ should be equal and given by $1/2\pi\sigma$. The difference between the original and renormalized values can be seen in Fig. 5.2a and 5.2b, respectively. The renormalized values $\widetilde{R}_\mathrm{ij,nm}$ in Fig. 5.2b are not exactly overlapping, as would be expected for a perfect system given in equation 5.3. However, one can see that the non-local measurements (voltage probes outside the current path), shown in green, which were in the original data smaller by a factor of 7.5 (8) from the blue (red) curve, deviates now only by a factor of 2 (1.6) after renormalization. On the other hand, the local measurements, the blue and red curves are in rather good agreement before and after renormalization. Overall, the rescaled values are much closer to each other than the unscaled ones, which indicates that the theoretical model is realistic.

The deviations from the ideal case can be related to the boundary conditions assumed for the model. The most significant deviations from the ideal model are probably i) the finite dimensions of the metallic PCs and ii) the finite size of the graphene sheet, which both change the electric field pattern. Besides, the sheet conductivity does not seem to be fully uniform within the sample as can be seen by the slight shift of the CNP between several measurements. The charge neutrality points are at −2.6 V, −2.8 V and −4.8 V respectively as shown in Fig. 5.2b. Finally, equation 5.3 was derived assuming a completely diffusive sample. However, the charge carriers in the sample are most likely in an intermediate regime between the diffusive and the ballistic regime. The scattering mean free path, as given in equation 2.41 can reach 1 µm at V_{BG} =30 V, which is in the same order as the contact distance a =2.2 µm. In this intermediate regime it can occur that the voltage drop over a larger, but clean (ballistic) area is lower compared to a smaller, but dirty (diffusive) area. Moreover, for ballistic trajectories the probability of arriving at a contact, which is farther away can be higher. This picture explains the negative resistance at certain doping values observed in the non-local measurement indicated with an arrow in Fig. 5.2b. For all the configurations where the voltage probes are (at least partially) within the current path, the bias voltage will be dominant and consequently no negative signal can be seen.

5.2.2. Two-terminal measurements and contact resistance

In order to extract the contact resistance R_{CT} which arises between the metal leads and the graphene, we turn to two-terminal measurements. To calculate the contact resistance the two-terminal resistance R_{2T} was measured between the outer contacts (1,4) as sketched in Fig. 5.3a. In this case the contact resistance can be calculated according to:

$$R_{\mathrm{2T}} = 2R_{\mathrm{CT}} + A \cdot R_{\mathrm{4T}}, \tag{5.4}$$

where $A \cdot R_{\mathrm{4T}} = A \cdot R_{14,23}$ is the intrinsic graphene resistance including a geometry factor A (which will be evaluated in the following) and $R_{\mathrm{2T}} = R_{14,14}$. Here we assumed the same contact resistance for the two contacts. Due to the higher electric field near the source and drain contacts, shown in Fig. 5.3a, the voltage changes faster near them. This can be seen in Fig. 5.3b, where the potential along the line connecting the contacts is sketched. The resistance coming from the non-linearity of the potential near the contacts is called spreading resistance and leads to a potential difference that is marked as V_{sp} in Fig. 5.3b [202]. It is of the same origin as Maxwell's resistance that occurs in metallic point contacts [203].

To calculate the geometrical factor A in equation 5.4, we used equation 5.2 in combination with a cut-off at $d/2$ away from the singularity, where d is the diameter of the contact. The cut-off is required because in reality the potential is not singular at position $\vec{r}_{\mathrm{i}}$ and $\vec{r}_{\mathrm{j}}$, but constant within the metallic PCs ($|\vec{r}_{\mathrm{i,j}} - \vec{r}| < d/2$) as sketched in Fig. 5.3a. For $i = 1$ and $j = 4$ both terms in the numerator and denominator of equation 5.2 become $(3a - d/2)$ and $d/2$ respectively, where a is the distance in between two neighbouring contacts. This leads to

$$R_{2T} = \frac{1}{2\pi\sigma} \ln\left[\left(\frac{6a}{d} - 2\right)^2\right] + 2R_{\mathrm{CT}}. \tag{5.5}$$

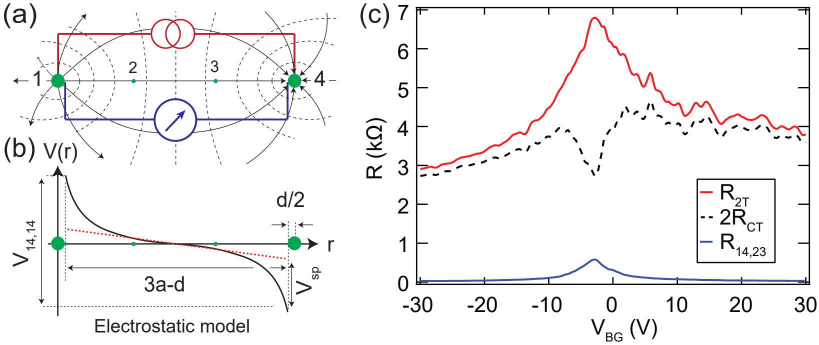

Figure 5.3. Contact resistance extracted from two- and four-terminal measurements. a, The two-terminal measurement setup and a sketch of the corresponding electric field profile. The two-terminal measurement is performed between the two outer-most PCs which have a distance of $3a$ from each other, whereas the reference four terminal measurement between contacts 2 and 3. **b,** The red, dashed line represents the linear interpolation of V_{23} compared to the actual electrostatic potential (black, solid line) along the line connecting the contacts. The resulting potential difference at distance d/2 from source- and drain-center is indicated with V_{sp}. **c,** Two-terminal resistance between 1 and 4 is shown in red, whereas the four-terminal resistance $R_{14,23}$ is shown in blue. Extracted contact resistance of the configuration given in (a) using equation 5.4 and 5.6

.

Using $R_{4\mathrm{T}} = R_{14,23}$ where $R_{14,23} = ln(4)/(2\pi\sigma)$ the geometrical factor becomes:

$$A = \ln\left[\left(\frac{6a}{d} - 2\right)^2\right] \frac{1}{\ln(4)}. \tag{5.6}$$

In Fig. 5.3c the extracted contact resistance is shown using a geometry factor of A=7.04 (a=2.2 µm and d =100 nm). The contact resistance of different contact configurations and different devices is of the order of R_{CT} =0.5 kΩ to 1.5 kΩ at high doping. This value is quite remarkable for PCs of only 100 nm in diameter since as well top-contacts with significantly larger areas (in the order of µm^2) have resistances in the kΩ range. Moreover, at high doping the graphene becomes very conductive and the voltage-drop over the graphene is minimal, therefore $R_{2\mathrm{T}} \sim 2R_{\mathrm{CT}}$.

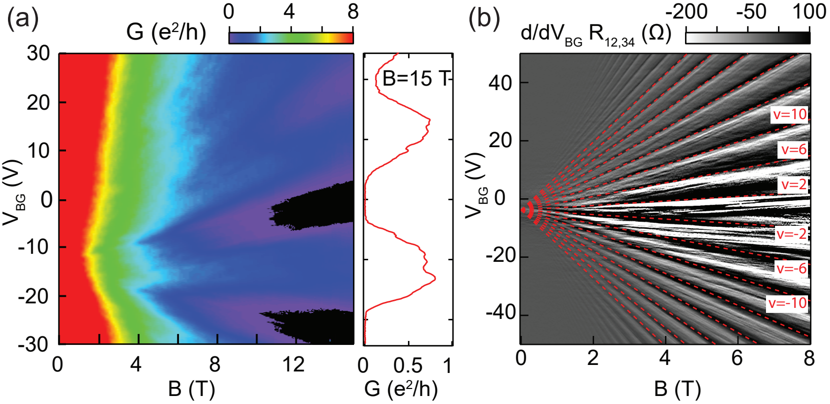

Figure 5.4. Two- and four-terminal conductance as a function of back-gate and magnetic field. a, The conductance between neighbouring PCs (a =1 µm) becomes zero at high magnetic fields. The black area shows the threshold for G <0.025 e^2/h (R >1 MΩ). A linecut at B =15 T is given on the right. **b,** Numerical derivative of the conductance (d/dV_{BG} $R_{12,34}$) of a non-local measurement for another device as shown in (a) (a =2.2 µm). The sequence of the filling factors (red, dashed lines), $\nu = \pm 2, \pm 6, \ldots$ is in agreement with the ones expected for SLG.

5.3. Magnetic field measurements

To further characterize the PCs a magnetic field perpendicular to the graphene sheet is applied, which forces the charge carriers to move along cyclotron orbits (section 2.1.3). With a sufficiently high magnetic field the device is driven into the quantum Hall regime, where the bulk of the sample is insulating, since charge carriers will be localized either around the PCs or along the edges of the sample, which decouples the PCs from each other and the edge of the sample. In the case of a ballistic device ($\omega_c \tau > 1$) which is homogeneously doped, one would expect complete insulation as soon as the cyclotron orbit and the magnetic length are smaller than the distance between the PCs between which the current flows. In Fig. 5.4a the two-terminal conductance between two neighbouring contacts (a =1 µm) is shown as a function of back-gate and magnetic field for a device with μ =15 000 $\mathrm{cm}^2\mathrm{V}^{-1}\mathrm{s}^{-1}$. The black region in Fig. 5.4a represents values with G <0.025 e^2/h (R >1 MΩ). It can be seen that the sample becomes insulating, however the fields required are much higher than expected. From simple consideration insulation should start around $2R_{\mathrm{CT}} < a$, which would lead to values of 0.5 T to 1 T. One possible explanation why such

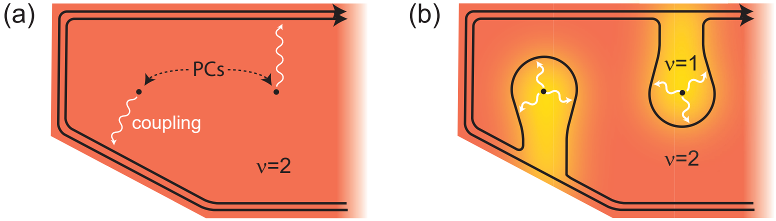

Figure 5.5. Coupling between PCs and edge states. a, If the graphene is homogeneously doped, the PCs are spatially well separated from the edge states and coupling between PCs and edge states (indicated with the white arrows) is suppressed. **b,** However, if the charge carrier doping in the graphene located below the contacts is different the separation between PCs and edge states decreases which favours the coupling between PCs and edge states.

high magnetic fields are required to decouple the neighbouring PCs is based on a variation of the charge carrier doping within the sample as sketched in Fig. 5.5. The latter might be explained by local screening of the back-gate by the top-contacts. This causes the back-gate to tune the charge carrier density in the graphene located directly below the leads and the gaphene elsewhere with a different efficiency. In this case some of the edge states will no longer be restricted to the edges of the graphene (Fig. 5.5a), but can as well flow within the bulk of graphene along boundaries of different filling factors (Fig. 5.5b). The reduced spacing between PCs and edge states consequently leads to an enhanced coupling between the latter, thus giving rise to short-cut currents between the different PCs. However, we estimate that the screening changes the gate efficiency by less than 4 % far away from the CNP, where the quantum capacitance is high. Only close to the CNP, where the quantum capacitance is small, the screening of the contacts changes the efficiency by up to 20 %. Furthermore, an additional offset potential may emerge in the regions of the top-contacts due the formation of a contact potential between the palladium contacts and hBN. It is worth to emphasize that substantial part of the voltage drops in the region close to the contact. As already mentioned, doping inhomogeneities exist within the sample, as can be seen from the shift of the charge neutrality point between different two-terminal measurements. The combination of all these effects can cause local differences in the filling factor, which can account for the observed high threshold fields. In future devices insulation at lower magnetic fields can be achieved by choosing devices with smaller doping inhomogeneities, which can result from bubbles present in the stacks. Moreover the inhomogeneous screening of the top-contacts or offset potentials can be circumvented by careful design, in which the flake would be fully covered with a metallic plane to achieve a homogeneous doping situation. Besides two-terminal measurements of neighbouring contacts, non-local measurements in a four-terminal measurement geometry are performed. While in a Hall-bar configuration a clear distinction between longitudinal- (R_{xx}) and Hall-resistance (R_{xy}) can be done, in the samples presented the situation is more complex due to the absence of a graphene edge which directly couples to the contacts. As all four contacts are situated in a row, a separation between longitudinal- and Hall-resistance is impossible. Nevertheless, in Fig. 5.4b the non-local measurement clearly shows the evolution of the filling factors sequence $\nu = \pm 2, \pm 6, ...$ with varying back-gate and magnetic field according to equation 2.30.

5.4. Conclusion

In this chapter a method to establish inner point contacts with dimensions of 100 nm in a hBN/graphene/hBN heterostructure was introduced. The presented technique is compatible with high-quality encapsulated graphene, since the hBN flake is patterned prior to the stacking and therefore the graphene remains clean. With further optimization of the cleanliness of the transfer process one can expect higher quality devices. Since the method relies on dry stacking technique mobilities around $100\,000\,\mathrm{cm^2V^{-1}s^{-1}}$ or higher should be achievable [1, 204, 205]. The technique also holds the potential to further decrease the contact size, since with the Ga-FIB hole diameters below d =20 nm are possible. The PCs introduced here give the possibility to complement side and top-contacts in complex devices. Since the publication of this work [92], novel proposals appeared which include PCs as basic elements. An example is given in Ref. [206] in which the creation of a highly directional electron beam using PCs in combination with a parabolic *p*-*n* junction is used. The efficiency of the latter was demonstrated by comparing the signal in a transverse magnetic focusing geometry (section 2.3.2), once with a collimation-lens, and once without one.

6

Fabry-Pérot resonances in a graphene/hBN Moiré superlattice

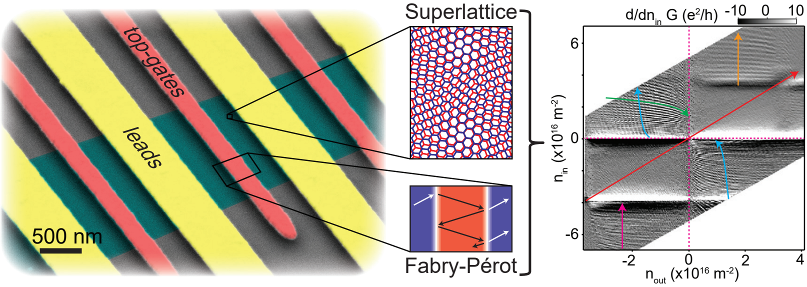

The study of Fabry-Pérot (FP) resonances have revealed themselves as a powerful tool to investigate various aspects of graphene. Examples are the π-shift of the FP resonances at low magnetic field originating from Klein tunnelling [14, 58, 59, 207] or the proof of ballistic transport over several microns [40, 41]. While FP resonances and Moiré superlattices are intensively studied in graphene on hBN, the two effects have not been discussed in their coexistence. In this chapter we show confinement using band engineering based on locally gated Moiré superlattices and the appearance of FP resonances defined by the main and satellite DPs, playing the role of reflective barriers. Although several aspects of FP cavities have been investigated, such as the effect of the p-n junction smoothness on the visibility of the FP resonances [41], the electronic tunability of the cavity size has not been studied. First, the effect of the smoothness of the confining potential on the visibility of the FP resonances is addressed. Furthermore the evolution of the FP cavity size as a function of densities inside and outside the cavity in the absence of a superlattice is mapped, when the cavity is formed by regular p-n junctions. Using a sample with a Moiré superlattice, it is shown that an FP cavity can also be formed by interfaces that mimic a p-n junction, but are defined through a satellite Dirac point due to the superlattice. By carefully analysing the FP resonances informations of the band reconstruction due to the superlattice can be deduced. The findings presented in this chapter are consistent with the electron-hole symmetry breaking of the Moiré superlattice [110].

6.1. Regular *p-n-p*

The measurement presented in this chapter were performed on a p-n-p junction using a global back-gate and a local top-gate as sketched in Fig. 4.3. The length of the overall device is roughly 1 µm while the width of the top-gate, which was placed in the center of the device, is 230 nm. The charge carrier mobility (μ) extracted from field-effect measurements yielded $\mu{\sim}150\,000\,\mathrm{cm^2V^{-1}s^{-1}}$.

6.1.1. Visibility of Fabry-Pérot resonances

In Fig. 6.1a the derivative of the differential conductance is shown as a function of n_{in} and n_{out} for $n_{\mathrm{out}} < 0$. The visible fringes are FP resonances appearing in the p-p'-p regime (bottom part, $n_{\mathrm{in}} < 0$) and p-n-p regime (upper part, $n_{\mathrm{in}} > 0$). Specific cuts within an extended (red) or limited (blue, green) gate range are shown in Fig. 6.1b. While the FP resonances in the inner (outer) cavities are tuned predominantly by n_{in} (n_{out}) as indicated with the blue (green) arrow in Fig. 6.1a, the FP resonances between the contacts depends on both densities as indicated by the red arrow. The three types of FP resonances are very different in their visibility $\Delta G/(2\langle G\rangle)$. Here ΔG is the difference between the conductance at constructive and destructive interference, and $\langle G\rangle$ denotes the mean conduction in between oscillation maximum and minimum. The FP resonances between the contacts yield the lowest visibility ($\sim 1\%$), those in the outer cavities yield an intermediate visibility ($\sim 4\%$) and FP resonances in the inner cavity yield the highest visibility ($\sim 11\%$). In ballistic graphene, the FP visibilities depend on the transmission/reflection properties of the confining boundaries (p-n junction) as shown in equation 2.45. The transmission/reflection probabilities of a p-n junction strongly depends on the angle of the incoming charge carrier [76]. In the case of a “sharp” p-n junctions (($d \ll \lambda_F$), section 2.2.3), transmission of charge carriers is possible up to large angles measured with respect to the p-n junction normal. In contrast, for a very “smooth” p-n junction ($d \gg \lambda_F$), only charge carriers at low angles are transmitted (here this is around $\sim 20^\circ$, although it depends strongly on the gate voltages). Since the performed conductance measurement is not angle resolved, the measured signal averages over all possible angles and leads to smearing of the FP resonances. It turns out that for a smooth p-n junction, which transmits a narrower range of angles, high FP visibilities can be observed [41].

In the investigated devices one can discriminate between two types of p-n junctions: i) the p-n junction created in the proximity of the contacts for $n_{\mathrm{out}} < 0$ and ii) the p-n junction created using the global back-gate and local top-gate. It is worth nothing that (ii) is much smoother compared to (i). Following the above given argument one sees that the FP resonance visibility is highest/lowest when the cavity is defined by two softer/sharper p-n junctions

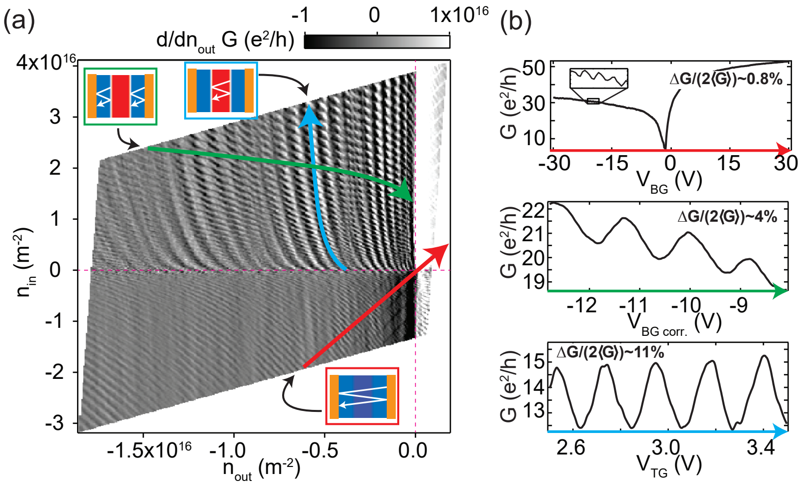

Figure 6.1. Fabry-Pérot resonances in a two-terminal *p-n-p* configuration. a, Numerical derivative of the conductance as a function of global back-gate (V_{BG}) and local top-gate (V_{TG}). Here it is replotted as a function of charge carrier density in the outer (n_{out}) and inner cavity (n_{in}). The three most important FP resonances present in the system are indicated. **b,** Visibilty $\Delta G/\langle 2G\rangle$ of the FP resonances indicated in (a) in comparison.

if $L \ll l_\Phi$ (l_Φ being the phase coherence length).

6.1.2. Extracting the cavity length

The effective cavity length (L) from the FP resonances in the central cavity (cyan arrow in Fig. 6.1) deviates in most cases from the physical width of the top-gate as shown in the following. The cavity width can be extracted from the FP oscillations by assuming a FP resonator with a hard-wall potential (fixed width of the cavity). Constructive interference occurs if the path-difference between directly transmitted and twice reflected waves is equal to $2L = j\lambda_{\mathrm{F}}$, where λ_{F} is the Fermi wavelength and j is an integer. The j-th FP resonance can be rewritten as $L\sqrt{n_{\mathrm{j}}} = j\sqrt{\pi}$ using $\lambda_{\mathrm{F}} = 2\pi/k_{\mathrm{F}} = 2\sqrt{\pi/n}$ which is valid for single layer graphene. For two neighbouring peaks, for example j-th peak at density n_{j} and $(j+1)$-th peak at density $n_{\mathrm{j+1}}$:

$$L = \frac{\sqrt{\pi}}{\sqrt{n_{\mathrm{j+1}}} - \sqrt{n_{\mathrm{j}}}}. \tag{6.1}$$

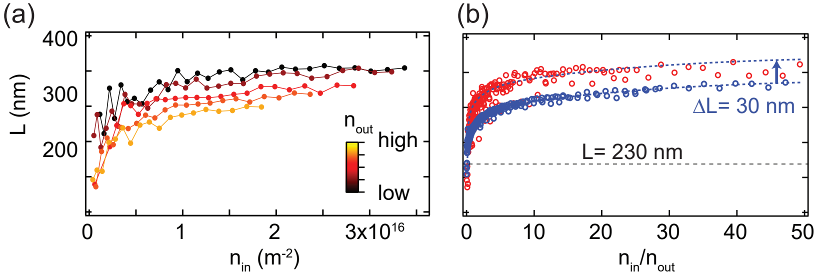

Figure 6.2. Cavity-length as a function of doping. a, Extracted cavity length of the central cavity as a function of n_{in}, as indicated with the cyan arrow in Fig. 6.1b for n_{out} ranging from $-0.1 \times 10^{16}\,\mathrm{m}^{-2}$ to $-1.7 \times 10^{16}\,\mathrm{m}^{-2}$. **b,** The same data as shown in (a), but now plotted as a function of $n_{\mathrm{in}}/n_{\mathrm{out}}$ for experiment (red) and theory (blue). The black, dashed line corresponds to the width of the top-gate measured with the SEM. The blue, dashed lines are a guide to the eye for the theoretical data and the theoretical data shifted by 30 nm respectively.

It is worth noting that in equation 6.1 L is independent of n_{out} which is an oversimplification of the problem. An alternative way to define the cavity length is to measure the distance between the two zero-density points of the right and left p-n junctions as it will be discussed in section 6.1.3. However, since the position of the p-n junction is experimentally not directly accessible, equation 6.1 will be used to deduce the cavity length.

The cavity length was extracted by taking various linecuts comparable to the one indicated with the blue arrow in Fig. 6.1a and then using equation 6.1. An increase of L with increasing n_{in} (for fixed n_{out}), and a decrease of L with increasing n_{out} (for fixed n_{in}) can be observed as shown in Fig. 6.2a. Consequently L does depend on n_{out}, as expected. Surprisingly, by plotting L as a function of $n_{\mathrm{in}}/n_{\mathrm{out}}$, all data points lie on one universal curve which is shown in Fig. 6.2b, independent of the exact position within Fig. 6.1a from which they have been extracted from. Within the applied gate range, L varies substantially, by up to 200 nm, which corresponds to a shift of around 100 nm per p-n junction. The evolution of L as a function of $n_{\mathrm{in}}/n_{\mathrm{out}}$ extracted from the experiment was compared with the one extracted from a transport simulation (based on the method described in Ref. [41]) using equation 6.1. The latter reveals good qualitative agreement with the experiment as shown in Fig. 6.2b. The most significant difference between experiment and theory are: i) an offset of $\Delta L \sim 30$ nm from the theory to the experiment and ii) a disagreement between the trends of the two curves when approaching very low charge carrier densities in the outer cavity, corresponding to large values of $n_{\text{in}}/n_{\text{out}}$ (the same is true when depleting the inner cavity, not shown here). In the experiment the cavity length L saturates while it increases continuously in the theory. A possible explanation for this might be that the measured sample bears a residual doping (n^*) which is not present in theory. The residual doping causes that for values below n^* the electrostatic gates are unable to further deplete the graphene, thus for $V_{\text{BG}} \rightarrow 0$ the effective value of $n_{\text{in}}/n_{\text{out}}$ (tuning L) remains fixed (section 2.3.1, Fig. 2.9c). On the other hand, the offset of the two curves might originate from a too narrow top-gate in the theoretical model if the top-gate in the experiment was measured with an error of ∼30 nm.

6.1.3. Definition of the cavity length

In equation 6.1 introduced in the previous section the cavity length was extracted from consecutive peaks of constructive interference in the measurement. However, the extracted cavity length in this case does not correspond to the distance between the two points of zero charge carrier density of the left and right *p*-*n* junction, as one might think intuitively. In this section the difference between the cavity length extracted from transport measurements (L_{tr}) and from electrostatic considerations (L_{el}) shall be elaborated. Furthermore, two additional aspects which account for minor corrections on the cavity length are discussed.

Cavity length from electrostatic calculations (L_{el})

Probably the most straight-forward definition of the cavity length in a *p*-*n*-*p* junction is by the distance between the two points where the charge carrier density is zero. In the simulation, for every set of (V_{BG},V_{TG}) a density profile along the x-axis (defined perpendicular to the *p*-*n* junction, $x = 0$ is centred in the middle of the top-gate) was calculated based on the quantum capacitance model for graphene [208] with classical self-partial capacitances simulated using FEniCS [209] and Gmsh [210]. The evolution of L_{el} (inner cavity) as a function of n_{in} for the linecuts indicated in Fig. 6.3a are shown in Fig. 6.3b (bold lines). Note that the transport simulation in Fig. 6.3a is based on the same electrostatic model. Furthermore, three exemplary profiles (zoom near the right *p*-*n* junction of the inner cavity) are shown in Fig. 6.3c.

Cavity length from transport measurements (L_{tr})

The cavity length extracted from the position of two neighbouring FP peaks, assuming a FP resonator with a hard-wall potential, is given by equation 6.1. Using a box-shaped potential is an oversimplification and can lead to a difference compared to L_{el} which is shown in Fig. 6.3b. The shaded region account

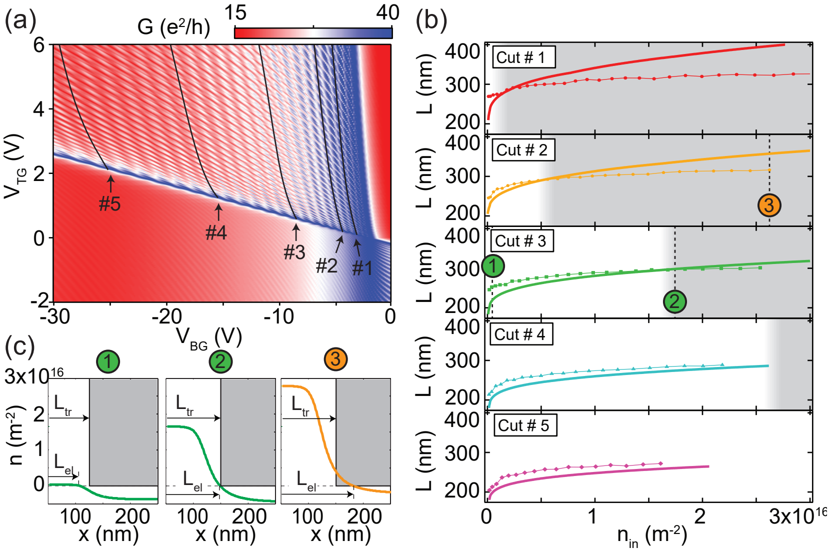

Figure 6.3. Definition of the cavity length. a, Transport simulation reproducing the Fabry-Pérot pattern observed for the regular p-n-p junction in the experiment. The linecuts indicated with 1-5 are at identical positions with those extracted from the experiment. **b,** Comparison of the cavity length extracted from the transport simulation (L_{tr}) using equation 6.1 (line + markers) and the cavity length extracted from electrostatic calculations (L_{el}, bold line) for different cuts as indicated in (a). Depending on the inner and outer cavity-doping, L_{tr} can be larger or smaller than L_{el}. The two models are in best agreement for high doping of n_{in} and n_{out} such as shown for cut 5. **c,** Three different density profiles where $L_{\mathrm{tr}} > L_{\mathrm{el}}$, $L_{\mathrm{tr}} = L_{\mathrm{el}}$ and $L_{\mathrm{tr}} < L_{\mathrm{el}}$. The inner cavity is centred around $x = 0\,\mathrm{nm}$.

for $L_{\mathrm{el}} > L_{\mathrm{tr}}$. Furthermore, in Fig. 6.3c the calculated L_{tr} is sketched in direct comparison with the calculated density profile from electrostatics simulations.

Second order corrections

Besides the major difference of assuming a box-shaped hard-wall potential, there are further smaller corrections leading to a difference between L_{tr} and L_{el}:

- Assume there is a density-profile as indicated in Fig. 6.4a. Since the trajectories contributing most to the FP signal have a finite incident

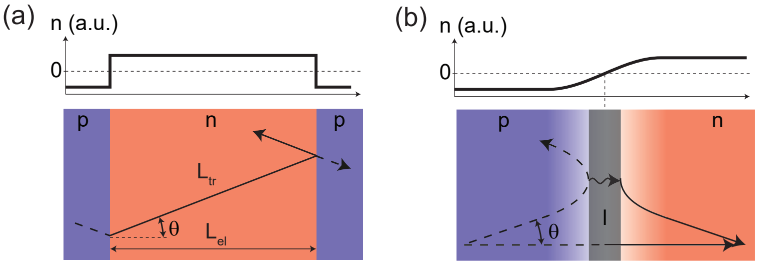

Figure 6.4. Second-order corrections of the cavity length. a, Finite-angles of the interfering trajectories and **b,** a gradual transition of the charge carrier density at the *p*-*n* junction causes an additional deviation of L_{tr} from L_{el}.

angle θ (for $\theta = 0$ one ends up with Klein tunneling, thus no contribution to the FP [14, 15, 211, 212]), the extracted L_{tr} actually corresponds to the diagonal distance. Therefore the real cavity length (which is given in this case by L_{el}) is given by $L_{\mathrm{el}} = L_{\mathrm{tr}} \cos(\theta)$. In this case L_{tr} overestimates the real cavity size. Since the charge carriers with a small incident angle (with respect to the *p*-*n* junction normal) account for most of the FP signal, this results only in a minor correction.

- Because the density profile is smooth and not abrupt, this leads to a bending of the charge carrier near the $n = 0$ density line as sketched in Fig. 6.4b. Charge carriers are therefore reflected before they hit the $n = 0$ density line, which will make the effective cavity size shorter [76] (section 2.2.3). However, since the trajectories of the charge carriers are bent, and in addition the density is varying while approaching the *p*-*n* junction, it is hard to make any statements if these two effects will lead to an over- or under-estimation of the cavity size.

In conclusion, using equation 6.1 to extract the cavity length from FP resonances gives slightly different results than using the definition based on simulated carrier densities. The extracted cavity lengths L_{tr} and L_{el} are only in good agreement (over a longer density range) when the outer and inner cavities are highly doped, which is best satisfied for Cut 5 as shown in Fig. 6.3c. The latter is understandable since at high doping the transition from *p*- to *n*-region is sharper than for low doping, thus best resembling a box-potential. Nevertheless, using equation 6.1 for the whole gate/density range is justified by the fact that for both, experiment and theory, the same quantity is extracted.

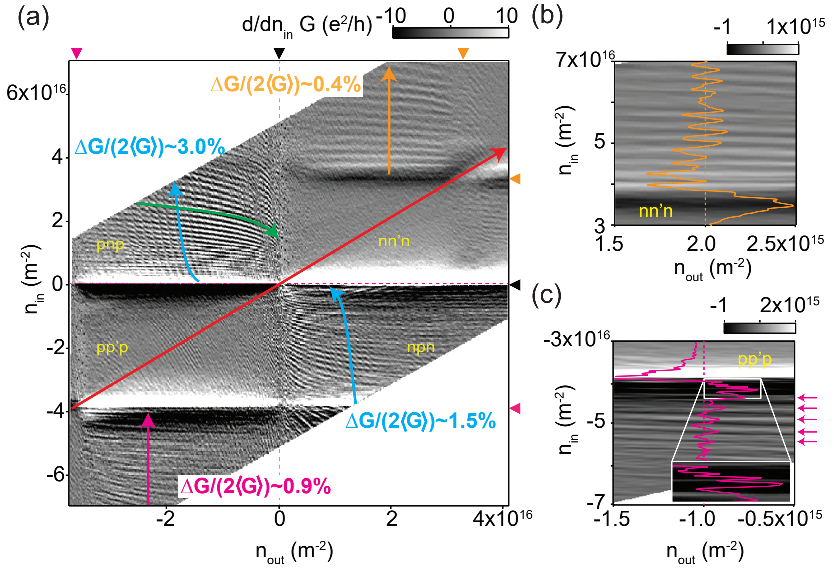

Figure 6.5. Fabry-Pérot resonances in in the presence of a Moiré superlattice. a, Numerical derivative of the conductance as a function of n_{in} and n_{out}. The red, cyan and green lines indicate the regular FP resonances described in Fig. 6.1. Additional FP resonances emerge if n_{in} or n_{out} is tuned beyond a satellite Dirac peak. These FP resonances are indicated with orange and purple arrows. The position of the main and satellite DPs are indicated with black and purple/orange triangles respectively. **b,c,** High-resolution measurements ($d/dn_{\text{in}}G$ (e^2/h)) of the regions where the inner cavity is tuned beyond the satellite DP and the additional FP resonances are present.

6.2. Moiré *p-n-p*

In the following, graphene which is aligned with a small twist angle with respect to the top hBN layer (section 2.4) is discussed. The resulting band reconstruction includes additional satellite DPs which are indicated with the purple and orange triangles in Fig. 6.5a where the derivative of the conductance is plotted. The main DP is indicated with the black triangle. At low doping the semi-transparent boundaries in the bipolar region are defined by the main DP (comparable to Fig. 6.1a) and FP resonances within inner and outer cavity are observed, marked by the green and cyan arrows, respectively.
Whereas in Fig. 6.1a,b the contacts are the only boundaries leading to FP

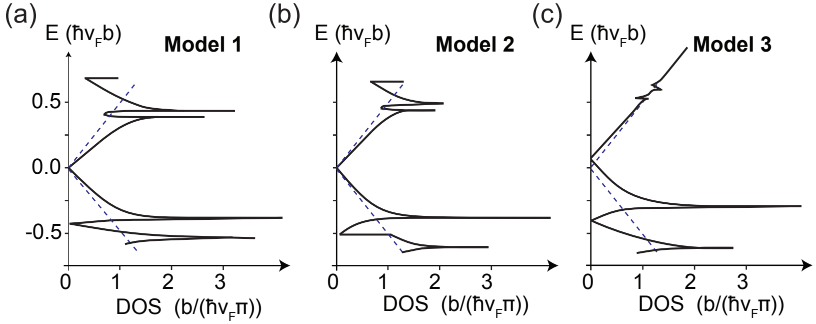

Figure 6.6. DOS of graphene in the presence of a Moiré superlattice. a-c, Calculations of three different families of band reconstructions using different model-parameters. The blue, dashed line indicates the DOS of graphene in the absence of a Moiré superlattice. Figure adapted from Ref. [110].

resonances in the unipolar regime (red arrow), additional semi-transparent boundaries, formed by the satellite DPs, emerge at high doping in the presence of a superlattice. As a result, novel FP oscillation are visible at high doping as indicated with the purple and orange arrows in Fig. 6.5a, which are absent in Fig. 6.1a (no Moiré superlattice). This new set of FP oscillation resembles again the pattern known from the bipolar regime and the transition from FP resonances across the whole sample to FP resonances within the inner and outer cavity is a direct consequence of the satellite DPs forming these additional semi-transparent boundaries. There are also charge carriers that bounce between the contacts and the satellite DP boundary, leading to weak resonances as a function of n_{out} (not shown).

6.2.1. Visibility of Fabry-Pérot resonances

Next, the visibility between FP resonances across the main DP and the satellite DPs within the inner cavity for $n_{\mathrm{in}} > 0$ and $n_{\mathrm{in}} < 0$ shall be compared separately ($\mu{\sim}100\,000\,\mathrm{cm}^2\mathrm{V}^{-1}\mathrm{s}^{-1}$). Charge carriers for $n_{\mathrm{in}} < 0$ (hole side) bouncing between boundaries formed by the satellite DPs ($\Delta G/(2\langle G\rangle) \sim 0.9\%$) show a visibility that is 40% lower than the visibility of the main DP oscillation ($\Delta G/(2\langle G\rangle) \sim 1.5\%$), as shown in Fig. 6.5a. In contrast, for $n_{\mathrm{in}} > 0$ (electron side), the visibility is reduced by 85% ($\Delta G/(2\langle G\rangle) \sim 0.4\%$ at the satellite DP compared to $\Delta G/(2\langle G\rangle) \sim 3\%$ at the main DP). To interpret these observations, a family of possible Moiré minibands for graphene on hBN substrate, as introduced in section 2.4 and shown again in Fig. 6.6, shall be considered. The latter were calculated by Wallbank *et al.* [110] using a general

symmetry-based approach.
For the case of $n_{\text{in}} < 0$, when crossing the satellite DP on the hole side, the DOS between inner and outer cavity decreases to zero for all $k_{\text{x,y}}$, independent on the model used. The latter can be seen in Fig. 6.6. The position of the satellite DP is indicated with the purple triangle in Fig. 6.5a. The decrease of the DOS to zero is experimentally supported by capacitance spectroscopy of hBN/graphene/hBN heterostructures in the presence of a Moiré superlattice [100]. The vanishing DOS leads to similar reflection/transmission coefficients as for the main DP, resulting in a comparable visibility of the two FP resonances. A representative cut at fixed $n_{\text{in}} < 0$ is shown in Fig. 6.5c.
For the electron side with $n_{\text{in}} > 0$, the significantly reduced visibility is as well in qualitative agreement with the band structures shown in Fig. 6.6, since the DOS at the satellite DP is reduced (depending on the parameters used in the calculation), but never vanishes. The position of the satellite DP is indicated with the yellow triangle in Fig. 6.5a. A representative cut at fixed $n_{\text{in}} > 0$ is shown in Fig. 6.5b. A direct implication of the finite DOS is that only some charge carriers have a non-zero reflection coefficient, thus contributing to the FP resonances, while the remaining ones account for a background current. It is worth noting, that even though the visibility of the FP resonances across the electron side satellite DP ($n_{\text{in,out}} > 0$) are significantly reduced, they seem to be more regular over a wider gate range compared to the FP resonances across the hole satellite DP ($n_{\text{in,out}} < 0$). However, this could be as well just sample-specific since the mobility in the hole side is significantly lower compared to the electron side.

6.2.2. Cavity length

In Fig. 6.7a,b the evolution of the position of the individual FP resonance peaks ($|n_{\text{out}}| \sim$ const.) and their relative spacing Δn_{in} as a function of n_{in} are compared. The latter analysis is performed instead of the cavity length analysis since equation 6.1 does not hold any more if the Fermi energy is tuned beyond the satellite DP. This is because in equation 6.1 a circular Fermi surface and linear dispersion relation are assumed, which do not hold in the presence of a strong band-modulation. In contrast, mapping the FP resonance peak position as a function of charge carrier density is free of any assumptions and therefore independent of the band structure. If the semi-transparent interfaces are defined via the main DP, the evolution of Δn_{in} between neighbouring peaks as a function of n_{in} is in good agreement with the values extracted from theory (transport simulation in the absence of a Moiré superlattice), which is indicated with the black, dashed line in Fig. 6.7b. If the semi-transparent interfaces are defined via the satellite DPs, the density-spacing between the FP resonance peaks is further increased on both, the electron and hole side.
Although a precise extraction of the cavity size is not possible with equa-

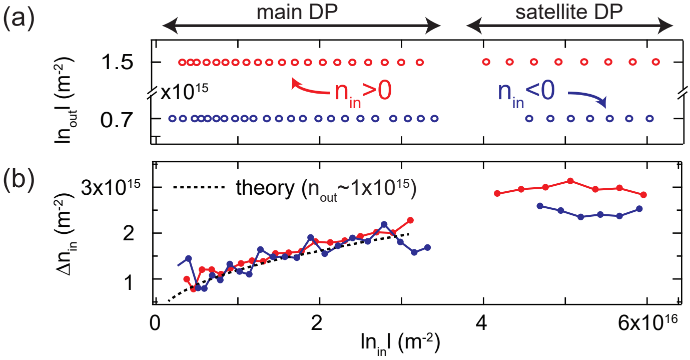

Figure 6.7. Fabry-Pérot resonances in in the presence of a Moiré superlattice. a, Position of the individual FP resonance peaks and **b,** their relative spacing Δn_{in} as a function of n_{in}. The black, dashed line indicates the values expected from theory. If the semi-transparent boundaries are defined via the satellite DP the spacing is further increased. However, no precise trend of Δn_{in} (increasing or decreasing) as a function of n_{in} can be seen from the few data-points extracted.

tion 6.1, an estimate can still be given. A cavity size of $L\sim 250\,\mathrm{nm}$ to $310\,\mathrm{nm}$ is found on the electron side if the density is measured from the main DP, whereas setting the density to zero at the satellite DP gives an unphysical cavity size ($L\sim 80\,\mathrm{nm}$ to $200\,\mathrm{nm}$). On the electron side the density of states seems almost unaltered (Fig. 6.6), however the band structure is substantially modified, which can be seen in Fig. 2.15. The band structure consists of two non-isotropic bands above the satellite DPs which makes the situation rather complex, with different visibilities and angle dependent transmissions for the two bands. On the hole side the cavity size analysis yields cavity sizes of $L\sim 280\,\mathrm{nm}$ to $360\,\mathrm{nm}$ if the density is measured from the main DP. At the satellite DP the density of states decreases to zero, meaning that a real Dirac point is formed. Therefore one might expect, that the density for the FP oscillations should be measured from the satellite DP. However by setting the charge carrier density to zero at the hole satellite DP, the analysis gives unphysical results. Note that that close to the hole satellite DP equation 6.1 should be valid if counting the charge carrier density from the satellite DP, since the band structure is isotropic.

Besides the most pronounced FP resonances indicated with the purple arrow in Fig. 6.5c, a second set of resonances with a much shorter period seem to appear in the very vicinity of the hole satellite DP (see inset of Fig. 6.5c). For these resonances the extracted cavity length leads only to reasonable values ($L\sim300\,\mathrm{nm}$) when counting the charge carrier density starting from the satellite DP. Unfortunately the residual doping ($n_{\mathrm{res}}\sim0.4\times10^{15}\,\mathrm{m}^{-2}$ to $1\times10^{15}\,\mathrm{m}^{-2}$) was too high in order to resolve more of these features in the very vicinity of the satellite DP. A possible explanation for the different behavior of the two sets of FP oscillation ($n_{\mathrm{out}}<0$) might be the following: The small resonances are only observed up to densities of $\Delta n<2\times10^{15}\,\mathrm{m}^{-2}$ (where Δn is measured from the satellite DP), where the Moiré miniband remains close to Dirac like (linear dispersion relation as shown in Fig. 2.2). The Fermi energy corresponding to theses small oscillations is consequently exclusively tuned in the linear part of the Moiré miniband. From the band structures it would be expected that the small oscillations should be visible up to higher doping values, namely values which are larger by a factor of up to ~10 depending on the model. This estimate is based on the energy-spacing between the satellite DP and the first van Hove singularity at higher energies, extracted from theory. Note that the extracted energy-spacing corresponds to an upper bound within which the dispersion relation might be considered as linear. The Fermi energy corresponding to the stronger resonances indicated with the purple arrow, does partially reside outside of the linear region of the Dirac cones where the band structure becomes more complex, including singularities and band-overlaps.

In the work of Lee *et al.* [33] they suggest that model 3 shown in Fig. 6.6c is the one describing the experimental situation best (see as well section 2.4.1). Furthermore, for models where multiple satellite DPs appear near every main DP (e.g. the model shown in Fig. 2.15a), equation 6.1 would have to be multiplied by a factor of $\sqrt{g_{\mathrm{SDP}}}$, where g_{SDP} is the additional degeneracy of the satellite Dirac cones. Upon including additional degeneracies and counting the density from the satellite DP, the more pronounced oscillations might give reasonable cavity sizes. However, for the small and fast oscillations, the additional degeneracies would definitely result in too large cavity sizes. Moreover, most experimental evidence including QHE measurements (section 2.4.1, Fig. 2.14) point to a single Dirac cone at the satellite DP.

6.3. Low magnetic field measurements

Magnetic field measurements can complement the measurements done at zero magnetic field as they reveal additional information on the charge carriers in the system such as the sign of the charge carriers (electrons or holes) in quantum Hall measurements [103] or their Berry-phase by measuring the evolution of the FP resonances with magnetic field [37, 58, 207]. FP resonances disperse towards higher doping (k values) with increasing magnetic field [37, 40, 41, 44, 58, 59]. This results from the resonance condition $\Delta\theta_{\mathrm{WKB}}+\Phi_{\mathrm{AB}}=\mathrm{const.}$ where $\Delta\theta_{\mathrm{WKB}}$ is the Wentzel-Kramers-Brillouin phase acquired

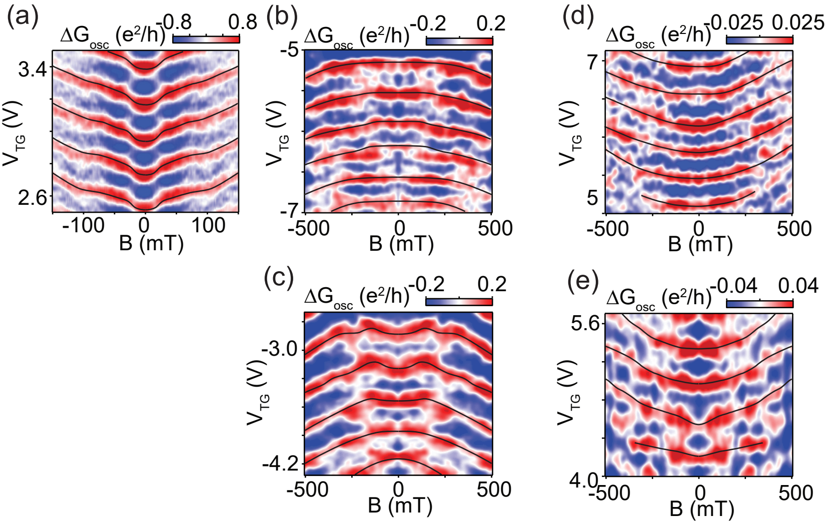

Figure 6.8. Low magnetic field measurements of the FP resonances across the main and satellite DPs. Conductance oscillations due to FP resonances where a background was subtracted. **a,** FP resonances across the main DP with $n_{\text{in}} > 0$ and $n_{\text{out}} \sim 0.3 \times 10^{16}\,\text{m}^{-2}$. **b,c,** Measurements across the satellite DP with $n_{\text{in}} < 0$ where $n_{\text{out}} \sim -0.7 \times 10^{16}\,\text{m}^{-2}$ and $n_{\text{out}} \sim -2.8 \times 10^{16}\,\text{m}^{-2}$. **d,e,** Measurements across the satellite DP with $n_{\text{in}} > 0$ where $n_{\text{out}} \sim 2.1 \times 10^{16}\,\text{m}^{-2}$ and $n_{\text{out}} \sim 2.8 \times 10^{16}\,\text{m}^{-2}$.

on the path of the charge carriers trajectory, and Φ_{AB} is the Aharonov Bohm phase [37, 207]. For single layer graphene the Berry's phase is π as discussed section 2.1.2. This has been observed experimentally in FP measurements [58] and quantum Hall measurements [12]. In Fig. 6.8 low magnetic field measurements are shown for FP oscillations across the main DP (a) and the satellite DP in the hole (b,c) and electron (d,e) doped region. The black lines in Fig. 6.8 were extracted numerically and track the peak position of the FP oscillations with magnetic field. In Fig. 6.8a the FP resonances across the main DP with a π-shift at roughly $B \sim 30\,\text{mT}$ to $50\,\text{mT}$ is shown. Following the previously given argument, one might expected as well a π-shift for the FP resonances across the satellite DP on the hole side, since there the DOS drops to zero comparable to the main DP. However, measurements at different n_{out}, shown in Fig. 6.8b,c, did not allow a conclusive statement whether such a π-shift is present or not. It seems however that for both of the presented situations an intriguing pattern appears at low magnetic fields (i.e. $B < 200\,\text{mT}$). At higher field, the FP oscillations disperse constantly. On the electron side ($n_{\mathrm{in}} > 0$, shown in Fig. 6.8d,e) the situation is even less clear.

6.4. Conclusion

In conclusion, *p*-*n*-*p* junction were first analyzed in the absence of a Moiré superlattice where the varying visibility of the different types of FP resonances could be linked to “sharp” and “smooth” *p*-*n* junctions in the system. Furthermore, the change of the effective cavity length depending on n_{in} and n_{out} could be mapped via the FP resonances. In a second sample, the presence of a Moiré superlattice gave rise to satellite DPs and the modified band structure resulted in confinement of electronic trajectories and in the appearance of FP resonances. Although the oscillations are formed in the Moiré minibands, they can mostly be described as if they would originate from the non-modified band structures. Further studies will be needed to explain these findings. The results presented in this section show that confinement of electrons can be obtained using miniband engineering. Future studies can investigate the angle dependent transmission properties of such an interface. Moreover combining the studies of transverse magnetic focusing [33] and bias spectroscopy studies of FP resonances or more detailed studies of the magnetic field dependence of FP resonances can reveal further details on the band reconstruction.

7 Co-existence of classical snake states and Aharanov-Bohm oscillations along graphene *p*-*n* junctions

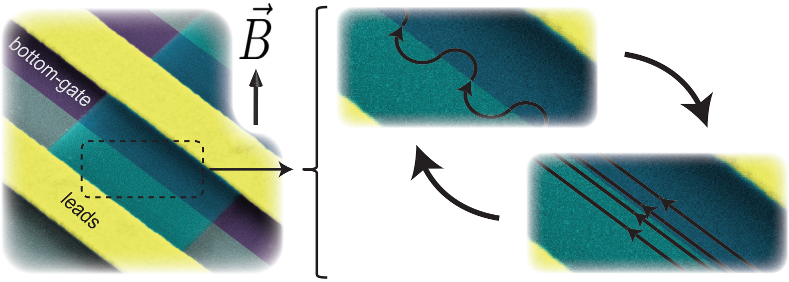

Snake states and Aharanov-Bohm interferences are examples of magnetoconductance oscillations which can be observed along a graphene *p*-*n* junction. Even though they have already been reported in suspended and encapsulated devices including different geometries, a direct comparison remains challenging as they were observed in separate measurements. Due to the similar experimental signatures of these effects a consistent assignment is difficult, leaving us with an incomplete picture. Here we present measurements on a single *p*-*n* junction revealing several sets of magnetoconductance oscillations allowing a direct comparison of the latter. We analysed them with respect to their charge carrier density, magnetic field, temperature and bias dependence in order to assign them to either the snake states or the Aharanov-Bohm oscillations. Surprisingly we find that snake states and Aharanov-Bohm interferences can co-exist within a limited parameter range[1].

---

[1] This chapter represents a preliminary version of a publication (parts of the measurements are still being discussed) which will be available soon.

7.1. Introduction

Magnetoconductance is the change of the conductance as a function of magnetic field B and is important from both application (e.g. GMR [213, 214], TMR [215], etc.) and a conceptual point of view (e.g. Aharanov-Bhom effect). Graphene, which is a zero-gap semiconductor, is an ideal platform to investigate magnetoconductance oscillations along p-n junctions - something which is difficult in conventional semiconductors. Prominent examples of the latter are snake states [35–38, 216, 217] and Aharonov-Bohm interferences [46, 218]. While the former effect is usually explained using the picture of classical skipping trajectories at low magnetic field, the latter is commonly explained using the picture of quantum Hall edge states at high magnetic fields. However, their signatures are very alike and it is difficult to distinguish the two from each other. Note that the observation of an Aharanov-Bohm effect requires phase coherent transport, while snake states are based on ballistic transport. Here we present measurements in a two-terminal graphene p-n junction in which both effects are observed simultaneously. This allows a direct comparison with respect to their gate, field, temperature and bias dependence, resulting in a consistent assignment of the different oscillations to their true origin.

This chapter is organized as follows: First we introduce the most relevant concepts of snake states and Aharanov-Bohm oscillations along graphene p-n junctions. Then we present measurements of several sets of magnetoconductance oscillations within the bipolar regime. These magnetoconductance oscillations are carefully analysed with respect to their gate, magnetic field, temperature and bias dependence. We show that these oscillations can be attributed to either snake states or Aharanov-Bohm oscillations as introduced previously. We furthermore support our findings with theoretical calculations and quantum transport simulations. Finally, we briefly discuss an additional type of magnetoconductance oscillations.

7.1.1. Snake states

Skipping trajectories which are moving along a p-n junction are referred to as snake states [35–38]. The name of snake states originates from the resemblance with a snake if the classical trajectories are drawn. The trajectories bend in opposite direction on the two sides of the p-n junction due to an opposite Lorentz force, as sketched in Fig. 7.1a. Charge carriers with trajectories having a small incident angle with respect to the p-n junction normal are transmitted very effectively from the n- to p-doped region of the graphene (and vice versa) due to Klein-tunneling [14, 15, 76]. In the simplest case the p-n junction is step-like and symmetric, and the cyclotron radius (equation 2.24) is the

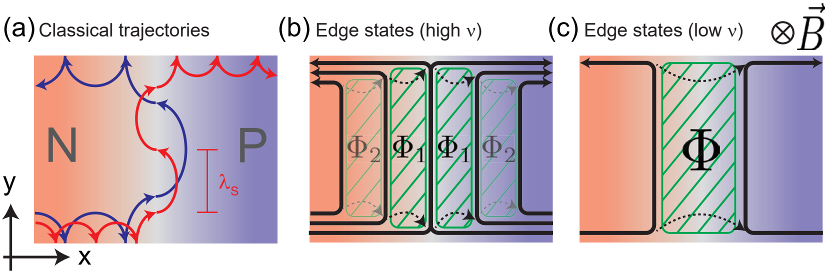

Figure 7.1. Concept of snake states and Aharanov-Bohm interference along a graphene p-n junction. a, Snake states seen in the framework of classical skipping orbits for two different magnetic field values (blue and red trajectories). **b,** Principle of Aharonov-Bohm interferences between edge-states propagating along a graphene p-n interface. At high filling factors (ν) several different areas are enclosed (green shaded area). However, the Aharonov-Bohm interference including the least scattering events (Φ_1) is expected to dominant over those which require more scattering events (Φ_2, indicated with the reduced opacity). **c,** At high magnetic fields Aharonov-Bohm interference can occur between the spatially separated edge states of the degeneracy lifted lowest Landau level. The green area corresponds to the insulating region with $\nu = 0$.

same constant value on both side. However, a more realistic model includes a gradual change of the charge carrier density across the p-n junction, which is illustrated in Fig. 7.1a. For a p-n junction which is located parallel to the y-direction this gives rise to an electric field $\vec{E}_\mathrm{x}$, and consequently a drift-velocity along the y-direction which results from $\vec{E} \times \vec{B}$ [37]. By solving the semiclassical equations of motion for an ideal graphene p-n junction where the charge carrier density changes linearly, the skipping-length λ_S is given by (see appendix B.1):

$$\lambda_\mathrm{S} = \left(\frac{\pi\hbar}{eB}\right)^2 \frac{|n_\mathrm{L} - n_\mathrm{R}|}{d_\mathrm{n}} \tag{7.1}$$

where n_L,n_R are the charge carrier densities in the bulk of graphene and d_n is the width across which the charge carrier density varies. Note that $S = |n_\mathrm{L} - n_\mathrm{R}|/d_\mathrm{n}$ corresponds to the slope of the charge carrier density profile. The conductance oscillations which can be measured across the p-n junction of length W can be described by the phenomenological model according to:

$$G(E) \sim \cos\left(\pi \frac{W}{\lambda_\mathrm{S}}\right), \tag{7.2}$$

which describes the commensurability between λ_S and W. The cosine itself accounts for a smooth conductance oscillation. The magnetic field spacing resulting from equation 7.2, which deviates from the equidistant magnetic field spacing using an abrupt *p*-*n* junction [38], and the temperature dependence will be discussed later.

7.1.2. Aharanov-Bohm oscillations

While at low magnetic fields the motion of the charge carriers is well described using the picture of skipping and snaking trajectories along edges and *p*-*n* junctions, upon increasing the magnetic field one enters the quantum regime where the transport is commonly described with edge states as discussed in section 2.1.3. The concept of interference formed by spatially separated edge states is already extensively studied in 2DEGs, including the realization of Fabry-Pérot and [219] Mach-Zehnder [220] interferometers. The concept of an interferometer formed by spatially separated edge states in graphene was first introduced by Morikawa et *al.* [46]. Coupling between the edge states across the *p*-*n* junction, illustrated in Fig. 7.1b,c with the black, dashed arrows, is restricted to the disordered graphene edges [46, 218]. As the edge states encircle an enclosed area A at finite perpendicular magnetic field B, the acquired Aharanov-Bohm phase is given by Φ where $\Phi = AB$ is the magnetic flux. The conductance oscillations can be described by the phenomenological model according to:

$$G(E) \sim \cos\left(2\pi\frac{\Phi}{\Phi_0}\right), \tag{7.3}$$

where Φ_0 =h/e is the magnetic flux quantum [221]. If multiple Landau levels are populated, several different areas might be enclosed. However, the Aharanov-Bohm interferences including the least scattering events between neighbouring edge states, which correspond to Φ_1 in Fig. 7.1b, dominate over those including more scattering events (Φ_2). At high magnetic fields the Landau levels can be partially (or fully) degeneracy lifted. This leads to a spatial seperation of the edge states associated with the lowest Landau level by an insulating region ($\nu = 0$), as shown in Fig. 7.1c. The idea of an Aharonov-Bohm interference was generalized by Wei et *al.* [218] by considering full degeneracy lifting of the Landau levels. In this case scattering between edge states is only possible if they are of identical spin, consequently giving rise to two sets of magnetoconductance oscillations - one for each spin-channel. An increase of the spacing between neighbouring edge states results in a decreases of the scattering rate at the flake edge between edge states, giving rise to a reduced oscillation amplitude. The magnetic field spacing and the temperature dependence of the Aharanov-Bohm dependence will be discussed later in this chapter.

7.2. Measurements

7.2.1. Gate-gate dependence

In Fig. 7.2 and Fig. 7.3 the two terminal conductance and its numerical derivative are shown as a function of the global back-gate (V_{BG}) and the local bottom-gate (V_{lbg}) within the bipolar regime at selected magnetic fields. Zero voltage of the global back-gate or local bottom-gate corresponds roughly to zero doping in the left or right cavity of the sample. In the gate-gate map, fine lines are visible along which the conductance is constant, and perpendicular to these lines the conductance oscillates. Within the measured gate and field range we find three different types of magnetoconductance oscillations which are labelled with the red, orange and cyan arrows/dashed lines. All of them have a roughly hyperbolic line shape being asymptotic with the zero-density lines related to either of the two sides of the samples. However, they are observed within different parameter ranges. The filling factors (equation 2.30) corresponding to the bulk value of the cavity tuned by the global back-gate and local bottom-gate are indicated with the green and purple arrows in Fig. 7.2/Fig. 7.3. The yellow, dashed lines correspond to $|\nu| = 1$ and $|\nu| = 2$ respectively. Upon comparing the different magnetoconductance oscillations it can be seen that the cyan ones exists at very low filling factors (starting at $|\nu| > 1$), the red ones exist at intermediate filling factors and the orange ones exist at the highest filling factors. For one orange set, the filling factor values where the oscillations start to appear are around $(\nu_{\mathrm{BG}}, \nu_{\mathrm{lbg}}) \sim (-4, 8)$, for the other orange set around $(\nu_{\mathrm{BG}}, \nu_{\mathrm{lbg}}) \sim (-8, 4)$. Furthermore, the spacing of neighbouring conductance oscillations as a function of charge carrier doping differs significantly for the cyan, red and orange oscillations. Additional lines at low filling factors, which become more pronounced at higher magnetic field, are fanning out linearly from the common charge neutrality point. These are attributed to valley-isospin oscillations and will be discussed in chapter 8.

While for the magnetoconductance oscillations which is labelled with red only one set is observed, two sets are observed each for the ones labelled with orange and cyan. The two sets of the orange and cyan magnetoconductance oscillations respectively are furthermore shifted in doping with respect to each other. Using a device with a geometry enabling gate defined *p*-*n*-*p* or *n*-*p*-*n* junctions (not shown here) it is possible to exclude that the two orange sets of magnetoconductance oscillations originate from an additional *p*-*n* junction formed between n-doped graphene near the Cr/Au contacts and a p-doped bulk.

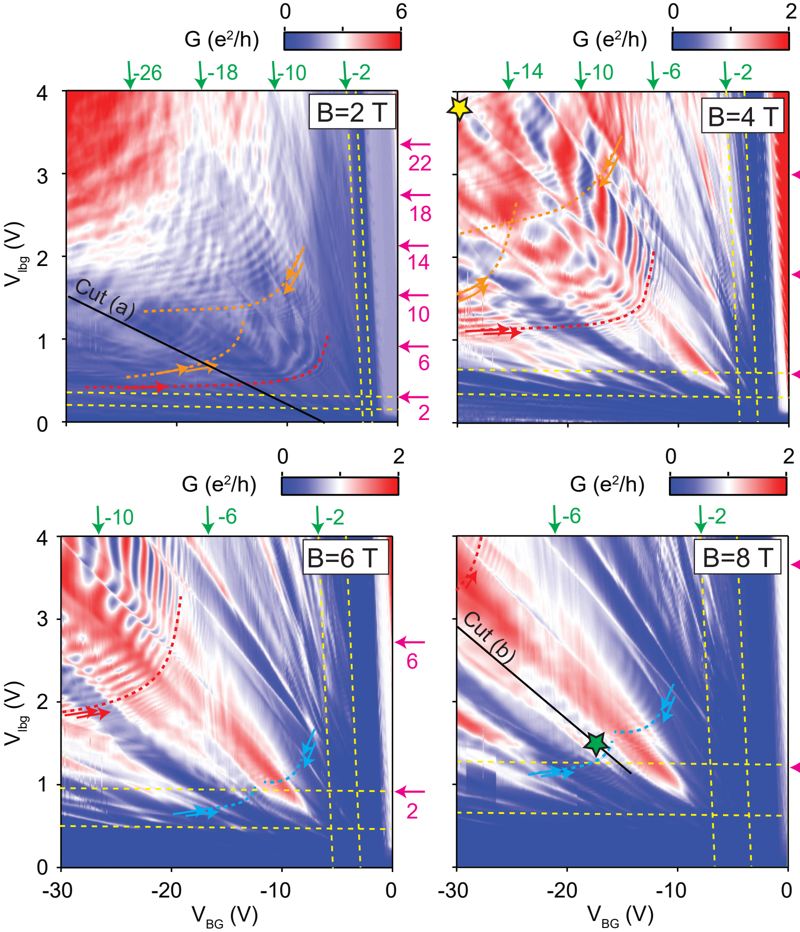

Figure 7.2. Conductance of a *p-n* junction in the bipolar regime for different magnetic fields. The filling factors are given in green for the cavity tuned by the global back-gate (ν_{BG}), and in purple for the cavity tuned by the local bottom-gate (ν_{lbg}). The yellow, dashed lines indicate filling factors 1 and 2. The different types of magnetoconductance oscillations are indicated with the red, orange and cyan arrows/dashed lines.

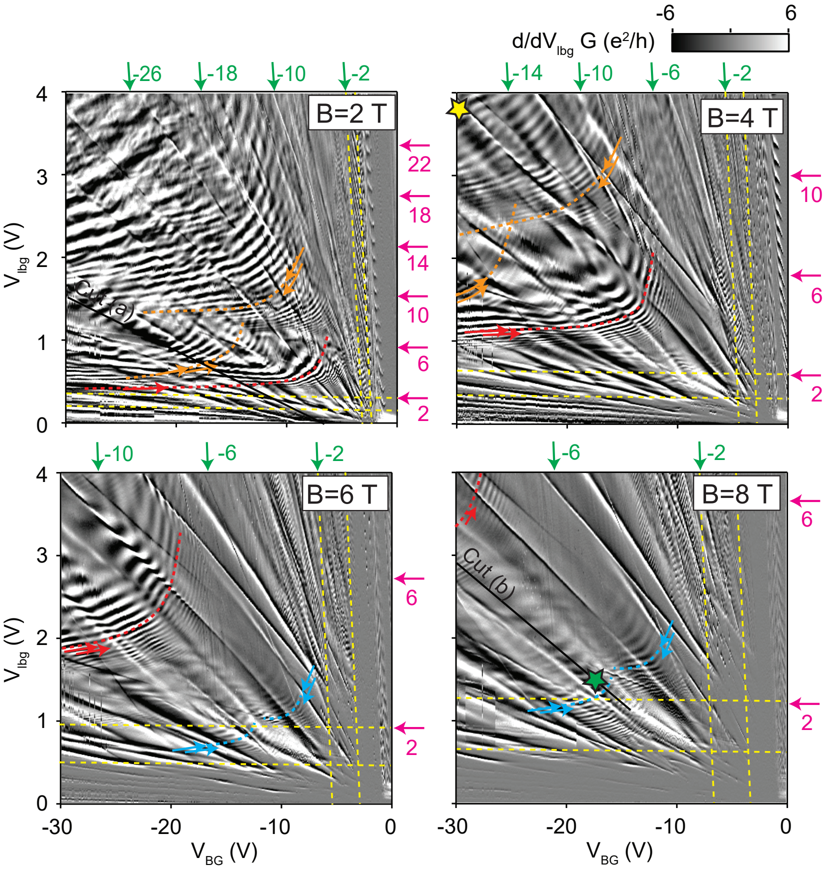

Figure 7.3. Numerical derivative of Fig. 7.2 with respect to V$_{\mathrm{lbg}}$. The labelling of the magnetoconductance oscillations and filling factors is equivalent to Fig. 7.2.

This is in agreement with quantum transport simulations (see section 7.5), where two sets of orange magnetoconductance oscillations are reproduced without including metal leads. Therefore, a double set of oscillations must be the sign of two different interferometer loops working simultaneously near the *p*-*n* junction in the bulk (see Fig. 7.1b).

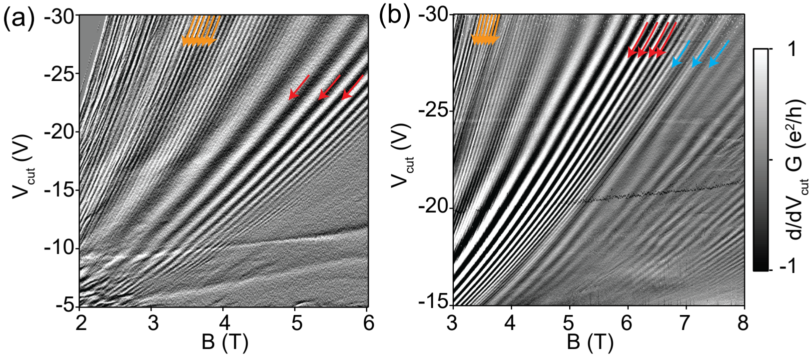

Figure 7.4. Magnetic field dependence. a, Numerical derivative of the conductance as a function of magnetic field and gate voltage as labelled in Fig. 7.2/Fig. 7.3 with “Cut (a)”. Within a limited parameter range the magnetoconductance oscillations indicated with the red and orange arrows and the red and the cyan arrows, are co-existing. The latter can be better seen in **b,** along the linecut as labelled in Fig. 7.2/Fig. 7.3 with “Cut (b)”.

7.2.2. Magnetic field dependence

Next we measured selected linecuts as indicated in Fig. 7.2/Fig. 7.3 with “Cut (a)” and “Cut (b)” as a function of magnetic field. The differential conductances as a function of magnetic field and gate voltage are show in Fig. 7.4a,b. The three magnetoconductance oscillations, which are labelled with the the red, orange and cyan arrows, follow a roughly (but not exactly) parabolic magnetic field dependence where the oscillations shift to higher gate voltages with increasing magnetic field. Furthermore, we observe a co-existence of multiple oscillations within a limited parameter range. The co-existence of the red and orange oscillations is seen in both Fig. 7.4a and Fig. 7.4b while the co-existence of the red and cyan oscillations is seen only in Fig. 7.4b. The conductance as a function of the magnetic field, while keeping the charge carrier densities on both sides of the *p*-*n* junction fixed, is plotted in Fig. 7.5a-c for three selected configurations. In Fig. 7.5a,b large oscillations (red in the previous graphs) with amplitudes reaching up to nearly $2\,e^2/h$ can be seen. Within a limited parameter range there are smaller oscillations (orange in the previous graphs) superimposed on top of the red oscillations, having amplitudes reaching up to $\sim 0.6\,e^2/h$. The magnetic field spacing (ΔB) between neighbouring peaks is given in Fig. 7.5d-f for the corresponding oscillations shown in Fig. 7.5a-c. Even though all three types of magnetoconductance oscillations reveal a different spacing of ΔB, they share a common trend, namely the decrease of ΔB

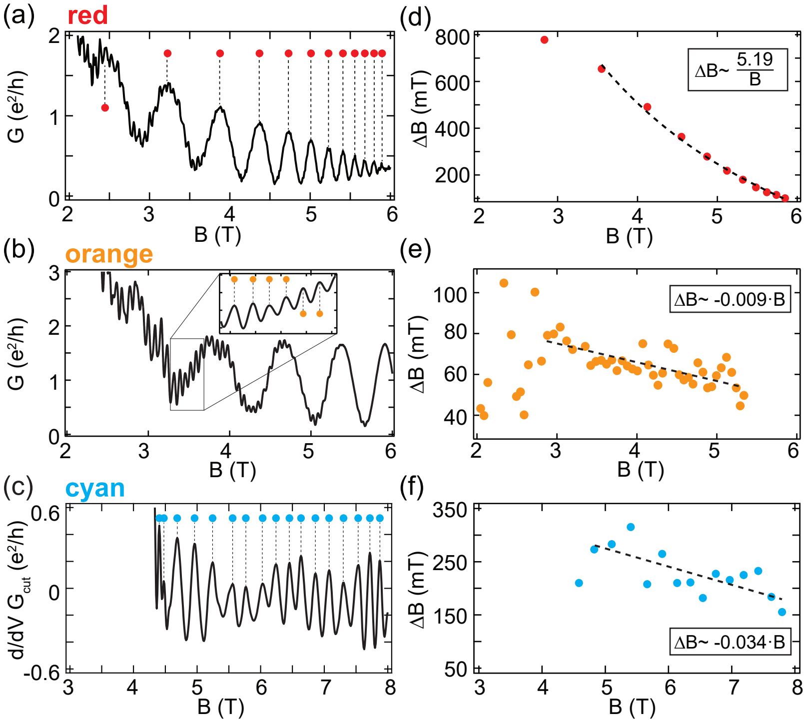

Figure 7.5. Magnetic field spacing. a-c, Conductance or its numerical derivative as a function of magnetic field for representative gate-gate configurations of the red ($V_{\mathrm{BG}} = -20\,\mathrm{V}, V_{\mathrm{lbg}} = 1.8\,\mathrm{V}$), orange ($V_{\mathrm{BG}} = -27.5\,\mathrm{V}, V_{\mathrm{lbg}} = 4\,\mathrm{V}$) and cyan ($V_{\mathrm{BG}} = -18.5\,\mathrm{V}, V_{\mathrm{lbg}} = 1.27\,\mathrm{V}$) magnetoconductance oscillations. The peak-positions are indicated with the red, orange and cyan dots. **d-f,** Magnetic field spacing (ΔB) extracted from (a-c,). A $1/B$ and linear dependence of ΔB as a function of B is indicated with the black, dashed lines for the snake states and Aharanov-Bohm interferences respectively.

with increasing B. Nevertheless, the rate of ΔB as a function of B is quite different for the red compared to the orange and blue magnetoconductance oscillations, which is an indication that a different physical mechanisms are involved.

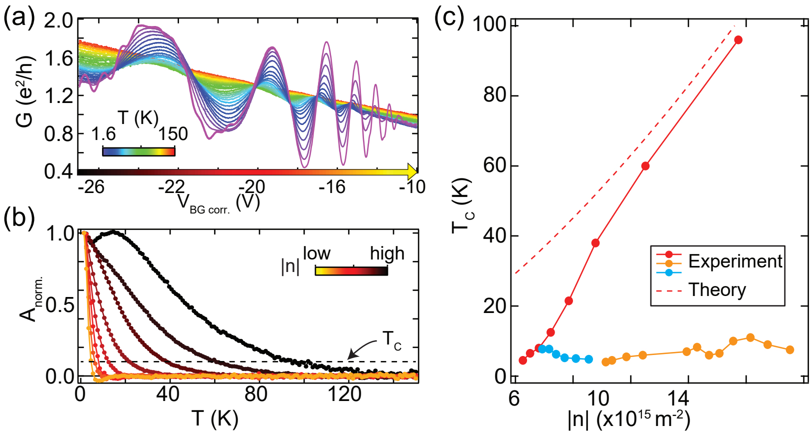

Figure 7.6. Temperature dependence. a, Red magnetoconductance oscillations as a of the global back-gates (V_{lbg} is chosen such that $n_{\mathrm{BG}} \sim n_{\mathrm{lbg}}$) and temperature. **b,** Normalized area extracted from (a) as a function of temperature for different oscillations. **c,** The solid lines/dots show the experimental values of T_{C} of the red, orange and cyan magnetoconductance oscillations (extracted at B =3.5 T, B =3 T and B =8 T respectively) as a function of charge carrier doping. The red, dashed line corresponds to the vanishing of snake states according to equation 7.7 using d_{n} =50 nm and W =1500 nm.

7.2.3. Temperature dependence

In Fig. 7.6 the temperature dependence of the red, orange and cyan magnetoconductance oscillations is given. We extract the temperature at which the magnetoconductance oscillations decrease to 10 % of their maximal value (T_{C}) as a function of the charge carrier density. In Fig. 7.6a the red oscillations are shown as a function of gate voltage and temperature ($n_{\mathrm{BG}} \sim n_{\mathrm{lbg}}$ and B =3.5 T). We characterize the temperature dependence of each oscillation by calculating the area under the oscillation A. From this the normalized area, which is defined as $A_{\mathrm{norm.}} = A(T)/A(T = 1.6K)$, can be extracted at different densities and is plotted as a function of temperature which is shown in Fig. 7.6b. In Fig. 7.6c T_{C} is plotted as a function of the density for all three types magnetoconductance oscillations. While the red magnetoconductance oscillations reveals a significant temperature dependence as a function of the charge carrier density, surviving up to T ∼100 K at high doping, the orange and cyan magnetoconductance oscillations vanish at temperatures around T ∼10 K roughly independent on the charge carrier density. This suggests again that different mechanism are responsible for the red magnetoconductance oscillations compared to the orange and cyan magnetoconductance oscillations. Ballistic effects, such as snake states and transverse magnetic focusing, are known to survive to temperatures up to T ~100 K to 150 K [31, 33, 38]. On the other hand, phase coherent transport in similar devices vanishes at temperatures around ~10 K (see Ref. [222]).

7.3. Discussion

We have observed different magnetoconductance oscillations, marked with red, orange and blue. All of the oscillations have a roughly hyperbolic line shapes in the gate-gate map, but the magnetic field spacing and the temperature dependence suggest that the red oscillations are governed by a different physical mechanism. Based on the experiments we suggest that the red oscillations can be assigned to classical snake states while the orange and cyan oscillations result from an Aharonov-Bohm interference as discussed below.

7.3.1. Red magnetoconductance oscillations

The red magnetoconductance oscillations start to appear in the range $|\nu| \sim 3-6$ as can be seen in Fig. 7.2/Fig. 7.3. This corresponds to an occupation of roughly two edge states ($\nu = \pm 4$, Landau levels 0 and ± 1) without taking degeneracy lifting into account. The gate spacing between neighbouring magnetoconductance oscillations extracted from Fig. 7.2/Fig. 7.3 is around ΔV_{BG} ~0.2 V to 1.5 V (at B =4 T). These values are roughly two orders of magnitudes larger than what is expected if the underlying physics were based on charging effects[2]. Therefore the latter seems rather unlikely to be the origin of these magnetoconductance oscillations. On the other hand, we now show that the shape and the gate spacing of the red magnetoconductance oscillations fit very well to what is expected for snake states following equation 7.1 and equation 7.2. As discussed in the introduction, the oscillation results from a commensurability relation where the conductance is high or low depending on where the charge carriers end up. If the magnetic field is fixed, the slope of the p-n junction is directly proportional to the skipping-length according to equation 7.1. In Fig. 7.7a the calculated charge carrier density profile at B =0 T is shown for three exemplary gate-gate configurations. From Fig. 7.7a it is possible to extract the slope S_0 at $n = 0$ at any gate-gate configuration, which then leads to Fig. 7.7b. In the latter, lines of constant S_0, and therefore a constant λ_{S} (if B remains fixed), follow a roughly hyperbolic line

---

[2] The gate spacing of a charging effect can be calculated according to $\Delta V_{\mathrm{g}} \cdot C = e$, where C is the total capacitance of the system. In the most simple model C is dominated by the capacitance associated with the electrostatic gates ($C \sim C_{\mathrm{g}}$), which is easy to calculate. Even though this is an oversimplification it allows to obtain a rough estimate, yielding ΔV_{BG} ~2 mV.

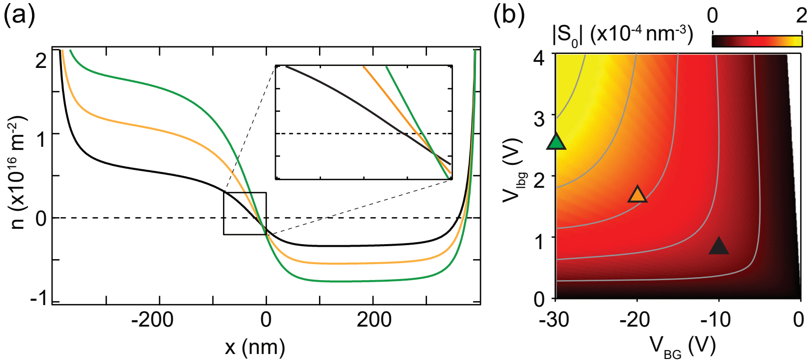

Figure 7.7. Charge carrier density profile and slope in the bipolar regime. a, Representative charge carrier density profiles calculated from electrostatics at positions as indicated in (b) with the triangles. At $n = 0$ the slope is nearly linear (inset). **b,** Slope $|S_0|$ which was extracted at $n = 0$ as a function of the gates. Grey lines represent constant values of $|S_0|$, and consequently as well of λ_S (equation 7.1).

shape in agreement with the shape of the red magnetoconductance oscillations (Fig. 7.2/Fig. 7.3). Based on S_0 (Fig. 7.7b) one can as well calculate the conductance as a function of an arbitrary linecut and magnetic field (not shown here), leading to a roughly parabolic magnetoconductance oscillation which strongly resembles the measurements shown in Fig. 7.4a,b.

By using the model with a constant density gradient the magnetic field spacing as a function of magnetic field is given by (see appendix B.4):

$$\Delta B \sim 2\frac{\pi^2\hbar^2 n}{e^2 W d_\mathrm{n}}\frac{1}{B} \tag{7.4}$$

where a symmetric p-n junction with $n \equiv n_\mathrm{L} = n_\mathrm{R}$ was assumed. By fitting the measurements shown in Fig. 7.5d with equation 7.4 we extracted a slope of $S = 1.82 \times 10^{-3}\,\mathrm{nm}^{-3}$ which is roughly one order of magnitude larger than what was calculated in Fig. 7.7b ($S_0 \sim 1.2 \times 10^{-4}\,\mathrm{nm}^{-3}$). The discrepancy between the values can be explained by the fact that strictly speaking S_0 is only valid at $B = 0\,\mathrm{T}$. However, at finite magnetic field the charge carrier density has to be calculated self-consistently leading to areas with a constant charge carrier density (compressible reigon) and areas where the charge carrier density changes rapidly ($S > S_0$, incompressible regions) [223].

Furthermore, the decrease of the oscillation amplitude with increasing magnetic field (Fig. 7.5a) is compatible with the picture of classical snake trajectories, where the conductance oscillation results from the sum over all trajectories

which form caustics along the p-n junction [195, 196]. Upon increasing the magnetic field the charge carriers have to pass the p-n junction more often (decreasing λ_{S}). This leads to the reduced oscillation amplitude [217] because only trajectories with an incident angles being perpendicular to the p-n junction ($\theta = 0$) have a transmission probability of $t = 1$, while for all remaining trajectories $t < 1$ is valid [15, 34, 76].
From equation 7.1 it is possible to calculate the temperature dependence of snake states. They are expected to vanish if:

$$2\left(\lambda_{\mathrm{S,max}} - \lambda_{\mathrm{S,min}}\right) \cdot N \sim \langle\lambda_{\mathrm{S}}\rangle \tag{7.5}$$

where $\lambda_{\mathrm{S,max}}$ and $\lambda_{\mathrm{S,min}}$ correspond to the maximal and minimal skipping-length due to the temperature smearing Δk_{F}, the average skipping-length $\langle\lambda_{\mathrm{S}}\rangle$ is given by equation 7.1 and $N = W/(2\langle\lambda_{\mathrm{S}}\rangle)$. By using the relations $k_{\mathrm{F,max}}^2 - k_{\mathrm{F,min}}^2 \sim 2k_{\mathrm{F}}\Delta k_{\mathrm{F}}$ equation 7.5 can be rereitten as:

$$\Delta k_{\mathrm{F}} \sim \frac{k_{\mathrm{F}}^3}{W d_{\mathrm{n}} \pi}\left(\frac{\pi\hbar}{eB}\right)^2 . \tag{7.6}$$

At finite temperatures T the Fermi-surface is broadened by $\Delta E \sim k_{\mathrm{B}}T$ (where k_{B} is the Boltzmann constant), thus leading to a spread of the Fermi-wavevector according to $\Delta k_{\mathrm{F}} \sim k_{\mathrm{B}}T/(\hbar v_{\mathrm{F}})$. Together with $k_{\mathrm{F}} = \sqrt{n\pi}$ (equation 2.18) one can rewrite equation 7.6 to:

$$T \sim \frac{2v_{\mathrm{F}}\hbar^3}{W d_{\mathrm{n}} k_{\mathrm{B}} e^2 B^2}\sqrt{n^3\pi^5}. \tag{7.7}$$

The vanishing of the red magnetoconductance oscillations with increasing charge carrier doping, which is plotted in Fig. 7.6c (red, dashed line), is in good agreement with what is expected for snake states according to equation 7.7.

7.3.2. Orange magnetoconductance oscillations

From all the observed magnetoconductance oscillations the orange ones occur at the highest filling factors starting at roughly $|\nu| \sim 6$ and persisting up to $|\nu| = 20$ or even higher, as shown in Fig. 7.2/Fig. 7.3. This corresponds to an occupation of at least two edge states ($|\nu| = 0$ and $|\nu| = 4$) without taking a possible degeneracy lifting into account. Similar to the red magnetoconductance oscillations, the gate spacing between neighbouring peaks (ΔV_{BG} ~0.4 V to 0.7 V at B =4 T) is roughly two orders of magnitudes larger than what is expected if the underlying physics were based on charging effects. We note that even though the orange magnetoconductance oscillations occur in the most classical regime (highest filling factors), the Landau levels remain well developed in the bulk of graphene down to B ~2 T (not shown here).

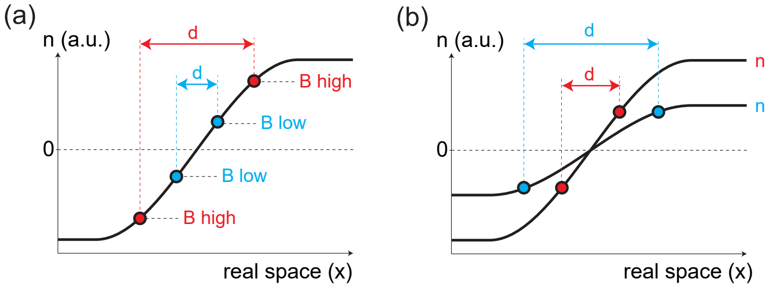

Figure 7.8. Edge state spacing d as a function of magnetic field and the slope of the p-n junction. a, Spacing for a fixed p-n junction density profile by varying the magnetic field. **b,** Spacing for a fixed magnetic field for different p-n junction density profiles. Figure adapted from Ref. [46].

In an Aharanov-Bohm interferometer, the magnetic field spacing ΔB between neighbouring conductance peaks is given by:

$$\Delta B = \frac{h}{e}\frac{1}{A}. \tag{7.8}$$

By considering the width of the sample W, the physical spacing (d) between the edge states is given by:

$$d = \frac{\Phi_0}{\Delta B \cdot W}. \tag{7.9}$$

In the experiments ΔB is not exactly constant because the real-space positions of the edge states, which define A, varies as a function of magnetic field and the p-n junctions density profile as illustrated in Fig. 7.8 [46]. By considering a linear charge carrier density profile across the p-n junction, ΔB decreases linearly with increasing B. This is in good agreement with what was measured in Fig. 7.5e,f, indicated with the black, dashed line, therefore likely suggesting an Aharanov-Bohm type of interference. Even though multiple areas might be enclosed between the various edge states, only one Aharanov-Bohm interferences will dominate as explained previously and sketched in Fig. 7.1b. Using equation 7.9 the magnetic field spacing of the orange magnetoconductance oscillations (Fig. 7.5e) was converted into a distance ranging from $d{\sim}30\,\mathrm{nm}$ at $B{\sim}2\,\mathrm{T}$ to $d{\sim}55\,\mathrm{nm}$ at $B{\sim}5.5\,\mathrm{T}$. The decreasing oscillation amplitude (ΔG_{osc}) with increasing magnetic field (Fig. 7.4b) directly indicates the vanishing coupling between edge states as they move further apart from each other at higher magnetic fields.

Next we calculate the gate-gate dependence of the Aharanov-Bohm interference. For this we start with the electrostatic density profile (as shown in

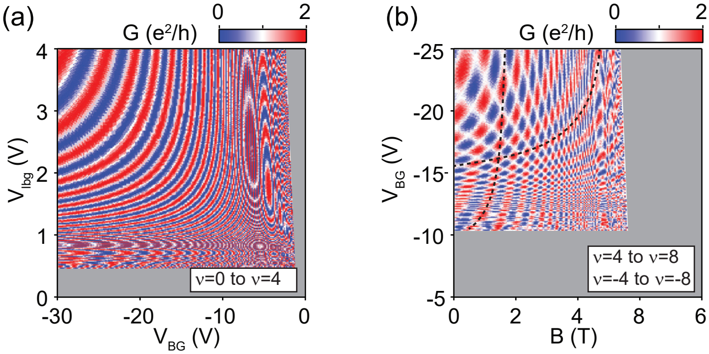

Figure 7.9. Aharanov-Bohm interference at B = 2 T. a, Calculation of the magnetoconductance between the edge states with $\nu = 0$ and $\nu = 4$ according to equation 7.3 as a function of the global back-gate and local bottom-gate. At low doping $\nu = 4$ is not populated (shaded in gray). **b,** Incoherent superposition of two Aharanov-Bohm interferences.

Fig. 7.7a), from which one can identify the spacing d between two edge state for any set of (V_{BG},V_{lbg}) within the gate-gate map. The magnetoconductance oscillation can then be calculate according to equation 7.3, leading to a roughly hyperbolic trend as a function of the two gates (at fixed magnetic field) as shown in Fig. 7.9a. The two sets of the orange oscillations can be reproduced with a double Aharanov-Bohm interferometer as sketched in Fig. 7.1b, where the conductance oscillations arising from the interferometers on the left (e.g. $\nu = 0$ and $\nu = \pm 4$) and right (e.g. $\nu = 0$ and $\nu = \mp 4$) side are added up incoherently as shown in Fig. 7.9b. The two sets of orange magnetoconductance oscillations are slightly shifted in doping with respect to each other because each of the two gates tunes one side of the p-n junction more effectively. Furthermore, measuring a linecut as a function of magnetic field reveals a roughly parabolic trend (not shown here). These findings are in good agreement with the measurements which are shown in Fig. 7.2/Fig. 7.3 and Fig. 7.4a,b respectively.

In interference experiments which depend on phase coherent transport, a vanishing of the oscillation patter with temperature can have different origins such as for example a loss of phase coherence due to enhanced scattierng events. As soon as $l_\Phi < L$, where l_Φ is the phase coherence length and L is the total path length, the interference pattern is completely lost. However, the interference can as well be lost at finite temperatures even if $l_\Phi > L$, if the interfering paths have different lengths ($\Delta L \neq 0$) as discussed in section 2.3.3 (see equation 2.46). Since for the Aharanov-Bohm interference along a graphene *p*-*n* junction ΔL is ideally zero (see Fig. 7.1b,c) or very small, this effect is negligible. Consequently the loss of the interference signal with increasing temperature depends on the decrease of l_Φ, which depends only weakly on the charge carrier doping [222] , which is shown in Fig. 7.6c.

7.3.3. Cyan magnetoconductance oscillations

The cyan magnetoconductance oscillations were observed at the lowest filling factors as low as $|\nu| \sim 2$ or even below and above B ~4 T as shown in Fig. 7.2/Fig. 7.3. Since full degeneracy lifting of the lowest Landau level (valley and spin) is observed for B >5 T, the edge states are spin and valley polarized. While the spin degree of freedom is conserved along the edges of graphene and along the *p*-*n* junction [218], the valley degree of freedom is only conserved along the *p*-*n* junction. Mixing between the edge states of the lowest Landau levels having equal spin is consequently prohibited along the *p*-*n* junction, but possible at the graphene edges. Comparable to the orange magnetoconductance oscillations, the magnetic field spacing of the cyan oscillations (extracted using equation 7.9) decreases monotonically, corresponding to an edge state spacing of d ~9 nm at B =4.5 T to d ~15 nm at B =8 T. These values were compared with the edge state spacing deduced from electrostatic simulations. Assuming that at the lowest filling factors the interference occurs between the spin-polarized edge states ($\Delta\nu = 2$) the spacing evolves from d ~22 nm at B =4.5 T to d ~38 nm at B =8 T. The discrepancy between experiment and calculation might have the following reasons: i) The real-space position of the edge states is deduced from a charge carrier density profile which is calculated at zero magnetic field as mentioned previously. However, one would have to take the self-consistent density profile at finite magnetic field into account [223]. ii) The edge states might be located at a charge carrier density which deviates slightly from the theoretically expected values of equation 2.30 [46, 72, 224]. The above mentioned effects might both account for the observed discrepancy by a factor of ∼ 2 between the values extracted experimentally and from our simple theoretical model.

The oscillation amplitude of the cyan magnetoconductance oscillation shown in Fig. 7.4c was rather constant with magnetic field including some irregularities. We note that the cyan magnetoconductance oscillations are predominantly visible at a charge carrier doping of $n_{\mathrm{BG}} \sim n_{\mathrm{lbg}}$ (Fig. 7.2/Fig. 7.3) for reasons which are unknown yet. Similar to the orange magnetoconductance oscillations, the temperature dependence of the cyan ones depends only slightly on the charge carrier density.

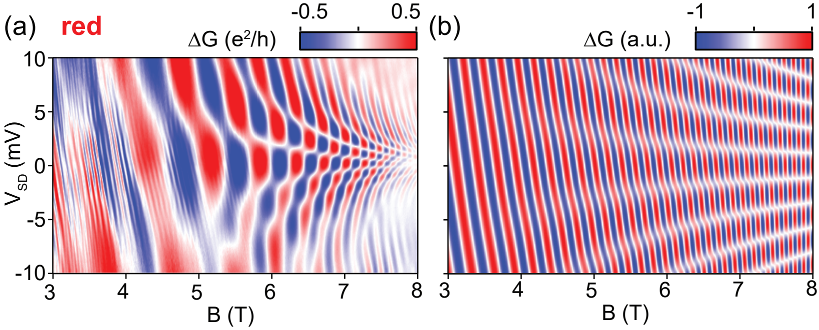

Figure 7.10. Bias spectroscopy of snake states. a Measurement of the red magnetoconductance oscillations as a function of bias and magnetic field where a smooth background was subtracted. Gate voltage remains fixed and is given as indicated in Fig. 7.2 with the yellow star. **b,** Simulation following equation 7.14 with the coefficients as given in 7.13. Parameters used: W =1.5 µm, d_n =100 nm, k_F corresponding to $n \sim 1.7 \times 10^{12}\,\mathrm{cm}^{-2}$.

7.4. Bias spectroscopy

Bias spectroscopy reveals information on how physical effects react under non-equilibrium conditions. In the following we show the measurements of the different magnetoconductance oscillations as a function of magnetic field and DC-bias while keeping the charge carrier densities fixed. The bias was applied asymmetrically at the source, while the drain remained grounded as sketched in Fig. 4.9.

7.4.1. Experiments

The red magnetoconductance oscillations which is attributed to snake states reveals features which are converging from a tilted pattern at lower magnetic field into a checker-board pattern at high magnetic field as shown in Fig. 7.10a. At high magnetic field the visibility of the checker-board pattern decreases with increasing V_SD while a similar behaviour is absent (within the applied bias range of ±10 mV) for the tilted pattern. The orange and cyan magnetoconductance oscillations, which are shown in Fig. 7.11a,c are attributed to Aharanov-Bohm interferences, both revealing a tilted pattern within the measured magnetic field range. The bias dependence of the orange oscillations persists to ±10 mV, while the bias dependence of the cyan oscillations vanishes around roughly ±2 mV. This seems to be roughly proportional to the oscillation amplitude, which is with ΔG_osc(cyan) $\sim 0.07\,\mathrm{e}^2/\mathrm{h}$ a factor

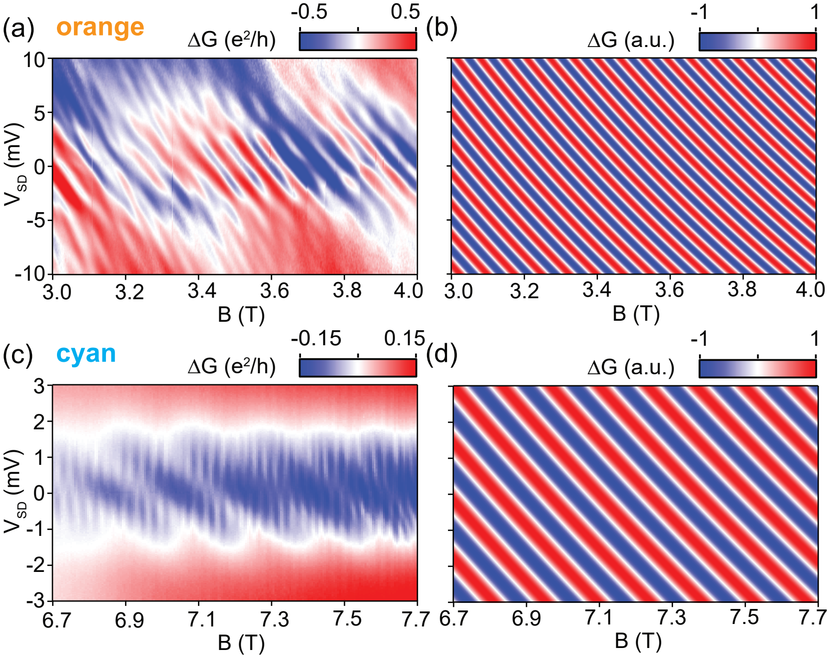

Figure 7.11. Bias spectroscopy of Aharanov-Bohm oscillations. a,c, Measurement of the orange and cyan magnetoconductance oscillations as a function of bias and magnetic field where a smooth background was subtracted. Gate voltage remain fixed and are given as indicated in Fig. 7.2 with the yellow (orange oscillation) and green (cyan oscillation) star. **b,d,** Simulations following equation 7.14 with the coefficients as given in 7.18. Here a bias dependent gating effect is considered using α =0.32 nm/meV$_{\mathrm{SD}}$ (orange oscillation) or α =0.25 nm/meV$_{\mathrm{SD}}$ (cyan oscillations), while a renormalization of the edge state velocity is neglected ($\beta = 1$). Further parameters used are W =1.5 µm, k_{F} corresponding to n ∼1.7 × $10^{12}\,\mathrm{cm}^{-2}$ and d =40 nm (orange oscillations) or n ∼0.8 × $10^{12}\,\mathrm{cm}^{-2}$ and d =20 nm (cyan oscillations).

of 6 smaller compared to the orange magnetoconductance oscillations, where ΔG_{osc}(orange) ∼0.45 e^2/h. In Fig. 7.11c an additional magnetoconductance oscillations with a narrow spacing of roughly ΔB ∼4 mT to 6 mT can be observed. These oscillations will be briefly discussed at the end of the chapter.

7.4.2. Simulations

In order to gain more insight to the physical origin of the different patterns seen in Fig. 7.10a and Fig. 7.11a,c we calculate the bias dependence for two different scenarios, namely the snake state model as given in equation 7.2 and an Aharonov-Bohm interference between edge states moving around an area [46] as given in equation 7.3. A charging effect for edge states which are moving around a charge carrier island [225, 226] can be excluded, as discussed previously.

Upon applying a bias to a conductance, which is defined at a specific energy by $G(E)$, the total current is the result of the integration of $G(E)$ over the bias-window according to:

$$I \sim \int_{-a(eV)}^{(1-a)(eV)} G(E)dE \tag{7.10}$$

where the parameter a $(0 < a < 1)$ defines the bias-window and eV is the corresponding energy to the applied bias. In the following we suppose that the bias drops predominantly over the p-n junction. In this case the measured conductance is given by $G \sim dI/dV$.

Snake state interference

By replacing λ_S in equation 7.2 with equation 7.1, and using $\hbar k = \hbar k_\mathrm{F} + E/v_\mathrm{F}$ ($\hbar k_\mathrm{F}$ is set by the electrostatic gates, E/v_F is set by the applied bias and E is measured with respect to E_F), equation 7.2 can be rewritten as:

$$G(E) \sim \cos\left[\frac{We^2 d_\mathrm{n} B^2}{2(\hbar k_\mathrm{F})^2}\left(1 + \frac{E}{\hbar k_\mathrm{F} v_\mathrm{F}}\right)^{-2}\right]. \tag{7.11}$$

Assuming $E \ll \hbar k_\mathrm{F} v_\mathrm{F}$, which is reasonable for the applied bias, the Taylor-expansion $1/(1+x)^2 \sim 1 - 2x$ can be used leading to:

$$G(E) \sim \cos\left[\frac{We^2 d_\mathrm{n} B^2}{2(\hbar k_\mathrm{F})^2} - \frac{We^2 d_\mathrm{n} B^2}{(\hbar k_\mathrm{F})^3 v_\mathrm{F}} E\right], \tag{7.12}$$

where we substitute:

$$b \equiv \frac{We^2 d_\mathrm{n}}{2(\hbar k_\mathrm{F})^2} B^2 \qquad \text{and} \qquad c \equiv \frac{We^2 d_\mathrm{n}}{(\hbar k_\mathrm{F})^3 v_\mathrm{F}} B^2. \tag{7.13}$$

Upon applying a finite bias (equation 7.10), the measured conductance is given by:

$$\begin{aligned} G \sim \Big\{ &(1-a)\cos\big[(1-a)\cdot eV \cdot c - b\big] \\ &+ a \cdot \cos\big[a \cdot eV \cdot c + b\big]\Big\}. \end{aligned} \tag{7.14}$$

In the case of a fully asymmetric biasing (e.g. $a = 1$), equation 7.14 simplifies to:

$$G \sim \cos\Big(eV \cdot c + b\Big) \tag{7.15}$$

reproducing the tilted pattern which is shown in Fig. 7.10b at low magnetic field. On the other hand, for the case of completely symmetric biasing ($a = 0.5$) equation 7.14 simplifies to:

$$G \sim \cos\Big(b\Big) \cdot \cos\Big(eV \cdot c\Big) \tag{7.16}$$

which leads to the checker-board pattern which is shown in Fig. 7.10b at high magnetic field. The checker-board pattern is in agreement with previous studies [46] where a similar behaviour was observed. Comparable to the experiment (Fig. 7.10a), the oscillation period decreases as well with increasing magnetic field in the simulation (Fig. 7.10b). In order to reproduce the transition from tilted (asymmetric biasing, equation 7.15) to checker-board pattern (symmetric biasing, equation 7.16), the parameter a was varied linearly from $1 \rightarrow 0.5$ by going from low to high magnetic field. While the increasing magnetic field seems to be responsible for the transition from $a = 1$ to $a = 0.5$, the precise reason remains unknown so far. We speculate that it might be related to the capacitances in the system, such as the capacitance related to the insulating region with $\nu = 0$ or the quantum capacitance from the bulk. The latter is directly proportional to the DOS [53, 227] and thus changes significantly upon tuning the Fermi energy from a Landau level into a Landau level gap. In contrast to the simulation, the checker-board pattern in the experiment vanishes upon increasing the bias. This was attributed to a dephasing rate of the charge carriers being proportional to the bias-energy [219, 220, 228–230]. However, this does not seem to apply for the tilted pattern, which persists up to $V_{\mathrm{SD}} = \pm 10\,\mathrm{mV}$.

Aharanov-Bohm interference

Next we calculate the the bias dependence for an Aharonov-Bohm interferometer. Starting from equation 7.3 the magnetoconductance oscillations of a slightly modified model is given by:

$$G(E) \sim \cos\left[2\pi \frac{W \cdot (d + \alpha E) \cdot B}{\Phi_0} + k\Delta L\right]. \tag{7.17}$$

Here the parameter α is a phenomenological parameter in order to account for a bias dependent gating effect [94]. For simplicity the edge state spacing d is modified proportional to the applied bias. The factor $k\Delta L$ in equation 7.17 accounts for a possible path-difference between the edge states, where k is replaced by $k = k_{\mathrm{F}} + E/(\hbar v_{\mathrm{F}} \beta)$. The parameter β ($0 \leq \beta \leq 1$) was introduced to account for the renormalized edge state velocity compared to the Fermi velocity [231]. Solving the bias-dependence for equation 7.17 leads again to equation 7.14, however the coefficients b and c are now given by:

$$b \equiv \frac{2\pi W d}{\Phi_0} B + k_{\mathrm{F}} \Delta L \qquad \text{and} \qquad c \equiv \frac{\Delta L}{\hbar v_{\mathrm{F}} \beta} - \frac{2\pi W \alpha}{\Phi_0} B. \tag{7.18}$$

By choosing realistic values for the path-difference ($\Delta L \sim 20\,\mathrm{nm}$), using $\alpha = 0$ and $\beta = 1$, the magnetoconductance oscillations reveal no bias dependence (not shown). Since both, α and β contribute to a bias dependent phase, we will analyse the two separately.

- **Bias dependent gating effect ($\alpha > 0$ while $\beta = 1$):**
  In order to increase the total flux by one flux-quantum, the edge state spacing d has to increase by $\Delta d = \Phi_0/(B \cdot W)$ while keeping the magnetic field fixed. This leads to values of $\Delta d \sim 0.79\,\mathrm{nm}$ at $B \sim 3.5\,\mathrm{T}$ (orange) and $\Delta d \sim 0.38\,\mathrm{nm}$ at $B \sim 7.2\,\mathrm{T}$ (cyan). Assuming that the applied bias affects the edge state spacing according to $\Delta d = \alpha \cdot \mathrm{eV}_{\mathrm{SD}}$, then α can be extracted from the bias spacing in Fig. 7.11a,c. This leads to values of $\alpha \sim 0.32\,\mathrm{nm/meV_{SD}}$ and $\alpha \sim 0.25\,\mathrm{nm/meV_{SD}}$ for the orange and cyan oscillations respectively (which is plotted as well in Fig. 7.11b,d). The additional doping coming from the biasing will change the electrostatic profile. In a simple estimate, we keep the width of the p-n junction fixed ($d_{\mathrm{n}} = \mathrm{const.}$) and account for the bias induced doping, which leads to a change of the slope (see appendix C for more details). From this simple model we obtain values in the order of $\alpha \sim 0.09\,\mathrm{nm/meV_{SD}}$ to $0.18\,\mathrm{nm/meV_{SD}}$ for the cyan magnetoconductance oscillations.

- **Renormalized edge state velocity ($\beta < 1$ while $\alpha = 0$):**
  In order to reproduce Fig. 7.11a,b by taking exclusively a renormalized edge state velocity into account leads to values of $\beta \geq 0.012$ (orange) and $\beta \geq 0.007$ (cyan) (using $\Delta L \leq 20\,\mathrm{nm}$). Even though for β all values between zero and one are possible, we suspect that a renormalized edge state velocity in the order of $\sim 1\,\%$ of v_{F} is too small.

Therefore we could imagine that the tilted pattern in Fig. 7.11a,c results mostly from the gating effect, but also the decreased edge state velocity can play a role.

7.5. Quantum transport simulations

To complement our measurements, we additionally performed quantum transport calculations based on scaled graphene [232] using the realistic device geometry. These calculations were able to reproduce the red and orange magnetoconductance oscillations. For the calculations electron-electron interaction were not taken into account, which explains the absence of the cyan magnetoconductance oscillations (which requires the formation of a $\nu = 0$ region). In Fig. 7.12a the conductance is shown as a function of the local bottom-gate and the global back-gate at $B = 3\,\mathrm{T}$ within the bipolar regime. Comparable to the measurements presented in Fig. 7.2, two sets of orange magnetoconductance oscillations can be seen which are shifted in doping. In Fig. 7.12b the evolution of the red and orange oscillations are shown as a function of gate and magnetic field. The calculations show that the orange magnetoconductance oscillations seen in the experiments can be reproduced without the splitting of the lowest Landau level.

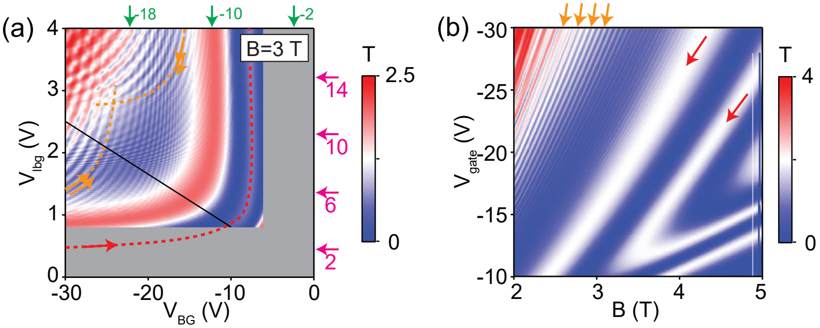

Figure 7.12. Quantum transport calculations. a, Transmission function (T) of charge carriers though the p-n junction as a function of a local bottom-gate and a global back-gate. Red and orange magnetoconductance oscillations are indicated with the dashed lines/arrows. Filling factors of the global back-gate and the local bottom-gate are indicated with the green/purple arrows. Low doping values (shaded in grey) were omitted to reduce the computational load. **b,** Linecut as indicated in (a) with the black line as a function of magnetic field.

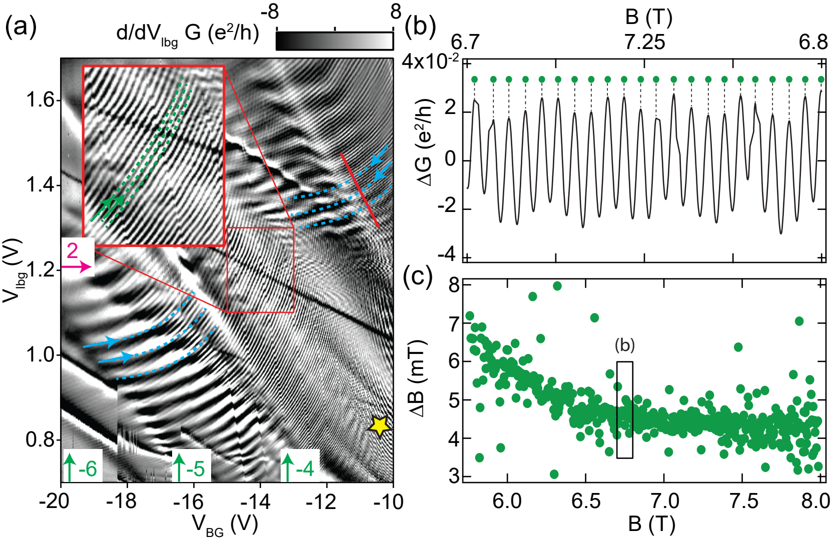

Figure 7.13. Additional magnetoconductance oscillation at high magnetic field. a, Numerical derivative of the conductance as a function of the global back- and local bottom-gate at B =8 T where two additional sets of fine oscillation can be seen, indicated with the green, dashed line. **b,** Net oscillation of the conductance ΔG as a function of magnetic field within a limited field range. The peak-positions are indicated with the green dots. **c,** Magnetic field spacing (ΔB) extracted from (b).

7.6. Additional magnetoconductance oscillations at high magnetic field

We now briefly describe and discuss the characteristics of the additional set of magnetoconductance oscillations which was observed already in Fig. 7.11c. From now on we will label this set of magnetoconductance oscillations with green. In Fig. 7.13a the gate-gate dependence of the green magnetoconductance oscillation is shown in the bipolar regime, revealing a gate spacing within the measured gate range from V_{BG} ∼40 mV at lower doping up to V_{BG} ∼150 mV at higher doping. In Fig. 7.13b the magnetic field dependence at a fixed gate-gate configuration, as indicated in Fig. 7.13a with the yellow star, is shown. From the latter a magnetic field spacing of ΔB =6 mT at B =5.8 T to ΔB =4 mT at B =8 T was extracted as shown in Fig. 7.13c. However, the magnetic field spacing of the second set of green magnetocon-

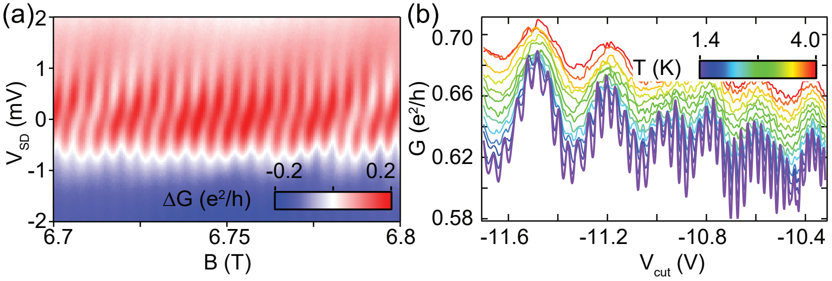

Figure 7.14. Bias and temperature dependence of the green magnetoconductance oscillations. a, Magnetoconductance oscillations as a function of bias and magnetic field where a smooth background was subtracted. The gate voltage remains fixed as indicated in Fig. 7.13a with the yellow star). **b,** Temperature dependence of the green magnetoconductance oscillation as indicated in Fig. 7.13a with the red line.

ductance oscillations, which is not shown here, yields different values ranging from ΔB =25 mT at B =6 T to ΔB ∼10 mT at B =8 T. The bias and temperature dependences are furthermore shown in Fig. 7.14 where a vanishing of the green magnetoconductance oscillations is seen around V_{SD} ∼±1 mV and T ∼2 K to 3 K.

From the narrow gate spacing we first suspected that the green magnetoconductance oscillations originate from a charging effect as illustrated in Fig. 7.15 [225]. In the latter a combination of edge states and charge carrier island co-exist in the device. Hopping of charge carrier from the edge states into the charge carrier island (or vice versa) is indicated in Fig. 7.15a with the black, dashed arrows. Such systems have been investigated in 2DEG Fabry-Pérot interferometers [226, 230]. The charging model could explain two different values of the magnetic field spacing for each set of the green magnetoconductance oscillations (while enclosing the same area A). This is because for the charging effect the magnetic field spacing ΔB depends on many parameters which can vary on the two sides of the p-n junction. As derived in Ref. [225] the magnetoconductance oscillation for the charging model is given by:

$$G \sim \cos\left[-2\pi\frac{\Phi}{\Phi_0} + 2\pi\frac{\Delta_{\mathrm{X}}}{\Delta}\left(\tilde{\nu}\frac{\Phi}{\Phi_0} + N - N_{\mathrm{gate}}\right)\right], \qquad (7.19)$$

where Φ and Φ_0 correspond to the magnetic flux though the area A and the magnetic flux quantum respectively, Δ_{X} describes the coupling energy for one extra electron on the island, Δ is the level spacing, $\tilde{\nu}$ is the number of completely filled edge states (integer part of equation 2.30), and N and N_{gate}

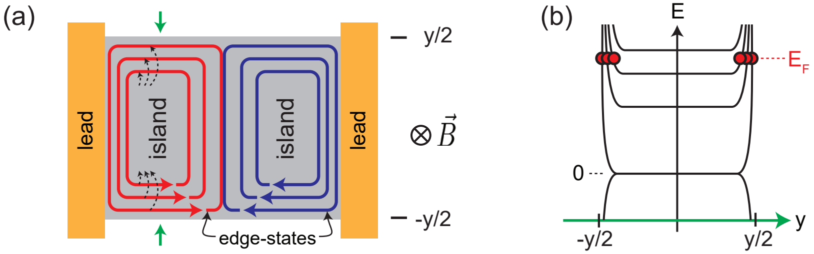

Figure 7.15. Charging effects in a graphene *p*-*n* junction at finite magnetic field. a, Formation of a charge carrier island which is capacitively coupled to the edge states (red/blue lines). **b,** Energy dispersion along a linecut as indicated in (a) with the green arrows. The edge states are indicated with the red dots.

give the number of charges on the island and attracted by the electrostatic gate. While the values of $\tilde{\nu}$ and $\Delta = 2\pi\hbar v_F/L$ [225], where L is the total interference path surrounding the island, are known, we do not have any knowledge of Δ_X. Equation 7.19 might explain the different magnetic field spacings. However the gate spacing does not match a charge carrier model where we would expect values of ΔV_{BG} (and ΔV_{lbg}) which are at least one order of magnitude smaller than what was measured. The green magnetoconductance oscillations are furthermore not parallel with respect to the charge neutrality lines of the left and right side of the *p*-*n* junction. This we would naively expect for a charging effect where each cavity is predominantly tuned by one of the two gates. A possible explanation might be the shift of the *p*-*n* junction position (see section 6.1.2), which depends on V_{BG} and V_{lbg}, consequently changing the area of the two cavities.

Note that the formation of a charge carrier island requires edge channels which are weakly coupled to the leads. However, our system is more likely in the strong coupling regime. This assumption is based on the observation of integer quantum Hall plateaus which are well developed throughout the whole unipolar regime (not shown here). If the edge states were weakly coupled to the leads one could measure fractional values of the quantum Hall plateaus in parts of the unipolar regime [134, 140], similar to what is shown Fig. 2.18b,c.

Even though the charging model does not fit the experiments in various points, an Aharanov-Bohm oscillation cannot explain the green magnetoconductance oscillations either. This is because the resulting edge state spacing extracted from the two sets would be very different, namely ~700 nm and ~150 nm. This contradicts the device geometry where the two cavities have roughly the same dimensions. To resolve these inconsistencies further studies will be needed.

7.7. Conclusion

In conclusion, we presented measurements on three sets of magnetoconductance oscillations which can be observed along a graphene *p-n* junction. From the gate-gate map at a fixed magnetic field alone it is challenging to properly assign the different magnetoconductance oscillations to their corresponding origin as most of them follow a similar, hyperbolic trend. We showed that by additionally analysing the magnetic field, temperature and bias dependence the different magnetoconductance oscillations can be consistently assigned to the two concepts of classical snake states and Aharanov-Bohm interferences. The magnetoconductance oscillations labelled with red, being present at intermediate filling factors, are best explained using a classical snake state model, while the magnetoconductance oscillations labelled with orange and cyan are best explained using an Aharanov-Bohm interference model. So far we always discussed the snake states and the Aharanov-Bohm interference independently, using either the picture of classical skipping trajectories or quantum Hall edge states - two models which seem to be based on different physical concepts. However, triggered by the co-existance of these two effects within our measurements, we now motivate why both models are compatible with each other. In *p-n* junctions the presence of an electric field mixes the Landau levels of the bulk (no electric field), and new states are formed from combination of the Landau level wavefunctions (obtained without E-field). In Ref. [231] it has been shown, that the lowest mode has similar weight on both sides of a *p-n* junction, mimicking classical snake states. Moreover, the edge state velocity obtained for this mode is in good agreement with the classical snake state velocity. Such a mixing can be naively describe as a coherent oscillation between the edge channels with the cyclotron frequency, since the edge channel wavefunctions (original Landau level wavefunctions) are not eigenstates of the *p-n* junction (similarly to Rabi-oscillations in qubits). In our case, the situation is a bit more complex compared to the one described in Ref. [231] since in real devices it is the slope of the charge carrier density which is (roughly) constant across the *p-n* junction, and consequently the electric field depends on the distance from the center of the *p-n* junction, which makes the quantitative analysis very challenging.

Finally, the orange magnetoconductance oscillations can be reproduced nearly perfectly using quantum transport simulations (where no Zeeman-term was included in the Hamiltonian). This makes us confident to exclude partial or full degeneracy lifting of the lowest Landau level in order to explain the latter. For the same reason the cyan magnetoconductance oscillations remain absent in the quantum transport simulations.

Further studies might focus on the origin of the green magnetoconductance oscillations, or discuss the origin of the transition between tilted and checkerboard pattern in the bias-dependence of the snake states.

8

Giant valley-isospin conductance oscillations in ballistic graphene

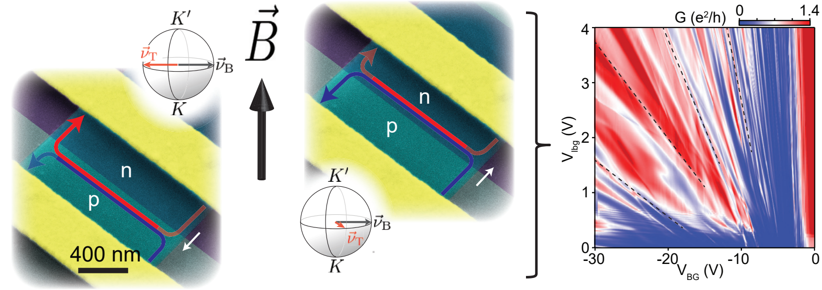

At high magnetic fields the conductance of graphene is governed by the half-integer quantum Hall effect [12, 13]. By local electrostatic gating a *p*-*n* junction perpendicular to the graphene edges can be formed, along which quantum Hall channels co-propagate [74, 134]. It has been predicted that if only the lowest Landau level (LLL) is filled on both sides of the *p*-*n* junction, the conductance is determined by the valley (isospin) polarization at the edges and by the width of the flake [45]. This effect remained hidden so far due to scattering between the channels co-propagating along the *p*-*n* junction (equilibration). Here we investigate *p*-*n* junctions in encapsulated graphene [1] with a movable *p*-*n* junction [233, 234] with which we are able to probe the edge configuration of graphene flakes. We observe large quantum conductance oscillations on the order of e^2/h which solely depend on the *p*-*n* junction position providing the first signature of isospin-defined conductance. Our experiments are underlined by quantum transport calculations.

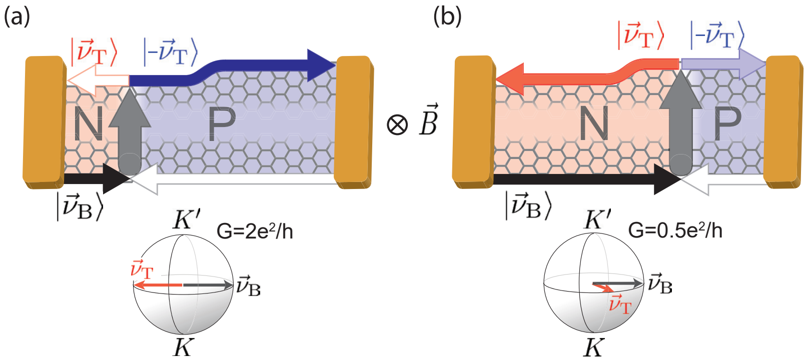

Figure 8.1. Valley-isospin-dependent conductance of a (simplfied) two-terminal *p*-*n* junction at high magnetic fields. a, Charge carriers are injected to the bottom-edge and guided along the *p*-*n* junction to the top-edge. If at the position of the *p*-*n* junction the relative angle between the valley-isospins at the two edges (same polarity) is equal to π, back-reflection is forbidden. The valley-isospin configuration for bottom- (black, $\vec{\nu}_\mathrm{B}$) and top-edge (red, $\vec{\nu}_\mathrm{T}$) is illustrated on the bottom. **b,** By moving the *p*-*n* junction to a region of the flake with a different width, the relative angle between $\vec{\nu}_\mathrm{B}$ and $\vec{\nu}_\mathrm{T}$, which is denoted by Φ, can change. For $\Phi \neq \pi$ a nonzero back-reflection is allowed. In the experiment multiple steps are present.

8.1. Concept to measure the valley-isospin

The working-principle of a valley-valve based on the idea of Tworzydło et *al.* [45] was introduced in section 2.5.2 and is summarized (for an armchair GNR) in Fig. 2.17. We recapitulate that the proposal of Ref. [45] suggests a two-terminal GNR (armchair or zigzag) with a fixed number of unit cells (N) between bottom- and top-edge which determines the width of the GNR, and a *p*-*n* junction which is located perpendicular to the transport direction. If only the LLL is occupied, the conductance is exclusively determined by the width and the chirality of the GNR in the vicinity of the *p*-*n* junction. It has been shown in Ref. [45] and section 2.5.2 that the conductance through a perfect armchair GNR is given by [45]:

$$G = \frac{e^2}{h} \left(1 - \cos \Phi\right), \tag{8.1}$$

where Φ denotes the relative angle between the two valley-isospin configurations at the bottom- ($\vec{\nu}_\mathrm{B}$) and top-edge ($\vec{\nu}_\mathrm{T}$) for the same polarity. The conductance can take the values 0.5 e^2/h or 2 e^2/h for armchair GNRs (equation 2.54) and 0 or 2 e^2/h for zigzag GNRs (equation 2.55). Even though considerable effort has been invested on theoretical studies [45, 235–237], an experimental proof remains missing. The latter can be attributed to the need of very clean samples where the valley-isospin information is preserved along the p-n junction (section 2.5.2) and the fact that the control over the edge structure in top-down[1] fabricated devices remained rather limited so far.

Here we combine a position-tunable p-n junctions with nonuniform edges in a ballistic device. The idea of our experiment is illustrated in Fig. 8.1, where an ideal armchair GNR with its width changing only at a single position is sketched. The valley-isospin configuration of the bottom- and top-edge in the vicinity of the p-n junction (valley-polarized along $\vec{\nu}_{\mathrm{B}}$ and $\vec{\nu}_T$ respectively, plotted at the same polarity of the junction) is shown for two different situations. Depending on the exact position of the p-n junction, which can be shifted as a function of electrostatic gate voltages [234], the edge polarization $\vec{\nu}_{\mathrm{T}}$ varies (while $\vec{\nu}_{\mathrm{B}}$ remains fixed), resulting in a different conductance as shown in Fig. 8.1a and Fig. 8.1b. By moving the p-n junction we are able to locally probe the valley-isospin configurations at different positions of the edge. We report on conductance oscillations appearing in the presence of a p-n junction and in the regime of the LLL. The oscillating conductance is observed to depend on the position of the p-n junction and agrees with quantum transport simulations. In contrast to former studies of diffusive, two-terminal p-n junctions in graphene [135], where the conductance is dominated by mode mixing [134], we enter a novel regime where the conductance is dominated by valley-isospin physics. Surprisingly, even though our samples have rough edges the conductance oscillations are still large in the order of e^2/h.

8.2. Setup and basic characterization

The same type of two-terminal p-n junction as introduced in chapter 7 was used as well in this chapter ($\mu\sim 80\,000\,\mathrm{cm}^2\mathrm{V}^{-1}\mathrm{s}^{-1}$). The position of the p-n junction (x_{pn}) is adjustable due to capacitive crosstalk of the gates and the ratio of $n_{\mathrm{lbg}}/n_{\mathrm{BG}}$ [233, 234], where n_{lbg} (n_{BG}) is the charge carrier density tuned by the local bottom-gate (global back-gate). With the above given device geometry, the potential profile of the p-n junction is well within the smooth limit with respect to the length scale of the lattice constant[2], a basic requirement to observe the valley-isospin dependent oscillations [45]. The devices show clear signs of ballistic transport, namely Fabry-Pérot resonances [39–44, 234]

---

[1] Even though two-terminal field-effect transistors based on bottom-up synthesized GNRs with a very controllable width and chirality [132] were reported recently [238], the combination of the latter with a p-n junction is even more challenging and has not been demonstrated so far.

[2] These information we extracted from electrostatic simulations which are not shown here.

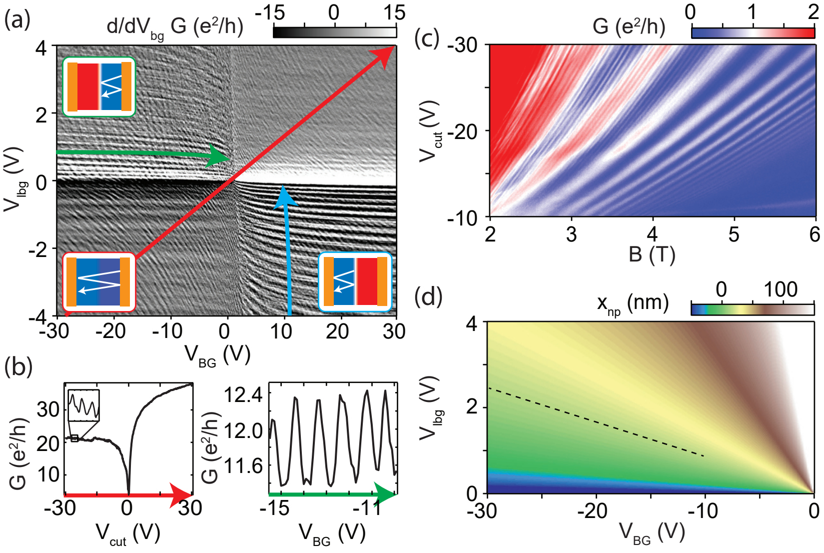

Figure 8.2. Signatures of ballistic and phase coherent transport. a, Numerical derivative of the conductance as a function of global back-gate (V_{BG}) and local bottom-gate (V_{lbg}) at zero magnetic field where Fabry-Pérot resonances are visible (indicated with the red, blue and green arrows respectively). **b,** Representative linecuts within a (restricted) gate range for two types of Fabry-Pérot resonances as indicated in (a). **c,** Magnetoconductance oscillations along the *pn*-junction as discussed in chapter 7. **d,** Simulated *p*-*n* junction position x_{pn} as a function of V_{BG} and V_{lbg}. $G(V_{\mathrm{cut}}, B)$ in (c) was measured along the linecut indicated with the black, dashed line.

(Fig. 8.2a,b) and snake states [37, 38] (Fig. 8.2c), which prove the absence of intervalley scattering within the bulk of graphene. A detailed description of the snake states can be found in chapter 7 and in Refs. [36–38, 217]. An electrostatic simulation of x_{pn} as a function of V_{BG} and V_{lbg} is shown in Fig. 8.2d, where lines of a constant x_{pn} are fanning out linearly from the global charge neutrality point (CNP).

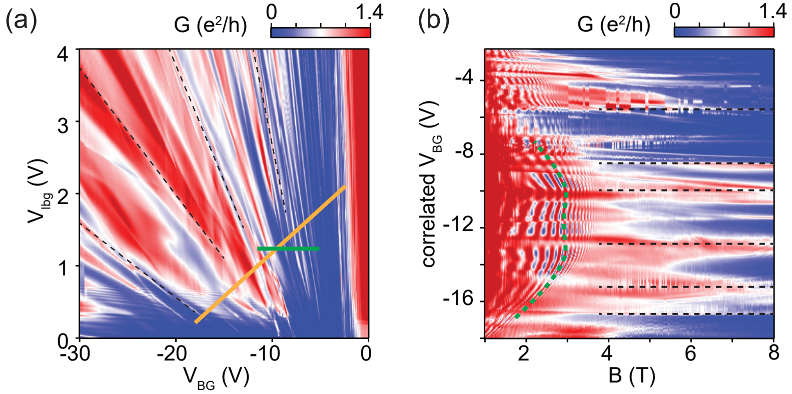

Figure 8.3. Conductance as a function of the gates and magnetic field. a, Conductance as a function of global back-gate (V_{BG}) and local bottom-gate (V_{lbg}) at $B = 8\,\mathrm{T}$. The valley-isospin oscillations emerge as radial fringes converging to the common CNP. The black, dashed lines are a guide to the eye showing the oscillation maximum for selected valley-isospin oscillations. **b,** Linecut as indicated with the orange line in (a) as a function of magnetic field. The x_{pn} dependent conductance oscillations are independent of magnetic field, and persist down to fields of roughly $B = 2\,\mathrm{T}$. For magnetic fields below $B{\sim}3\,\mathrm{T}$ snake states (chapter 7) appear as curved features indicated with the green, dashed line.

8.3. Measurements

8.3.1. Gate and field dependent measurements

We now concentrate on the regime of small filling factors. Features appearing at higher filling factors are discussed in chapter 7. A conductance map at $B = 8\,\mathrm{T}$ is shown in Fig. 8.3a as a function of the two gate voltages in the bipolar regime. Most prominent are the conductance oscillations on the order of e^2/h, fanning out linearly from the common CNP. The linear dependence on the two gates implies that the conductance is determined by the position of the *p*-*n* junction (see Fig. 8.2d). In Fig. 8.3b a linecut (orange line in Fig. 8.3a) is shown as a function of B. By tuning the gates, x_{pn} can be shifted by several tens of nanometers. The conductance oscillation fringes (dashed, black lines) remain mostly unchanged (horizontal) over a large range of B and thus depend only on x_{pn}. With decreasing magnetic field the oscillation peaks become wider and remain visible as long as edge states are present. This is in qualitative agreement with what is expected for conductance oscillations originating from

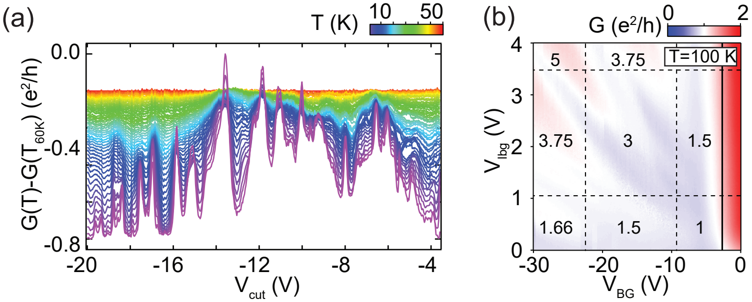

Figure 8.4. Temperature dependence of the conductance in the bipolare regime. a, Temperature dependence of the linecut indicated with the orange line in Fig. 8.3a where a background ($G(T = 60$ K$)$) was subtracted. With increasing temperature the valley-isospin signal becomes weaker and eventually vanishes. **b,** Same conductance as shown in Fig. 8.3a but at T =100 K. Expected conductance values assuming full edge state equilibration along the p-n junction according to equation 2.56 are given with the black numbers.

valley-isospin physics since it is the valley-isospin in the range of the magnetic length l_B ~25.6 nm/$\sqrt{\mathrm{B}\ [\mathrm{T}]}$ which matters [45].

8.3.2. Temperature dependence

The temperature dependence of the oscillations is shown in Fig. 8.4a where we observe an increase of the oscillation amplitude up to the order of e^2/h while approaching the base-temperature of 1.6 K. On the other hand, the valley-isospin oscillations vanish around ~60 K due to the scattering processes which start to be more dominant at elevated temperature [1, 33, 239, 240].
At this point we emphasize that the theory of the valley-isospin oscillation is based on the fact that p- and n-doped regions are at their LLL ($|\nu| = 2$), while within the measured gate range Landau levels with $|\nu| > 2$ are populated as shown in Fig. 8.3a. Insight in the underlying mechanisms can be gained from measurements at elevated temperature where the scattering probability of the charge carrier is enhanced such that e.g. the valley-isospin oscillations are washed-out. According to the diffusive model presented in section 2.5.2 the conductance in the bipolar regime is given by equation 2.56. However, the expected conductance values according to equation 2.56, which are indicated in Fig. 8.4b with the black numbers, do obviously not match with the conductance of the measurement which always remains ~1 e^2/h independent of the filling factor (in the bipolar regime). This indicates that at high magnetic

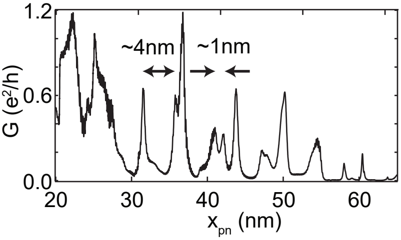

Figure 8.5. Position correlation. Rescaling an exemplary linecut (indicated in Fig. 8.3a with the green line) from $G(V_{\mathrm{BG}})$ to $G(x_{\mathrm{pn}})$.

fields higher Landau levels remain too far away to interact with the lowest Landau level due to the smoothness of the *p*-*n* junction in agreement with other theoretical and experimental studies [133, 141]. Landau levels with $|\nu| > 2$ can therefore be considered to be decoupled from the LLL and do not play a role in the transport.

8.3.3. Position correlation

Having knowledge about the correlation between x_{pn} and (V_{BG},V_{lbg}), which is shown in Fig. 8.2d, it is possible to rescale the magnetoconductance $G(V_{\mathrm{BG}})$ as a function of x_{pn} as shown in Fig. 8.5. Using the rescaled magnetoconductance one can deduce a characteristic spacing between peaks corresponding roughly to the edge disorder correlation length. We extracted values on the order of a few nanometers (with l_{B} ~9 nm). It comes as a surprise that even for edges defined by reactive ion etching, which are expected to be rough, the conductance oscillations do not fully average out [236].

8.3.4. Resolution limit

The resolution with which it is possible to resolve edge properties depends on several factors. Here we discuss two effects, namely the magnetic length and the stepsize Δx_{pn} (shift of the *p*-*n* junction between two measurement points).

Magnetic length

It was pointed out by Tworzydło et *al.* [45] that one probes the valley-isospin configuration between $\vec{\nu}_{\mathrm{B}}$ and $\vec{\nu}_{\mathrm{T}}$ within the magnetic length l_{B}. In Fig. 8.6a the evolution of a selected valley-isospin oscillation is plotted as a function of magnetic field. The evolution of the oscillation-width for a given B-field was extracted by fitting a Gaussian to each cut from which the full width at

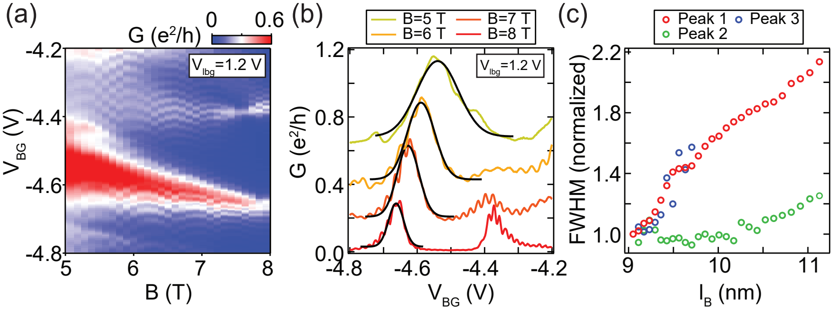

Figure 8.6. Resolution limit due to the magnetic length l_B. a, Zoom at a valley-isospin oscillation as a function of magnetic field. **b,** Representative slices from (a) for different magnetic fields (slices are offset by $0.15\,e^2/h$ for clarity). The width of the peaks were fitted with a Gaussian as shown in black. **c,** The evolution of the full width half maximum (FWHM), normalized by the FWHM at $B = 8\,$T, is plotted as a function of magnetic length l_B for three individual peaks. The data from (a,b) corresponds to Peak 1.

half maximum (FWHM) was extracted. In Fig. 8.6b four exemplary cuts from Fig. 8.6a are shown. At $B = 8\,$T two individual peaks are clearly visible and the corresponding FWHM is smallest. However, with increasing l_B (decreasing magnetic field) the peaks broaden and eventually merge into one single peak, as seen at $B = 5\,$T in Fig. 8.6b. The normalized FWHM were then plotted as a function of the magnetic length for three individual peaks, as shown in Fig. 8.6c. The increase of the extracted peak-width with increasing l_B is in qualitative agreement with what is expected. However, a more quantitative analysis seems very challenging since for the exact width-dependence as a function of l_B an isolated step (with otherwise perfectly flat edges) would be needed, which requires atomically precise control of the edges. We suspect that the different dependences of the normalized FWHM with l_B in Fig. 8.6c might be explained by the different edge configuration. This seems reasonable since at a given magnetic field the latter can give rise to various widths of the valley-isospin oscillations even without any averaging (see simulations on armchair and zigzag GNRs). Moreover, averaging over multiple steps can also lead to different dependences of the width in magnetic field.

Stepsize

The resolution with which one can map the edge properties of the GNR using the valley-isospin oscillation, as shown in Fig. 8.5, does not only depend on the magnetic length, but as well on the stepsize $\Delta x_{\rm pn}$, which must be chosen

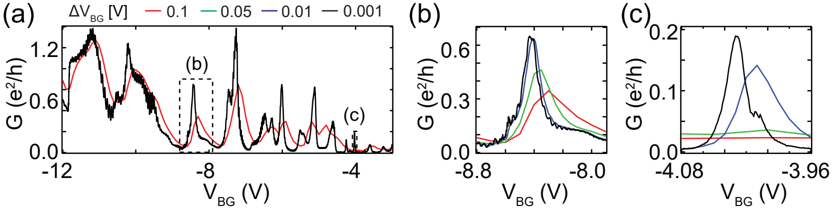

Figure 8.7. Resolution limit and rescaling. a, Linecut as indicated in Fig. 8.3a with the green line for different resolutions of ΔV_{BG}. **b,** The same linecut rescaled to x_{pn} using the correlation between x_{pn} and (V_{BG},V_{lbg}) as given in Fig. 8.2d.

accordingly[3] ($\Delta x_{\mathrm{pn}} \leq l_{\mathrm{B}}$). However, the stepsize Δx_{pn} varies as a function of V_{BG} and V_{lbg}. For a given set of values (ΔV_{BG},ΔV_{lbg}) it turns out that the resolution is highest at high charge carrier doping while it increases dramatically as soon as either of the cavities approaches its CNP [234]. The linecut shown in Fig. 8.7a was measured with different resolutions of ΔV_{BG} while V_{lbg} was fixed at 1.2 V. Far away from the Dirac peak ($V_{\mathrm{BG}} < -10\,\mathrm{V}$) a resolution of ΔV_{BG} =0.1 V seems sufficient to resolve all the peaks which are seen as well with the highest resolution (ΔV_{BG} =0.001 V). But for V_{BG} approaching the CNP only the traces with smaller stepsize of ΔV_{BG} seem to capture all the relevant features as shown in Fig. 8.7b,c. The decrease of the conductance and the absence of oscillation upon approaching the CNP (at very low doping) is explained by the extension of an insulating state with $\nu = 0$. This is in contrast to the simulation (section 8.4) where no decrease of the oscillation amplitude is observed because electron-electron interaction is not taken into account, an ingredient essential for the formation of an insulating state ($\nu = 0$ plateau).

8.3.5. Hot-spot equilibration

Another effect which might give rise to a *p*-*n* junction position dependent oscillation could be the probing of equilibration hot-spots along the sample edge. These hot spots could originate from increased local disorder or chemical doping. At high magnetic field the LLL splits due to electronic interactions [69, 70, 241], and instead of a single channel localized at zero doping two (or four) channels are formed on opposite side of the zero density region. These channels can equilibrate at the edges of the sample, where their mixing is possible, and by moving the *p*-*n* junction the equilibration rates can change

---

[3] In order to measure with sub-atomic resolution$\Delta x_{\mathrm{pn}} \sim l_{\mathrm{B}} \leq a_0$, where $a_0 \sim 1.42$ Å is the inter-carbon distance.

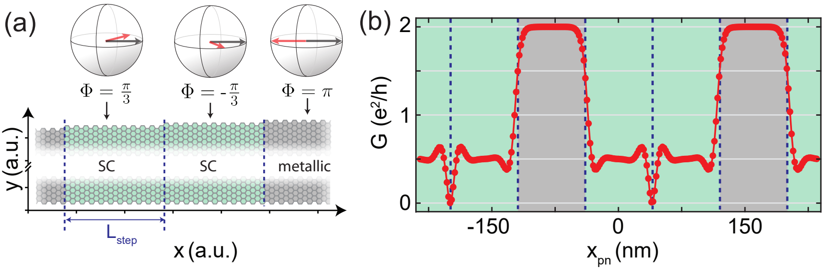

Figure 8.8. Quantum transport simulations for armchair GNRs. **a,** Illustration of the model used for the calculation shown in **b,** where the conductance as a function of x_{pn} for a ribbon with $L_{\text{step}} \gg l_{\text{B}}$ (L_{step} defined in (a)) and magnetic field B =16 T is shown. Metallic sections of the GNR are shaded in black, and semiconducting (SC) ones in green.

leading to conductance oscillation. However, since these channels are not positioned at zero charge carrier density any more, their position relative to the center of the p-n junction is also tuned by the magnetic field. This contradicts our finding, because the position of these oscillations remains magnetic field independent as shown in Fig. 8.3b. Also in the gate-gate map such oscillations might lead to more complex, hyperbolic lines as shown in chapter 7 (e.g. in Fig. **??**). The latter is opposite to our findings where the lines are fanning out linearly from the common CNP. Finally, our simulations (see below) reproduce the experimental findings even in the absence of electron-electron interaction and splitting of the lowest Landau level.

8.3.6. Summary

In summary, we see conduction oscillations with an amplitude on the order of e^2/h, which are independent of doping and magnetic field to a wide extent, but depend on x_{pn}. The latter suggests that the conductance is determined by the edge configuration and therefore by the local isospin configuration of the edges. This is supported by quantum transport simulations as shown in the next section.

8.4. Quantum transport simulations on armchair GNR

In the following transport simulations, we focus on armchair GNRs unless state otherwise. In contrast to the experiment, the exact edge profile of the GNR is known, allowing us to draw a direct relation between the edge profile and the conductance. The quantum transport simulations are based on unscaled

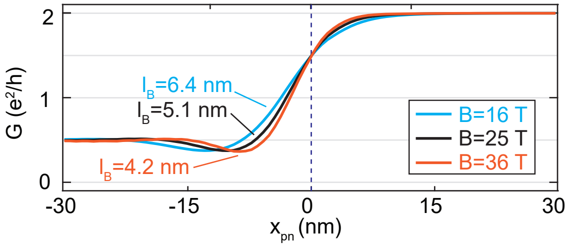

Figure 8.9. Conductance as a function of x_{pn} and magnetic field. Calculations of the conductance though a GNR (SC for $x_{\mathrm{pn}} < 0$ and metallic for $x_{\mathrm{pn}} > 0$) as a function of x_{pn} for different magnetic fields.

graphene since we want to investigate edge effects, which would scale correspondingly as well upon using scaled graphene [27, 37, 234, 242]. In order to minimize the computational load we chose small GNRs (∼40 nm in width and ∼100 nm to ∼300 nm in length) for the calculation presented in the following unless specified otherwise.

8.4.1. Ideal model

For our model we considered nonparallel edges with one side flat and one side tilted (flat regions followed by a change of the ribbon width by one row of atoms), as sketched in Fig. 8.8a. The resulting conductance G will be solely determined by the position of the p-n junction x_{pn}. Figure 8.8b shows $G(x_{\mathrm{pn}})$ for a ribbon with at a constant magnetic field $B = 16\,\mathrm{T}$. Note that the rather strong B (corresponding to $l_{\mathrm{B}} \sim 4.3\,\mathrm{nm}$) is considered here to ensure $l_{\mathrm{B}} \ll W$ as in our experiment. If the p-n junction is tuned far away from the transition regions, where Φ is π or $\pm\pi/3$, the conductance shows plateaus with 0.5 or $2\,\mathrm{e}^2/\mathrm{h}$ (conductance values as expected by equation 8.1). However, by approaching a transition region, the conductance $G(x_{\mathrm{pn}})$ undergoes a smooth transition between the two adjacent conductance plateaus, deviating from 0.5 or $2\,\mathrm{e}^2/\mathrm{h}$ [243]. In Fig. 8.9 the transition-region[4] is calculated for three different magnetic fields. From the calculation in Fig. 8.9 one can see that the transition length between two adjacent plateaus clearly depends on l_{B}, which is in agreement with the expectations of Ref. [45] and our measurements.

---

[4] The quantum-transport calculation in Fig. 8.9 is based on a GNR with a single-atomic step at the top-edge located at $x = 0$.

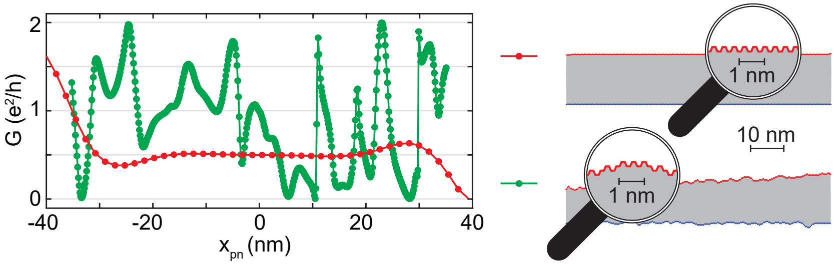

Figure 8.10. Influence of edge roughness. Calculation comparable to Fig. 8.8b (B =16 T, l_{B}~6.5 nm) in the absence (red, $L_{\mathrm{step}} \gg l_{\mathrm{B}}$) and presence (green, δL~1 nm, δW~4 nm) of edge disorder. The real-space structure of the ideal and disordered edge is shown on the right of the graph (same scale in the horizontal axes).

8.4.2. Edge disorder

Having perfect armchair edges, it is L_{step} which defines the distance at which the number of unit cells between bottom- and top-edge varies. However, upon introducing a random edge roughness (details see below), the regular pattern of $G(x_{\mathrm{pn}})$ naturally randomizes where oscillations with high amplitudes remain, although they become irregular. These findings are summarized in Fig. 8.10 directly comparing a GNR with perfect (red curve) and disordered (green curve) edges. The distance between neighbouring peaks in the disordered case is on the order of the magnetic length, similar to what has been observed in the experiment in Fig. 8.7b. The exact edge configuration of the GNRs used in the simulation is shown on the right-hand side of Fig. 8.10.

The mathematical model describing the edge roughness includes two relevant parameters, namely the correlation length (dL) and the correlation amplitude (dW) [244, 245]. For the calculation presented in Fig. 8.10 we used dL =1 nm and dW =4 nm, where the resulting edges are stabilized such that no dangling bonds remain.

8.4.3. Zigzag GNR

To complement the quantum transport calculations on armchair GNRs we performed similar calculations on zigzag GNRs as shown in Fig. 8.11. The conductance takes the values of 0 and 2 e^2/h far away from the transition region (Fig. 8.11a), which is in perfect agreement with the values expected from theory [45]. However, in contrast to the armchair GNRs, the transition region in between plateaus is shorter for the case of zigzag GNRs but still remains roughly within the predicted value of $\sim l_{\mathrm{B}}$. Upon introducing edge

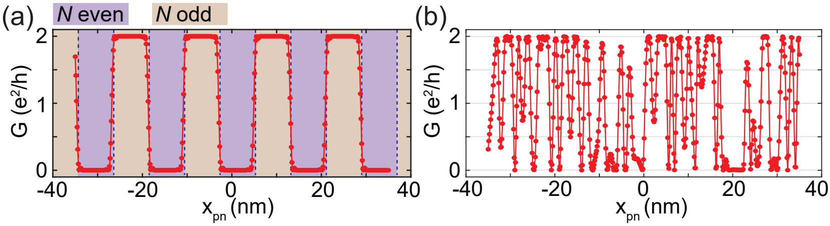

Figure 8.11. Quantum transport simulations for zigzag GNRs. a, Calculation of the conductance as a function of x_{pn} similar to Fig. 8.8b using the same values of L =100 nm, W =40 nm, B =16 T. **b,** Calculation as in (a) but with disordered edges, including the same correlation length (dL =1 nm) and correlation amplitude (dW =4 nm) as in Fig. 8.10.

disorder an oscillation of the conductance results as shown in Fig. 8.11b. The faster oscillations can be attributed to the shorter transition region in between plateaus as described above. The results obtained for zigzag GNR are in agreement with the results expected from ideal [45] and disordered GNRs [236].

8.4.4. Gate and field dependent simulations

To qualitatively reproduce the features reported in our experiment, we consider (for simplicity) a clean and edge disorder-free ribbon (W~80 nm and L~100 nm) with its charge carrier density individually tunable in the left (n_{L}) and right (n_{R}) region. The slope of the tilted edge is such that the chirality changes about every 2 nm, and the p-n junction shifts a few tens of nanometers. With a fixed magnetic field of B =36 T, Fig. 8.12a shows a radial oscillation pattern fanning out from the common CNP of $G(n_{\mathrm{R}}, n_{\mathrm{L}})$, similar to Fig. 8.3a. Finally, we examine the magnetic field dependence of the conductance along the density sweep indicated in Fig. 8.12a by the black arrow. The horizontal fringes clearly visible in Fig. 8.12b indicate the independence of the conductance on B, similar to our measurement reported in Fig. 8.3b. Note that within the density range marked in Fig. 8.12a and considered in Fig. 8.12b, the position of the p-n junction shifts by about 30 nm, covering about 15 steps and hence 5 periods of the alternating edge chirality, well agreeing with the number of the observed fringes shown in Fig. 8.12a and Fig. 8.12b.

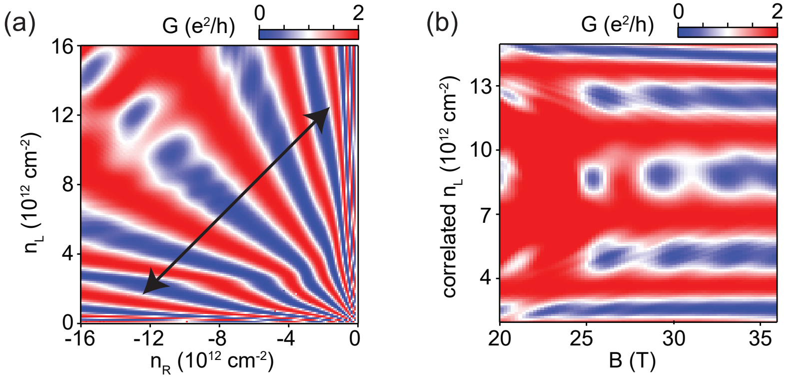

Figure 8.12. Quantum transport simulations of the conductance as a function of the gates and magnetic field at B = 36 T. a, Conductance of another ribbon (see text) as a function of left and right densities, $G(n_\mathrm{R}, n_\mathrm{L})$. The black arrow indicates the density sweep considered in **b,** where the conductance as a function of the correlated n_L and B is shown.

8.5. Conclusion

In summary, we have shown first signatures of conductance oscillations originating from the local isospin configuration of the edges of a graphene flake. Although the edge of the flake is not controlled, the conductance is still defined by the local properties of the edges and the local width of the flake, in agreement with transport simulations. Furthermore, we can exclude that the equilibration between edge states at the intersection between p-n junction and the graphene edges (so called hot-spots) is responsible for the conductance oscillations. We have observed similar oscillation in more than 15 p-n and p-n-p devices, some of them also having naturally cleaved graphene flakes [179] (presumably less edge defects compared to reactive ion etching), and also on suspended p-n junctions (not shown). Finally, there are new techniques appearing, such as hydrogen-plasma etching [129–131] or chemical synthesis of GNRs [132], allowing for a much better control over the edges. This could be used in further studies to draw a correlation between transport measurement and the edge of the measured samples (e.g. via atomic resolution imaging) underlining the isospin origin of these oscillations.

9 Michelson Morley interferometer

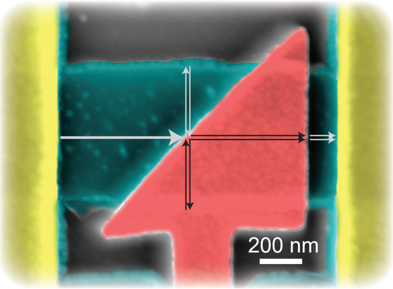

In this last experimental chapter, another type of interference experiment is discussed, which complements the Fabry-Pérot interferometer presented in chapter 6. While the latter belongs to the class of multi-mode interferometers, another class is the two-path interferometer. Probably one of the most famous two-path interference experiment is the so-called Michelson-Morley interferometer (MMI) by A. Michelson and E. Morley [246]. With this experiment the two physicists investigated in 1887 the hypothesis that the propagation of light requires a medium which was called "ether". The experiment consists of several key-components, namely a (monochromatic) light-source, a beam-splitter which is basically a semi-transparent mirror splitting the incoming light into two separate paths with a fixed length, mirrors at the end of each path which reflect the light back to the semi-transparent mirror where they can recombine and finally reach the detector. The experiment was based on the idea that if the light propagates in the "ether", penetrating the universe and therefore moving with a certain velocity with respect to the earth - then the observed interference pattern should change by changing the global orientation of the experiment. However, by doing so no change was observed, thus the hypothesis of the "ether" could be disproved.

With the recent progress in graphene, providing an excellent platform to realize semi-transparent interfaces via *p*-*n* junction in combination with ballistic and phase coherent transport [40, 41, 234], the realization of an electronic counterpart of the Michelson Morley experiment seems within reach. While various two-path interferometers such as double-slit experiments [247–249] or the electronic version of a Mach-Zehnder interferometer [220] have been realized in 2DEGs, their realization in graphene is yet to happen. In this chapter a measurement configuration to realize a Michelson Morley interferometer in graphene is presented which might provide a conclusive method to directly prove negative refraction in graphene [28, 34] and to demonstrate the utility of graphene based electron-optical elements such as beam-splitters or mirrors. This could be of great interest for the realization of entangled states [250] in graphene.

9.1. Concept and Theory

The electronic counter-part of the MMI experiment in graphene, where the source and drain take the place of the light-source and detector respectively, the *p*-*n* junction acts as a semi-transparent mirror and the graphene edges act as mirrors as sketched in Fig. 9.1a. The position of one of the mirrors and the detector is reversed with respect to the optical setup as a consequence of the negative refraction at the *p*-*n* junction in graphene. In Fig. 9.1b the two-terminal realization in a hBN/graphene/hBN heterostructure is shown. Assuming an ideal device including ballistic and phase coherent transport, specular reflection at the graphene edges and a very-sharp *p*-*n* junction (section 2.2) results in $T(\theta) = \cos(45°)^2 = 0.5$, the phase ($\phi$) acquired by a wave ($\Psi$) being once reflected and once transmitted (includes two possible combinations) at the *p*-*n* junction is given by:

$$\phi_1 = \int_0^{\mathrm{l_p}+2\mathrm{w_p}} \vec{k}_{\mathrm{p}} d\vec{l} + \int_0^{\mathrm{l_n}} \vec{k}_{\mathrm{n}} d\vec{l} = -|\vec{k}_{\mathrm{p}}|(l_{\mathrm{p}} + 2w_{\mathrm{p}}) + |\vec{k}_{\mathrm{n}}|l_{\mathrm{n}} \tag{9.1}$$

and

$$\phi_2 = \int_0^{\mathrm{l_p}} \vec{k}_{\mathrm{p}} d\vec{l} + \int_0^{2\mathrm{w_n}+\mathrm{l_n}} \vec{k}_{\mathrm{n}} d\vec{l} = -|\vec{k}_{\mathrm{p}}|l_{\mathrm{p}} + |\vec{k}_{\mathrm{n}}|(2w_{\mathrm{n}} + l_{\mathrm{n}}) \tag{9.2}$$

where the minus sign in the p-doped region comes from the fact that the $\vec{k}$-vectors in p- and n-doped regime are of opposite sign (section 2.2). Interference between electrons and holes has already been demonstrated in diffusive, but phase-coherent devices, using a dual-gated Aharanov-Bohm rings [251]. Furthermore, for an efficient operation of the MMI negative refraction with $|\theta_{\mathrm{in}}| = |\theta_{\mathrm{out}}|$ is required, thus one can write $|\vec{k}_{\mathrm{p}}| = |\vec{k}_{\mathrm{n}}| = |\vec{k}|$ (symmetric *p*-*n* junction). The phase difference between Ψ_1 and Ψ_2, which accounts for the interference effect, is then given by:

$$\Delta\phi = -2|\vec{k}|(w_{\mathrm{n}} + w_{\mathrm{p}}) \tag{9.3}$$

where $w_{\mathrm{n}} + w_{\mathrm{p}}$ defines the total width (W) of the device. This implies that the resonance condition is equivalent for all incoming waves (as long as they

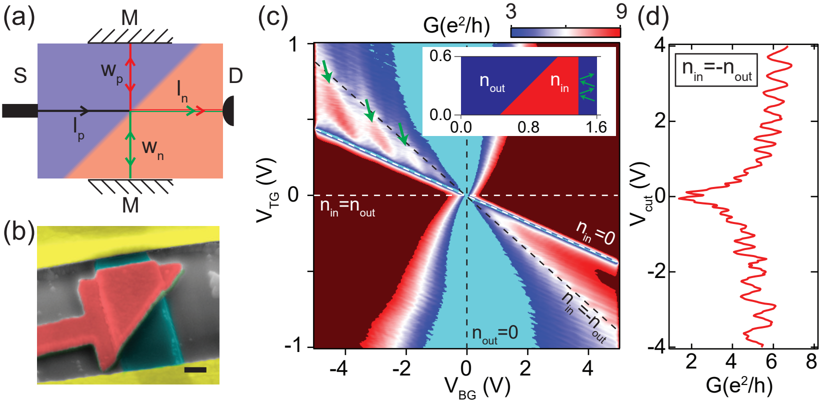

Figure 9.1. Michelson-Morley interferometer in hBN/graphene/hBN heterostructures. a, Schematic of the device where a p-n junction is tilted by 45° with respect to the charge carrier trajectories. S,D and M indicate source, drain and the edges which operate as mirrors. **b,** False-color SEM image of a two-terminal device. The leads are indicated in yellow, the top-gate in red and the hBN/graphene/hBN heterostructure in cyan. The thin MgO layer below the top-gate (green) passivates the exposed graphene edges of the etched heterostructure. Scale-bar equals 200 nm. **c,** Tight-binding simulation of a device as shwon in the inset (values in µm) or in (b). **d,** Linecut along symmetric doping in the bipolar regime ($n_{\text{in}} = -n_{\text{out}}$) where interference is observed.

hit the p-n interface under a 45° angle) and only depends on the total width of the device and the $\vec{k}$-vector of the charge carriers. The spacing between the expected interference peaks is given by equation 6.1 as derived for the Fabry-Pérot resonances, but the width of the device replaces the cavity-width.

The main challenges in the experiment are the realization of a very sharp p-n junction to allow large transmission angles and well defined edges which reflect specularly and phase coherently. A tight-binding simulation on scaled graphene for a device geometry as shown in Fig. 9.1b is given in Fig. 9.1c. Note that in contrast to the sketch shown in Fig. 9.1a, in the real device an additional p-n junction parallel to the contacts is added due to the use of a triangular shaped top-gate. This is not only because the fabrication of local top-gates overlapping with a contact is challenging (section 4.3), but more because it acts as a collimator for the charge carriers which are injected with a random angle from the source [34, 252]. The signal of the MMI is present along the line of symmetric p-n junction ($|n_{\text{in}}| = -|n_{\text{out}}|$) as shown in

Fig. 9.1d, however it is rather small. A small signal is expected because: i) The transmission probability at 45° is below the ideal value of 0.5 because the *p*-*n* junction cannot be classified as "sharp" where $d \ll \lambda_\mathrm{F}$ (section 2.2). ii) However, for an effective collimation, a very soft *p*-*n* junction would be ideal. Even-though the *p*-*n* junction parallel to the leads will be responsible for a certain degree of collimation, charge carriers with a quite large angular spread will be transmitted, giving rise to a smearing of the signal. The pronounced features in the bipolar regime ($n_\mathrm{out} < 0$) indicated with the green arrows are attributed to Fabry-Pérot resonances between the lead and the parallel *p*-*n* junction (collimator).
Note that in this calculation perfect edges were used, but upon introducing a random edge disorder of around ∼10 nm[1] the interference signal vanishes. The latter might be one of the main-challenges to overcome in experimental devices as shown in the following section.

9.2. Measurements

We performed measurements on various types of devices, divided into different "generations". With each generation we tried to implement major improvements. In the following a chronological list of the different device generations is given. For all devices we used a combination of the global back-gate and a local top-gate to tune the charge carriers in the different cavities independently.

1st generation (two-terminal, edges defined via reactive ion etching):
We started with the most simple device geometry, namely a two-terminal device where the edges were defined via reactive ion etching shown in Fig. 9.1b. A representative measurement of such a device is shown in Fig. 9.2a where the MMI signal is absent. The charge carrier mobility of $\mu \sim 90\,000\,\mathrm{cm^2V^{-1}s^{-1}}$ might be one among several limiting factors to see the Michelson Morley interference. Since in *p*-*n*-*p* devices Fabry-Pérot resonances (chapter 6) over comparable distances were observed it does not seem to be the only limiting factor. Two further major drawbacks of this design are: i) The edge roughness induced via reactive ion etching might be strong enough to completely wash-out the signal upon reflection. This assumption is supported by tight-binding simulations, but we lack experimental proof of this hypothesis. It is worth noting that in TMF experiments (section 2.3.2) specular reflection at edges defined via reactive ion etching did not pose a major problem. However, the latter does not depend on phase coherent transport either. Currently we lack a deeper knowledge on how effectively rough edges influence the phase coherence upon reflection. ii) Due to the exposed graphene edges a thin layer of MgO

---

[1] This number is realistic for edges defined via reactive ion etching.

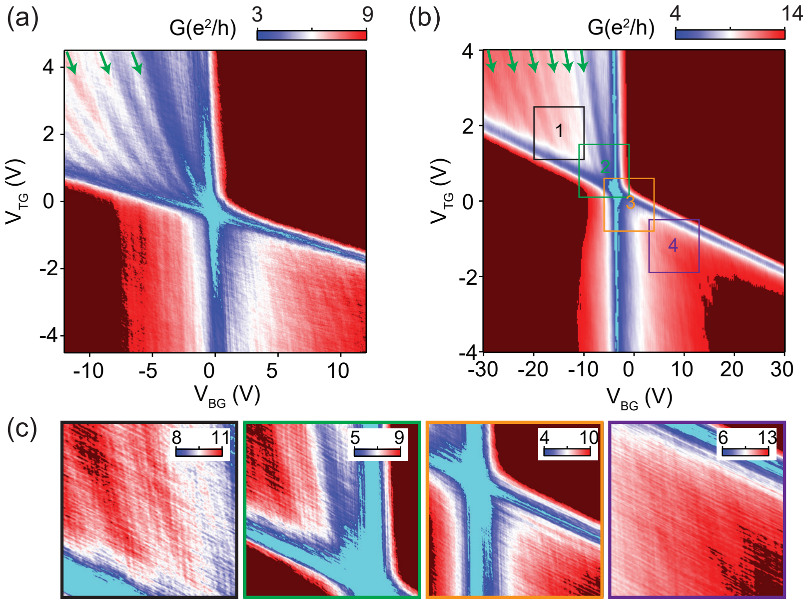

Figure 9.2. Measurements in two-terminal devices. a, Conductance as a function of the global bottom-gate and the local top-gate for a device where the graphene edges were defined via reactive ion etching as shown in Fig. 9.1b. The green arrows indicate Fabry-Pérot resonances between the leads and the collimator. **b,** Comparable measurement for a device with naturally torn edges. **c,** Zoom of the insets shown in (b).

was evaporated between the metallic top-gates and the hBN/graphene/hBN heterostructure in order to prevent a short (section 4.3). This additional layer significantly increases the *p*-*n* junction smoothness, thus lowering the transmission probability at the tilted *p*-*n* junction.

2nd generation (two-terminal, naturally torn edges):

In the 2$^{\text{nd}}$ generation of devices we tried to overcome the problem of rough edges by choosing naturally torn graphene flakes with parallel edges, which are presumably much smoother compared to the ones defined via reactive ion etching [179]. Furthermore, using natural edges allows the fabrication of sharper *p*-*n* junctions since no additional dielectric to passivate the exposed graphene edges is required (section 4.3.1). The sharper *p*-*n* junction is an advantage and disadvantage at the same time, because the transmission probability at

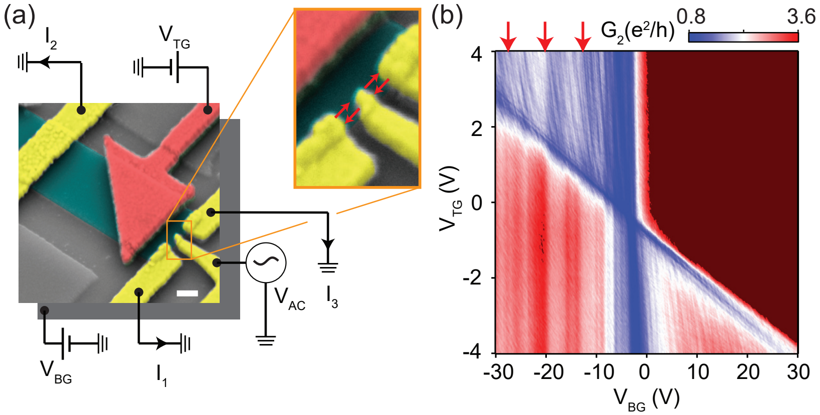

Figure 9.3. Split-contacts. a, False-color SEM image of a device with split-contacts. Zoom: Indicates the possibility of additional Fabry-Pérot oscillations. Scale-bar equals 200 nm.**b,** Measurement of the conductance G_2 as a function of global back-gate and local top-gate.

the tilted *p*-*n* junction will be increased, while the collimator operates less effectively. In Fig. 9.2b a measurement of such a device having a charge carrier mobility of $\mu \sim 60\,000\,\mathrm{cm}^2\mathrm{V}^{-1}\mathrm{s}^{-1}$ is shown. The MMI is expected to be most pronounced at low doping[2] because there the wavelength is the longest and consequently the *p*-*n* junction appears effectively much sharper. Therefore high-resolution maps at lower doping are shown in Fig. 9.2c. Unfortunately no MMI signal was observed in this configuration either. We speculate that the large background signal originating from charge carriers being reflected at the *p*-*n* junctions and thus being scattered within the different cavities, account for a large background signal which makes it very challenging to observe the small signal of the MMI.

3rd generation (multi-terminal, edges defined via reactive ion etching):

The last generation of devices produced is based on the idea to absorb the charge carriers which are reflected at the collimator *p*-*n* junction. In Fig. 9.3a a false-color SEM image with the measurement configuration of a four-terminal device is shown. Here the charge carriers are injected at the central contact on the right, while the current is simultaneously measured at the three remaining

---

[2] Note that in a diffusive sample the mean free path will be shortest at low doping according to equation 2.41. However, in a fully ballistic sample this might not hold.

contacts. Two of them (I_1 and I_3) are responsible to drain the reflected charge carriers, while the signal of interest is measured at I_2. The conductance (G_2) as a function of local top-gate and global back-gate is plotted in Fig. 9.3b. In the presented device the mobility is too low ($\mu \sim 40\,000\,\mathrm{cm^2V^{-1}s^{-1}}$) to observe ballistic transport over the full device length, therefore it is not surprising that no MMI signal was observed. However, interference over a shorter distance could be observed, namely the oscillations indicated in Fig. 9.3b with the red arrows. The period of the latter roughly fits to the distance between the split-contacts. Therefore we suspect that these oscillations can be attributed to Fabry-Pérot resonances as sketched in the inset of Fig. 9.3a with the red arrows.

9.3. Outlook and Conclusion

In conclusion, multiple devices were measured, having different types of edges and different lead configurations. So far the observation of the MMI signal remains elusive, which can have several reasons, ranging from disordered graphene edges, non-ideal measurement configurations (leads, top-gates) up to a limited bulk graphene quality. For further devices the following improvements are suggested:

- **Reduce edge roughness to a minimum**: The use of naturally torn graphene edges seems a reasonable start, but significant improvement could yield the use of edges defined via plasma-etching [129–131, 253], which are atomically precise.
- **Sharp *p*-*n* junction**: Using either natural edges or defined via plasma-etching does not require an additional passivation of the edges otherwise exposed by reactive ion etching. Upon using a local graphite bottom-gate and local top-gates the thickness between both gates and graphene is exclusively defined via the thickness of the bottom- and top-hBN layer respectively. A *p*-*n* junction where the charge carrier density varies within $d \sim 20\,\mathrm{nm}$ seems therefore realistic, thus leading to significantly sharper *p*-*n* junctions.
- **Improved collimator**: Implementing a more effective collimator in order to approach the ideal case where all incoming charge carriers have a 45° angle with respect to the tilted *p*-*n* junction. For an efficient collimator the parallel and tilted *p*-*n* junctions have to be fabricated independently, since the former should be as soft as possible, while the latter should be as sharp as possible. Two alternative approaches are presented in Ref. [254] and Ref. [206]. The former is based on a pin-hole collimator while in the latter a parabolic-shaped *p*-*n* junction is used

to create an beam of parallel charge carrier trajectories. In addition, absorbers, such as shown in Fig. 9.3a, might be implemented on both sides of the devices.

Implementation of all improvements might complicate the device fabrication significantly, therefore a detailed analysis on the impact of each of the suggested improvements should be useful. However, these analysis go beyond the scope of this Thesis and are therefore left for other studies.

10 Summary and Outlook

In this Thesis various quantum transport phenomena in encapsulated graphene *p*-*n* or *p*-*n*-*p* junctions were discussed. A short introduction covering the most important physical concepts with respect to this Thesis was given in **chapter 2**, followed by a short comparison between suspended and encapsulated graphene devices in **chapter 3**. While each of the two techniques have their own advantages and disadvantages, encapsulation of graphene in hexagonal boron nitride qualified itself to be more suitable for the experiments performed in this Thesis. The fabrication details which were presented in **chapter 4** consequently covered the encapsulation technique. This included details how electrical contacts, electrostatic-gates or constrictions with respect to this system were fabricated.

Chapter 5 introduced a novel method to establish inner point contacts, which complement the side- [1] and top-contacts to graphene. In contrast to the side- and top-contacts, inner point contacts hold the potential to create an isolated contact in the middle of a graphene sheet. The herein presented method, which is compatible with the dry-stacking technique, enables its combination with ballistic transport studies [193, 195, 206]. The use of a Ga-FIB instead of conventional e-beam lithography and subsequent etching allows a higher degree of control on the point contact size and shape. As a proof of principle we fabricated four inner point contacts in a row, which allowed to perform multiple two- and four-terminal measurements. In high magnetic fields we demonstrated insulation between neighbouring contacts, a characteristic expected for inner point contacts. In future studies inner point contacts might be combined with an electrostatic lens in order to create highly directional (collimated) electron beams [206]. The latter might significantly increase the signal visibilities of several electron-optical experiments such as for example transverse magnetic focusing [31, 206].

In **chapter 6** the observation of Fabry-Pérot resonances in a *p*-*n*-*p* junction in the absence and presence of a Moiré superlattice was discussed. It was shown that the visibility of the Fabry-Pérot resonances can be used to deduce informations about the *p*-*n* junction, such as its relative smoothness. The experimental findings are in good agreement with quantum transport simulations suggesting that the *p*-*n* junctions defined via electrostatic gates are significantly softer compared to the *p*-*n* junctions formed in the proximity of the contacts (n-doped) if the bulk is p-doped. Furthermore, using a simple model assuming a cavity which is defined via a “hard-wall potential”, the effective cavity length could be deduced considering two neighbouring peaks of the conductance oscillations. Even more, the exceptional quality of the Fabry-Pérot resonances allowed to study the exact evolution of the cavity-length as a function of charge carrier density, yielding a tunability of nearly 100 nm per p-n junction within the applied gate range. In the presence of a Moiré superlattice it was shown that it is not only possible to establish a semi-transparent interfaces in the bipolar regime, but as well in the unipolar regime if the Fermi-energies on opposite sides of the interface are tuned across the satellite DP. The different visibilities of the Fabry-Pérot resonances resulting from semi-transparent interfaces created by either the main or the satellite DPs are in qualitative agreement with what would be expected considering the theoretical calculated band reconstruction [110]. In future experiments it would be interesting to study the evolution of the Fabry-Pérot resonances as a function of density, or the Berry-phase attributed to the satellite DPs. In a wider context, the detailed study of semi-transparent interfaces (beam-splitter) is of great interest since they can be used for electron optical elements or for creating entangled states [250, 255].

Upon applying a magnetic field, the charge carriers start to move in skipping orbits (edges) and snake states (p-n junction) respectively. By applying a stronger magnetic field, the classical picture of skipping orbits and snake states is normally replaced with the picture of edge states. In **chapter 7** we presented experimental results of three different types of magnetoconductance oscillations along a graphene p-n junction within the same measurement. These oscillations are carefully characterized with respect to their doping, magnetic field, bias and temperature dependence. This allows us to consistently assign the different types of magnetoconductance oscillations to either snake states or Aharanov-Bohm interferences. Motivated by the co-existence of the two effects within a limited parameter range in our experiments, we have motivated the appearance of snake states as coherent oscillation between Landau levels.

In **chapter 8** transport through a p-n junction at high magnetic field is discussed. In this regime the transport is dominated by the lowest Landau level. The fact that in the lowest Landau level the K/K' valleys are directly linked to the A/B sublattice [57] allows to access the valley degree of freedom with the measurement-configuration as presented in this chapter [45]. We demonstrate by shifting the position of the p-n junction at high magnetic fields that the variation of the local edge configuration is responsible for the observed conductance oscillation faning out linearly from the common charge neutrality point. Even though the exact configuration of the graphene edges is not known, it was shown that the spacing of the conductance oscillation is on the same order than the correlation length of the edge disorder in GNR which are defined via reactive ion etching. Furthermore, quantum transport simulations were performed to investigate the transition from perfect to disordered GNRs, revealing a good qualitative agreement with our experimental results. It is for the first time that experimental results observing conductance oscillations originating from valley-isospin physics are presented. It is surpirising that the oscillations survived even though the edges are disordered. This includes experimental and theoretical studies which might focus on GNRs with well controlled edges or the role of interacting and splitting of Landau levels. In a wider context, being able to access the valley degree of freedom in graphene [105] allows to manipulate, process and store informations other than using the electrical charge or the spin-degree of freedom [138]. This might be of special interest for a new generation of device operation in the future.

In the last experimental chapter, **chapter 9**, the electronic counterpart of a Michelson Morley interferometer was introduced. In contrast to the Fabry-Pérot interferometer which belongs to the class of multi-mode interferometers, the Michelson Morley interferometer is a two-path interferometer similar to the Mach-Zehnder interferometer. Even though no interference signal could be detected in the experiment yet, conceptual ideas, theoretical calculations and preliminary results were discussed. Furthermore, suggestions on how to circumvent the currently encountered problems based on the experimental findings, eventually leading to a possible realization of this experiment are given. Similar to the knowledge gained from the experiment observing Fabry-Pérot resonances, this experiment might lead to a deeper understanding on the realization of beam-splitters and mirrors in graphene and how to efficiently use them. Furthermore, it would be an elegant way to directly proof negative refraction in graphene, complementing the results of previous studies [28, 34].

To sum up, the results presented within this Thesis can help to better understand the behaviour of p-n junctions in graphene. There are still several open questions which require a better understanding of some details, however, soon more complex device architectures including interferometers based on p-n junctions, point contacts and quantum point contacts will be investigated. The advance of graphene fabrication, the modification of its properties such as inducing ferromagnetic or superconducting correlations, pave the road to novel device concepts. Interesting times and devices are ahead of us.

Bibliography

[1] L. Wang, I. Meric, P. Y. Huang, Q. Gao, Y. Gao, H. Tran, T. Taniguchi, K. Watanabe, L. M. Campos, D. A. Muller, J. Guo, P. Kim, J. Hone, K. L. Shepard, and C. R. Dean, Science **342**, 614 (2013).

[2] T. Ando, A. B. Fowler, and F. Stern, Rev. Mod. Phys. **54**, 437 (1982).

[3] K. S. Novoselov, A. K. Geim, S. V. Morozov, D. Jiang, Y. Zhang, S. V. Dubonos, I. V. Grigorieva, and A. A. Firsov, Science **306**, 666 (2004).

[4] H. W. Kroto, J. R. Heath, S. C. O'Brien, R. F. Curl, and R. E. Smalley, Nature **318**, 162 (1985).

[5] S. Iijima, Nature **354**, 56 (1991).

[6] P. R. Wallace, Phys. Rev. **71**, 622 (1947).

[7] R. E. Peierls, Ann. I. H. Poincare **5**, 177 (1935).

[8] L. D. Landau, Phys. Z. Sowjetunion **11**, 545 (1937).

[9] J. A. Venables, G. D. T. Spiller, and M. Hanbucken, Reports on Progress in Physics **47**, 399 (1984).

[10] J. Evans, P. Thiel, and M. Bartelt, Surface Science Reports **61**, 1 (2006).

[11] J. Warner, F. Schaffel, M. Rummeli, and A. Bachmatiuk, *Graphene* (Elsevier, 2012).

[12] K. S. Novoselov, A. K. Geim, S. V. Morozov, D. Jiang, M. I. Katsnelson, I. V. Grigorieva, S. V. Dubonos, and A. A. Firsov, Nature **438**, 197 (2005).

[13] Y. Zhang, Y.-W. Tan, H. L. Stormer, and P. Kim, Nature **438**, 201 (2005).

[14] O. Klein, Z. Phys. **53**, 157 (1929).

[15] M. I. Katsnelson, K. S. Novoselov, and A. K. Geim, Nat Phys **2**, 620 (2006).

[16] S. V. Morozov, K. S. Novoselov, M. I. Katsnelson, F. Schedin, L. A. Ponomarenko, D. Jiang, and A. K. Geim, Phys. Rev. Lett. **97**, 016801 (2006).

[17] F. V. Tikhonenko, D. W. Horsell, R. V. Gorbachev, and A. K. Savchenko, Phys. Rev. Lett. **100**, 056802 (2008).

[18] F. V. Tikhonenko, A. A. Kozikov, A. K. Savchenko, and R. V. Gorbachev, Phys. Rev. Lett. **103**, 226801 (2009).

[19] A. K. Geim and I. V. Grigorieva, Nature **499**, 419 (2013).

[20] J. R. Schaibley, H. Yu, G. Clark, P. Rivera, J. S. Ross, K. L. Seyler, W. Yao, and X. Xu, Nature Reviews Materials **1**, 16055 (2016).

[21] C. R. Dean, A. F. Young, I. Meric, C. Lee, L. Wang, S. Sorgenfrei, K. Watanabe, T. Taniguchi, P. Kim, K. L., Shepard, and J. Hone, Nat Nano **5**, 722 (2010).

[22] F. Withers, O. Del Pozo-Zamudio, A. Mishchenko, A. P. Rooney, A. Gholinia, K. Watanabe, T. Taniguchi, S. J. Haigh, A. K. Geim, A. I. Tartakovskii, and K. S. Novoselov, Nat Mater **14**, 301 (2015).

[23] K. Takada, H. Sakurai, E. Takayama-Muromachi, F. Izumi, R. A. Dilanian, and T. Sasaki, Nature **422**, 53 (2003).

[24] D. K. Efetov, L. Wang, C. Handschin, K. B. Efetov, J. Shuang, R. Cava, T. Taniguchi, K. Watanabe, J. Hone, C. R. Dean, and P. Kim, Nat Phys **12**, 328 (2015).

[25] B. Huang, G. Clark, E. Navarro-Moratalla, D. R. Klein, R. Cheng, K. L. Seyler, D. Zhong, E. Schmidgall, M. A. McGuire, D. H. Cobden, W. Yao, D. Xiao, P. Jarillo-Herrero, and X. Xu, Nature **546**, 270 (2017).

[26] J. R. Williams, T. Low, L. M. S., and M. C. M., Nat Nano **6**, 222 (2011).

[27] P. Rickhaus, M.-H. Liu, P. Makk, R. Maurand, S. Hess, S. Zihlmann, M. Weiss, K. Richter, and C. Schönenberger, Nano Lett. **15**, 5819 (2015).

[28] G.-H. Lee, G.-H. Park, and H.-J. Lee, Nat Phys **11**, 925 (2015).

[29] A. S. Mayorov, R. V. Gorbachev, S. V. Morozov, L. Britnell, R. Jalil, L. A. Ponomarenko, P. Blake, K. S. Novoselov, K. Watanabe, T. Taniguchi, and A. K. Geim, Nano Lett. **11**, 2396 (2011).

[30] L. Banszerus, M. Schmitz, S. Engels, M. Goldsche, K. Watanabe, T. Taniguchi, B. Beschoten, and C. Stampfer, Nano Lett. **16**, 1387 (2016).

[31] T. Taychatanapat, K. Watanabe, T. Taniguchi, and P. Jarillo-Herrero, Nat Phys **9**, 225 (2013).

[32] V. E. Calado, S.-E. Zhu, S. Goswami, Q. Xu, K. Watanabe, T. Taniguchi, G. C. A. M. Janssen, and L. M. K. Vandersypen, Appl. Phys. Lett. **104**, 023103 (2014).

[33] M. Lee, J. R. Wallbank, P. Gallagher, K. Watanabe, T. Taniguchi, V. I. Fal'ko, and D. Goldhaber-Gordon, Science **353**, 1526 (2016).

[34] S. Chen, Z. Han, M. M. Elahi, K. M. M. Habib, L. Wang, B. Wen, Y. Gao, T. Taniguchi, K. Watanabe, J. Hone, A. W. Ghosh, and C. R. Dean, Science **353**, 1522 (2016).

[35] M. Barbier, G. Papp, and F. M. Peeters, Appl. Phys. Lett. **100**, 163121 (2012).

[36] Milovanović, M. Ramezani Masir, and F. M. Peeters, Appl. Phys. Lett. **105**, 123507 (2014).

[37] P. Rickhaus, P. Makk, M.-H. Liu, E. Tóvári, M. Weiss, R. Maurand, K. Richter, and C. Schönenberger, Nat Commun **6**, 6470 (2015).

[38] T. Taychatanapat, J. Y. Tan, Y. Yeo, K. Watanabe, T. Taniguchi, and B. Özyilmaz, Nat Commun **6**, 6093 (2015).

[39] L. Campos, A. Young, K. Surakitbovorn, K. Watanabe, T. Taniguchi, and P. Jarillo-Herrero, Nat Commun **3**, 1239 (2012).

[40] A. L. Grushina, D.-K. Ki, and A. F. Morpurgo, Appl. Phys. Lett. **102**, 223102 (2013).

[41] P. Rickhaus, R. Maurand, M.-H. Liu, M. Weiss, K. Richter, and C. Schönenberger, Nat Commun **4**, 2342 (2013).

[42] A. Varlet, M.-H. Liu, V. Krueckl, D. Bischoff, P. Simonet, K. Watanabe, T. Taniguchi, K. Richter, K. Ensslin, and T. Ihn, Phys. Rev. Lett. **113**, 116601 (2014).

[43] M. Shalom, M. J. Zhu, V. I. Fal'ko, A. Mishchenko, A. V. Kretinin, K. S. Novoselov, C. R. Woods, K. Watanabe, T. Taniguchi, A. K. Geim, and J. R. Prance, Nat Phys **12**, 318 (2016).

[44] E. V. Calado, S. Goswami, G. Nanda, M. Diez, A. R. Akhmerov, Akhmerov, K. Watanabe, T. Taniguchi, T. M. Klapwijk, and L. M. K. Vandersypen, Nat Nano **10**, 761 (2015).

[45] J. Tworzydło, I. Snyman, A. R. Akhmerov, and C. W. J. Beenakker, Phys. Rev. B **76**, 035411 (2007).

[46] S. Morikawa, S. Masubuchi, R. Moriya, K. Watanabe, T. Taniguchi, and T. Machida, Appl. Phys. Lett. **106**, 183101 (2015).

[47] D. S. Wei, T. van der Sar, J. D. Sanchez-Yamagishi, K. Watanabe, T. Taniguchi, P. Jarillo-Herrero, B. I. Halperin, and A. Yacoby, "Mach-zehnder interferometry using spin- and valley-polarized quantum hall edge states in graphene," ArXiv:1703.00110.

[48] A. Young, Y. Zhang, and P. Kim, *Physics of graphene*, edited by H. Aoki and M. Dresselhaus (Springer International Publishing, 2014).

[49] C. Kittel, *Introduction to Solit State Physics* (Wiley, 2nd edition, 1986).

[50] A. H. Castro Neto, F. Guinea, N. M. R. Peres, K. S. Novoselov, and A. K. Geim, Rev. Mod. Phys. **81**, 109 (2009).

[51] G. W. Semenoff, Phys. Rev. Lett. **53**, 2449 (1984).

[52] M. O. Goerbig, Rev. Mod. Phys. **83**, 1193 (2011).

[53] G. Yu, R. Jalil, B. Belle, A. Mayorov, P. Blake, F. Schedin, S. Morozov, L. Ponomarenko, F. Chiappini, S. Wiedmann, U. Zeitler, M. Katsnelson, A. Geim, K. Novoselov, and D. Elias, Proc. Nat. Acad. Sci. **110**, 3282 (2013).

[54] P. L. McEuen, M. Bockrath, D. H. Cobden, Y.-G. Yoon, and S. G. Louie, Phys. Rev. Lett. **83**, 5098 (1999).

[55] T. Ando, T. Nakanishi, and R. Saito, Journal of the Physical Society of Japan **67**, 2857 (1998).

[56] G. P. Mikitik and Y. V. Sharlai, Phys. Rev. Lett. **82**, 2147 (1999).

[57] Y. Zheng and T. Ando, Phys. Rev. B **65**, 245420 (2002).

[58] A. F. Young and P. Kim, Nat Phys **5**, 222 (2009).

[59] A. V. Shytov, M. S. Rudner, and L. S. Levitov, Phys. Rev. Lett. **101**, 156804 (2008).

[60] E. Hall, American Journal of Mathematics **2**, 287 (1879).

[61] K. v. Klitzing, G. Dorda, and M. Pepper, Phys. Rev. Lett. **45**, 494 (1980).

[62] M. Monteverde, C. Ojeda-Aristizabal, R. Weil, K. Bennaceur, M. Ferrier, S. Guéron, C. Glattli, H. Bouchiat, J. N. Fuchs, and D. L. Maslov, Phys. Rev. Lett. **104**, 126801 (2010).

[63] F. D. M. Haldane, Phys. Rev. Lett. **61**, 2015 (1988).

[64] K. S. Novoselov, Z. Jiang, Y. Zhang, S. V. Morozov, H. L. Stormer, U. Zeitler, J. C. Maan, G. S. Boebinger, P. Kim, and A. K. Geim, Science **315**, 1379 (2007).

[65] M. Tsukada, J. Phys. Soc. Jpn. **41**, 1466 (1976).

[66] S. Iordansky, Solid State Communications **43**, 1 (1982).

[67] R. E. Prange and R. Joynt, Phys. Rev. B **25**, 2943 (1982).

[68] M. O. Goerbig, Comptes Rendus Physique **12**, 369 (2011).

[69] Y. Zhang, Z. Jiang, J. P. Small, M. S. Purewal, Y.-W. Tan, M. Fazlollahi, J. D. Chudow, J. A. Jaszczak, H. L. Stormer, and P. Kim, Phys. Rev. Lett. **96**, 136806 (2006).

[70] A. F. Young, C. R. Dean, L. Wang, H. Ren, P. Cadden-Zimansky, K. Watanabe, T. Taniguchi, J. Hone, K. L. Shepard, and P. Kim, Nat Phys **8**, 550 (2012).

[71] X. Du, I. Skachko, F. Duerr, A. Luican, and E. Y. Andrei, Nature **462**, 192 (2009).

[72] L. Zhang, Y. Zhang, M. Khodas, T. Valla, and I. A. Zaliznyak, Phys. Rev. Lett. **105**, 046804 (2010).

[73] D. A. Abanin and L. S. Levitov, Phys. Rev. B **78**, 035416 (2008).

[74] J. R. Williams, D. A. Abanin, L. DiCarlo, L. S. Levitov, and C. M. Marcus, Phys. Rev. B **80**, 045408 (2009).

[75] P. Rickhaus, *Electron optics in ballistic graphene*, Ph.D. thesis, University of Basel (2015).

[76] V. V. Cheianov and V. I. Fal'ko, Phys. Rev. B **74**, 041403 (2006).

[77] F. Sauter, Zeitschrift für Physik **73**, 547 (1932).

[78] E. Pallecchi, A. C. Betz, J. Chaste, G. Fève, B. Huard, T. Kontos, J.-M. Berroir, and B. Placais, Phys. Rev. B **83**, 125408 (2011).

[79] K. Nomura and A. H. MacDonald, Phys. Rev. Lett. **98**, 076602 (2007).

[80] N. Shon and T. Ando, Journal of the Physical Society of Japan **67**, 2421 (1998).

[81] K. Ziegler, Phys. Rev. Lett. **97**, 266802 (2006).

[82] I. L. Aleiner and K. B. Efetov, Phys. Rev. Lett. **97**, 236801 (2006).

[83] P. M. Ostrovsky, I. V. Gornyi, and A. D. Mirlin, Phys. Rev. B **74**, 235443 (2006).

[84] M. Katsnelson and A. Geim, Philosophical Transactions of the Royal Society of London A: Mathematical, Physical and Engineering Sciences **366**, 195 (2008).

[85] E. H. Hwang and S. Das Sarma, Phys. Rev. B **77**, 115449 (2008).

[86] A. S. Mayorov, D. C. Elias, I. S. Mukhin, S. V. Morozov, L. A. Ponomarenko, K. S. Novoselov, A. K. Geim, and R. V. Gorbachev, Nano Lett. **12**, 4629 (2012).

[87] B. Terres, L. A. Chizhova, F. Libisch, J. Peiro, D. Jorger, S. Engels, A. Girschik, K. Watanabe, T. Taniguchi, S. V. Rotkin, J. Burgdorfer, and C. Stampfer, Nat Commun **7**, 11528 (2016).

[88] J. J. Palacios, Phys. Rev. B **82**, 165439 (2010).

[89] S. Das Sarma, S. Adam, E. H. Hwang, and E. Rossi, Rev. Mod. Phys. **83**, 407 (2011).

[90] G. L. Klimchitskaya and V. M. Mostepanenko, Phys. Rev. B **93**, 245419 (2016).

[91] V. S. Tsoi, J. Bass, and P. Wyder, Rev. Mod. Phys. **71**, 1641 (1999).

[92] C. Handschin, B. Fülöp, P. Makk, S. Blanter, M. Weiss, K. Watanabe, T. Taniguchi, S. Csonka, and C. Schönenberger, Appl. Phys. Lett. **107**, 183108 (2015).

[93] V. S.-W. Chung, P. Samuelsson, and M. Büttiker, Phys. Rev. B **72**, 125320 (2005).

[94] E. Bieri, M. Weiss, O. Schöktas, M. Hauser, C. Schönenberger, and S. Oberholzer, Phys. Rev. B **79**, 245324 (2009).

[95] V. V. Cheianov, V. Fal'ko, and B. L. Altshuler, Science **315**, 1252 (2007).

[96] G. Seelig and M. Büttiker, Phys. Rev. B **64**, 245313 (2001).

[97] C. Johansson and J. Linde, Annalen der Physik **78**, 439 (1925).

[98] M. Yankowitz, J. Xue, D. Cormode, J. D. Sanchez-Yamagishi, K. Watanabe, T. Taniguchi, P. Jarillo-Herrero, P. Jacquod, and B. J. LeRoy, Nat Phys **8**, 382 (2012).

[99] C. R. Woods, L. Britnell, A. Eckmann, R. S. Ma, J. C. Lu, H. M. Guo, X. Lin, G. L. Yu, Y. Cao, R. V. Gorbachev, A. V. Kretinin, J. Park, L. A. Ponomarenko, M. I. Katsnelson, Y. N. Gornostyrev, K. Watanabe, T. Taniguchi, C. Casiraghi, H.-J. Gao, A. K. Geim, and K. S. Novoselov, Nat Phys **10**, 451 (2014).

[100] G. L. Yu, R. V. Gorbachev, J. S. Tu, A. V. Kretinin, Y. Cao, R. Jalil, F. Withers, L. A. Ponomarenko, B. A. Piot, M. Potemski, D. C. Elias, X. Chen, K. Watanabe, T. Taniguchi, I. V. Grigorieva, K. S. Novoselov, V. I. Fal'ko, A. K. Geim, and A. Mishchenko, Nat Phys **10**, 525 (2014).

[101] Z. Shi, C. Jin, W. Yang, L. Ju, J. Horng, X. Lu, H. A. Bechtel, M. C. Martin, D. Fu, J. Wu, K. Watanabe, T. Taniguchi, Y. Zhang, X. Bai, E. Wang, G. Zhang, and F. Wang, Nat Phys **10**, 743 (2014).

[102] B. Hunt, J. D. Sanchez-Yamagishi, A. F. Young, M. Yankowitz, B. J. LeRoy, K. Watanabe, T. Taniguchi, P. Moon, M. Koshino, P. Jarillo-Herrero, and R. C. Ashoori, Science **340**, 1427 (2013).

[103] L. A. Ponomarenko, R. V. Gorbachev, G. L. Yu, D. C. Elias, R. Jalil, A. A. Patel, A. Mishchenko, A. S. Mayorov, C. R. Woods, J. R. Wallbank, M. Mucha-Kruczynski, B. A. Piot, M. Potemski, I. V. Grigorieva, K. S. Novoselov, F. Guinea, V. I. Fal'ko, and A. K. Geim, Nature **497**, 594 (2013).

[104] C. R. Dean, L. Wang, P. Maher, C. Forsythe, F. Ghahari, Y. Gao, J. Katoch, M. Ishigami, P. Moon, M. Koshino, T. Taniguchi, K. Watanabe, K. L. Shepard, J. Hone, and P. Kim, Nature **497**, 598 (2013).

[105] R. V. Gorbachev, J. C. W. Song, G. L. Yu, A. V. Kretinin, F. Withers, Y. Cao, A. Mishchenko, I. V. Grigorieva, K. S. Novoselov, L. S. Levitov, and A. K. Geim, Science **346**, 448 (2014).

[106] L. Wang, Y. Gao, B. Wen, Z. Han, T. Taniguchi, K. Watanabe, M. Koshino, J. Hone, and C. R. Dean, Science **350**, 1231 (2015).

[107] P. Wang, B. Cheng, O. Martynov, T. Miao, L. Jing, T. Taniguchi, K. Watanabe, V. Aji, C. N. Lau, and M. Bockrath, Nano Lett. **15**, 6395 (2015).

[108] M. T. Greenaway, E. E. Vdovin, A. Mishchenko, O. Makarovsky, A. Patane, J. R. Wallbank, Y. Cao, A. V. Kretinin, M. J. Zhu, S. V. Morozov, V. I. Fal'ko, K. S. Novoselov, A. K. Geim, T. M. Fromhold, and L. Eaves, Nat Phys **11**, 1057 (2015).

[109] C. Kumar, M. Kuiri, J. Jung, T. Das, and A. Das, Nano Lett. **16**, 1042 (2016).

[110] J. R. Wallbank, A. A. Patel, M. Mucha-Kruczynski, A. K. Geim, and V. I. Fal'ko, Phys. Rev. B **87**, 245408 (2013).

[111] P. Moon and M. Koshino, Phys. Rev. B **90**, 155406 (2014).

[112] J. R. Wallbank, M. Mucha-Kruczynski, X. Chen, and V. I. Fal'ko, Annalen der Physik **527**, 359 (2015).

[113] G. Chen, M. Sui, D. Wang, S. Wang, J. Jung, P. Moon, S. Adam, K. Watanabe, T. Taniguchi, S. Zhou, M. Koshino, G. Zhang, and Y. Zhang, Nano Lett. **17**, 3576 (2017).

[114] E. Wang, X. Lu, S. Ding, W. Yao, M. Yan, G. Wan, K. Deng, S. Wang, G. Chen, L. Ma, J. Jung, A. V. Fedorov, Y. Zhang, G. Zhang, and S. Zhou, Nat Phys **12**, 1111 (2016).

[115] J. Jung, A. M. DaSilva, A. H. MacDonald, and S. Adam, Nat Commun **6**, 6308 (2015).

[116] W. Yao, D. Xiao, and Q. Niu, Phys. Rev. B **77**, 235406 (2008).

[117] D. Xiao, G.-B. Liu, W. Feng, X. Xu, and W. Yao, Phys. Rev. Lett. **108**, 196802 (2012).

[118] Y. Shimazaki, M. Yamamoto, I. V. Borzenets, K. Watanabe, T. Taniguchi, and S. Tarucha, Nat Phys **11**, 1032 (2015).

[119] M. Sui, G. Chen, L. Ma, W.-Y. Shan, D. Tian, K. Watanabe, T. Taniguchi, X. Jin, W. Yao, D. Xiao, and Y. Zhang, Nat Phys **11**, 1027 (2015).

[120] F. Guinea, M. I. Katsnelson, and A. K. Geim, Nat Phys **6**, 30 (2010).

[121] F. Guinea, A. K. Geim, M. I. Katsnelson, and K. S. Novoselov, Phys. Rev. B **81**, 035408 (2010).

[122] D. Bischoff, F. Libisch, J. Burgdörfer, T. Ihn, and K. Ensslin, Phys. Rev. B **90**, 115405 (2014).

[123] K. Nakada, M. Fujita, G. Dresselhaus, and M. S. Dresselhaus, Phys. Rev. B **54**, 17954 (1996).

[124] Y.-W. Son, M. L. Cohen, and S. G. Louie, Nature **444**, 347 (2006).

[125] Z. Qiao, S. A. Yang, B. Wang, Y. Yao, and Q. Niu, Phys. Rev. B **84**, 035431 (2011).

[126] M. Y. Han, B. Özyilmaz, Y. Zhang, and P. Kim, Phys. Rev. Lett. **98**, 206805 (2007).

[127] J. Llinas, G. Fairbrother, A Borin Barin, W. Shi, K. Lee, S. Wu, B. Yong Choi, R. Braganza, J. Lear, N. Kau, W. Choi, C. Chen, Z. Pedramrazi, T. Dumslaff, A. Narita, X. Feng, K. Müllen, F. Fischer, A. Zettl, P. Ruffieux, E. Yablonovitch, M. Crommie, R. Fasel, and J. Bokor, "Short channel field effect transistors with 9-atom and 13-atom wide graphene nanoribbons," ArXiv:1605.06730.

[128] Z. Chen, Y.-M. Lin, M. J. Rooks, and P. Avouris, *International Symposium on Nanometer-Scale Quantum Physics*, Physica E: Low-dimensional Systems and Nanostructures **40**, 228 (2007).

[129] G. Dobrik, L. Tapasztó, and L. Biró, Carbon **56**, 332 (2013).

[130] Z. Shi, R. Yang, L. Zhang, Y. Wang, D. Liu, D. Shi, E. Wang, and G. Zhang, Adv. Mater. **23**, 3061 (2011).

[131] R. Yang, L. Zhang, Y. Wang, Z. Shi, D. Shi, H. Gao, E. Wang, and G. Zhang, Adv. Mater. **22**, 4014 (2010).

[132] J. Cai, P. Ruffieux, R. Jaafar, M. Bieri, T. Braun, S. Blankenburg, M. Muoth, A. P. Seitsonen, M. Saleh, X. Feng, K. Mullen, and R. Fasel, Nature **466**, 470 (2010).

[133] N. N. Klimov, S. T. Le, J. Yan, P. Agnihotri, E. Comfort, J. U. Lee, D. B. Newell, and C. A. Richter, Phys. Rev. B **92**, 241301 (2015).

[134] D. A. Abanin and L. S. Levitov, Science **317**, 641 (2007).

[135] J. R. Williams, L. DiCarlo, and C. M. Marcus, Science **317**, 638 (2007).

[136] V. Lukose, R. Shankar, and G. Baskaran, Phys. Rev. Lett. **98**, 116802 (2007).

[137] J. M. Pereira, F. M. Peeters, and P. Vasilopoulos, Phys. Rev. B **75**, 125433 (2007).

[138] N. Tombros, C. Jozsa, M. Popinciuc, H. T. Jonkman, and B. J. van Wees, Nature **448**, 571 (2007).

[139] C. W. J. Beenakker, Rev. Mod. Phys. **80**, 1337 (2008).

[140] B. Özyilmaz, P. Jarillo-Herrero, D. Efetov, D. A. Abanin, L. S. Levitov, and P. Kim, Phys. Rev. Lett. **99**, 166804 (2007).

[141] S. W. LaGasse and J. U. Lee, Phys. Rev. B **94**, 165312 (2016).

[142] J. Xue, J. Sanchez-Yamagishi, D. Bulmash, P. Jacquod, A. Deshpande, K. Watanabe, T. Taniguchi, P. Jarillo-Herrero, and B. J. LeRoy, Nat Mater **10**, 282 (2011).

[143] R. Decker, Y. Wang, V. W. Brar, W. Regan, H.-Z. Tsai, Q. Wu, W. Gannett, A. Zettl, and M. F. Crommie, Nano Lett. **11**, 2291 (2011).

[144] M. Ishigami, J. H. Chen, W. G. Cullen, M. S. Fuhrer, and E. D. Williams, Nano Lett. **7**, 1643 (2007).

[145] C. Neumann, S. Reichardt, P. Venezuela, M. Drögeler, L. Banszerus, M. Schmitz, K. Watanabe, T. Taniguchi, F. Mauri, B. Beschoten, S. V. Rotkin, and C. Stampfer, Nat Commun **6**, 8429 (2015).

[146] J. Martin, N. Akerman, G. Ulbricht, T. Lohmann, J. H. Smet, K. von Klitzing, and A. Yacoby, Nat Phys **4**, 144 (2008).

[147] T. Ando, Journal of the Physical Society of Japan **75**, 074716 (2006).

[148] C. Dean, A. Young, L. Wang, I. Meric, G.-H. Lee, K. Watanabe, T. Taniguchi, K. Shepard, P. Kim, and J. Hone, Solid State Communications **152**, 1275 (2012).

[149] I. Martin, Y. M. Blanter, and A. F. Morpurgo, Phys. Rev. Lett. **100**, 036804 (2008).

[150] D. C. Elias, R. V. Gorbachev, A. S. Mayorov, S. V. Morozov, A. A. Zhukov, P. Blake, L. A. Ponomarenko, I. V. Grigorieva, K. S. Novoselov, F. Guinea, and A. K. Geim, Nat Phys **7**, 701 (2011).

[151] K. I. Bolotin, K. J. Sikes, J. Hone, H. L. Stormer, and P. Kim, Phys. Rev. Lett. **101**, 096802 (2008).

[152] K. Bolotin, K. Sikes, Z. Jiang, M. Klima, G. Fudenberg, J. Hone, P. Kim, and H. Stormer, Solid State Communications **146**, 351 (2008).

[153] N. Tombros, A. Veligura, J. Junesch, J. J. van den Berg, P. J. Zomer, M. Wojtaszek, I. J. V. Marun, H. T. Jonkman, and B. J. van Wees, J. Appl. Phys. **109**, 093702 (2011).

[154] Y. D. Kim, H. Kim, Y. Cho, J. H. Ryoo, C.-H. Park, P. Kim, Y. S. Kim, S. Lee, Y. Li, S.-N. Park, Y. Shim Yoo, D. Yoon, V. E. Dorgan, E. Pop, T. F. Heinz, J. Hone, S.-H. Chun, H. Cheong, S. W. Lee, M.-H. Bae, and Y. D. Park, Nat Nano **10**, 676 (2015).

[155] F.-M. Zhang, Y. He, and X. Chen, Appl. Phys. Lett. **94**, 212105 (2009).

[156] R. T. Weitz, M. T. Allen, B. E. Feldman, J. Martin, and A. Yacoby, Science **330**, 812 (2010).

[157] G. Liu, J. Velasco, W. Bao, and C. N. Lau, Appl. Phys. Lett. **92**, 203103 (2008).

[158] R. Maurand, P. Rickhaus, P. Makk, S. Hess, E. Tóvári, C. Handschin, M. Weiss, and C. Schönenberger, Carbon **79**, 486 (2014).

[159] X. Du, I. Skachko, A. Barker, and E. Y. Andrei, Nat Nano **3**, 491 (2008).

[160] D. S. Lee, V. Skakalova, R. T. Weitz, K. von Klitzing, and J. H. Smet, Phys. Rev. Lett. **109**, 056602 (2012).

[161] F. Freitag, J. Trbovic, M. Weiss, and C. Schönenberger, Phys. Rev. Lett. **108**, 076602 (2012).

[162] M. Oksanen, A. Uppstu, A. Laitinen, D. J. Cox, M. F. Craciun, S. Russo, A. Harju, and P. Hakonen, Phys. Rev. B **89**, 121414 (2014).

[163] Y. Zhao, P. Cadden-Zimansky, F. Ghahari, and P. Kim, Phys. Rev. Lett. **108**, 106804 (2012).

[164] V. Veselago, Sov. Phys. Usp. **10**, 509 (1968).

[165] A. M. Goossens, V. E. Calado, A. Barreiro, K. Watanabe, T. Taniguchi, and L. M. K. Vandersypen, Appl. Phys. Lett. **100**, 073110 (2012).

[166] A. V. Kretinin, Y. Cao, J. S. Tu, G. L. Yu, R. Jalil, K. S. Novoselov, S. J. Haigh, A. Gholinia, A. Mishchenko, M. Lozada, T. Georgiou, C. R. Woods, F. Withers, P. Blake, G. Eda, A. Wirsig, C. Hucho, K. Watanabe, T. Taniguchi, A. K. Geim, and R. V. Gorbachev, Nano Lett. **14**, 3270 (2014).

[167] W. Xing, Y. Chen, P. Odenthal, X. Zhang, W. Yuan, T. Su, Q. Song, T. Wang, J. Zhong, X. Jia, X. Xie, Y. Li, and W. Han, 2D Materials **4**, 024009 (2017).

[168] M. Xu, T. Liang, M. Shi, and H. Chen, Chem. Rev. **113**, 3766 (2013).

[169] A. Castellanos-Gomez, L. Vicarelli, E. Prada, J. O. Island, K. L. Narasimha-Acharya, S. I. Blanter, D. J. Groenendijk, M. Buscema, G. A. Steele, J. V. Alvarez, H. W. Zandbergen, J. J. Palacios, and H. S. J. van der Zant, 2D Materials **1**, 025001 (2014).

[170] L. Li, F. Yang, G. J. Ye, Z. Zhang, Z. Zhu, W. Lou, X. Zhou, L. Li, K. Watanabe, T. Taniguchi, K. Chang, Y. Wang, X. H. Chen, and Y. Zhang, Nat Nano **11**, 593 (2016).

[171] Z. Wang, D.-K. Ki, H. Chen, H. Berger, A. H. MacDonald, and A. F. Morpurgo, Nat Commun **6**, 8339 (2015).

[172] Z. Wang, D.-K. Ki, J. Y. Khoo, D. Mauro, H. Berger, L. S. Levitov, and A. F. Morpurgo, Phys. Rev. X **6**, 041020 (2016).

[173] B. Yang, M.-F. Tu, J. Kim, Y. Wu, H. Wang, J. Alicea, R. Wu, M. Bockrath, and J. Shi, 2D Materials **3**, 031012 (2016).

[174] T. Taniguchi and K. Watanabe, Journal of Crystal Growth **303**, 525 (2007).

[175] S. J. Haigh, A. Gholinia, R. Jalil, S. Romani, L. Britnell, D. C. Elias, K. S. Novoselov, L. A. Ponomarenko, A. K. Geim, and R. Gorbachev, Nat Mater **11**, 764 (2012).

[176] S. Engels, B. Terres, F. Klein, S. Reichardt, M. Goldsche, S. Kuhlen, K. Watanabe, T. Taniguchi, and C. Stampfer, Phys. Status Solidi B (2014).

[177] M. Drienovsky, F.-X. Schrettenbrunner, A. Sandner, D. Weiss, J. Eroms, M.-H. Liu, F. Tkatschenko, and K. Richter, Phys. Rev. B **89**, 115421 (2014).

[178] M. Drienovsky, A. Sandner, C. Baumgartner, M.-H. Liu, T. Taniguchi, K. Watanabe, K. Richter, D. Weiss, and E. Eroms, "Few-layer graphene patterned bottom gates for van der waals heterostructures," ArXiv:1703.05631.

[179] A. K. Geim and K. S. Novoselov, Nat Mater **6**, 183 (2007).

[180] D. Wang, G. Chen, C. Li, M. Cheng, W. Yang, S. Wu, G. Xie, J. Zhang, J. Zhao, X. Lu, P. Chen, G. Wang, J. Meng, J. Tang, R. Yang, C. He, D. Liu, D. Shi, K. Watanabe, T. Taniguchi, J. Feng, Y. Zhang, and G. Zhang, Phys. Rev. Lett. **116**, 126101 (2016).

[181] C. R. Woods, F. Withers, M. J. Zhu, Y. Cao, G. Yu, A. Kozikov, M. Ben Shalom, S. V. Morozov, M. M. van Wijk, A. Fasolino, M. I. Katsnelson, K. Watanabe, T. Taniguchi, A. K. Geim, A. Mishchenko, and K. S. Novoselov, Nat Commun **7**, 10800 (2016).

[182] M. J. Rooks, E. Kratschmer, R. Viswanathan, J. Katine, R. E. Fontana, and S. A. MacDonald, Journal of Vacuum Science & Technology B **20**, 2937 (2002).

[183] S. Minke, J. Bundesmann, D. Weiss, and J. Eroms, Phys. Rev. B **86**, 155403 (2012).

[184] S. Minke, S. H. Jhang, J. Wurm, Y. Skourski, J. Wosnitza, C. Strunk, D. Weiss, K. Richter, and J. Eroms, Phys. Rev. B **85**, 195432 (2012).

[185] D. Bischoff, T. Krähenmann, S. Dröscher, M. A. Gruner, C. Barraud, T. Ihn, and K. Ensslin, Appl. Phys. Lett. **101**, 203103 (2012).

[186] F. Oberhuber, S. Blien, S. Heydrich, F. Yaghobian, T. Korn, C. Schäller, C. Strunk, D. Weiss, and J. Eroms, Appl. Phys. Lett. **103**, 143111 (2013).

[187] A. Sandner, T. Preis, C. Schell, P. Giudici, K. Watanabe, T. Taniguchi, D. Weiss, and J. Eroms, Nano Lett. **15**, 8402 (2015).

[188] T. Müller, J. Güttinger, D. Bischoff, H. S., E. K., and T. Ihn, Appl. Phys. Lett. **101**, 012104 (2012).

[189] D. Bischoff, A. Varlet, P. Simonet, T. Ihn, and K. Ensslin, New Journal of Physics **15**, 083029 (2013).

[190] J. Gramich, *Anreev and Spin Transport in Carbon Nanotube Quantum Dot Hybrid Devices*, Ph.D. thesis, University of Basel (2016).

[191] S. Gómez, P. Burset, W. J. Herrera, and A. L. Yeyati, Phys. Rev. B **85**, 115411 (2012).

[192] J. L. Garcia-Pomar, A. Cortijo, and M. Nieto-Vesperinas, Phys. Rev. Lett. **100**, 236801 (2008).

[193] C. G. Péterfalvi, L. Oroszlány, C. J. Lambert, and J. Cserti, New Journal of Physics **14**, 063028 (2012).

[194] A. G. Moghaddam and M. Zareyan, Phys. Rev. Lett. **105**, 146803 (2010).

[195] A. A. Patel, N. Davies, V. Cheianov, and V. I. Fal'ko, Phys. Rev. B **86**, 081413 (2012).

[196] N. Davies, A. A. Patel, A. Cortijo, V. Cheianov, F. Guinea, and V. I. Fal'ko, Phys. Rev. B **85**, 155433 (2012).

[197] M. Kumar, A. Laitinen, and P. Hakonen, arXiv:1611.02742 (2016).

[198] A. Laitinen, M. Kumar, and P. Hakonen, arXiv:1612.03414 (2016).

[199] L. Onsager, Phys. Rev. **37**, 405 (1931).

[200] L. van der Pauw, Philips Research Reports **13**, 1 (1958).

[201] L. van der Pauw, Philips Technical Review **20**, 220 (1958).

[202] P. Zhang, Y. Lau, and R. Timsit, *Electron Devices, IEEE Transactions on*, IEEE Transactions on Electron Devices **59**, 1936 (2012).

[203] J. C. Maxwell, *A Treatise on Electricity and Magnetism.* (Clarendon Press, Oxford, (1904).).

[204] P. J. Zomer, M. H. D. Guimarães, J. C. Brant, N. Tombros, and B. J. van Wees, Appl. Phys. Lett. **105**, 013101 (2014).

[205] A. Castellanos-Gomez, M. Buscema, R. Molenaar, V. Singh, L. Janssen, H. S. J. van der Zant, and G. A. Steele, 2D Materials **1**, 011002 (2014).

[206] M.-H. Liu, C. Gorini, and K. Richter, Phys. Rev. Lett. **118**, 066801 (2017).

[207] A. Varlet, M.-H. Liu, D. Bischoff, P. Simonet, T. Taniguchi, K. Watanabe, K. Richter, T. Ihn, and K. Ensslin, Phys. Status Solidi RRL **10**, 46 (2016).

[208] M.-H. Liu, Phys. Rev. B **87**, 125427 (2013).

[209] A. Logg, K.-A. Mardal, and G. N. Wells, *Automated Solution of Differential Equations by the Finite Element Method* (Springer, Berlin, Heidelberg, 2012).

[210] C. Geuzaine and J.-F. Remacle, International Journal for Numerical Methods in Engineering **79**, 1309 (2009).

[211] T. R. Robinson, American Journal of Physics **80**, 141 (2012).

[212] N. Stander, B. Huard, and D. Goldhaber-Gordon, Phys. Rev. Lett. **102**, 026807 (2009).

[213] M. N. Baibich, J. M. Broto, A. Fert, F. N. Van Dau, F. Petroff, P. Etienne, G. Creuzet, A. Friederich, and J. Chazelas, Phys. Rev. Lett. **61**, 2472 (1988).

[214] G. Binasch, P. Grünberg, F. Saurenbach, and W. Zinn, Phys. Rev. B **39**, 4828 (1989).

[215] M. Julliere, Phys. Lett. A **54**, 225 (1975).

[216] J. R. Williams and C. M. Marcus, Phys. Rev. Lett. **107**, 046602 (2011).

[217] K. Kolasiński, A. Mreńca-Kolasińska, and B. Szafran, Phys. Rev. B **95**, 045304 (2017).

[218] D. S. Wei, T. van der Sar, J. D. Sanchez-Yamagishi, K. Watanabe, T. Taniguchi, P. Jarillo-Herrero, B. I. Halperin, and A. Yacoby, Sci Adv **3** (2017).

[219] C. de C. Chamon, D. E. Freed, S. A. Kivelson, S. L. Sondhi, and X. G. Wen, Phys. Rev. B **55**, 2331 (1997).

[220] Y. Ji, Y. Chung, D. Sprinzak, M. Heiblum, D. Mahalu, and H. Shtrikman, Nature **422**, 415 (2003).

[221] Y. Aharonov and D. Bohm, Phys. Rev. **115**, 485 (1959).

[222] S. Zihlmann, P. Makk, K. Watanabe, T. Taniguchi, and S. Schönenberger, “Large spin-orbit relaxation anisotropy in wse2/gr/hbn heterostructures with large proximity induced spin-orbit coupling,” .

[223] D. B. Chklovskii, B. I. Shklovskii, and L. I. Glazman, Phys. Rev. B **46**, 4026 (1992).

[224] J. G. Checkelsky, L. Li, and N. P. Ong, Phys. Rev. B **79**, 115434 (2009).

[225] B. Rosenow and B. I. Halperin, Phys. Rev. Lett. **98**, 106801 (2007).

[226] Y. Zhang, D. T. McClure, E. M. Levenson-Falk, C. M. Marcus, L. N. Pfeiffer, and K. W. West, Phys. Rev. B **79**, 241304 (2009).

[227] J. Xia, J. Chen, F. andLi, and N. Tao, Nat Nano **4**, 505 (2009).

[228] W. G. van der Wiel, Y. V. Nazarov, S. De Franceschi, T. Fujisawa, J. M. Elzerman, E. W. G. M. Huizeling, S. Tarucha, and L. P. Kouwenhoven, Phys. Rev. B **67**, 033307 (2003).

[229] P. Roulleau, F. Portier, P. Roche, A. Cavanna, G. Faini, U. Gennser, and D. Mailly, Phys. Rev. Lett. **100**, 126802 (2008).

[230] D. T. McClure, Y. Zhang, B. Rosenow, E. M. Levenson-Falk, C. M. Marcus, L. N. Pfeiffer, and K. W. West, Phys. Rev. Lett. **103**, 206806 (2009).

[231] L. Cohnitz, A. De Martino, W. Häusler, and R. Egger, Phys. Rev. B **94**, 165443 (2016).

[232] M.-H. Liu, P. Rickhaus, P. Makk, E. Tóvári, R. Maurand, F. Tkatschenko, M. Weiss, C. Schönenberger, and K. Richter, Phys. Rev. Lett. **114**, 036601 (2015).

[233] P. Rickhaus, P. Makk, M.-H. Liu, K. Richter, and C. Schönenberger, Appl. Phys. Lett. **107**, 251901 (2015).

[234] C. Handschin, P. Makk, P. Rickhaus, M.-H. Liu, K. Watanabe, T. Taniguchi, K. Richter, and C. Schönenberger, Nano Lett. **17**, 328 (2016).

[235] A. R. Akhmerov and C. W. J. Beenakker, Phys. Rev. Lett. **98**, 157003 (2007).

[236] T. Low, Phys. Rev. B **80**, 205423 (2009).

[237] C. Frässdorf, L. Trifunovic, N. Bogdanoff, and P. W. Brouwer, Phys. Rev. B **94**, 195439 (2016).

[238] J. Llinas, G. Fairbrother, A Borin Barin, W. Shi, K. Lee, S. Wu, B. Yong Choi, R. Braganza, J. Lear, N. Kau, W. Choi, C. Chen, Z. Pedramrazi, T. Dumslaff, A. Narita, X. Feng, K. Müllen, F. Fischer, A. Zettl, P. Ruffieux, E. Yablonovitch, M. Crommie, R. Fasel, and J. Bokor, Nature Communications **8**, 633 (2017).

[239] S. Sarkar, K. R. Amin, R. Modak, A. Singh, S. Mukerjee, and A. Bid, **5**, 16772 (2015).

[240] D. A. Bandurin, I. Torre, R. K. Kumar, M. Ben Shalom, A. Tomadin, A. Principi, G. H. Auton, E. Khestanova, K. S. Novoselov, I. V. Grigorieva, L. A. Ponomarenko, A. K. Geim, and M. Polini, Science **351**, 1055 (2016).

[241] F. Amet, J. Williams, K. Watanabe, T. Taniguchi, and D. Goldhaber-Gordon, Phys. Rev. Lett. **112**, 196601 (2014).

[242] H. Overweg, H. Eggimann, M.-H. Liu, A. Varlet, M. Eich, P. Simonet, Y. Lee, K. Watanabe, T. Taniguchi, K. Richter, V. I. Fal'ko, K. Ensslin, and T. Ihn, Nano Lett. **17**, 2852 (2017).

[243] T. Sekera, C. Bruder, E. J. Mele, and R. P. Tiwari, Phys. Rev. B **95**, 205431 (2017).

[244] S. M. Goodnick, D. K. Ferry, C. W. Wilmsen, Z. Liliental, D. Fathy, and O. L. Krivanek, Phys. Rev. B **32**, 8171 (1985).

[245] M. Pourfath, *The Non-Equilibrium Green's Function Method for Nanoscale Device Simulation*, edited by S. Selberherr (Springer, 2014).

[246] A. Michelson and E. Morley, American Journal of Science **34**, 333 (1887).

[247] A. Yacoby, U. Sivan, C. P. Umbach, and J. M. Hong, Phys. Rev. Lett. **66**, 1938 (1991).

[248] A. Yacoby, M. Heiblum, V. Umansky, H. Shtrikman, and D. Mahalu, Phys. Rev. Lett. **73**, 3149 (1994).

[249] R. Schuster, E. Buks, M. Heiblum, D. Mahalu, V. Umansky, and H. Shtrikman, Nature **385**, 417 (1997).

[250] G. Weihs and A. Zeilinger, "Coherence and statistics of photons and atoms," (Wiley, 2001) Chap. Photon statistics at beam-splitters: an essential tool in quantum information and teleportation.

[251] D. Smirnov, H. Schmidt, and R. J. Haug, Appl. Phys. Lett. **100**, 203114 (2012).

[252] S. Morikawa, Q. Wilmart, S. Masubuchi, K. Watanabe, T. Taniguchi, B. Placais, and T. Machida, Semiconductor Science and Technology **32**, 045010 (2017).

[253] D. Hug, S. Zihlmann, M. K. Rehmann, Y. B. Kalyoncu, T. N. Camenzind, L. Marot, K. Watanabe, T. Taniguchi, and D. M. Zumbühl, NPJ 2D Materials and Applications **1**, 21 (2017).

[254] A. W. Barnard, A. Hughes, A. L. Sharpe, K. Watanabe, T. Taniguchi, and D. Goldhaber-Gordon, Nat Commun **8**, 15418 (2017).

[255] M. Nielsen and I. Chuang, *Quantum Computation and Quantum Information*, 10th ed. (Cambridge University Press, 2010).

A Fabrication Recipes

Already in the chapter 4, fabrication techniques are discussed. The aim of this appendix is to provide details of the fabrication recipes.

A.1. hBN/graphene/hBN assembly

A.1.1. cleaning the wafer for graphene exfoliation

1. Dicing the wafer in $\sim 1\,\mathrm{cm}^2$ large chips

2. Clean in Acetone, IPA and H_2O for each $\sim 5\,\mathrm{min}$ in ultrasonic

3. Clean in Piranha solution (1:3 ratio of H_2O_2 (30 wt%):H_2SO_4 (98 wt%)) for $\sim 15\,\mathrm{min}$

4. Clean in H_2O (high purity) in a ultrasonicator for $\sim 5\,\mathrm{min}$ (3 times)

5. Blow-dry with N_2

A.1.2. Markers on Si^{++}/SiO_2 chip ($\sim$300 nm oxide)

1. Spin-coat full wafer (3 inch) with $\sim 1\,\mu\mathrm{m}$ AZ 1512 optical resist

2. Bake at 100 °C for 60 s

3. Expose with marker-grid to UV (wavelength of 365 nm)

4. Develop with MIF 726 for 17 s, stop in DI-water for 30 s

5. Metallization with 5 nm Ti + 40 nm to 60 nm Au

6. Lift-off in Acetone

A.1.3. Assembly of hBN/graphene/hBN stack following Ref. [1]

1. Spin-coat ∼1 µm Poly-propylene carbonate (PPC) (dissolved in anisole) on a Si^{++}/SiO_2 chip

2. Exfoliate top-hBN on (PPC)

3. Exfoliate graphene on Piranha cleaned Si^{++}/SiO_2 chip

4. Exfoliate bottom-hBN on the Si^{++}/SiO_2 chip (∼1 cm^2)

5. Peel-off PPC from support and transfer on home-made PDMS stamp (∼1 nm thick) which is on a glass-slide

6. Pick-up graphene at room-temperature

7. Only for devices with local bottom-gates: Pick-up bottom-hBN at room temperature

8.1. Devices with local top-gates (or no top-gates): Release half-stack (top-hBN/graphene) on bottom-hBN (raise temperature to 80 °C to release PPC from PDMS)

8.2. Devices with local bottom-gates: Release full-stack (top-hBN/graphene/bottom-hBN) on pre-patterned local bottom-gates (raise temperature to 80 °C to release PPC from PDMS)

9. Remove PPC from the complete stack with chloroform (∼1 h)

10. Thermally anneal the complete stack in a Ar/H_2 atmosphere for 3 h at 300 °C

A.2. E-beam lithography and development

A.2.1. PMMA resist for contacts and etching (negative mask)

1. Spin-coat PMMA (thickness may vary, bake at 250 °C for 15 s)

2. Expose with E-beam (V 20 keV; Dose=500 $\mu C/cm^2$)

3. Cold-development in IPA:H_2O (ratio 7:3) at ∼5 °C for 60 s, blow-dry

A.2.2. PMMA/HSQ resist for etching (positive mask)

1. Spin-coat PMMA (200 nm, bake at 250 °C for 15 s)
2. Spin-coat HSQ (100 nm, bake at 90 °C for 5 min)
3. Expose with E-beam (V =20 keV; Dose=100 µC/cm^2, use smallest current possible)
4. Develop HSQ in TMAH (25 wt%):H_2O (ratio 1:1) for 30 s, stop in H_2O for 30 s, blow-dry

A.3. Reactive ion etching

A.3.1. CHF_3:O_2 plasma

1. Parameters: CHF_3:O_2 (40 sccm/4 sccm), P =60 W, p =60 mTorr, t =60 s to 90 s
2. Etching rates:
   hBN: 20 nm/min to 30 nm/min
   SiO_2: ∼60 nm/min
   PMMA: <10 nm/min

It is used for:

- The exposure of the side-contacts before evaporation, as it yields the lowest contact resistances (down to ∼50 Ωµm).
- As it allows a very precise control of how much hBN is etched (small etching rates) it is well suited for any etching purposes if e.g. the stack must not be fully etched though (e.g. section A.5.1).

A.3.2. SF_6:Ar:O_2 plasma

1. Parameters: SF_6:Ar:O_2 (20 sccm/5 sccm/5 sccm), P =50 W, p =25 mTorr, t =20 s
2. Etching rates:
   hBN: 600 nm/min
   SiO_2: ∼20 nm/min
   PMMA: 80 nm/min

It is used for:

- It is used to define the shape of a device if the hBN/graphen/hBN heterostructure can be fully etched through.

A.3.3. O_2 plasma

1. Parameters: O_2 (20 sccm), P =60 W, p =40 mTorr, t =4 min
2. Etching rates:

   hBN: negligible

   SiO_2: negligible

   PMMA: ∼100 nm/min

   graphene: several layers per minute

It is used for:

- Etching of PMMA used as a spacer between HSQ (negative etching resist) and the device.

- Etching of the few-layer graphene which define the local bottom-gates.

A.4. Cr/Au leads

1. Type: E-beam evaporation
2. Pumping to base-pressure of $<2 \times 10^{-7}$ Pa
3. Evaporate away ∼30 nm of Cr before opening the shutter since the Cr-target was stored in ambient condition (where it oxidises)
4. Open shutter
5. Evaporate 10 nm of Cr (0.7 Å/s to 1.2 Å/s)
6. Evaporate 50 nm to 70 nm of Au (0.7 Å/s to 1.2 Å/s)

A.5. Local gated devices

A.5.1. Bottom-gates

1. Exfoliate graphite on a Si^{++}/SiO_2 chip with markers
2. Define PMMA/HSQ etching mask (section A.2.2)
3. Reactive ion etching with O_2-plasma for 4 min.
4. Remove PMMA/HSQ in warm acetone (∼2 h), flush with IPA, blow-dry with N_2

5. Anneal bottom-gates (section A.1.3)
6. Release full-stack on bottom-gates, remove PPC and anneal (section A.1.3)
7. Define PMMMA mask for contacts (section A.2.1)
8. Expose side-contacts with CHF_3:O_2 (section A.3.1)
9. Metallize (E-beam evaporation) with Cr/Au (10 nm/70 nm), lift-off in warm acetone
10. If needed, shape device with a 200 nm thick PMMA mask (section A.2.1) and a CHF_3:O_2 plasma (section A.3.1). It is important that the bottom-hBN must not be fully etched though as otherwise a short to the bottom-gates is more likely.
11. Remove PMMA mask in warm acetone.

A.5.2. Top-gate (no shaping of device required)

1. Starting with the full stack being on the Si^{++}/SiO_2 chip with markers
2. Define PMMMA mask for contacts (section A.2.1)
3. Expose side-contacts with CHF_3:O_2 (section A.3.1)
4. Metallize (E-beam evaporation) with Cr/Au (10 nm/70 nm), lift-off in warm acetone
5. Define PMMMA mask for top-gates (section A.2.1)
6. Metallize (E-beam evaporation) with Ti/Au (5 nm/70 nm), lift-off in warm acetone

A.5.3. Top-gate (shaping of device required)

1. Starting with the full stack being on the Si^{++}/SiO_2 chip with markers
2. Define PMMMA mask for contacts (section A.2.1)
3. Expose side-contacts with CHF_3:O_2 (section A.3.1)
4. Metallize (E-beam evaporation) with Cr/Au (10 nm/70 nm), lift-off in warm acetone
5. Shaping of the device with a 200 nm thick PMMA mask (section A.2.1) and a SF_6:Ar:O_2 plasma (section A.3.2).

6. Remove PMMA mask in warm acetone.
7. Define PMMMA mask for top-gates (section A.2.1)
8. Evaporate a thin MgO layer (12 nm to 14 nm) (E-beam evaporation) to passivate the exposed graphene-edges.
9. Subsequently metallize (E-beam evaporation) with Ti/Au (5 nm/70 nm) using the same PMMA layer, lift-off in warm acetone

B Skipping-trajectories along a smooth *p*-*n* junctions

B.1. Skipping-length along a smooth *p*-*n* junctions

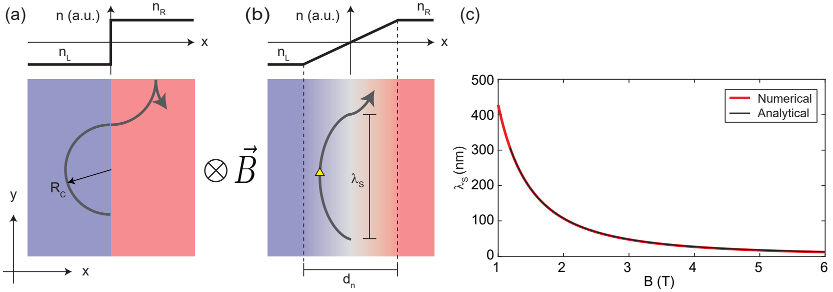

Figure B.1. Simplified and realistic snake state models. a, Simplified snake state model including a step-function which models the p-n junction. **b,** More realistic snake state model including a linear change within the distance d_n between the charge carrier density n_L and n_R across the two sides of the p-n junction. **c,** Comparison between analytically extracted skipping length λ_S from equation 7.1 in direct comparison with the values extracted from numerical calculations. Used parameters are d_n =200 nm and $n_\mathrm{L} = n_\mathrm{R}$ =$1 \times 10^{16}\,\mathrm{m}^{-2}$.

For the most simple snake state picture one considers a situation as sketched in Fig. B.1a where the p-n junction is modelled by a step-function where the absolute value of the density is constant, but opposite in sing on both sides of the p-n junction. The cyclotron radius is therefore everywhere given by:

$$R_\mathrm{C} = \frac{\hbar k_\mathrm{F}}{eB} \tag{B.1}$$

where $k_\mathrm{F} = \sqrt{|n|\pi}$. However, a more realistic model as illustrated in Fig. B.1b includes a gradual change of the charge carrier density across the p-n junction within the distance d_n. If the p-n junction is centred at $x = 0$, the bulk the charge carrier density is given by n_L and n_R for $|x| > d_\mathrm{n}/2$ while across the p-n junction (for $|x| < d_\mathrm{n}/2$) it is given by:

$$n(x) = \frac{|n_\mathrm{L} - n_\mathrm{R}|}{d_\mathrm{n}} x = S \cdot x \tag{B.2}$$

where S defines the slope. In the following we assume a positive slope as sketched in Fig. B.1b. In the following we concentrate on the regime where $|x| < d_\mathrm{n}/2$. The total force acting on a charge carrier is given by:

$$\vec{F} = \hbar \dot{\vec{k}}_\mathrm{F} = q \left(\vec{E} + \dot{r} \times \vec{B} \right), \tag{B.3}$$

where $\dot{r} = (\dot{x}, \dot{y}, 0)$, $\vec{E} = (E_\mathrm{x}, 0, 0)$ and $\vec{B} = (0, 0, B_\mathrm{z})$ as sketched in Fig. B.1b. In graphene we can write $q = -\chi e$ ($e < 0$ being the elementary charge and $\chi = \pm 1$ accounts for the electron (+) and hole (−) branch). By explicitly working out $\dot{r} \times \vec{B}$, equation B.3 can be written component wise according to:

$$\hbar \dot{k}_\mathrm{x} = -\chi e \left(E_\mathrm{x} + \dot{y} B_\mathrm{z} \right) \qquad \text{and} \qquad \hbar \dot{k}_\mathrm{y} = \chi e \dot{x} B_\mathrm{z}. \tag{B.4}$$

Furthermore, using the energy dispersion relation of graphene ($E = \chi \hbar v_\mathrm{F} k_\mathrm{F}$), where $k_\mathrm{F} = \sqrt{k_\mathrm{x}^2 + k_\mathrm{y}^2}$, the values of $\dot{x}$ and $\dot{y}$ are given by:

$$\dot{x} = \frac{\partial E(k_\mathrm{x}, k_\mathrm{y})}{\partial k_\mathrm{x}} = v_\mathrm{F} \frac{k_\mathrm{x}}{k_\mathrm{F}} \qquad \text{and} \qquad \dot{y} = \frac{\partial E(k_\mathrm{x}, k_\mathrm{y})}{\partial k_\mathrm{y}} = v_\mathrm{F} \frac{k_\mathrm{y}}{k_\mathrm{F}}. \tag{B.5}$$

Based on the semiclassical equation of motions (equation B.4 and equation B.5) we now verify for a charge carrier starting perpendicular from the p-n junction that:

- k_x and k_y perform a circular motion in k-space
- the real-space trajectory of a charge carrier is given by a cycloid.

To do so, the equation of motions are formed in such a way that the particles switche their charge when crossing the junction, but no the group velocity.

B.2. Circular motion of k_x and k_y in k-space

To prove that $\dot{k}_\mathrm{x}$ and $\dot{k}_\mathrm{y}$ perform a circular motion in k-space we start by forming the ratio of the two according to $\dot{k}_\mathrm{x}/\dot{k}_\mathrm{y} = dk_\mathrm{x}/dk_\mathrm{y}$. Using equation B.4 where $\dot{k}_\mathrm{x}$ and $\dot{k}_\mathrm{y}$ are defined, and equation B.5 leads to:

$$\frac{\dot{k}_\mathrm{x}}{\dot{k}_\mathrm{y}} = -\frac{\left(E_\mathrm{x} + v_\mathrm{F} B_\mathrm{z} \frac{k_\mathrm{y}}{k_\mathrm{F}} \right)}{v_\mathrm{F} B_\mathrm{z} \frac{k_\mathrm{x}}{k_\mathrm{F}}}. \tag{B.6}$$

The electric field E_{x} is given by:

$$E_{\mathrm{x}} = -\chi \frac{\hbar v_{\mathrm{F}}}{e} \frac{dk_{\mathrm{F}}}{dx}. \tag{B.7}$$

where

$$\frac{dk_{\mathrm{F}}}{dx} = \frac{\chi S \pi}{2k_{\mathrm{F}}}. \tag{B.8}$$

having used $k_{\mathrm{F}} = \sqrt{|n|\pi} = \sqrt{S|x|\pi}$. Finally, plugging equation B.8 into equation B.7 leads to:

$$E_{\mathrm{x}} = -\frac{\hbar v_{\mathrm{F}} S \pi}{2k_{\mathrm{F}} e}. \tag{B.9}$$

With equation B.9 we can now evaluate equation B.6, leading to:

$$\frac{dk_{\mathrm{x}}}{dk_{\mathrm{y}}} = \frac{k_0 - k_{\mathrm{y}}}{k_{\mathrm{x}}} \tag{B.10}$$

where $k_0 \equiv (\hbar S \pi)/(2eB_{\mathrm{z}})$ is a constant. Solving equation B.10 leads to:

$$k_{\mathrm{x}}^2 + (k_{\mathrm{y}} - k_0)^2 = k_0^2 \tag{B.11}$$

which describes a circular motion in k-space. From equation B.11 we can learn that at the extremum of the trajectory (yellow triangle in Fig. B.1b), $k_{\mathrm{x}} = 0$ and therefore $k_{\mathrm{y}} = k_{\mathrm{F}} = 2k_0$. The local cyclotron radius (equation B.1) at the extremum is given by:

$$R_{\mathrm{cyc}} = \frac{\hbar 2k_0}{eB} = \left(\frac{\hbar}{eB}\right)^2 S\pi. \tag{B.12}$$

B.3. Cycloid motion in real space

To verify that the circular motion in k-space describes indeed a cycloid motion in real space, we parametrize k_{x} and k_{y} on the hole side ($\chi = -1$) according to:

$$k_{\mathrm{x}} = k_0 \sin(\phi(t)) \tag{B.13}$$

and

$$k_{\mathrm{y}} = k_0(1 - \cos(\phi(t))) \tag{B.14}$$

where the initial conditions are given by: $\phi(t=0) = 0$, $k_{\mathrm{y}}(t=0) = 0$ which is increasing with time and $k_{\mathrm{x}}(t=0) = 0$ which is decreasing with time. Assuming that the cycloid motion has the same parameter $\phi(t)$, the real-space trajectory is described by:

$$x = r(\cos(\phi(t) - 1) \tag{B.15}$$

$$y = r(\phi(t) - \sin(\phi(t))) \tag{B.16}$$

and its derivative after t is then given by:

$$\dot{x} = -r\dot{\phi}(t)\sin(\phi(t)) \tag{B.17}$$

$$\dot{y} = r\dot{\phi}(t)(1 - \cos(\phi(t))) \tag{B.18}$$

The value of $\dot{\phi}(t)$ is determined the following way: The value of $\hbar\dot{k}_\mathrm{y}$ is given once by combining equation B.4 and equation B.5, and once by taking the time-derivative of equation B.14 multiplied with $\hbar$. This leads to:

$$-ev_\mathrm{F}\frac{k_\mathrm{x}}{k_\mathrm{F}}B_\mathrm{z} = \hbar k_0 \sin(\phi(t))\dot{\phi}(t). \tag{B.19}$$

By replacing k_x with equation B.13 this leads to:

$$\dot{\phi}(t) = \frac{ev_\mathrm{F}B_\mathrm{z}}{\hbar k_\mathrm{F}}. \tag{B.20}$$

Finally, by plugging

$$\begin{aligned} \sin(\phi(t)) \quad &\rightarrow \quad \text{from equation } B.13 \\ (1-\cos(\phi(t))) \quad &\rightarrow \quad \text{from equation } B.14 \\ k_0 \quad &\rightarrow \quad \text{see below equation } B.10 \\ \dot{\phi}(t) \quad &\rightarrow \quad \text{from equation } B.20 \end{aligned}$$

into the cycloid motion (equation B.17 and equation B.18) we find that the latter are equivalent with the equation of motion as given in equation B.5, if:

$$r = \frac{R_\mathrm{cyc}}{2} \quad \rightarrow \quad R_\mathrm{cyc} \text{ is defined in equation } B.12. \tag{B.21}$$

The skipping-length λ_S in a cycloid is given by $\lambda_\mathrm{S} = 2\pi r$, where r is the radius of the ”rolling circle", therefore leading to:

$$\lambda_\mathrm{S} = \left(\frac{\hbar\pi}{eB}\right)^2 S \tag{B.22}$$

which is equivalent to equation 7.1. A direct comparison between numerical result and analytical formula according to equation 7.1 is shown in Fig. B.1c, revealing an excellent agreement.

B.4. Magnetic field spacing

The magnetic field spacing can be extracted from equation 7.1. For simplicity we substitute $c \equiv (\pi\hbar)^2 S/e^2$, such that it can be written as $\lambda_\mathrm{S} = c/B^2$.

Undergoing one full oscillation period, one goes from $2\lambda_{\mathrm{S}}N = W$ to $2\lambda_{\mathrm{S}}(N+1) = W$. With equation 7.1, this can be rewritten as:

$$2\frac{c}{B_{\mathrm{N}}^2}N = W \qquad \text{and} \qquad 2\frac{c}{B_{\mathrm{N+1}}^2}(N+1) = W \tag{B.23}$$

and consequently:

$$2c = W(B_{\mathrm{N+1}}^2 - B_{\mathrm{N}}^2) = W(B_{\mathrm{N+1}} - B_{\mathrm{N}})(B_{\mathrm{N+1}} + B_{\mathrm{N}}). \tag{B.24}$$

For large N one can approximate $(B_{\mathrm{N+1}} - B_{\mathrm{N}}) \sim \Delta B$ and $(B_{\mathrm{N+1}} - B_{\mathrm{N}}) \sim 2B$. Finally, this leads to

$$\Delta B = \frac{c}{W}\frac{1}{B} \tag{B.25}$$

which is equivalent to equation 7.4.

C Biasd dependent gating effect

Here we present a very simple model in order to estimate the shift of the edge states in real space upon applying a finite bias to an Aharanov-Bohm interferometer (section 7.1.2). In the following we assume that the Aharanov-Bohm interferometer is located in the center of the p-n junction around the insulating region ($\nu = 0$), as shown in Fig. 7.1c, and we neglect a renormalization of the edge state velocity ($\beta = 0$). Furthermore, we consider a symmetric p-n junction for simplicity, where the slope S_1 is given by $S_1 = 2n_1/d_\mathrm{n}$, and n_1 corresponds to the charge carrier doping induced by the electrostatic gates. By symmetrically applying a bias of energy $E = eV_\mathrm{SD}/2$ at each sides of the p-n junction the bulk density increases from n_1 to:

$$n_2 = \frac{\left(\sqrt{n_1\pi} + \frac{eV_\mathrm{SD}}{2\hbar v_\mathrm{F}}\right)^2}{\pi} \tag{C.1}$$

as illustrated in Fig. C.1 with the grey arrows. The increase of the bulk density leads to a shift of the real space position of the edge states by Δx as indicated with the red and blue dots. Assuming that at n_1 the edge states are located

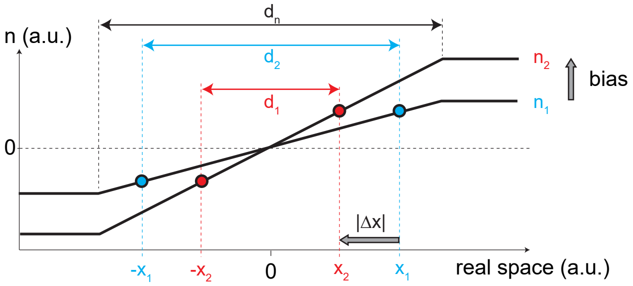

Figure C.1. Bias dependent gating effect. By applying a finite bias, the charge charier density in the bulk changes, consequently leading to a different slope across the p-n junction (if d_n remains fixed). Comparable to what is shown in Fig. 7.8b, this then leads to a shift of the real space location of the edge state (red and blue dots).

at $\pm x_1$ (symmetric p-n junction), then the new locations are given by:

$$\pm x_2 = \pm x_1 \frac{S_1}{S_2}. \tag{C.2}$$

Finally, the shift of the edge state is given by $|\Delta x| = |x_1 - x_2|$, or:

$$|\Delta x| = x_1 \left| 1 - \frac{n_1}{n_2} \right|, \tag{C.3}$$

where $S \propto n$ ($d_\mathrm{n} = \mathrm{const.}$) was used.
For the cyan magnetoconductance oscillations the gate induced bulk density was given by $n_1 \sim 9 \times 10^{15}\,\mathrm{m}^{-2}$, and the bias spacing was extracted to $V_\mathrm{SD} \sim 1.5\,\mathrm{mV}$ (Fig. 7.11c). Using equation C.1, then n_2 is given by $n_2 \sim 9.122\,\mathrm{m}^{-2}$ (at $V_\mathrm{SD} \sim 1.5\,\mathrm{mV}$). Based on the charge carrier density profile calculated from electrostatics we estimate $x_1 \sim 5\,\mathrm{nm}$ to $10\,\mathrm{nm}$. Note that the change of the edge state spacing $\Delta d = d_1 - d_2$ is given by $|2\Delta x|$, leading to $|2\Delta x| \sim 0.13\,\mathrm{nm}$ to $0.25\,\mathrm{nm}$, or $\alpha \sim 0.09\,\mathrm{nm/meV_{SD}}$ to $0.18\,\mathrm{nm/meV_{SD}}$.

Publications

- *“Co-existence of classical snake states and Aharanov-Bohm oscillations along graphene p-n junctions”*
  P. Makk*, **C. Handschin***, E. Tovari, K. Watanabe, T. Taniguchi, K. Richter, M.-H. Liu and C. Schönenberger
  in preparation

- *“Giant valley-isospin conductance oscillations in ballistic graphene”*
  C. Handschin*, P. Makk*, P. Rickhaus*, R. Maurand, K. Watanabe, T. Taniguchi, K. Richter, M.-H. Liu and C. Schönenberger
  Nano Letters **17**, 5389 (2017)

- *“Fabry-Pérot Resonances in a Graphene/hBN Moiré Superlattice”*
  C. Handschin, P. Makk, P. Rickhaus, M.-H. Liu, K. Watanabe, T. Taniguchi, K. Richter and C. Schönenberger
  Nano Letters **17**, 328 (2016)

- *“Point contacts in encapsulated graphene”*
  C. Handschin, B. Fülöp, P. Makk, S. Blanter, M. Weiss, K. Watanabe, T. Taniguchi, S. Csonka and C. Schönenberger
  Applied Physics Letters **107**, 183108 (2015)

- *“Fabrication of ballistic suspended graphene with local-gating”*
  R. Maurand, P. Rickhaus, P. Makk S. Hess, E. Tóvári, **C. Handschin**, M. Weiss and C. Schönenberger
  Carbon **79**, 486 (2014)

- *“Specular interband Andreev reflections at van der Waals interfaces between graphene and $NbSe_2$”*
  D. K. Efetov, L. Wang, **C. Handschin**, K. B. Efetov, J. Shuang, R. Cava, T. Taniguchi, K. Watanabe, J. Hone, C. R. Dean, and P. Kim
  Nat Phys **12**, 328 (2015)

* Equal contribution

Talks

- *“Fabry-Pérot resonances in a graphene/hBN Moiré superlattice”*
  QSIT Lunch Seminar, Basel, November 2016
- *“Fabry-Pérot oscillations and tunable cavity sizes”*
  Annual meeting of the Swiss Nanoscience Institute, Lenzerheide, September 2016
- *“Electron optics in encapsulated graphene”*
  Annual meeting of the Swiss Nanoscience Institute, Lenzerheide, September 2015
- *“Towards the realization of a Veselago lens”*
  Winter School of the Swiss Nanoscience Institute, Belalp, January 2015

Poster Contributions

- *Signatures of valley-isospin conductance oscillations in ballistic graphene*
  Swiss Nano Convention, Fribourg (Switzerland), May 2017
- *“Fabry-Pérot resonances in a graphene/hBN Moiré superlattice”*
  Graphene2017, Barcelona (Spain), March 2017
- *“Fabry-Pérot resonances in a graphene/hBN Moiré superlattice”*
  Winter School of the Swiss Nanoscience Institute, Zermatt (Switzerland), February 2017
- *“Novel quantum transport features in graphene”*
  QSIT General Meeting, Arosa (Switzerland), February 2017
- *“Point contacts in encapsulated graphene”*
  Swiss Nano Convention, Basel (Switzerland), June 2016
- *“Point contacts in encapsulated graphene”*
  Winter School of the Swiss Nanoscience Institute, Zinal (Switzerland), February 2016
- *“Point contacts in encapsulated graphene”*
  IWEPNM, Kirchberg (Austria), February 2016
- *“Electron optics in suspended and encapsulated graphene”*
  IWEPNM, Kirchberg (Austria), February 2015
- *“Veselago Lens in Suspended Graphene”*
  CNRS PhD School, Cargese (France), April 2014

Acknowledgements

> *If we knew what it was we were doing, it would not be called research, would it?*
>
> Albert Einstein (1879-1955)

All the results and achievements presented in this PhD-Thesis would not have been possible without the help and guidance of many people. First of all I would like to express my gratitude towards my Thesis-advisor Prof. Christian Schönenberger who offered me the opportunity to perform my PhD work in his group. His enthusiastic spirit about the topic of graphene was always inspiring for me, a constant source of motivation to push my research further. During meetings it was often Christian who challenged me with the "uncomfortable" type of questions, pointing towards weak aspects of my research. This helped me a lot to grow as a scientist, constantly trying to get to the bottom of my own research. Furthermore I greatly appreciated the scientific freedom Christian left me to pursue my projects nearly "at will" - given that reasonable scientific arguments could be presented. This allowed me to shift gears after one year moving from suspended to encapsulated devices. As I was the first one to introduce this technique here in Basel this was certainly a certain risk on how fast I can make it work. Not to forget all the group excursions or the ability to share common interests which Christian, such as mountain-biking or other outdoor-experiences, were never granted for me, and therefore I appreciated them even more.

I am very much honoured that Prof. Philip Kim and Dr. Jonathan Eroms were taking their time to read my thesis and to be part of my PhD committee. Special thanks go to Prof. Philip Kim, who gave me the opportunity to do my Master-Thesis in his group at the Columbia University. In fact it was during that year I learned many of the relevant details about the encapsulation technique of graphene in hBN, which was to my greatest benefit during the PhD. Concerning that scientific exchange I would like to thank again Prof. Christian Schönenberger, who introduced me to Prof. Philip Kim at that time, thus finally making this exchange happen.

During my PhD work, it was Dr. Péter Makk, my "super-PostDoc", who often found the right way/balance to push me, without overdoing it. Without him I would not have re-measured many samples - measurements which turned out

to be relevant later on. Furthermore, he gave me the best support one could imagine, be it by explaining physical concepts, discussing data, proof-reading papers and the Thesis or simply by filling a cryostat if needed. He always made me feel comfortable to approach him, no matter for what question, which I appreciate a lot. For his further career, starting his own group at Budapest University, I wish him nothing else than the best. Apart from Dr. Péter Makk it were Dr. Andreas Baumgartner and Dr. Gergő Fülöp who provided me with valuable inputs.
I am very grateful for the great collaboration with Ming-Hao Liu who constantly provided us with tight-binding simulations. The latter did not only give us a deeper understanding of the physics, but without him several of our publications would certainly have less relevance. I always enjoyed the mails we sent back and forth between Basel and Regensburg, or the personal meetings we had. As he recently moved back to Taiwan starting his own group, I wish him all the best for the future and I'm sure our collaboration will continue.
Besides the people mentioned so far, there are more I would like to acknowledge personally: Peter Rickhaus, who is now doing his PostDoc at ETH Zürich, introduced me passionately and patiently into the topic of (suspended) graphene during the first two years of my PhD work. With Simon Zihlmann I shared almost my entire university-career starting with the 1^{st}-semester course in Nanoscience. The many discussion on our related research projects, the ongoing help he provided me in terms of fabrication and data analysis and the long lasting friendship are priceless. Further thanks go to Srijit Goswami from TU Delft, who provided me with several valuable ideas and inputs, and with whom I had many great discussions. I would like to further acknowledge Endre Tóvári, Mirko Rehmann, Yemliha Bilal Kalyoncu, Marius Eich and Hiske Overweg for fruitfull discussion on graphene related topics. From Jörg Gramich I did not only learn many valuable fabrication details, but he also became great friend with whom I shared many adventures such as climbing, ski-touring and windsurfing. As fabrication and measurements would be much more challenging without the custom made tools from the technical and electrical workshop I would like to thank all those people as well, in particular Patrick Stöcklin, Dominik Sifrid and Michael Steinacher. Further I would like to thank former and present group-members for making my time in this group very enjoyable: Thomas Hasler, Samuel d'Hollosy, Vishal Ranjan, Lujun Wang, David Indolese, Christian Jünger, Jan Overbeck, Roy Haller, Gulibusitan Abulizi, Kishan Todkar, Frederick Thomas, Dr. Raphaelle Delagrange, Maria El Abbassi, Mihai-Cezar Harabula, Anton Vladyka and Arunav Bordoloi.

As social life was always a very crucial component to balance my life as a scientist, I would like to thank my parents Jürg and Catherine, as well as my sister Anja, who always supported me throughout my life and professional education. Visiting my parents at the countryside allowed me to leave work

related problems in the city (at least partially) and free my mind in nature. My friends outside the research group take another a special place, which is by far bigger than the length of the text I can write about them. The great time I spent with all of them often gave me the extra motivation and energy I needed to move on after scientific drawbacks.

Without all these people I would not be where I am today.

Curriculum Vitae

Clevin Jürg Handschin
Born on 5th September 1988 in Basel (Switzerland)

Education

10/2013–8/2017 **PhD in experimental physics at the University of Basel**

- Dissertation in the group of Prof. C. Schönenberger
  “Quantum-Transport in Encapsulated Graphene PN-junctions”

9/2011–8/2013 **Masters of Science in Nanoscience at the University of Basel**

- Master thesis in the group of Prof. P. Kim (Columbia University)
  “Andreev reflections and superconducting Proximity effect in lateral hBN/graphene/$NbSe_2$ quantum Hall devices”
- Project thesis in the group of Prof. P. Kim (Columbia University)
  “Manufacturing of hBN supported high quality graphene Hall bar devices with a superconducting source (drain) made of $NbSe_2$”
- Project thesis at Swiss Center for Electronics and Microtechnology (CSEM)
  “Fabrication and characterization of semi-transparent organic light emitting diodes”

8/2008–7/2011 **Bachelors of Science in Nanoscience at the University of Basel**

2007 **Matura Gymnasium Kirschgarten, Basel**

Positions

3/2014–7/2017 *Teaching assistant for physics at the University of Basel*